The Design, Modelling and Control of an Autonomous Tethered Multirotor UAV

by

Piero Graziano Ioppo

Thesis presented in partial fulfilment of the requirements for the degree of

Master of Science in Electrical & Electronic Engineering

at the University of Stellenbosch

Department of Electrical & Electronic Engineering,
Stellenbosch University,
Private Bag X1, MATIELAND 7602, South Africa

Supervisor: Mr J Treurnicht

March 2017

Declaration

By submitting this thesis electronically, I declare that the entirety of the work contained therein is my own, original work, that I am the sole author thereof (save to the extent explicitly otherwise stated), that reproduction and publication thereof by Stellenbosch University will not infringe any third party rights and that I have not previously in its entirety or in part submitted it for obtaining any qualification.

Date: .....March 2017.....

Abstract

This work details the design, modelling, control and successful demonstration of a tethered multirotor UAV system; as a first iteration towards an alternative, and more accessible, persistent aerial platform. The project focusses specifically on the development of appropriate modelling and flight control strategies, in addition to the development of a suitable practical testing platform.

The tether model is developed based on the assumption of a quasi-static catenary, which sufficiently encapsulates the dominant tether forces. The flight control strategy is catered towards the civilian landscape with a minimalist sensor configuration that aims to keep the system simple and cost-effective. A conventional control system is initially developed for the untethered system, and thereafter adapted to cater for the unique aspects of tethered flight. The control architecture implements variations of linear PID control in a successive loop closure approach.

A physical test platform is developed consisting of a $0.8\,\mathrm{m} \times 0.8\,\mathrm{m}$ quadrotor vehicle, modified to accommodate a tether. Results are presented for hardware-in-the-loop simulations as well as practical flight tests. The practical flight tests served to successfully demonstrate the developed flight control strategy, in addition to providing insight into some of the observed idiosyncrasies of tethered flight.

Acknowledgements

This project has been a massive challenge to me personally, and has been responsible for evincing every feeling in the emotional spectrum, many times over. Having said that, above all it has provided me with an incredible learning opportunity; one that I found richly rewarding. I owe an enormous amount to the various individuals who contributed to this project in various different ways. While a simple thank you does their contributions a disservice, it is the very least they deserve.

1. Firstly, to my supervisor Johann Treurnicht, who served as a great source of technical knowledge and advice, in addition to generally being a fantastic human being from whom I learned an incredible amount.
2. To Wessel Croukamp, Petro Petzer and their respective technical teams for the assistance with the hardware components of this project, and their willingness to always go the extra mile.
3. To the anomaly that is Michael Basson, our incredibly skilled safety pilot, who provided valuable insight and went out of his way to assist in the completion of the practical flight tests.
4. To my colleagues in the ESL who were always willing to offer a helping hand during testing, and who generally provided a great source of entertainment.
5. To my friends who helped out in various different ways, whether in offers to proofread or assistance elsewhere when it was needed.
6. To Ryan Maggot, to whom I probably owe my fingers, for ensuring I always operated safely and who served as a wonderful sounding board and source of advice.
7. To our one-time lab engineer extraordinaire, Cornelus le Roux, who served as a similarly wonderful sounding board and source of advice.
8. To Maxi and Ron Nosworthy who generously welcomed me into their home during the final stretch.
9. To Nonna, Anita and the Mazzaro's for the many cooked meals during the final phase of writing up; in addition to the love and support of my extended family generally.

10. To Bronwyn, my loving girlfriend and confidant, I really can't thank you enough. You served as a happy constant that made the good times better, and the difficult times that much more bearable.

11. Finally, to my amazing parents, whose love and selfl conspess support truly knows no bounds. In a wonderful upbringing and fantastic education you've given me the greatest gift, and for that I'll be forever grateful.

Contents

List of Figures

List of Tables

Chapter 1

Introduction

This chapter provides a brief introduction and summary of the research project. It begins by establishing the project context, and provides the motivation behind the research topic. Thereafter, the project objectives, research method and scope are defined, whilst the chapter concludes with an overview of the thesis structure.

1.1 Project Background

Small Unmanned Aerial Vehicles (UAVs) are being subjected to extensive research and development for use in an ever-increasing range of applications. While the exploration of UAV technology has traditionally been performed predominantly for military purposes, advances in integrated avionics systems have rendered UAV technology more accessible and UAV platforms are, as a result, rapidly growing in popularity for a number of civilian applications. This has led to an increasing demand for reliable UAV platforms, with the versatility of UAVs offering Vertical Take-off and Landing (VTOL) capabilities proving particularly attractive.

Multirotor aerial vehicles are defined as rotorcraft with three or more rotors, although they are conventionally referred to using their specific numerical prefixes (e.g. Quadrotor) with reference to the number of rotors employed. Multirotors have, in recent times, begun to fill the 'VTOL-capable UAV' niche and have emerged as a popular alternative to the standard helicopter configuration, particularly within the civilian setting. This is due to the reduced complexity of the rotorhead mechanics, which lack the intricate swashplates and linkages required for flight control in traditional helicopters. As a result, multirotor vehicles are significantly less maintenance intensive in comparison to their single or dual-rotor counterparts [1]. Flight control of multi-rotors is achieved by independently varying the speeds of the aircraft's rotors, with the symmetric nature of the rotor blade configurations subsequently resulting in reduced control complexity. The trade-off, however, lies in the loss of

Figure 1.1: Hovermast by SkySapience (left) & PARC Robot by CyPhy Works

efficiency incurred as a result of the smaller rotors employed, which are more energy intensive. The reduced efficiency levels, coupled with the current battery technology available, have resulted in limited payload capacities and flight times, typically to payloads of less than 1 kg and/or flight times of less than 20 minutes [2]. Furthermore, the relatively small sizes of these vehicles result in them being especially sensitive to small mass fluctuations. This creates somewhat of a design paradox, in that extending the flight time of the aircraft requires additional battery mass which can significantly reduce the payload capability, and visa-versa.

Recently a small number of developments in the commercial landscape have begun addressing these issues. LaserMotive [3] is currently investigating a means of wireless power transmission for various UAV platforms via laser transmitters. The benefits of such a system include the preservation of the vehicle mobility as well as impressive range, with useful beam intensities reported at distances of up to 10 km, line-of-sight permitting. However, current limitations of the concept include the low power transmission efficiencies (less than 20% for an ideal hover case) and the high capital costs involved, which look set to restrict accessibility primarily to high-resource military applications. Alternatively, the Hovermast by SkySapience [4] and the PARC robot by Cyphy Works [5] (illustrated in Figure 1.1) are two variations of proposed tethered multirotor UAV systems. In addition to providing a more efficient means of continuous power transmission, tethers can simultaneously be used for vehicle recovery and/or as a reliable, rapid and secure communications channel. The recently developed Fotokite [6] system extends this utility by using a tether as a novel means of user-vehicle interaction.

While tethered solutions do pose some obvious drawbacks, most notably to the mobility and manoeuvrability of the aircraft, they do offer a unique set of characteristics and have the potential to fulfil a number of both civil and military applications. In particular, a tethered multirotor platform provides a potentially appealing addition to the field of persistent surveillance, with the ability to monitor large areas with radar and/or high resolution cameras on land or at sea. Such platforms would offer extended range and mobility to traditional mast-mounted antennas. Furthermore, they would provide a more mobile and lesonsps conspicuous alternative to conventional tethered aerostats (blimps) and parafoils, with further benefits of rapid

deployment and retrieval, as well as a potentially broader range of environmental operating conditions.

This research forms part of the Electronic Systems Laboratory (ESL) at Stellenbosch University where the autonomous flight control of both fixed and rotary wing UAVs has been studied for several years. This work builds on the previous SLADe project [7] where the full autonomous flight capability, including landing on a translating platform, of an unmanned quadrotor vehicle was developed.

1.2 Problem Statement

In recent times, multirotor UAVs have seen a tremendous growth in popularity, primarily due to their mechanical simplicity and the increased availability and affordability of integrated avionics systems. While advances in battery technology and general aircraft efficiencies have improved things somewhat, the utility of such systems continues to be shackled by short flight times and small payload capabilities.

A tethered solution offers the possibility of continuous power transmission and indefinite flight times. Although this advantage is tempered significantly by the resulting lack of lateral and longitudinal mobility, such a system could fulfil a niche role within the industry, particularly in the field of persistent surveillance.

There is currently a very limited amount of literature and research available on tethered multirotor UAV systems, with almost none in the public domain. Thus, this research aims to provide a contribution towards the industry by extending the versatility of multirotor UAVs, and thereby broadening the boundaries of application, through the investigation of a tethered multirotor UAV system.

1.3 Project Objectives

The **principal objective** of this research is the design and practical demonstration of a multirotor UAV system capable of autonomous tethered flight. Successful tethered flight requires that the autonomous control strategy accommodates the influence of a tether on the stability of the aircraft, and makes provision for the lengthening and shortening of the tether. In addition to being capable of countering disturbances, the vehicle must be able to manoeuvre safely and effectively in a predefined flight envelope, whilst maintaining sufficient tension to keep the tether elevated in its entirety. In order to further extend its usability, the developed system is catered towards a civilian setting. This requires a concerted effort towards both cost-effectiveness and simplicity. This places limitations on the sensor configurations available, as certain sensors can prove prohibitively expensive (e.g. DGPS, RTK, load cells etc.) in the civilian landscape.

The **secondary objective** is to gain insight into the tether influence on the vehicle stability and dynamics, with the aim of benefiting future designs. This analysis includes identifying the effects of both a 'taut' and 'loose' tether configurations on the system dynamics in addition to the effect of varying the tether length.

1.4 Project Overview

A brief overview of the research methodology, with the primary project activities required to realise the research objectives, is provided in Table 1.1.

Table 1.1: Project Outline

Project Component	**Description**
Literature Survey	An analysis of similar work performed aims to identify a research gap as well as any useful modelling and control techniques.
Vehicle Modelling	The derivation of a sufficiently accurate mathematical model of the developed vehicle is required in order to adequately control the vehicle.
Tether Modelling	A similar mathematical model of the tether is required in order to investigate potential failure modes as well as to verify the control system through numerical simulation.
Control System Design	A suitable control strategy and design is required to accommodate the tether influence on the vehicle dynamics.
Hardware Implementation	In addition to the need for a practical testing platform, the physical implementation of the final designs enables Hardware-In-the-Loop (HIL) testing as a valuable final verification step before practical flight testing.
Practical Verification	Practical evaluation of the designed system is desired to substantiate the simulation results and potentially expose any unmodelled phenomena.

Certain elements of the project, such as the vehicle modelling, have been well researched and are already well established in the industry. The novel aspects of this research focus on the changes to the numerical model and autonomous flight

controller to account for the introduction of a tether. Thus, the primary project components listed in Table 1.1 can be further abridged into three core project components; namely the:

1. Tether modelling
2. Autonomous control system for tethered flight
3. Practical testing platform

Tether Modelling

To-date the tethered-UAV problem has remained relatively unexplored and, therefore, the tether model forms a focal point of this study. A mathematical model of the tether is required primarily for simulation purposes, which forms the basis of the controller design verification. The aim is to accurately simulate the resultant forces on the vehicle (originating from the tether) and how these forces fluctuate during flight. The model must accurately simulate the tether forces during both 'loose' and 'taut' tether configurations. Of particular importance are the force fluctuations during these 'loose' to 'taut' transitions.

Flight Control Strategy and Design

A tethered UAV system, with its inherently limited flight envelope and mobility, will not require prodigious performance capabilities in a traditional sense. The constrained nature of tethered flight also poses considerable risk, particularly during 'loose' to 'taut' tether transitions. Such transitions are capable of generating large impulse forces which could cause instability and lead to the vehicle crashing, especially in the likely event of the tether attachment point being offset from the vehicle centre of mass. This offset could induce an undesirable 'tether moment' which would cause the vehicle to rotate. Furthermore, taut tethered flight presents a unique control challenge as any uncertainty in the position measurement could lead to controller saturation if the tether prevents the vehicle from reaching a commanded set-point. Thus, in light of these challenges, the control philosophy adopted is a pragmatic one with an emphasis on conservatism. Disturbance rejection and general flight stability is favoured over speed of response. The flight controllers are first developed and tested on the conventional, untethered quadrotor before being adapted for the tethered case.

Practical Testing Platform

Practical flight data is desirable in effectively evaluating the proposed autonomous flight control strategy as it includes any previously unmodelled phenomena; which

may not be properly accounted for within the simulation model. A physical test platform is developed consisting of a 0.8 m×0.8 m (large by conventional standards) quadrotor vehicle, modified to accommodate a tether. A quadrotor configuration is preferred to alternative multirotor configurations primarily due to the cost-effectiveness and availability of the required hardware and components. Furthermore, the disk loading (ratio of the vehicle weight to the rotor disk area) of rotary wing aircraft is generally reduced with a reduction in the number of rotors employed, with traditional helicopters having the lowest disk loading. Lowering the disk loading improves the rotor efficiency[1] by minimising the change in velocity of the fluid through the rotor disk which, in turn, allows for longer flight times for a given vehicle mass and battery capacity.

1.5 Scope and Limitations

This research serves as a departure point, somewhat of a feasibility study if you will, into the tethered flight of multirotor UAVs. The scope and limitations associated with the research project serve to narrow the project focus in line with the defined research objectives.

Representative Tether

Typical dual data and power transmission cables commonly available are not generally designed for the purposes of tethered flight. A full working prototype will require significant research towards an optimal tether design and power supply strategy. Thus, power transmission via the tether is considered beyond the scope of this work. Batteries are instead used to power the aircraft, and further serve to simulate an added payload. The tether employed aims to be representative both in its mass and aerodynamic drag characteristics.

Flight Modes

A final working product would, in all likelihood, require a winch or similar system to control the amount of slack in the tether, particularly during take-off and landing. This would influence the dynamics during these flight modes and consequently alter the final take-off and landing strategies. Such a system might also offer an additional general flight control technique that incorporates both the aircraft and winch in controlling the tether tension. The development of such a winch system was not considered in order to limit the project scope. Thus, the developed autonomous flight controller does not consider the full flight envelope, but instead focusses on the general autonomous flight behaviour of the aircraft with a tether

[1] The mathematical justification of this concept is provided in Chapter 3.3.4

that is fixed to a stationary point on the ground. Autonomous take-off and landing strategies under a 'loose tether' configuration were not considered in order to mitigate the risks associated with the practical flight tests, especially considering that they would soon be made redundant with the development of an appropriate winch system. An additional student within the ESL is currently building on this research and investigating an autonomous tethered landing strategy, by incorporating a new winch system with the aircraft and general flight controller developed in this project.

Hardware and Sensor Configuration

The aircraft developed in this project is based on a conventional quadrotor design, primarily using off-the-shelf components. There is no attempt to radically optimise the vehicle design for use in a surveillance environment. A minimalist approach is adopted in terms of the sensor configuration selected in order to reduce the system cost and complexity, by not deviating too far from current conventional practice in the civilian landscape. Many of the specific hardware choices are based on existing legacy hardware within the ESL. This includes the onboard avionics system, which was previously developed in-house and serves as a generic kit for all current UAV projects, with modifications made as required. Additionally, optimisation of the state estimation techniques used in the ESL are considered beyond the scope of this work, with the current systems used *talis qualis*.

1.6 Thesis Outline

Having established the project context and research objectives, Chapter 2 continues with a review of the available literature that the author deemed pertinent to the research topic. It begins with a summary of the current state of research on tethered multirotor UAV systems. Thereafter the analysis is extended to include additional tethered aerial vehicles such as traditional helicopters and several flying concepts for electricity generation. A brief review of the prevailing autonomous flight control techniques employed on quadrotor vehicles is presented, including the previous work carried out internally in the ESL.

Chapter 3 presents the layout and system design of the project's practical component. Specific hardware choices and component designs are presented, along with the layout and integration of the testing hardware.

Details of the vehicle and tether models are presented separately in Chapters 4 and 5. Each includes mathematical derivations as well as a discussion on the assumptions employed and the resulting limitations.

Chapter 6 begins with a discussion on the control problem and the considerations required. An analysis of the expected tether influence on the system dynamics is

included in order to coordinate the autonomous flight control strategy.

Chapter 7 provides the details of the control system design. It begins with the design of the conventional quadrotor control system before presenting the extended, tethered flight controller.

Chapter 8 presents the non-linear simulation environments utilised in the evaluation of the control designs. These include the Software-In-the-Loop and Hardware-In-the-Loop simulations (SIL and HIL respectively). SIL and HIL simulation results are presented for both the tethered and untethered cases.

Chapter 9 serves as the penultimate chapter, and provides the results of the practical tests. These include flight test data for both the untethered and tethered systems.

The thesis concludes with a summary of the research project and the notable project outcomes. Finally, recommendations are made for future work and improvement.

Chapter 2

Literature Study

A literature study was conducted in order to evaluate the current state of research into tethered multirotor UAVs. The survey yielded very little work on tethered multirotor systems, and thus, the scope was extended to include work performed on tethered flight systems in general. This included the tethering of traditional helicopters, in addition to tethered aerial systems designed for the purpose of electricity generation. The study concludes with a brief analysis on different autonomous flight control approaches for quadrotor UAVs.

2.1 Tethered Multirotor Vehicles

The limited nature of the literature available on the use of tethered multirotor systems as persistent surveillance platforms suggests that the technology is currently in its infancy. The only notable developments identified by the author were Skysapience's Hovermast and CyphyWorks' PARC robot, previously illustrated in Figure 1.1. The PARC robot utilises a conventional quadrotor vehicle tethered to a ground station, whilst the Hovermast utilises an alternative multirotor configuration in an effort to boost efficiency by lowering the rotor disk loading. The Hovermast configuration is effectively a merger between a central ducted fan design, which acts as the primary lift source, surrounded by a traditional quadrotor which provides lateral and longitudinal mobility. In both systems the primary function of the tether is to provide power and data transmission to and from the vehicle. Both systems are commercial projects still currently in development at the time of writing.

A study by Lupashin and D'Andrea [8] investigates the development of a tethered quadcopter system aimed at reducing the costs and complexities associated with VTOL-capable UAVs, in order to render the technology more accessible. The authors propose a cost-effective stabilisation approach and create a novel, user-friendly method of vehicle control.

The system uses a simplified on-board inertial sensor configuration and an Unscented Kalman Filter (UKF) to estimate the tether and vehicle attitude states. A Proportional-Derivative (PD) controller is used to stabilise the system for a fixed tether angle relative to the anchor point. The vehicle commands an open-loop thrust value, sufficiently high to keep the tether taut. The tether constrains the vehicle in the vertical direction, and offers a simple means of controlling the vehicle's movement in the horizontal plane by simply moving the anchor point. The study uses a simplified mathematical tether model with the effects of the tether mass and elasticity neglected. The authors determine an estimate of the tension force in the tether using the 'known' thrust and attitude states. Subsequent commercial development of the system has resulted in the Fotokite system [6], illustrated in Figure 2.1.

Figure 2.1: Demonstration of the Fotokite System (Lupashin and D'Andrea, 2013)

2.2 Tethered Helicopters

A report by Slegers [9] proposes the tethering of a traditional helicopter as a persistent surveillance platform. The report outlines the modelling process followed, the control implemented and the results of a single flight simulation. The author models the tether as a series of lumped-mass viscoelastic elements, with each element comprising of a spring and a viscous damper. The model includes the effects of both the mass and aerodynamic drag of the tether. A solution is obtained via a recursive process using a fourth order Runge-Kutta algorithm. A linear PID controller is implemented for the flight control of the helicopter UAV. The report vaguely documents a single 35 second flight simulation. The emphasis seemingly being on the evaluation of the recursive tether model, the results of which are unclear, whilst an analysis of the autonomous performance is not provided.

Sandino *et al* [10] propose the use of a tether to improve the hover performance of helicopter UAVs in high winds. The authors postulate that the tether produces two primary effects on the system. Firstly, that it provides an advantageous stabilising influence on the translational dynamics of the aircraft, thereby providing robustness to external disturbances such as wind. Secondly, that it renders control of the system more difficult as a result of the 'tether moment' induced by the tether tension force. The induced tether moment is generated as a result of an offset between the tether attachment point on the fuselage and the aircraft's CoM; and has a negative effect on the controllability of the aircraft by producing coupling between the translational and rotational dynamics of the vehicle. The tether is modelled as a single viscoelastic element, comprising of a parallel spring and viscous damper system, connected in series to an additional spring. Forces due to the tether mass and aerodynamic drag are assumed negligible relative to the tether tension. The authors assume the tether tension force and tether attitude states are known (in addition to the full state knowledge of the vehicle itself), with a ground device controlling the tether tension. A PI control scheme is developed for the ground device and Linear-Quadratic Integral control (LQI) implemented on the helicopter with the feed-forward of the induced tether moment. In a subsequent study by the same authors [11], the LQI helicopter control is replaced by a more elaborate strategy comprising of linearisation through model inversion and PID control. The system was validated through simulation with both wind and additional sinusoidal and impulse disturbance forces applied to the vehicle CoM in both the lateral and longitudinal directions. The paper concludes that the nonlinear control scheme achieved significant improvements in performance over the LQI predecessor, while both systems offered substantial benefits in hover performance over a similar, untethered system.

A study by Schimdt and Swik [12] conducted in 1974, proposes the design of an Automatic Hover Control System (AHCS) for a tethered rotor-platform. The system uses the tether for fuel supply, data transmission and altitude control. A special emphasis is placed on the tether dynamics in the system model and two approaches are proposed for the design of the AHCS. The rotor-platform considered consists of a single two-bladed rotor system, powered by a light gas turbine. The design avoids the use of a tail rotor and achieves yaw control through a controllable exhaust nozzle. Collective and cyclic pitch control of the rotor constitute the remainder of the system control inputs. The tether is modelled as a series of elastic elements, with each element consisting of a spring and damper in parallel and subjected to external aerodynamic forces. Optimal linear control constituted the first of the two approaches investigated for the AHCS. Due to a lack of complete state information, the optimal controller did not prove feasible, which led to the design of a suboptimal controller using classical root-locus methods. The analysis considered two alternative control strategies. The first being pure attitude stabilisation with position regulated by the feedback property of the tether. The second included active lateral and longitudinal position control, and proved the most effective. Flight tests of the system yielded mixed results, with the aircraft exhibiting good attitude stability but poor translational performance, as slow circular motions were experienced. This led to manual control inputs being required to counter these slow drift motions, particularly during

take-off and landing. The performance difficulties experienced by the system was attributed to sensor drift and threshold issues.

2.3 Tethered Electricity Generating Systems

Figure 2.2: Top (from left): The KE60 & BAT Aerostat. Bottom: The Makani AWT & a conceptual design of the Jabiru FEG.

Developments in the renewable energy sector have investigated the use of tethered flying systems to generate electricity from high altitude winds, as they provide an abundant and persistent source of kinetic energy. Several alternative systems have been developed but the basic mechanism of electricity generation remains the same, with each using an aerofoil to power either an airborne or land-based generator. Four commercial examples of alternative concepts are listed below:

The **BAT aerostat** by Altaeros Energies [13] consists of a tethered airborne wind turbine housed in a lighter-than-air aerostat (see Figure 2.2) and tethered to a ground station.

The **Makani AWT** (Airborne Wind Turbine) [14] consists of a tethered airfoil similar in design to a conventional fixed-wing model glider. The vehicle flies cross-wind in large vertical loops, generating lift across the wing which keeps the tether taut and the vehicle aloft. Four rotor-generator combinations are fitted to the wing to generate electricity during normal operation. These generators are also used to power the vehicle during the start-up and shut-down phases of operation, enabling the vehicle to hover.

The **KE60** by KITEnergy [15] produces electricity by using a tethered kite to power a ground-based generator. The tension in the tether can be controlled by manipulating the forces on the kite. The system operates by reeling the kite in and out, with the tether attached to a drum which powers a generator. A net power gain is achieved by dispensing the tether out (power generation phase) at high tension and reeling it back in (the power absorption phase) at a lower tension value.

The **Jabiru** by Sky Windpower [16] utilises a tethered multirotor system, which uses four airborne wind turbines to generate electricity and simultaneously provide lift. The design is based on the concept of autorotation, with the large wind velocities at high altitudes used to rotate the rotors, simultaneously generating electricity and providing lift. Like the Makani AWT, the generators can be used as conventional motors to power the vehicle during start-up and shut-down phases, or during periods of low wind.

While these developments differ in both design and application from the proposed tethered multirotor system, they do provide useful insight into the flight dynamics and stability of similar flying tethered systems. Comparing the effect of the tether on various aerial vehicles provides a basis from which to anticipate the effects on the proposed system. Furthermore, the investigation of such concepts provides a useful review of the techniques and methods used in the modelling of various tethered aerial systems.

Tethered inflatable kite systems have followed recent advances in kite technology as a promising prospect in the field of high-altitude wind power, and as a result, the available literature on the subject is comprehensive. A paper by Williams *et al* [17] presents modelling and control techniques for a tethered kite system. The authors develop an elaborate tether model derived from Newton's second law, with the dynamic equations solved simultaneously using a Gaussian elimination algorithm. In the analyses the tether is discretised into 200 m long, straight and inelastic lengths, based on the lumped mass principle. The tether drag forces are similarly lumped to each of the discretised lengths. String-like vibrations resulting from the tether dynamics are ignored. A later paper by Williams *et al* [18] investigates the accuracy of alternative kite modelling techniques and compares them with recorded flight test data. The authors quantify the effect of the tether mass, drag and resulting tether torque on the system dynamics, on the basis that the angular accelerations of the kite are decoupled from those of the tether. Breukels [19] proposes a simplified, but computationally efficient, means of including the effects of slow vibrations in kite tethers. A similar multi-body approach is adopted for the tether model, with the effects of the tether elasticity again neglected. A paper by de Groot *et al* [20] investigates an alternative kite model with an alternative tether model also provided, and valid for 'short' tether lengths less than 150 m. In this instance the authors include the effects of the tether elasticity by modelling the tether as a spring-damper system, but neglect the effects of the tether mass and aerodynamic drag. Goela [21] develops a set of governing equations for the tether dynamics based on a static catenary, more accurately taking the effects of the tether sag into account.

Hobbs [22] follows a similar approach in his dissertation, advocating the quasi-static assumption. Goela *et al* [23] investigate wind loading effects on several tether modelling strategies. The authors identify two important performance characterising parameters and determine applicability limits for each of the strategies investigated. Relationships for the tether drag and lift forces, as a function of wind speed, air density and tether inclination, are also provided based on practical data compiled by Hoerner [24]. Similarly, Argatov *et al* [25] develop a tether model based on the quasi-static assumption in addition to providing a single simplified expression for the tether drag, neglecting terms tangential to the tether with little loss in accuracy.

Figure 2.3: Testing of the Gyromill Mk2 (Roberts and Blackler, 1980)

Roberts and Blackler [26] investigated a method of harnessing high-altitude wind power using a tethered rotary vehicle, resulting in the 1980 Gyromill Mk2 prototype. The twin-rotor vehicle concept was successfully demonstrated at low altitude and under manual control, but it seems no further development took place until 2003 when the concept was revisited by Roberts and Shephard [27]. This work led to the development of an updated, four-rotor concept. Recent papers by Roberts *et al* [28, 29] profile the aforementioned Jabiru by Sky Windpower. The prototype is a 240 kW craft with rotors 10.7 m in diameter. The craft is designed to operate at attitudes of 15000 ft and above, with flight control achieved via collective pitch control on each of the individual rotors. A single electromechanical tether, comprising of an aluminium conductor and a high-strength fibre-optic cable, is used for power transmission and communication. The developed tether is 10 mm in diameter with a density of 115 kg/km and has a transmission efficiency of 90%. The analyses focus on the economics of the concept development with a brief overview of the theoretical power generation capabilities. The modelling and control specifics of the design are not provided.

A paper by Terink et al. [30] investigates the flight dynamics and stability of a tethered inflatable kite-plane. The kite-plane is similar in shape to a conventional glider airplane but is constructed from inflatable beams and wing surfaces. The aircraft

is attached to a single-line tether by means of a two-line bridle. The bridle system constrains the rotational freedom of the aircraft. The tether and bridle are both modelled as single, massless, straight-line elements. The investigation determined the longitudinal stability to be comparable to that of a similar untethered aircraft, but new stability issues in the lateral motion were observed and attributed to the introduction of the tether. This lateral instability, dubbed '*pendulum instability*', manifested in unstable roll and yaw motions when the aircraft was offset in the lateral direction. Significant improvements in stability were achieved by increasing the dihedral angle of the primary wing and the surface area of the vertical tail plane. The pendulum instability identified is expected to be less prevalent in a multirotor system due to the alternative method of vertical lift generation (hover capable) as well as the symmetric nature of the vehicle geometry.

2.4 Quadrotor Flight Control Techniques

The intrinsic physical nature of multirotor UAVs (with their multiple rotors distributed around the vehicle centre of mass) coupled with their small 'UAV-scale' sizes, render these vehicles uncontrollable by a human without some form of artificial damping. The layout of these vehicles causes unpredictable pitching and rolling moments due to factors such as inconsistent airflows to each of the rotors, discrepancies in the vehicle layout and variations in the performance characteristics of the coupled battery, speed-controller, motor and propeller systems. While the small vehicle sizes, and their correspondingly small moments of inertia, result in fast pitch and roll dynamics which generally exceed the bandwidth limitations for human control.

Apart from the popularity of multirotor UAVs as convenient robotic platforms, and their subsequent military and civilian utility, the nonlinear and underactuated nature of a multirotor's dynamics have led to their increased usage in academic circles for control systems research. This has contributed to an abundance of research on differing control techniques for multirotor UAVs, and quadrotors in particular. The various control approaches cater for a wide variety of performance characteristics, each with varying degrees of complexity.

Attitude stabilisation forms the basis of both the manual and autonomous flight control of quadrotor UAVs, with various linear and nonlinear techniques investigated. The bulk of the practically implemented control techniques are linear Single-Input Single-Output (SISO) nested systems, with independent controllers for pitch, roll, yaw and heave. The nested architecture has the advantage of arming or disarming control loops independently to allow easy transitioning between full-autonomous and stability-augmented manual flight modes. This is a particularly attractive feature in a research environment in order to mitigate risks associated with practical flight testing. The most common linear control approaches consist of Proportional-Integral-Derivative (PID) and Optimal Control (typically Linear-Quadratic Regu-

lators - LQR) techniques; while Backstepping, Feedback Linearisation and Sliding Mode controllers form the large majority of the nonlinear control techniques investigated. Some less common, but perhaps more recent, approaches include intelligent control techniques such as Fuzzy logic and Neural networks, whilst traditional Robust controllers have also been studied.

The performance of autonomous quadrotor controllers is typically evaluated in terms of attitude stabilisation and either trajectory-tracking and/or path-following control. These results are used to provide an indication of controller performance, but it is pertinent to note that several additional factors (e.g. variations in software implementation, state estimation techniques, hardware choices and quality etc.) can have a significant influence on the final performance.

Linear PID control is presently the overwhelming favourite for quadrotor vehicles across-the-board; in academic, hobbyist and commercial environments alike. Multiple studies [31, 32, 33, 34, 35, 36, 2], including projects completed internally within the ESL [7], have achieved good performance with comparatively simple designs around the linearised hover equilibrium condition. Furthermore, PID control has proved notably robust to disturbances and model uncertainties [37] due to the integral action. However, the propitiously simple design can prove problematic away from the hover set-point, with a loss in reference-tracking performance as the model nonlinearities (typically due to aerodynamic effects such as drag and blade flapping) become more pervasive [36]. Bouabdallah [34], in his dissertation, investigates four conventional control techniques for a quadrotor UAV; specifically, PID, LQR, Sliding Mode and Backstepping control schemes, with the PID and Backstepping schemes achieving the best performance in terms of attitude stabilisation and waypoint tracking respectively. Ultimately a combination between the two approaches, dubbed Integral Backstepping, is provided resulting in subtle performance improvements. In a similar survey conducted by Özbek *et al* [38], Sliding Mode Control (SMC) is preferred, somewhat conversely, to several nonlinear control techniques, including a conventional Backstepping approach. The study sanctions SMC as an improvement to benchmark PID control performance away from the hover equilibrium condition. Chen and Huzmezan [39] develop a hybrid H_∞ and Model Predictive Control (MPC) strategy as an improvement to a conventional H_∞ Loop shaping approach [40] by the same authors. Finally, several studies performed under the guidance of Professor D'Andrea in the widely publicised, and highly specialised, ETH Zurich Flying Machine Arena[1] [41] have demonstrated the precise and highly acrobatic flight of small quadrotors using both linear PID [42] and linear Optimal Control strategies [43, 44, 45] in conjunction with iterative learning techniques.

[1]The Flying Machine Arena is an advanced $10 \times 10 \times 10\,\text{m}$ testing platform containing a high-precision infrared motion tracking system capable of providing millimetre-accurate position and altitude measurements at 200 Hz. An independent state observer uses these measurements to provide full state feedback while the controller computation is also performed off-board on an accompanying computer.

Chapter 3

Hardware and System Design

This chapter presents details of the project's practical component. Specific hardware choices and component designs are presented, along with the layout and integration of the testing hardware.

3.1 System Overview

The overall system command structure is outlined in Figure 3.1. The quadrotor vehicle is operated by a RC pilot, via a conventional RC remote (transmitter), and a Ground Station Officer, via a laptop computer (running the Ground Station software) and a RF transceiver module.

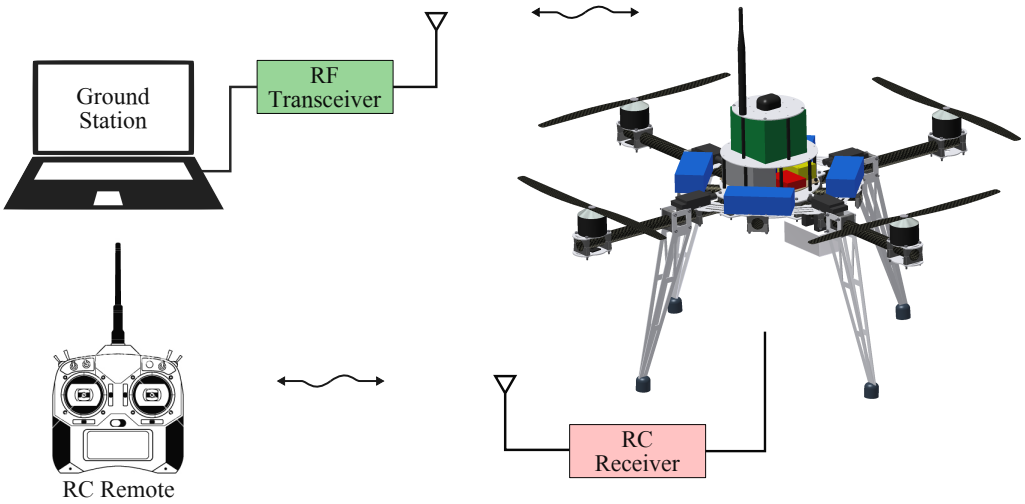

Figure 3.1: System command structure.

Quadrotors, by nature, require a stability augmentation system, typically in the form of attitude rate feedback, as a minimum requirement in order to be manually controllable by a human pilot. The RC pilot is capable of arming the innermost (attitude rate) control loops, from a switch on the RC remote, in order to manually pilot the vehicle independently from the Ground Station Officer. Additional capabilities of the RC pilot include the ability to control the tether release servo and, more significantly, to disarm the higher-level autonomous flight controllers at any time, in order to return the vehicle to a manual flight control state. These precautionary functions are controlled via separate switches on the RC remote.

Higher-level system functionality is controlled by the Ground Station Officer and executed by the on-board avionics systems. The on-board avionics can be broadly categorised as the on-board communications hardware, the on-board computer (OBC), the servoboard and the hardware interfaces to the various on-board sensors. The basic layout and functionality of the on-board avionics is illustrated in Figure 3.2, with detailed operational and component specifics provided in Chapter 3.2.2.1.

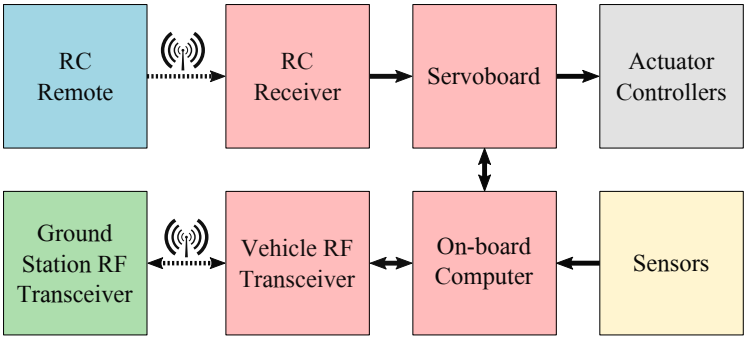

Figure 3.2: Basic system definitions and functionality.

The OBC is the main on-board processing device, with it's functions including (but not limited to) the execution of the flight control and state estimation algorithms. The Ground Station communicates directly with the OBC via the RF link, transmitting high-level system commands and receiving pertinent telemetry data. Final control commands to the actuator controllers[1] are transmitted via the servoboard, as per Figure 3.2.

3.2 Vehicle Hardware

3.2.1 Design Rationale

In a purpose-built tethered UAV system, final performance requirements would largely dictate the vehicle design strategy. Such requirements would likely include

[1]The electronic speed controllers (ESCs) and the tether release servo.

Figure 3.3: The fully assembled, untethered aircraft.

factors such as the desired operational altitude, the power transmission strategy, payload requirements and additional operational considerations based on unique environmental specifics. As this research project focusses on the investigation of tethered flight with a multirotor UAV, the vehicle design specifications are much more loosely defined.

The chief system design consideration is that of the mechanical characteristics of the tether, which are treated as 'black-box' specifications. The tether specifications relate to the cable density, aerodynamic profile and, to a lesser extent, the material composition. The tether profile is specified as circular, with no attempt made to optimise the design for aerodynamic performance. The material composition is loosely based on an insulated conductor, while the cable density specification is listed in Table 3.1.

Further design specifications include an additional on-board payload capacity of 1.5 kg, which effectively translates into a minimum battery mass, and a maximum total thrust to vehicle mass ratio, $\frac{T_{max}}{mg}$. The thrust to mass ratio pertains to the total thrust headroom available above the required hover thrust for the untethered aircraft. This ratio has a significant bearing on the control sensitivity of the aircraft, particularly from the perspective of manual flight control. Prior academic research using similarly sized multirotor vehicles have favoured ratios in the region of $\frac{T_{max}}{mg} \approx 1.25 - 1.3$, while implementations in the general RC community, that typically employ large multirotor aircraft for aerial photography and filmography purposes, have found a ratio of $\frac{T_{max}}{mg} \approx 2$ to be optimal in terms of total payload capacity and manual controllability.

The on-board avionics hardware and the vehicle sensor configuration were first fi-

Table 3.1: System design specifications.

Tether density	0.05 kg/m
On-board payload capacity	1.5 kg
$\frac{T_{max}}{mg}$	$2 - 2.5$

nalised, with the remaining hardware (airframe, propulsion system and tether attachment and release mechanism) selected concurrently via a recursive process. Hardware choices for the airframe and propulsion system were based on the system design specifications, with the aim of maximising the operational ceiling of the tethered system, and were limited to available off-the-shelf components; while the tether attachment and release mechanism were designed and manufactured separately based on the airframe specifics, with the aim of minimising the distance between the tether attachment point and the vehicle CoM.

3.2.2 Hardware Components

3.2.2.1 On-board Avionics and Sensors

Designs for the on-board avionics hardware were previously developed in-house at the ESL, and are modular by design in order to cater for various UAV platforms. The avionics package is compatible with a conventional[2] sensor configuration, which provides measurements for the kinematic state estimator. The sensor configuration used in this project comprises of the following components:

1. GPS receiver.
2. Inertial Measurement Unit.
3. Magnetometer.
4. Status sensors.

The GPS receiver used on the aircraft is a NEO-7P module by ublox which provides position and velocity measurements at an update rate of 5 Hz. The NEO-7P is a stand-alone, single frequency GPS receiver that uses *Precise Point Positioning* (PPP) technology to achieve sub-meter[3] horizontal position accuracy at a significantly lower cost relative to Differential GPS (DGPS) or Real-Time Kinematic (RTK) solutions.

The Inertial Measurement Unit (IMU) employed is the ADIS16355 by Analog Devices. The IMU is a complete 3-axis gyroscope and 3-axis accelerometer inertial

[2]Typically used on UAV systems.
[3]$<$ 1 m, 50% Circular Error Probability (CEP), $>$ 6 SV.

sensing unit, that provides angular rate and acceleration measurements at a frequency of 100 Hz.

The magnetometer employed is the HMC2003 by Honeywell. The magnetometer provides measurements of the geomagnetic field vector in body axes at 50 Hz. The kinematic state estimator compares these measurements against a reference geomagnetic field vector in the inertial axis system, in order to determine the 'measured' attitude state of the aircraft.

The status sensors comprise of standard hall-effect current and voltage sensors which are used to monitor the currents and voltages of all the on-board batteries. These sensors are mounted on a separate Status Board and their measurements are communicated wirelessly to the Ground Station at 2 Hz, to enable pre- and in-flight monitoring by the Ground Station Officer as a precautionary measure.

Individual sensors are mounted to purpose-built sensor boards which handle the analog-to-digital conversion and subsequent transmission of the sensor measurements. The on-board electronic hardware architecture and communication specifics are illustrated in Figure 3.4. A Controller Area Network (CAN) bus facilitates communication between the OBC and the Servoboard, and between the OBC and the vehicle sensors, with the exception of the GPS receiver which communicates with the OBC via UART. The on-board avionics hardware and sensors are adequately powered by a single 3-cell (12.6 V), 1200 mA h lithium polymer (LiPo) battery by X-power RC.

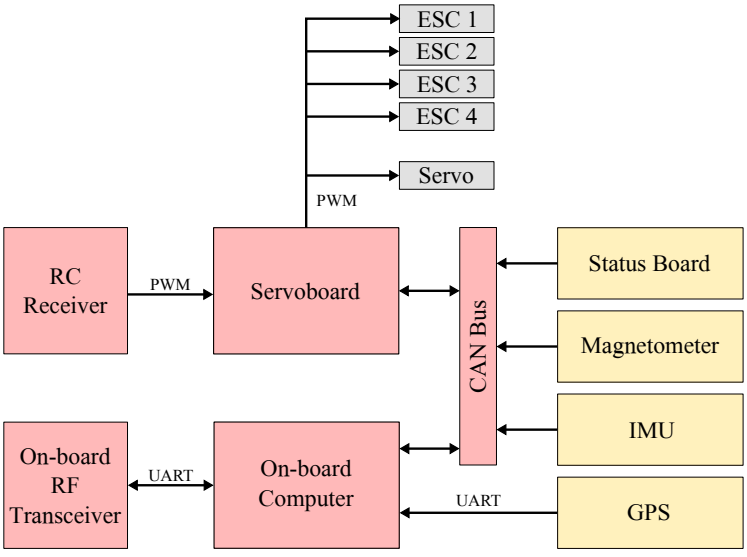

Figure 3.4: Overview of the on-board avionics architecture and sensor configuration with communication specifics.

The OBC is the main on-board processing device containing two dsPIC30F microcontrollers (MCUs) by Microchip Technology Inc. The OBC executes the control,

state estimation, data logging and data transmission algorithms on a single MCU, while the remaining MCU is limited to GPS packet parsing. Wireless data transmission from the OBC to the Ground Station is implemented via two paired XStream 2.4 GHz RF modules by Digi International.

The servoboard serves purely as an analog-to-digital and digital-to-analog converter, between the RC receiver and OBC, and the OBC and actuator controllers[4] respectively. Pilot commands are received wirelessly by the RC receiver as Pulse Width Modulation (PWM) pulses before being quantised for use on the OBC. Conversely, digital control commands from the OBC are converted to 'analog' PWM control inputs to the tether release servo and the electronic speed controllers.

The physical separation of the servoboard and OBC was originally implemented as an additional safety feature for alternative UAV platforms (such as fixed-wing aircraft), as it enables manual flight control independent of the OBC. This independence is desirable as it mitigates the risk associated with the commissioning of new vehicles as expensive avionics hardware and sensing equipment can be removed during initial test flights. Furthermore, it ensures that manual flight controllability of the vehicle is preserved in the event of an OBC failure and/or a loss of power to the avionics system. In this project, however, manual flight control requires the augmented stability system, which is executed by the OBC. Consequently, this feature is rendered redundant for the quadrotor UAV case.

A final consideration is the vibration isolation of sensitive avionics and sensor hardware. Even with proper balancing, during operation the four rotors induce significant vibrations in the airframe corresponding to their rotational velocities. To mitigate these effects, the OBC stack, which houses the especially sensitive IMU, is mechanically isolated via rubber vibration mounts. The vibration mounts are selected to have a cut-off frequency of 50 Hz in order to negate the $65 - 125$ Hz frequency range of the rotors.

3.2.2.2 Airframe and Propulsion System

The airframe used in this project is the Syn-X4 by Syndrones which is illustrated in Figure 3.5. The airframe was selected based on several practical and mechanical design factors. Several alternative airframes were initially short-listed based on the practical considerations of whether they possessed sufficient space for the on-board avionics and sensor requirements, and whether this space was easily adaptable to the on-board hardware. Mechanical considerations included the distribution of mass of the fully assembled aircraft, minimising rotor aerodynamic interference and ensuring the airframe was structurally sound and mechanically rigid enough considering the tethered application, whilst still remaining lightweight. The distribution of mass is of particular importance in order to maximise the aircraft control sensitivity by

[4]The electronic speed controllers (ESCs) and the tether release servo.

minimising the aircraft mass moments of inertia.

Figure 3.5: Syn-X4 airframe by Syndrones.

Minor modifications were made to the original airframe in order to adapt it for the current project. Custom 'feet', illustrated in Figure 3.6, were added to the landing gear, which were identified as a potential vulnerability. The feet reduce the risk of the landing gear fracturing by significantly increasing the surface area of the contact point and by reducing the impact loads through the introduction of high-density foam which serves to absorb some of the impact forces. The feet are encased in a rigid plastic housing with a low-friction coefficient in order to reduce the risk of the aircraft toppling over during take-off and landing by minimising potential shear forces. Furthermore, custom parts were 3D-printed to mount some of the on-board hardware, whilst the battery trays were modified to manipulate the battery mounting positions, in order to balance the aircraft and minimise aerodynamic shear.

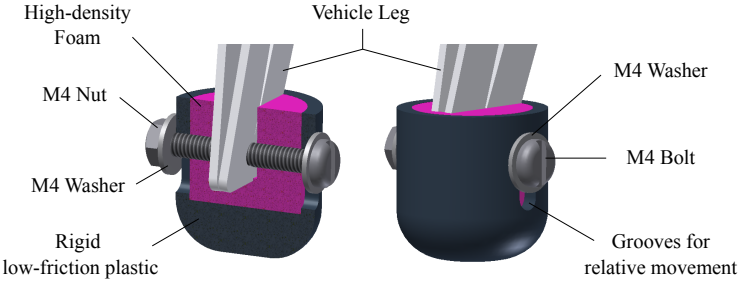

Figure 3.6: Details of the vehicle 'feet' design and assembly.

Propulsion System

The vehicle propulsion system comprises of four individual propulsion units which, in turn, each consist of a rotor, a BLDC motor, an electronic speed controller and a battery power source. The rotor blades employed are fixed-pitch 16x5.5" carbon fibre props by RC Timer. Carbon fibre props are selected for their stiffness characteristics and lower inertias. The increased stiffness reduces the flexural characteristics of the blades and mitigates against the effects of blade flapping. While the lower rotational inertias result in faster dynamic response times, which ultimately improves the autonomous performance.

The rotors are driven by T-motor MN4120 BLDC motors, with a kV rating of 400 kV and a 12N14P magnet configuration. The motors are specially designed for large multirotor applications with their high torque capabilities, and optimised thermal dissipation design.

The motors are controlled by T-motor 60 A electronic speed controllers. The ESCs were selected based on their continuous 60 A output capability as well as their compatibility with the T-motor BLDC motors.

Each ESC-motor-rotor combination is powered by an individual 6-cell (22.2 V), 2600 mA h lithium-ion polymer (LiPo) battery by X-power RC. LiPo batteries are the preferred power source for RC applications due to their attractive energy densities and power delivery capabilities. The batteries were selected primarily based on the battery voltage and 35C continuous discharge rate capability.

The individual battery capacities of 2600 mA h enable an untethered flight time of roughly 8 minutes, based on the final, untethered vehicle mass of 5.8 kg. The total battery mass is 1.7 kg, which is marginally greater than the desired 1.5 kg additional payload capability for the aircraft. Each propulsion unit is capable of a maximum thrust output of 3.5 kg, which translates to a final maximum thrust to weight ratio of $\frac{T_{max}}{mg} \approx 2.4$.

3.2.2.3 Tether Attachment and Release Mechanism

The tether attachment forms the physical interface between the aircraft and the tether. It incorporates a remotely operated release mechanism in order to enable the in-flight detachment of the tether from the aircraft. Motivation for the in-flight detachment of the tether is two-fold. Firstly, it mitigates the risk associated with landing the aircraft and is a necessary safety feature in the event of an in-flight emergency. Secondly, it provides a useful testing feature by enabling tethered-to-untethered flight transitions. These transitions provide insight into the influence of the tether on the aircraft and can be used in the development of recovery strategies.

The tether release is operated by both the pilot, via a switch on the RC remote,

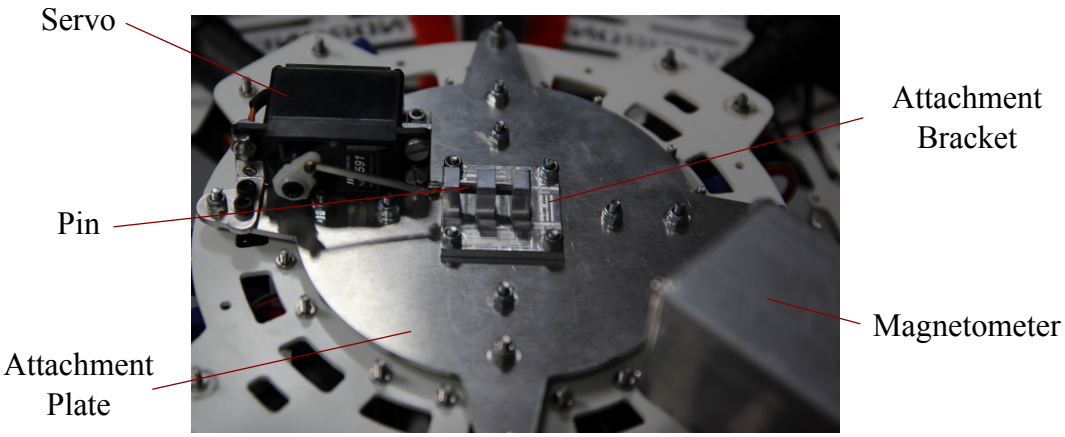

(a) Tether attachment and release mechanism.

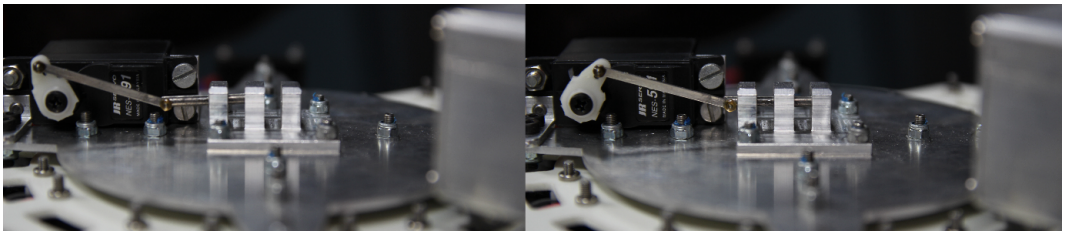

(b) Operation of the tether release mechanism.

Figure 3.7: Tether release mechanism operation and component details.

and the ground station officer, via a button on the GUI of the Ground Station software. To assist with recovery the pilot release switch simultaneously disarms the higher-level autonomous controllers and resets the integrator values (to zero) of the innermost control loops.

The tether attachment and release mechanism are mounted on the underside of the central hub of the aircraft, and are illustrated in Figure 3.7a. The tether attachment consists of the attachment plate and bracket; while the servo, pin and associated fasteners constitute the tether release mechanism. The servo employed on the release mechanism a JR NES 591 servo. A safety factor (SF), in terms of the servo torque capability, is determined in Appendix A.1 as $SF_s \approx 1.25$ which is sufficient for this research project.

The central hub, tether attachment and release mechanism pin are identified as critical parts as they are exposed to significant impact forces, known as 'shock' or 'snap' loads, as the aircraft transitions suddenly from a loose to taut tether configuration. Designs of these components aim to ensure that they are able to withstand these forces without the need for an auxiliary mechanical damping mechanism, which would introduce additional dynamics and complexity to the vehicle model and design.

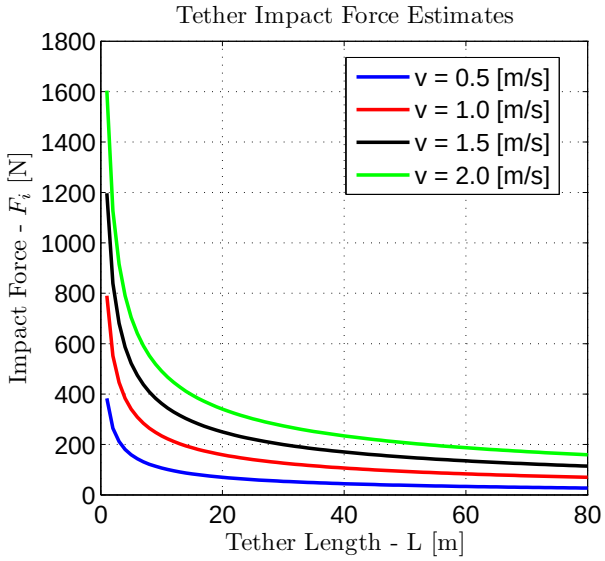

Figure 3.8: Tether Impact Force Estimates

Conservative estimates of the impact forces are determined in Appendix A.2 for various tether lengths and initial transition velocities, with the results illustrated in Figure 3.8. Considering the aircraft flight envelope, an impact force of 400 N is utilised in the structural analysis of the critical components.

The tether attachment plate and bracket were manufactured from 6082 T6 aluminium. The bracket was machined from a solid block of material while the plate was laser-cut from a 2 mm-thick sheet. The material properties of 6082 T6 aluminium are taken from Gale and Totemeier [46] and are listed in Table A.1. Aluminium was used for the tether attachment due to both it's material and pragmatic suitably. The 6082 T6 grade is characterised by a low density (relative to other metals) and particularly stout structural properties, whilst remaining easily machinable and locally available. Furthermore, aluminium is a *paramagnetic* material with a positive but inconsequential magnetic susceptibility, resulting in a relative[5] permeability near unity (see Table A.1). The size and proximity of the tether attachment assembly to the on-board magnetometer made this property a necessity.

The tether release pin is manufactured from tool steel (specifically from an old drill bit), which is a high carbon, water-hardened steel alloy with good mechanical characteristics. The load bearing portion of the vehicle hub is made from 3 mm-thick sheets of FR-4, which is a glass-reinforced epoxy laminate. The mechanical properties of the two materials are provided in Table A.2.

A structural assessment of the critical parts is conducted prior to fabrication in order to identify any potential mechanical vulnerabilities. A safety factor against yielding is determined in Appendix A.3 for each component exposed to an impact force of

[5]Relative to the permeability of free space.

400 N. The tether attachment and vehicle hub are modelled as thin plates of various geometries while the release pin is modelled as a cantilever beam. While the release pin is well represented by the general boundary and loading conditions presented in Figure A.2, approximations for the tether attachment and vehicle hub are less representative. Considering the uncertainty in these approximations a minimum safety factor of $SF \geq 2$ is desired for each of the components under a 400 N load.

Table 3.2: Safety factors against yielding of critical parts ($P = 400$ N).

Component	$\frac{\sigma_Y}{\sigma_{max}}$
Release Pin	$> 10^3$
Attachment Bracket	3.39
Attachment Plate	1.23
Vehicle Hub	4.27

The results of the assessment, presented in Table 3.2, indicate that the design safety margins for the release pin, attachment bracket and vehicle hub are satisfactory. However, the safety margin of the attachment plate is insufficient. Simply increasing the plate thickness is not possible due to limited supply, therefore the plate is subjected to further mechanical analysis.

The maximum bending stress in the plate is determined based on the general case of a central concentrated load and with the plate simply supported along its outer edge. The loading case applied is a conservative approximation considering that the force transfer to the plate occurs through four mechanical fasteners situated in the corners of the attachment bracket. Contrastingly, the simply supported boundary condition is a generous approximation. In reality the supporting mechanical fasteners provide localised fixed support, but due to the fastener placement and total surface area, the slope at the component outer edge remains largely unconstrained, and the boundary condition is more accurately represented using a simply-supported assumption.

In order to more accurately represent the actual boundary and loading conditions, a Finite Element Analysis (FEA) is conducted on a 3D CAD model of the tether attachment plate. From the FEA a revised safety factor against yield of $SF = 3.9$ is determined for the plate under a 400 N load. Details of the Finite Element Analysis are presented in Appendix A.4.

3.3 Identification of System Parameters

A pragmatic approach is followed in the identification of the system parameters using a combination of analytical and empirical methods. The system parameters

addressed in this section include the relationship between PWM-input to thrust-output for each of the vehicle propulsion units, the actuator time constant, the vehicle body aerodynamic coefficients, the virtual yaw moment arm, the vehicle mass moments of inertia and the elastic modulus of the tether.

3.3.1 Thrust vs PWM Mapping

Thrust vs PWM mapping of the propulsion units is required in order to convert the OBC control commands from newton units to the corresponding PWM pulse lengths. Subtle manufacturing differences between the individual components in each propulsion unit can prove significant when accumulated, and thus, mapping is performed to determine the unique relationship between PWM-input to thrust-output for each unit.

Mapping is performed on a custom-built thrust test jig, illustrated in Figure 3.9. The test jig was previously developed at the ESL and incorporates both hardware and software components. The hardware components include a beam-type load cell, hall-effect voltage and current sensors, an optical tachometer, a custom PCB and a mounting stand assembly. The PCB incorporates a microcontroller that integrates the sensor data and generates PWM commands to drive an electronic speed controller.

The microcontroller firmware and a test jig GUI application form the non-hardware components of the test jig. The test jig GUI application is run on an accompanying laptop computer and enables user-specifiable PWM commands to the electronic speed controller with a command resolution of 10 µs, in addition to the logging of the test sensor data at 400 Hz. A FTDI RS232-USB converter on the PCB facilitates communication between the laptop computer and the PCB microcontroller.

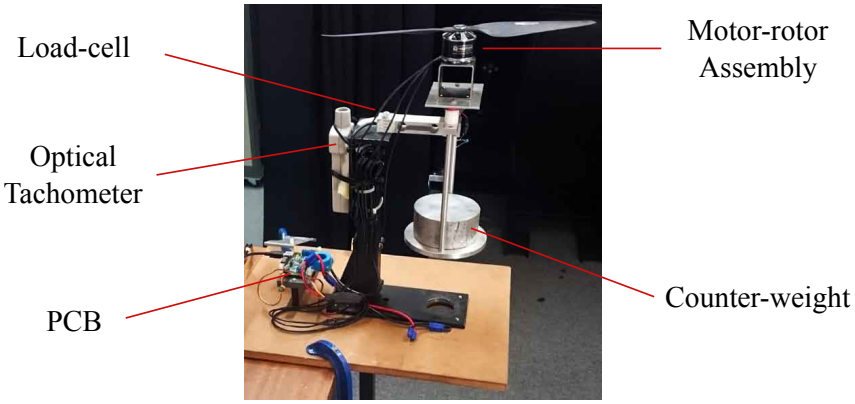

Figure 3.9: Illustration of the thrust test jig.

The mapping test consists of running each of the propulsion units from standstill to

the maximum rated current of the motors[6], at (PWM) step increments of 10 µs. The recorded thrust measurements are averaged at each PWM interval, excluding measurements during the transient states, with the results illustrated in Figure 3.10a.

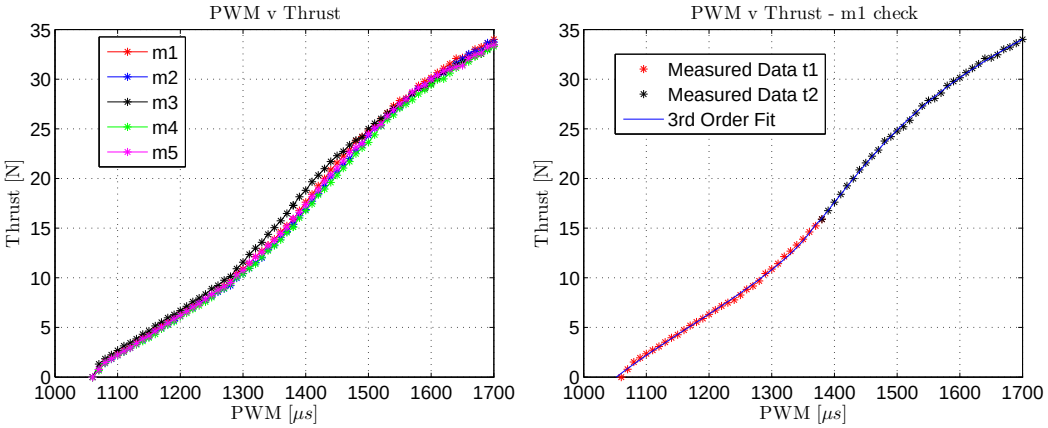

(a) Test Measurements (b) Curve Verification

Figure 3.10: Thrust vs PWM Mapping Test Results

Thereafter, Matlab's *polyfit* function is used to determine a best-fit third order polynomial function, $f_i(x)$, via the method of least squares, such that,

$$y_i = f_i(x) \text{ [µs]} \tag{3.1}$$

where,

$$f_i(x) = \begin{cases} a_3^i x^3 + a_2^i x^2 + a_1^i x + a_0^i, & x \leq y_t \\ b_3^i x^3 + b_2^i x^2 + b_1^i x + b_0^i, & x > y_t \end{cases} \tag{3.2}$$

x	is the desired motor thrust output
y_i	represents the corresponding PWM input for the ith motor
y_t	is the PWM curve transition point of 1380 µs

The Thrust-PWM curve generated by Equation 3.1 for Motor 1 is illustrated in Figure 3.10b, while the polynomial coefficients in Equation 3.2 and the Thrust-PWM curves for the remaining motors are provided in Appendix B.1.

3.3.2 Actuator Time Constant

The actuator lag dynamics are sufficiently encapsulated by a first-order transfer function. Numerous studies [34, 47, 32] have shown this to be a reasonable assumption. From the virtual actuator definitions provided in Equations 4.26–4.29, the

[6] As indicated by the motor data-sheet.

virtual actuator dynamics can be shown to be,

$$\dot{\delta}_i = -\frac{1}{\tau}\delta_i + \frac{1}{\tau}\delta_{i_R} \tag{3.3}$$

where, δ_i represents the output in newtons for the ith actuator and δ_{i_R} represents the commanded/reference value.

The motor time constant, τ from Equation 3.3, is determined empirically for a given $\triangle$PWM command input differential. This results in a lumped value that includes the additional time delays associated with the battery dynamics, the ESC commands, and the actuator dynamics.

The rotor PWM-Rotor Speed relationship is determined using the thrust test jig in Figure 3.9, in an identical manner to the PWM-Thrust relationship from Chapter 3.3.1. An optical tachometer enables the measurement the rotor speed, with the results illustrated in Figure 3.11a.

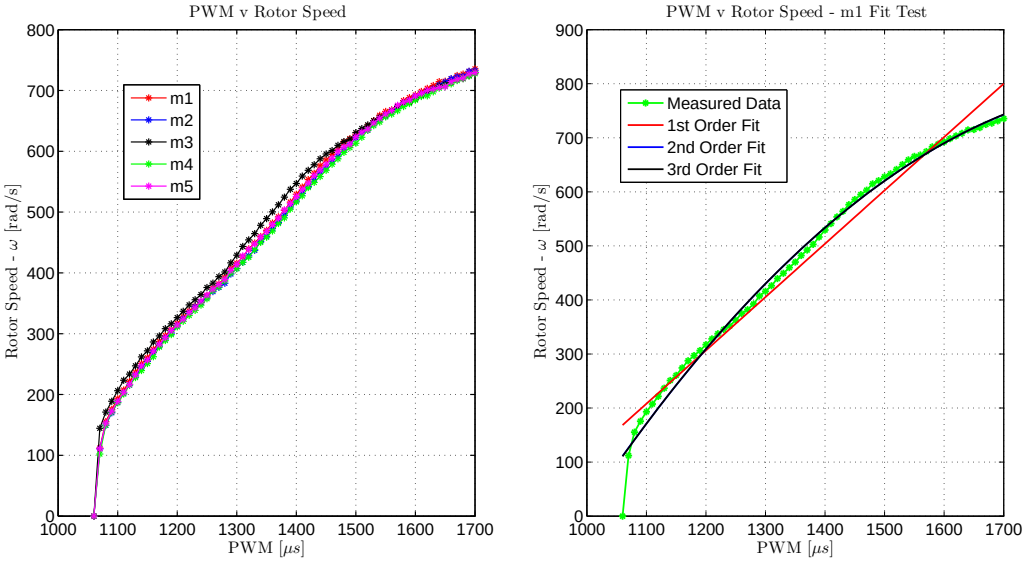

(a) Test Measurements (b) Curve Verification

Figure 3.11: Rotor Speed vs PWM Mapping Test Results

Matlab's *polyfit* function is, once again, used to determine a best-fit polynomial function, $g_i(x_i)$, via the method of least squares. Comparisons between 1st, 2nd and 3rd order polynomial functions for the Rotor Speed-PWM curve of Motor 1 are illustrated in Figure 3.11b. In this instance a second-order equation was deemed sufficient for simulation purposes.

$$\omega_i = g_i(x_i) \text{ [rad/s]} \tag{3.4}$$

where,

$$g_i(x) = \begin{cases} c_1^i x^2 + c_1^i x + c_0^i, & x \geq x_s \\ 0, & x < x_s \end{cases} \tag{3.5}$$

ω_i represents the rotor speed of the ith motor
x_i is the OBC PWM output for the ith motor
x_s is the motor start-up PWM value of 1070 µs

The motor constant is a particularly important parameter for the quadrotor UAV case as it determines the fundamental controller bandwidth limits, and can subsequently have a dramatic influence of the aircraft stability. A thrust step test is performed (as illustrated in Figure 3.12) on each of the propulsion units in order to determine the average motor constants, τ, for various $\triangle$PWM command input step sizes around the untethered, hover-thrust set-point.

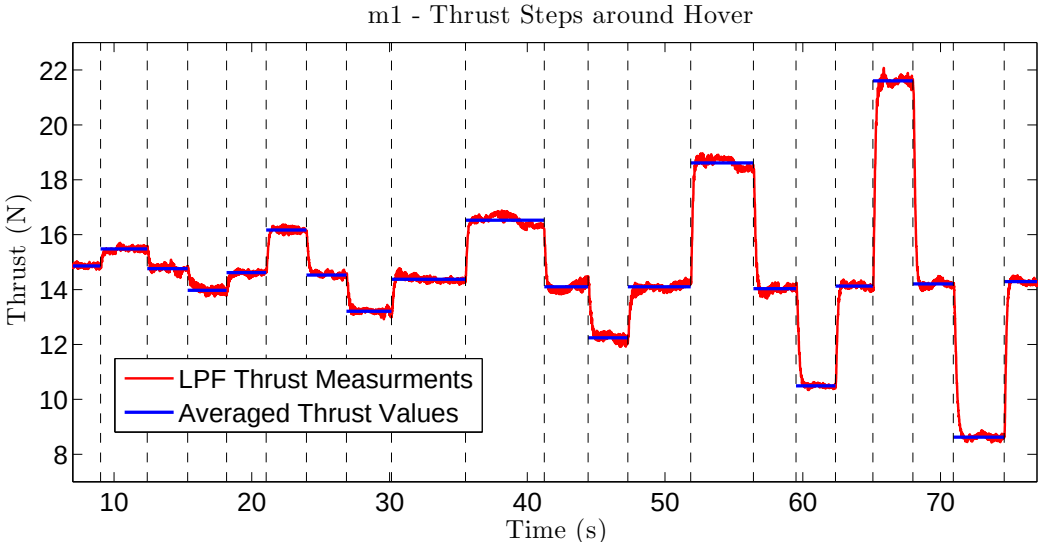

Figure 3.12: Motor 1 Thrust Steps Test

From the test results presented in Table 3.3, it is clear that the motor constant varies significantly for differing $\triangle$PWM step commands. Thus, in the absence of a more comprehensive actuator model, the choice of a reference $\triangle$PWM command forms a critical design consideration for the quadrotor UAV case.

Table 3.3: Average Motor Constants for all Motors.

$\triangle$PWM	10	20	30	60	100	[µs]
τ_{avg}	5.0	17.5	28.5	51	58	[ms]

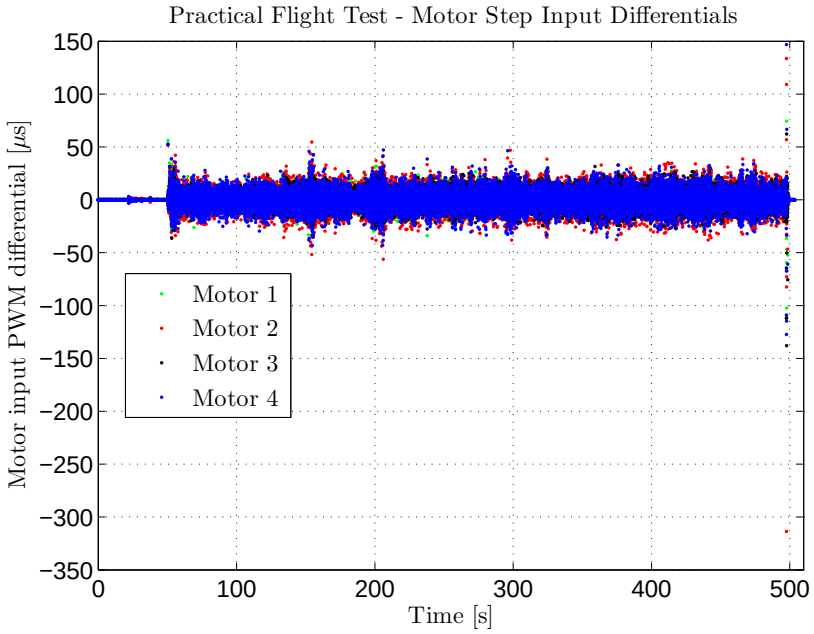

(a) All recorded △PWM step commands.

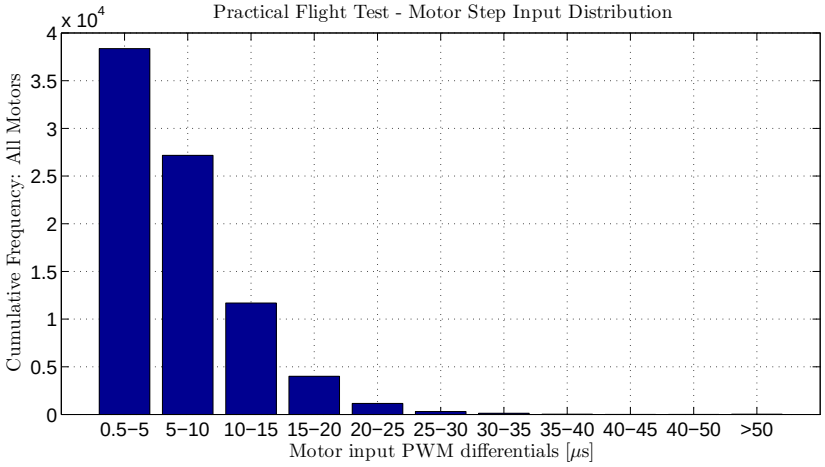

(b) △PWM step command distribution.

Figure 3.13: Motor input command data from a practical flight test.

An iterative approach is followed in the selection of an appropriate reference △PWM command. A reference step command size of △PWM = 10 µs is initially selected after analysing the motor input data from Hardware-In-the-Loop simulations. This results in a selected motor constant of $\tau = 5$ ms.

Figure 3.13a presents the recorded motor input data from a practical flight test involving both manual and fully autonomous flight control. Figure 3.13b illustrates the △PWM step command distribution after accounting for measurement noise.

The mean command input size, including measurements during the take-off and landing phases, is determined as $\overline{\triangle \text{PWM}} = 5$ µs, which is comfortably within the $\triangle \text{PWM} = 10$ µs command assumption.

3.3.3 Vehicle Aerodynamic Coefficients

Lumped vehicle drag coefficients are determined analytically for each of the body-axis directions using the method of *superposition* [48]; whereby the individual components of the vehicle assembly are analysed independently and combined using Equation 3.6 to determine an approximate value for the total vehicle drag coefficient.

$$C_{D_i} = \sum C^j_{D_i} A^j_i \ [\text{m}^2] \tag{3.6}$$

where, $C^j_{D_i}$ and A^j_i represent the drag coefficient and frontal surface area, respectively, of the jth component in the ith body-axis direction.

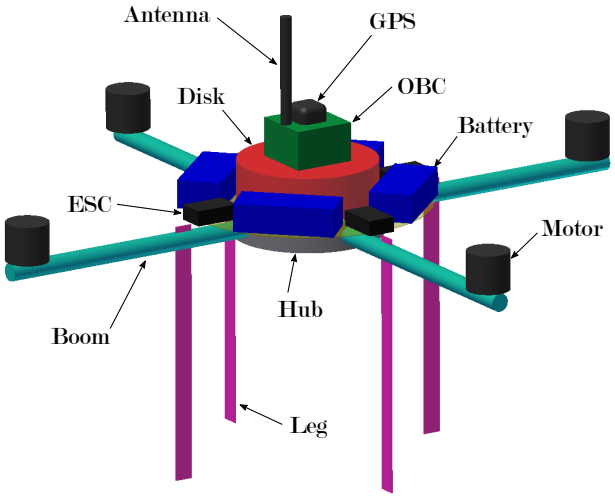

Figure 3.14: Illustration of the vehicle assembly simplification in the determination of lumped drag coefficients.

The vehicle components are represented by various simplified three-dimensional bodies as per Figure 3.14. Drag coefficients for various common 3D geometries are determined experimentally and provided by Çengel and Cimbala [48, Table 11-2]. The behaviour of these drag coefficients can vary significantly between the the creeping, laminar and turbulent flow regimes which are characterised by low, moderate and high Reynolds numbers (Re) respectively.

The coefficients employed in this project are based on the laminar flow regime ($10^4 < Re \leq 5 \times 10^5$) where they remain essentially constant. The Reynolds number is determined using Equation 3.7, with the relationship between the external fluid flow velocity and Reynolds number (for each of the component profiles in the x_B and y_B

axes) illustrated in Figure 3.15. The representative body sizes are scaled relative to the actual frontal surface areas of the real-life components in order to accommodate for variations between the component profiles and those of the representative bodies.

$$Re = \frac{\rho V_i D_j}{\mu} \tag{3.7}$$

where, μ is the dynamic viscosity of the fluid and D_j is the characteristic length of the jth component profile.

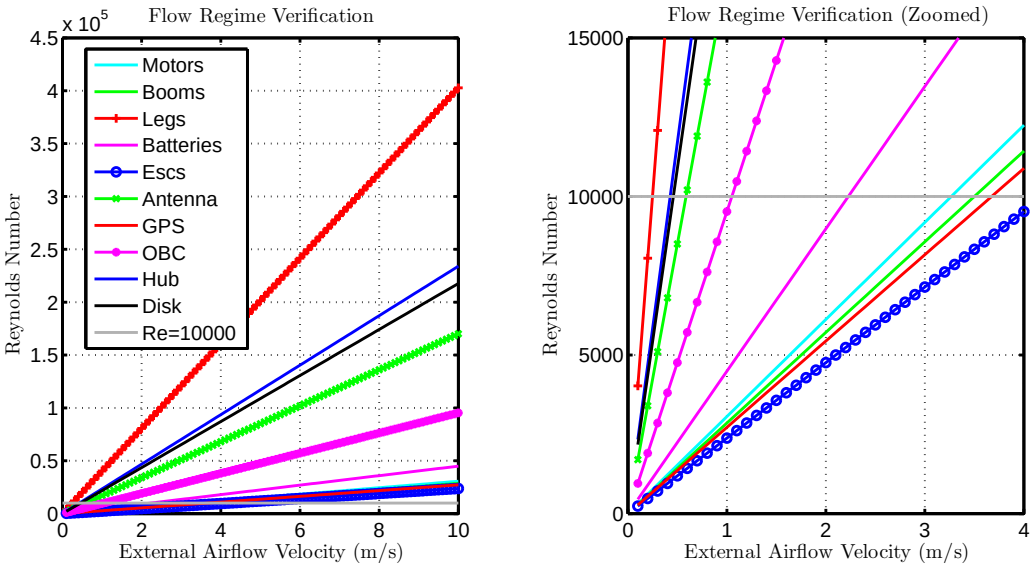

Figure 3.15: Flow Regime Verification

From Figure 3.15 it is clear that the laminar flow assumption is valid for relative flow velocities between 1 m/s $\lesssim V_{x/y} \lesssim$ 12 m/s for the legs, hub, disk, and OBC components, which form the major contributors towards the total aerodynamic drag in the x_B and y_B axes. The drag coefficients are typically underestimated for Reynolds numbers $Re < 10^4$ but the resulting drag forces in this range are small enough relative to the vehicle mass and inertia to render these effects insignificant.

The drag coefficient in the z_B axis direction is simpler, comprising only of the booms, motors and a single circular disk; with the latter used to model the components in the central portion of the vehicle. Here the central disk dominates the aerodynamic drag calculation, with the laminar flow assumption valid for relative flow velocities greater than $V_z \gtrsim 0.5$ m/s, while the velocity range for the booms and motors is comparable to the x_B and y_B axes in Figure 3.15.

The final lumped vehicle drag coefficients, relative to their respective frontal surface

areas in each of the aircraft's body axes, are given by Equations 3.8 – 3.10 as,

$$C_{D_x} = 0.064 \text{ [m}^2\text{]} \tag{3.8}$$

$$C_{D_y} = 0.067 \text{ [m}^2\text{]} \tag{3.9}$$

$$C_{D_z} = 0.089 \text{ [m}^2\text{]} \tag{3.10}$$

These values are used in Equations 4.61 and **??** from Chapter 4.4.3 to calculate the final aerodynamic forces in the body axis coordinate system.

3.3.4 Virtual Yaw Moment Arm

The virtual yaw moment arm is a theoretical coefficient, R_N [m], that determines the rotor drag torque, τ_R, acting on the vehicle about the z_B body axis as a function of the rotor thrust output. The rotor drag torque, which is used to control the vehicle in yaw, can therefore be defined as,

$$\tau_{R_i} = R_N T_i \text{ [N m]} \tag{3.11}$$

where, T_i is the thrust output of the ith actuator.

The rotor drag torque is dependent on the unique aerodynamic characteristics of the rotor, which can be highly variable and notoriously difficult to accurately determine. The approach followed in this thesis uses blade element theory, based on a general set of aerodynamic assumptions for the rotor, to determine an estimate for R_N. This analytically calculated value is then compared against the expected mechanical and electrical efficiencies of the propulsion system as a final sanity check.

The rotor drag torque is determined in a similar fashion to the rotor thrust and hub forces in Chapter 4.4.1.2. From blade element theory, the rotor drag torque is determined by Johnson [49] as,

$$\tau_{R_i} = \rho A C_{Ri} (\omega_i R)^2 R \text{ [N m]} \tag{3.12}$$

where,

ρ	is the air density
A	rotor blade area
C_{Ri}	rotor torque coefficient of the ith rotor
ω_i	rotational speed of the ith rotor
R	rotor disk radius

The total mechanical power output, P_{mech}, is determined as the sum of the individual rotor mechanical power outputs as,

$$P_{mech} = \sum_{i}^{4} \rho A C_{Pi} (\omega_i R)^3 = \sum_{i}^{4} \tau_{R_i} \omega_i \text{ [W]} \tag{3.13}$$

From Equations 3.12 and 3.13, it follows that the rotor torque and power coefficients are equivalent,

$$C_{Ri} = C_{Pi} \tag{3.14}$$

The rotor power coefficient is related to the rotor thrust coefficient, C_{Ti}, according Johnson via,

$$C_{Pi} = \frac{\kappa {C_{Ti}}^{\frac{3}{2}}}{\sqrt{2}} + \frac{\sigma c_d}{8} \tag{3.15}$$

where, κ is a constant used to incorporate additional rotor blade tip losses, c_d is the rotor blade drag coefficient and σ is the rotor solidity ratio as defined in Equation 4.37.

The relation for the constant, κ, is provided by Johnson in terms of the rotor tip-loss factor, B as,

$$\kappa = \frac{1.13}{B} \tag{3.16}$$

where,

$$B = 1 - \frac{\sqrt{2C_{Ti}}}{N} \tag{3.17}$$

where, N is the number of blades.

A relation for the blade drag coefficient, c_d, is given by Johnson as a function of the rotor disk angle of attack, α as,

$$c_d = 0.0087 - 0.0216\alpha + 0.4\alpha^2 \tag{3.18}$$

which simplifies to $c_d = 0.0087$ for the hover case of $\alpha = 0$.

Average values for the electrical power in, $\bar{P}_{elec} = \bar{V}_{in}\bar{I}_{in}$ [W], and the actuator thrust coefficient, $\bar{C}_T$ (using Equation 4.35), are determined around the hover set-point of $T_i = 14.25$ [N]. Measurement data for each of the individual propulsion units is recorded using the thrust test jig. The averaged test measurements are listed in Table 3.4.

The total system efficiency can then be calculated as the mechanical power-out to electrical power-in ratio,

$$\eta_t = \frac{P_{mech}}{P_{elec}} \tag{3.19}$$

The rotor efficiency is defined by Johnson as,

$$\eta_r = \frac{T_i v_h}{P_{in}} = \frac{C_{Ti}^{\frac{3}{2}}}{C_{Pi}\sqrt{2}} \tag{3.20}$$

Table 3.4: Averaged test measurements around hover.

T_i	14.25	N
$\bar{\omega}_r$	482	rad/s
$\bar{C}_T$	0.009	-
$\bar{V}_{in}$	24.7	V
$\bar{I}_{in}$	9.7	A
$\bar{P}_{elec}$	239.6	W

A lumped motor-ESC efficiency, $\eta_{m/e}$, can subsequently be deduced from the rotor and total system efficiency as,

$$\eta_{m/e} = \frac{\eta_t}{\eta_r} \tag{3.21}$$

To summarise, from measurement recorded using the thrust test jig one can empirically determine the constants listed in Table 3.4. This allows the analytical determination of the rotor power coefficient, via Equation 3.15, and subsequently the virtual yaw moment arm via Equation 3.11. Following this method, a virtual yaw moment arm of $R_N = 0.018$ m is determined for the vehicle around the untethered, hover set-point. Thereafter, the recorded measurement data are used to determine the rotor and total system efficiencies from Equations 3.20 and 3.19 respectively. With knowledge of these efficiencies one can determine the lumped motor-ESC efficiency from Equation 3.21, which can be further separated by taking the motor efficiency as provided by the manufacturer. These system efficiencies are used purely as a final sanity check considering the number of general assumptions employed in the blade element theory derivation of R_N. The resulting total and component-specific efficiencies are listed in Table 3.5, with each component falling within the plausible efficiency limits, thereby lending confidence to the calculated value of R_N. The ESC efficiency, η_e, is calculated based on a motor efficiency of $\eta_m = 0.8$ as provided by the manufacturer.

Table 3.5: Expected vs calculated component and system efficiencies.

Component	Unit	Expected Efficiency	Calculated
Motor	η_m	0.75 - 0.85	$0.8^{\dagger}$
Rotor	η_r	0.7 - 0.75	0.73
ESC	η_e	0.85 - 0.95	0.88
Total	η_t	0.45 - 0.60	0.51

† Assumption based on manufacturer data.

3.3.5 Mass Moments of Inertia

Three alternative methods were utilised in the determination of the vehicle mass moments of inertia, including a detailed CAD assembly model, a simple experiment and simplified hand calculations as a final verification.

The CAD assembly model is illustrated in Figure 4.4, and is made up of separate parts for all the major aircraft components using measured values for the component masses and dimensions. The masses of any associated wiring are lumped to the appropriate components to increase the model fidelity. A CAD assembly model provides a simple means of incorporating unique component shapes and positioning details, in terms of both placement and orientation, in determining the physical parameters of the aircraft assembly. The CAD assembly model is, however, limited to a uniform density assumption for each of the individual components.

The moment of inertia experiment is based on work by Treurnicht [50], and is used to determine the mass moment inertia about the z_B body axis, I_{zz}. The aircraft is suspended by two ropes attached to opposite ends of the aircraft as illustrated in Figure 3.16. The aircraft is orientated upside down in this case due to the mounting plane being offset in the positive z_B axis from the vehicle CoM. From a stationary starting position, the aircraft is perturbed in yaw and left to oscillate about the z_B body axis. The mass moment of inertia, I_{zz}, is determined using Equation A.27 by measuring the period of oscillation of the perturbed hanging system.

Figure 3.16: Mass moment of inertia experiment setup.

For the hand calculations the aircraft components are represented by simplified geo-

metric shapes in an identical manner to the aerodynamic drag coefficient calculation in Chapter 3.3.3. The individual mass moments of inertia are calculated based on equations provided by Budynas and Nisbett [51, Appendix A-18], and combined using Equation 3.22 as,

$$I = \sum_{i}^{n} (I_i + m_i d_i^2) \text{ [kgm}^2\text{]} \tag{3.22}$$

The results of the analyses are listed in Table 3.6. The CAD model overestimates the total vehicle mass slightly due to discrepancies between the actual mechanical fastener masses used on the vehicle, and those used in the CAD assembly which are generic fasteners taken from the CAD component library. The hand calculations and experiment results match well for I_{zz}, while the CAD model prediction is marginally greater. The final mass moments of inertia are based predominantly on the experimental test and the hand calculations. The assumptions employed in the hand calculations assume $I_{xx} = I_{yy}$ and, therefore, the CAD prediction is used to differentiate between the two axes.

Table 3.6: Aircraft Mass Moments of Inertia

Method	m_v [kg]	I_{xx} [kgm^2]	I_{yy} [kgm^2]	I_{zz} [kgm^2]
CAD	6.03	0.172	0.177	0.310
Calculations	5.79	0.151	0.151	0.271
Experiment	5.79	-	-	0.266
Final	5.79	0.149	0.153	0.268

3.3.6 Tether Mechanical Properties

PVC-coated steel wire rope (SWR) is selected for the system tether as it satisfies the desired physical characteristics at a low-cost. The PVC-coated stranded wire configuration resembles that of an insulated conductor, particularly in an aerodynamic sense. While the strong mechanical properties represent a worst-case scenario with respect to the flexural stiffness of the tether, in addition to snap loading events. This ensures a comprehensive evaluation of the autonomous control strategy.

The calculation of the tether impact forces on the vehicle in Appendix A.2 is highly dependent on the modulus of elasticity, E, of the tether. Variations between specific lay-up configurations can have a significant effect on the resulting mechanical properties of stranded materials. Furthermore, manufacturer-provided mechanical data for SWR is typically limited to maximum breaking loads/forces due to the nature

of typical application. Consequently, the tether modulus of elasticity is determined via a series of tension tests.

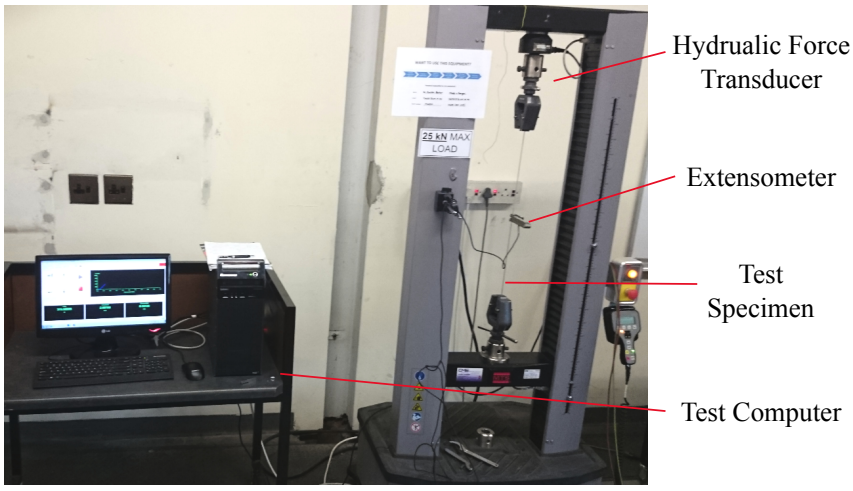

Figure 3.17: Tether Tension Test Setup

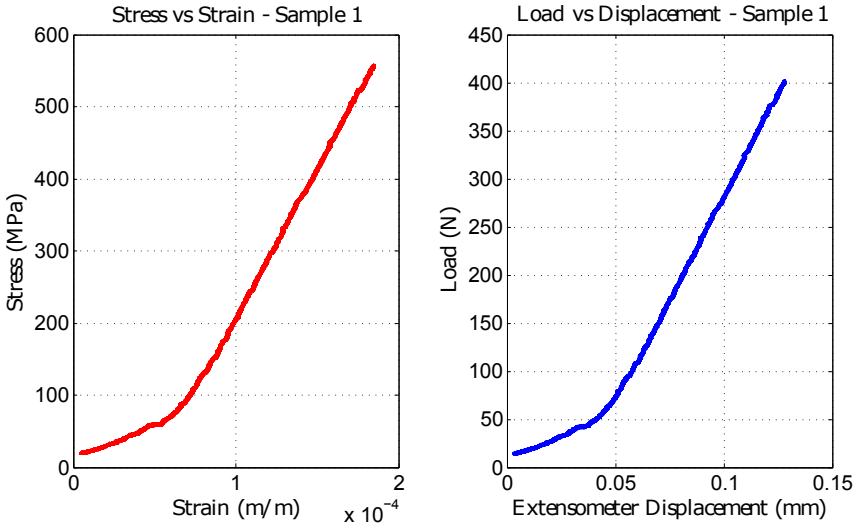

Figure 3.18: Specimen 1 - Tether Tension Test Results

The tension tests were carried out in accordance with the *Standard Test Method for Tension Testing of Wire Ropes and Strand* as provided by ASTM A931-08 (2013). The tests were conducted on a 30 kN MTS Universal Testing Machine with a MFA 25 mm extensometer, as illustrated in Figure 3.17.

The tests consisted of measuring the deformation of the wire rope test specimens under an increasing tensile load. The strain, ϵ, in each test specimen can be determined

from the specimen deformation as,

$$\epsilon = \frac{\triangle l}{l} \tag{3.23}$$

where, l is the length of the original, undeformed test specimen.

The stress, σ, in the test specimen is determined as the applied force, F, over the cross-sectional area, A, of the undeformed specimen as,

$$\sigma = \frac{F}{A} \text{ [Pa]} \tag{3.24}$$

Thereafter, the elastic modulus of the specimen can be calculated via,

$$E = \frac{\sigma}{\epsilon} \text{ [Pa]} \tag{3.25}$$

The results of the tether tension tests provide valuable insight into the behaviour of the tether under an applied load. From Figure 3.18 it is clear that there exists a definite change in gradient of the stress-strain slope, and therefore the 'perceived' elastic modulus, at an applied load of roughly 50 N. This is a result of the wire rope strands 'tightening' as the stress in the tether increases, until a point where the cable begins to deform elastically.

The results from tether tension tests are averaged for three test specimens and result in the following values for the tether modulus of elasticity, E_t, for an applied tether tension, F_t,

$$E_t = \begin{cases} 43 \text{ GPa}, & F_t \leq 50 \text{ N}. \\ 166 \text{ GPa}, & F_t > 50 \text{ N}. \end{cases} \tag{3.26}$$

Chapter 4

Vehicle Modelling

A mathematical model of the complete tethered system is required in order to evaluate the autonomous flight controller via numerical simulation before practical testing can be attempted. The model aims to replicate the real-world behaviour of the system, with a higher-fidelity model providing more meaningful results.

This chapter presents the quadrotor UAV model utilised in this project. The rigid-body assumption is applied universally when modelling conventional quadrotor UAV designs, with models commonly derived using either of the Euler-Lagrangian or Newton-Euler approaches. The derived system model follows the Newton-Euler formalism, and is similar in approach to modelling strategies implemented by Pounds [31], Bouabdallah [34] and Mahony *et al* [35].

The chapter begins with a discussion on the assumptions employed in the model derivation and their applicability to the research project. A definition of the coordinate systems utilised is then provided, followed by the rigid-body kinetics and kinematics. Thereafter, the dominant forces and moments acting on the vehicle are described. The chapter concludes with a derivation of the actuator model utilised in this project.

4.1 Assumptions and Limitations

The major assumptions employed in the derivation of the vehicle model are discussed in the context of this research project.

4.1.1 Airframe Properties

The aforementioned rigid-body assumption greatly simplifies the analysis by neglecting the effects of mechanical elasticity in the airframe. Numerous studies on quadrotor UAVs have proven this to be a reasonable assumption. The addition of a tether does, however, increase the possibility of flex in the airframe, particularly during 'loose to taut' tether transitions. However, any flex-related dynamics occurring in the airframe are expected to be outside of the controller bandwidth. Concerted efforts were made to mitigate these effects through the design of the tether attachment assembly.

Furthermore, the vehicle geometry is assumed symmetric about the XZ- and YZ-planes, with a similarly balanced distribution of mass. This assumption simplifies the inertia tensor matrix and is reasonable for the vehicle developed in this project.

4.1.2 Dissymmetry of Lift & Blade Flapping

Dissymmetry of lift is a phenomenon that affects rotary wing aerial vehicles, particularly during periods of fast 'forward'[1] flight. It manifests, ostensibly, as a tilting of the rotor plane, and consequently the thrust vector, which is caused by a lift force differential between the advancing and retreating rotor blades. A difference in lift arises when opposite blades experience differing tip speeds relative to the incoming airflow; either due to the vehicle translating horizontally or in the presence of strong winds. In reality the resulting asymmetric thrust profile causes dynamic flapping of the rotor, dubbed 'blade flapping'. However, the rotor flap dynamics correspond with the rotor RPM and are extremely fast relative to the vehicle rigid body dynamics. Consequently, analyses are limited to the steady-state dynamics as a function of the planar velocity [49]. The time-scale separation is even greater for multirotors relative to similarly sized helicopters, as the former employ smaller blade diameters and operate at higher RPM values.

Full-size helicopters exploit this phenomenon with rotor blades designed to intentionally flap both vertically and horizontally. This is achieved either through the use of mechanically articulated rotors or by incorporating an added degree of elastic flexibility in the rotor blade design. This has two primary functions; specifically, it helps compensate for the dissymmetry of lift phenomenon as the blade angle of incidence can be manipulated effectively through careful design. Additionally, it serves to alleviate the large bending stresses generated in the rotor blades, mitigating their effects on the rotor hub assembly.

Multirotor UAVs follow a different approach, and typically utilise fixed pitch unar-

[1] It is worth noting that the 'forward' flight reference used here is typically based on traditional helicopters flying nose-forward. The symmetric nature of multirotor designs result in an omni-directional flight capability, and thus, 'forward' flight may refer to the horizontal translation of the vehicle in either the lateral or longitudinal directions.

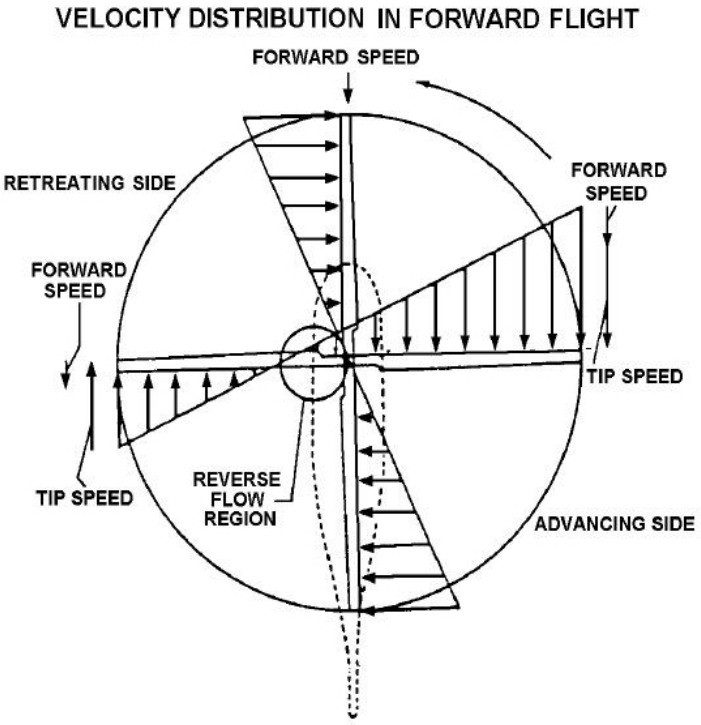

Figure 4.1: An illustration of the dissymmetry of lift phenomenon

ticulated rotor blades. Their multiple rotor configurations render the effects of the dissymmetry of lift phenomenon less pronounced than in helicopters with their larger single-rotor designs. In conventional quadrotor designs the two pairs of counter-rotating rotors result in the rolling moments generated by the lateral tilt of the rotor planes largely cancelling, with the dissymmetry of lift effects comprising primarily of the pitching moments resulting from the longitudinal tilt of the rotor plane [36]. Furthermore, the smaller rotor diameters and UAV-scale vehicle sizes result in reduced bending stresses in the rotor blades, permitting the use of hinge-less designs. While plastic rotors with significant flex characteristics are commonly used, this is typically an economic decision as opposed to a purposeful design consideration. Carbon fibre rotor blades form the bulk of the premium propeller market, especially for larger multirotor applications.

Rotor blades are commonly modelled as 'rigid', with the effects of blade flexibility frequently neglected. Studies [34, 36] have proved this to be a reasonable assumption at slow velocities near the hover equilibrium condition. The derived model follows a similar approach. This is an acceptable omission considering the hardware choices, flight envelope and research objectives of this project.

4.1.3 Rotor Thrust Variations

A variety of factors can cause inconsistencies in the rotor thrust output of rotary wing aerial vehicles. These thrust variations can be significant in certain scenarios, and have led to a number of notable military crashes [52, 53]. Factors that influence the rotor thrust output include,

i. The free stream velocity and angle of inclination with respect to the rotor plane.

ii. Rotor inflow variations due to aerodynamic interference from the airframe and/or other propellers on the free stream.

iii. Flow states of the rotor.

iv. Proximity to the ground.

v. Mechanical wear.

Thrust variations due to changes in the free stream velocity are largely modelled through the real-time determination of the rotor thrust coefficient, as described in Chapter 4.4.1.2. This includes airflow velocity changes due to wind and translational movements of the vehicle, but the effects of rotational movements (rolling, pitching and yawing about the CoM) remain unmodelled. Rotational movements will result in additional discrepancies in the rotor thrust outputs of opposing motor pairs, due to the motor mounting positions being situated away from the vehicle CoM. These effects are frequently neglected in literature and, thus, the effects of which are expected to be small. Changes in the angle of inclination of the rotor plane with respect to the free stream are inherently included in the analysis by resolving the free stream into body axis components.

Accurately quantifying the impact of the aerodynamic interference of the airframe and the multiple rotors on one another is a more challenging endeavour. Hoffmann *et al* [36] found that alternative airframe configurations had a significant influence on attitude stability, although these differences were primarily attributed to the use of protective shrouds around the rotors, which can be considered somewhat of an extreme case. These effects are acutely vehicle-specific, and without comprehensive wind-tunnel testing or Computational Fluid Dynamics (CFD) studies there remains a great deal of uncertainty in any attempt to quantify these effects. A suitable wind-tunnel test facility was not available for this project and CFD studies were deemed beyond the project scope. Thus, the effects of aerodynamic interference are neglected in the derived model. The low-speed flight envelope, low wind-speed flight testing conditions and specific hardware choices all contribute to mitigate these effects during practical testing, and therefore, this is deemed a reasonable assumption.

The rotor flow states are the differing airflow conditions through the rotor for various cases of the three general vertical flight regimes; namely, climb, hover and descent. In this project analytical solutions for rotor performance are developed using a combination of momentum and blade element theory, as described in Chapter 4.4.1.2. Momentum theory is based on a simplified wake model, with airflow in the same direction and a well-defined slipstream [49]. These assumptions are invalid for certain flow conditions, which can result in drastic discrepancies in performance from the predicted results. Four alternative rotor flow states for vertical flight are defined by Johnson [49] as,

a. Normal working state

b. Vortex ring state

c. Turbulent wake state

d. Windmill brake state

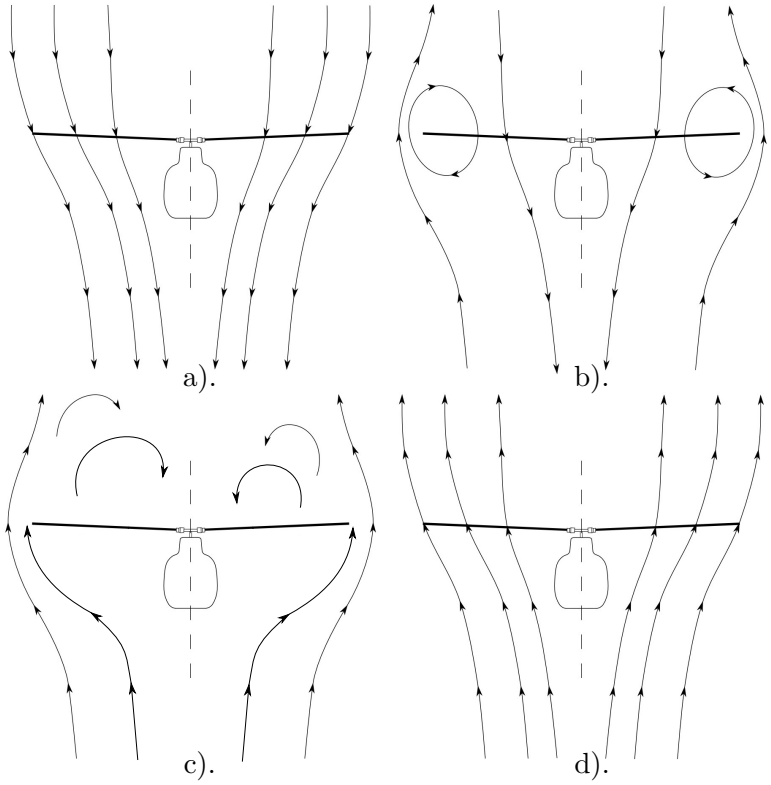

Figure 4.2: Rotor flow states: a). Normal working state b). Vortex ring state c). Turbulent wake state d). Windmill brake state. Adapted from: Cel 84 / CC-BY-SA-3.0

The normal working state includes both the climb and hover flight regimes, where the wake assumptions are reasonable and momentum theory provides good results. Although hover is theoretically the lower boundary limit for the normal working state, momentum theory solutions have shown to provide reasonable results for small rates of descent (up to $V/v_h < -\frac{1}{2}$), even though the flow model is technically incorrect. The remaining flow states occur during the descent flight regime. The vortex ring state is characterised by recirculation and unsteady flow over the rotor disk, caused by the rotor descending within it's own downwash. This condition leads to a loss of lift which can prove insensitive to subsequent power increases, as it can merely exacerbate recirculation. The vortex ring state escalates with increasing descent velocities until the point of ideal equilibrium autorotation (in the absence of rotor power losses), which represents the turbulent wake state boundary. At this point the flow pattern is similar to that of a solid circular plate in a perpendicular flow stream, with no airflow through the rotor and a turbulent wake. The windmill brake state is encountered at very high descent velocities (almost exclusively during autorotation manoeuvres). The flow is once again smooth and steady, but in this case, upwards through the rotor. However, unlike the gradual flow changes between the vortex ring and normal working states, the boundary between the windmill brake and turbulent brake states is decisive with the flow state changing abruptly. Momentum theory again provides a good indication of rotor performance during the windmill brake state, while empirical methods are required to determine the performance during the vortex ring and turbulent wake states.

The model derived in this project assumes that the rotor flow remains at all times within the normal working state. Considering the project objectives and flight envelope, it is expected that the turbulent wake and windmill brake states will not be encountered at any point during practical flight testing. However, exposure to the vortex ring state is unavoidable to some degree, and this might have an influence on the autonomous performance during periods of descent. These effects are mitigated by limiting the maximum permissible sink rate to within the aforementioned momentum theory region of applicability.

Additional unmodelled effects include thrust variations due to ground effect and mechanical deterioration. Ground effect reduces the rotor induced velocity by constraining the rotor wake, which increases the rotor thrust output for a given power input. Variations due to ground effect are significant when the rotors are within one rotor diameter from the ground [49]. Over time, mechanical deterioration will degrade the rotor performance but this is expected to occur over longer time frames relative to the current project. Thus, these are reasonable omissions considering the project flight envelope and time-scale.

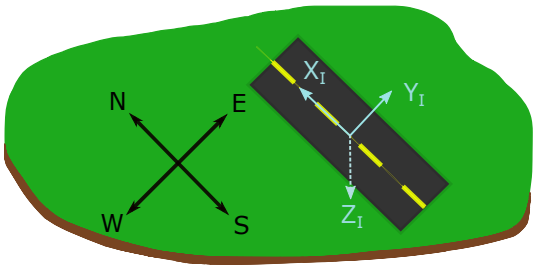

Figure 4.3: Inertial axes definition

4.2 Coordinate Systems

Two coordinate systems are used in this project for modelling purposes; namely, an **inertial axis system** and an **aircraft body-fixed axis system**. Both axis systems are right-handed orthogonal Cartesian axis systems. The body-fixed and inertial axis systems initially coincide, and are otherwise related by Equations 4.19 and 4.24 as defined in Chapter 4.3.2.

$\{A\} = \{X_I, Y_I, Z_I\}$ denotes the inertial axis system which conforms to the North-East-Down (NED) standard (see Figure 4.3) and assumes a non-rotating, flat earth. This is a reasonable assumption for short range applications [54] and one commonly applied to UAVs. The axis origin is selected to coincide with the runway centre, with the X_I and Y_I axes pointing in North and East directions respectively. The remaining Z_I axis points downwards, perpendicular to the 'flat' earth surface.

$\{B\} = \{x_B, y_B, z_B\}$ denotes the aircraft body-fixed axis system as illustrated by Figure 4.4 in Chapter 4.3. The body-fixed axes are selected to coincide with the vehicle's principal axes of inertia, with the body-fixed axis origin at the aircraft's centre of mass (CoM). The x_B axis is selected as the 'forward', longitudinal axis with the y_B axis selected as the 'sideways', lateral axis. The remaining z_B axis points downwards, opposite in direction to the rotor thrust plane. The symmetric nature of the quadrotor configuration results in near-identical values for the I_{xx} and I_{yy} principal axes of inertia, which results in correspondingly similar lateral and longitudinal flight dynamics. As a result, allocation of the vehicle principal axes to specific lateral and longitudinal directions is a mere formality.

4.3 Equations of Motion

The derivation of the equations of motion for the quadrotor vehicle is based on work performed by Blakelock [55] on fixed-wing aircraft, using the rigid-body assumption.

4.3.1 Kinetics

The translation and rotation (about the CoM) of a rigid body in an inertial reference frame, subjected to external forces and moments applied to or about the CoM, is described by Newton's 2nd Law which equates the external forces and moments to the time derivative of the linear and angular momenta respectively as,

$$\mathbf{F}_A = \left(\frac{d\mathbf{P}}{dt}\right)_A = \frac{d}{dt}(m\mathbf{V}_A) = m\dot{\mathbf{V}}_A \tag{4.1}$$

$$\mathbf{M}_A = \left(\frac{d\mathbf{L}}{dt}\right)_A = \frac{d}{dt}(\mathbf{I}_A \cdot \boldsymbol{\Omega}_A) = \mathbf{I}_A \cdot \dot{\boldsymbol{\Omega}}_A \tag{4.2}$$

Where $\mathbf{P}$ & $\mathbf{L}$ are the linear and angular momentum vectors of the rigid body respectively, and $\mathbf{I}_A$ is the inertia tensor calculated in the inertial frame $\{A\}$. The drawback of this method of analysis is that $\mathbf{I}_A$ can vary as the body moves in the inertial frame, which complicates matters. In order to simplify the analysis, we analyse the system dynamics in the rotating, body-fixed reference frame $\{B\}$. This permits the use of a constant inertia tensor $\mathbf{I}_B$ as the vehicle's mass is constant and the vehicle structure is assumed rigid. The external forces and moments are subsequently determined in the body-fixed reference frame $\{B\}$ that is rotating relative to $\{A\}$ as,

$$\mathbf{F}_B = \left(\frac{d\mathbf{P}}{dt}\right)_B + \boldsymbol{\Omega}_B \times \mathbf{P}_B = m\dot{\mathbf{V}}_B + \boldsymbol{\Omega}_B \times m\mathbf{V}_B \tag{4.3}$$

$$\mathbf{M}_B = \left(\frac{d\mathbf{L}}{dt}\right)_B + \boldsymbol{\Omega}_B \times \mathbf{L}_B = \mathbf{I}_B\dot{\boldsymbol{\Omega}}_B + \boldsymbol{\Omega}_B \times \mathbf{I}_B\boldsymbol{\Omega}_B \tag{4.4}$$

Equations 4.3 and 4.4 include fictitious forces due to centrifugal and Coriolis effects, and are presented more succinctly in matrix form by Equation 4.5 as,

$$\begin{bmatrix} m\mathbf{I_n} & \mathbf{0} \\ \mathbf{0} & \mathbf{I}_B \end{bmatrix} \begin{bmatrix} \dot{\mathbf{V}}_B \\ \dot{\boldsymbol{\Omega}}_B \end{bmatrix} + \begin{bmatrix} \boldsymbol{\Omega}_B \times m\mathbf{V}_B \\ \boldsymbol{\Omega}_B \times \mathbf{I}_B\boldsymbol{\Omega}_B \end{bmatrix} = \begin{bmatrix} \mathbf{F}_B \\ \mathbf{M}_B \end{bmatrix} \tag{4.5}$$

$\mathbf{I}_n$ is a 3×3 identity matrix and $\mathbf{I}_B$ is given by Equation 4.6, with the subsequent simplification in accordance with the vehicle layout assumption in Chapter 4.1.1 and the body-axis coordinate system definition in Chapter 4.2.

$$\mathbf{I}_B = \begin{bmatrix} I_{xx} & -I_{xy} & -I_{xz} \\ -I_{yx} & I_{yy} & -I_{yz} \\ -I_{zx} & -I_{zy} & I_{zz} \end{bmatrix} \approx \begin{bmatrix} I_{xx} & 0 & 0 \\ 0 & I_{yy} & 0 \\ 0 & 0 & I_{zz} \end{bmatrix} \tag{4.6}$$

Defining the force, moment, linear velocity and angular velocity vectors in the body-

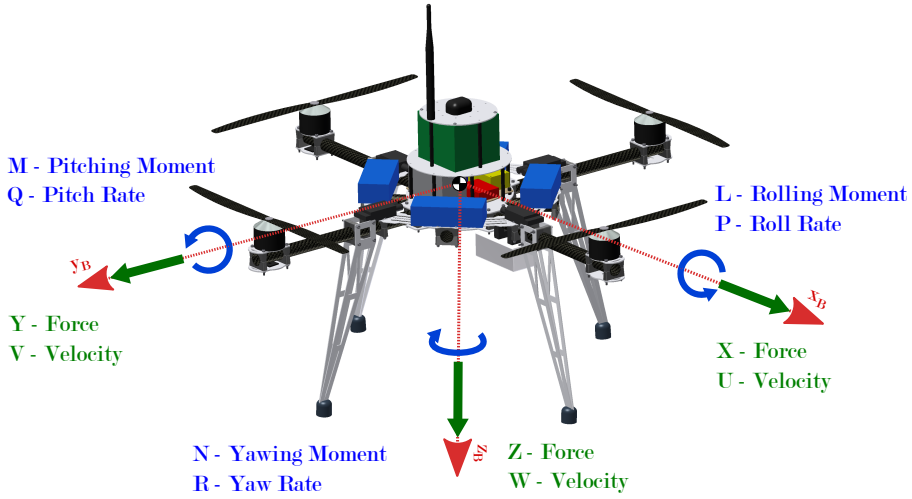

Figure 4.4: Aircraft Notation

axis coordinate system as,

$$\mathbf{F}_B = \{X, Y, Z\}^T \tag{4.7}$$
$$\mathbf{M}_B = \{L, M, N\}^T \tag{4.8}$$
$$\mathbf{V}_B = \{U, V, W\}^T \tag{4.9}$$
$$\mathbf{\Omega}_B = \{P, Q, R\}^T \tag{4.10}$$

Equation 4.5 can be expanded, with the final dynamic equations defined as,

$$\sum_i X_i = m\left(\dot{U} - VR + WQ\right) \tag{4.11}$$
$$\sum_i Y_i = m\left(\dot{V} - UR + WP\right) \tag{4.12}$$
$$\sum_i Z_i = m\left(\dot{W} - UQ + VP\right) \tag{4.13}$$
$$\sum_i L_i = \dot{P}I_{xx} + QR\left(I_{zz} - I_{yy}\right) \tag{4.14}$$
$$\sum_i M_i = \dot{Q}I_{yy} + PR\left(I_{xx} - I_{zz}\right) \tag{4.15}$$
$$\sum_i N_i = \dot{R}I_{zz} + PQ\left(I_{yy} - I_{xx}\right) \tag{4.16}$$

4.3.2 Kinematics

Having derived the vehicle equations of motion in the convenient body-fixed axis coordinate system, a method of relating the vehicle dynamics between the body-

fixed and inertial axis systems (and visa versa) is required. Euler angles and a transformation matrix, known as the Direction Cosine Matrix (DCM), are used to provide relationships between the two coordinate systems for both the orientation dynamics and flight path information respectively.

4.3.2.1 Orientation Dynamics

Euler angles describe the orientation, or attitude, of the body-axis system relative to the inertial axis system. Three Euler angles are required to fully describe the vehicle attitude; these angles are illustrated in Figure 4.5 and defined below as,

1. Roll angle, ϕ - Vehicle rotation about the x_B axis.
2. Pitch angle, θ - Vehicle rotation about the y_B axis.
3. Yaw angle, ψ - Vehicle rotation about the z_B axis.

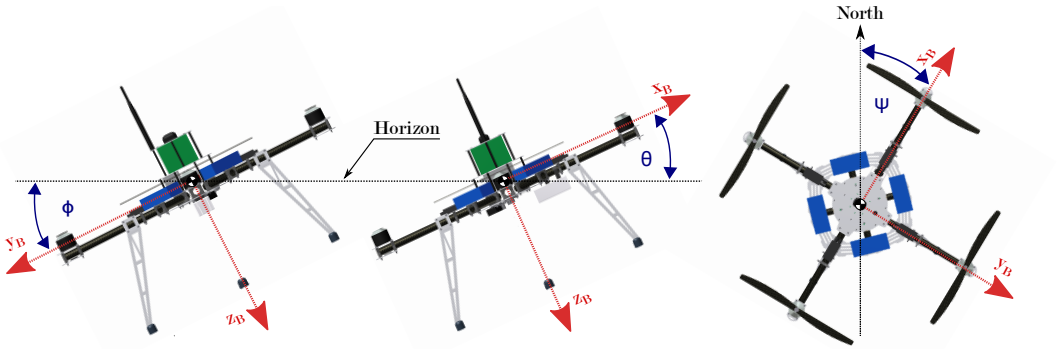

Figure 4.5: Euler Attitude Parameters

The orientation dynamics are derived via the Euler 3-2-1 method, where the body-fixed axis initially coincides with the inertial axis system before being rotated consecutively through a specific three-angle sequence; specifically, yaw, pitch and roll. The result is an expression in terms of the body axis angular velocity $\mathbf{\Omega}_B$, shown by Etkin and Reid [56] to be,

$$\mathbf{\Omega}_B = \begin{bmatrix} P \\ Q \\ R \end{bmatrix} = \mathbf{R}_\Omega \begin{bmatrix} \dot{\phi} \\ \dot{\theta} \\ \dot{\psi} \end{bmatrix} \tag{4.17}$$

Where,

$$\mathbf{R}_\Omega = \begin{bmatrix} 1 & 0 & -\sin\theta \\ 0 & \cos\phi & \sin\phi\cos\theta \\ 0 & -\sin\phi & \cos\phi\cos\theta \end{bmatrix} \tag{4.18}$$

The time rate of change of the Euler angles can be calculated through Equation 4.19 by taking the inverse of Equation 4.18.

$$\begin{bmatrix} \dot{\phi} \\ \dot{\theta} \\ \dot{\psi} \end{bmatrix} = \mathbf{T}_\Omega \begin{bmatrix} P \\ Q \\ R \end{bmatrix} \tag{4.19}$$

Where,

$$\mathbf{T}_\Omega = \begin{bmatrix} 1 & \sin\psi\tan\theta & \cos\phi\tan\theta \\ 0 & \cos\phi & -\sin\phi \\ 0 & \sin\phi\sec\theta & \cos\phi\sec\theta \end{bmatrix} |\theta| \neq \frac{\pi}{2} \tag{4.20}$$

The drawback of the Euler 3-2-1 method is the resulting singularity at $\theta = \pm 90\,\text{deg}$. This is, however, an acceptable limitation for the current project as the pitch angle is limited to $\theta_{max} = \pm 25\,\text{deg}$.

4.3.2.2 The Flight Path

The Direction Cosine Matrix relates the vehicle flight path information between the two axis systems, by transforming the coordinates of the vehicle state vector from one axis system to the other, using the vehicle attitude state information. A similar sequence of transformations (yaw, pitch and roll rotations) is employed in the derivation of the DCM, meaning it is essentially the matrix product of three separate transformation matrices, with each representing a single axis rotation. The resulting DCM presented here is defined in terms of the velocity vector, but the position vector can be used interchangeably.

The body axis linear velocities $\mathbf{V}_B = \{U, V, W\}^T$ are related to the inertial axis by the DCM $\mathbf{R}_V$ as,

$$\begin{bmatrix} U \\ V \\ W \end{bmatrix} = \mathbf{R}_V \begin{bmatrix} V_N \\ V_E \\ V_D \end{bmatrix} \tag{4.21}$$

Where,

$$\begin{bmatrix} V_N \\ V_E \\ V_D \end{bmatrix} = \begin{bmatrix} \dot{N} \\ \dot{E} \\ \dot{D} \end{bmatrix} \tag{4.22}$$

$$\mathbf{R}_V = \begin{bmatrix} c\psi c\theta & s\psi c\theta & -s\theta \\ c\psi s\theta s\phi - s\psi c\phi & s\psi s\theta s\phi + c\psi c\phi & c\theta s\phi \\ c\psi s\theta c\phi + s\psi s\phi & s\psi s\theta c\phi - c\psi s\phi & c\theta c\phi \end{bmatrix} \tag{4.23}$$

$$cx = cos(x)$$
$$sx = sin(x)$$

Whilst the inverse, $\mathbf{T}_V$, of $\mathbf{R}_V$ in Equation 4.23 relates the linear velocities in the inertial axis system to those in the body axis system as per Equation 4.24.

$$\begin{bmatrix} V_N \\ V_E \\ V_D \end{bmatrix} = \mathbf{T}_V \begin{bmatrix} U \\ V \\ W \end{bmatrix} \tag{4.24}$$

Where,

$$\mathbf{T}_V = \begin{bmatrix} c\psi c\theta & c\psi s\theta s\phi - s\psi c\phi & c\psi s\theta c\phi + s\psi s\phi \\ s\psi c\theta & s\psi s\theta s\phi + c\psi c\phi & s\psi s\theta c\phi - c\psi s\phi \\ -s\theta & c\theta s\phi & c\theta c\phi \end{bmatrix} \tag{4.25}$$

4.4 Forces and Moments

The external forces and moments acting on or about the vehicle CoM are used to determine the vehicle rigid-body dynamics as per Equation 4.5. The forces and moments acting on the quadrotor vehicle developed in this project arise from four alternative sources; namely,

1. Actuators
2. Tether
3. Body aerodynamics
4. Gravity

4.4.1 Actuators

4.4.1.1 Definitions

As previously stated in Chapter 1.1, the popularity of multirotor UAVs emanates from their inherently simple designs which lack the sophisticated rotorhead mechanics of traditional helicopter designs. Helicopters achieve flight control through the use of intricate swashplates, which allow the operator to vary the angle of attack of both the main and tail rotors whilst maintaining a consistent rotor speed. In contrast, multirotors employ several fixed-pitch, unarticulated rotors with flight control achieved by manipulating the thrust outputs of each of the aircraft's rotors by independently varying the individual motor speeds. Movement in the lateral and longitudinal directions is achieved by tilting the vehicle thrust vector in the desired direction of travel, while yaw movements exploit the differences in aerodynamic drag on the rotor blades rotating at different rotational velocities.

The positive quadrotor roll, pitch and yaw control inputs are illustrated in Figure 4.6. Virtual actuator definitions are applied in a similar fashion to those in traditional

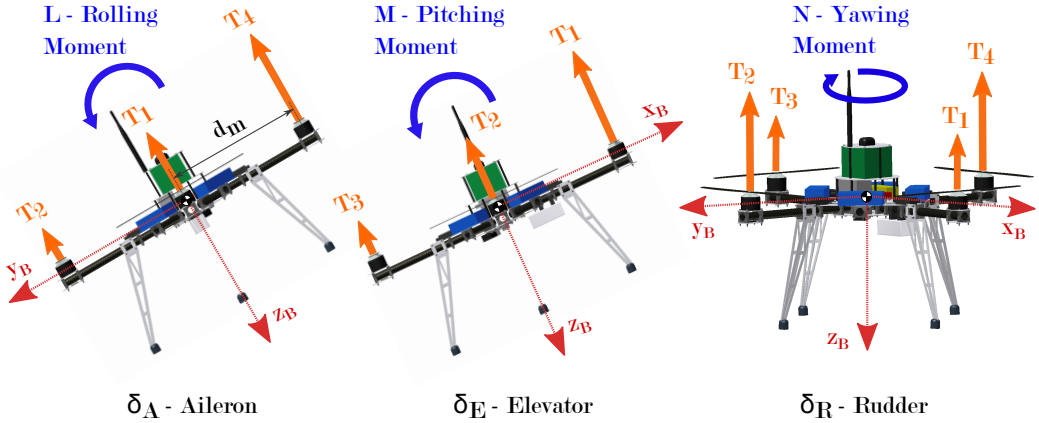

Figure 4.6: Virtual Actuator Definitions

fixed-wing aircraft; namely, aileron - δ_A, elevator - δ_E and rudder - δ_R, for roll, pitch and yaw commands respectively. The heave control input, δ_T, is omitted in Figure 4.6 but the concept is trivial in comparison as it simply involves changes in the total thrust output. The control inputs are therefore defined as,

$$\delta_T = T_{1_R} + T_{2_R} + T_{3_R} + T_{4_R} \text{ [N]} \tag{4.26}$$
$$\delta_A = T_{4_R} - T_{2_R} \text{ [N]} \tag{4.27}$$
$$\delta_E = T_{1_R} - T_{3_R} \text{ [N]} \tag{4.28}$$
$$\delta_R = -T_{1_R} + T_{2_R} - T_{3_R} + T_{4_R} \text{ [N]} \tag{4.29}$$

The aileron and elevator control inputs result in net rolling, L, and pitching, M, moments, respectively, about the vehicle CoM due to the motor mounting positions. The rudder control input instead generates a yawing moment by spinning each pair of counter-rotating rotors at differing rotational velocities, effectively exploiting the resulting rotor drag force differential to produce a net torque on the vehicle. The thrust control input simply results in a force input in the negative z_B body-axis direction.

4.4.1.2 Rotor Aerodynamics

The rotor aerodynamics are derived using a combination of both momentum and blade element theory based on work by Johnson [49] and Fay [57]. Momentum theory follows a global approach, whereby the rotor is modelled as a disk of zero thickness capable of supporting a pressure discontinuity. Estimates of the rotor performance are calculated using overall flow velocities and the conservation of momentum principle. Contrarily, blade element theory estimates the specific forces acting on the rotor blades due to their relative motion with a fluid.

From momentum theory the inflow velocity through the rotor disk in hover can be

shown to be,

$$v_h = \sqrt{\frac{T_h}{2\rho A}} \text{ [m/s]} \tag{4.30}$$

where T_h is the hover thrust, ρ is the density of the air and A is the rotor disk area. Considering the case of purely horizontal relative motion between the rotor and the fluid (with the rotor shaft perpendicular to the fluid flow) the inflow velocity is determined as,

$$v_1 = \sqrt{\frac{-{V_H}^2}{2} + \sqrt{\left(\frac{{V_H}^2}{2}\right)^2 + v_h^4}} \text{ [m/s]} \tag{4.31}$$

with,

$$V_H = \sqrt{{V_x}^2 + {V_y}^2} \text{ [m/s]} \tag{4.32}$$

where V_x and V_y are the relative airflow velocities in the x_B and y_B axes, as defined in Equation 4.65.

The inflow ratio, λ_i, is used to relate the inflow velocity to the rotational speed of the ith rotor. The inflow ratio is a dimensionless value and also serves to incorporate the effects of relative airflow in the z_B body axis as,

$$\lambda_i = \frac{v_1 - V_z}{\omega_i R} \tag{4.33}$$

where, ω_i is the rotational speed of the ith rotor and R is the rotor disk radius.

Similarly, the rotor advance ratio, μ_i, relates the horizontal relative airflow velocity to the rotational speed of the ith rotor as,

$$\mu_i = \frac{V_H}{\omega_i R} \tag{4.34}$$

From blade element theory the total thrust output is calculated as,

$$T_i = \rho A C_{Ti} (\omega_i R)^2 \text{ [N]} \tag{4.35}$$

$$\frac{C_{Ti}}{\sigma a} = \left(\frac{1}{6} + \frac{1}{4}\mu_i^2\right)\theta_{r0} - \left(1 + \mu_i^2\right)\frac{\theta_{tw}}{8} - \frac{1}{4}\lambda_i \tag{4.36}$$

where σ is the rotor solidity ratio, defined as,

$$\sigma = \frac{N\bar{c}}{\pi R} \tag{4.37}$$

with the equation variables defined as:

C_{Ti}	rotor thrust coefficient of the ith rotor
a	blade two-dimensional lift curve slope
θ_{r0}	rotor blade pitch-angle constant
θ_{tw}	rotor blade linear twist rate
N	number of blades
$\bar{c}$	mean blade chord length

4.4.1.3 Rotor Hub Forces and Moments

In additional to the vertical thrust forces, the rotor blades also generate significant horizontal (relative to the rotor disk plane) forces, which, when integrated over all the blade elements, result in a net drag force acting on the rotor hub. This net hub force acts perpendicular to the motor shaft in the direction of the net relative airflow. Following a similar derivation to the total thrust output, the rotor hub force is calculated as,

$$H_i = \rho A C_{Hi} (\omega_i R)^2 \text{ [N]} \tag{4.38}$$

$$\frac{C_{Hi}}{\sigma a} = \frac{1}{4a}\mu_i \bar{C_d} + \frac{1}{4}\lambda_i \mu_i \left(\theta_{r0} - \frac{\theta_{tw}}{2}\right) 6 \tag{4.39}$$

The total rotor hub force is resolved into x_B and y_B body axis components by Equations 4.40–4.41.

$$H_{xi} = \begin{cases} \dfrac{V_x}{V_H} H_i \text{ [N]}, & \text{if } V_H > 0 \\ 0, & \text{if } V_H = 0 \end{cases} \tag{4.40}$$

$$H_{yi} = \begin{cases} \dfrac{V_y}{V_H} H_i \text{ [N]}, & \text{if } V_H > 0 \\ 0, & \text{if } V_H = 0 \end{cases} \tag{4.41}$$

These forces consequently result in additional rolling and pitching moments in proportion to the perpendicular distance, d_r, from the vehicle CoM to the rotor disk plane in the z_B body axis; as well as yawing moments due hub force unbalances between the individual rotors. The resulting rotor hub moments are calculated as,

$$L_H = d_r \left(\sum_{i=1}^{4} H_{yi}\right) \text{ [N m]} \tag{4.42}$$

$$M_H = -d_r \left(\sum_{i=1}^{4} H_{xi}\right) \text{ [N m]} \tag{4.43}$$

$$N_H = d_m \left(H_{y1} - H_{x2} - H_{y3} + H_{x4}\right) \text{ [N m]} \tag{4.44}$$

4.4.1.4 Rotor Gyro Effects

During changes in pitch and roll orientation, the spinning rotor blades impart additional torques on the vehicle dynamics due to gyroscopic precession. With the rotors mounted vertically in the z_B body axis, it follows that changes in pitch and roll orientation of the vehicle (and hence the rotor plane) cause resulting torques that manifest orthogonal to the initial external torque input. The resultant gyroscopic torques are calculated as,

$$L_{gyro} = J_r Q \left(\omega_1 - \omega_2 + \omega_3 - \omega_4\right) \text{ [N m]} \tag{4.45}$$

$$M_{gyro} = J_r P \left(-\omega_1 + \omega_2 - \omega_3 + \omega_4\right) \text{ [N m]} \tag{4.46}$$

where J_r is the rotor inertia and P and Q are the vehicle rates of angular rotation about the x_B and y_B body axes respectively.

4.4.1.5 Summary of Actuator Forces and Moments

The final forces and moments resulting from the actuators are summarised as,

$$X^A = H_{xi} \text{ [N]} \tag{4.47}$$

$$Y^A = H_{yi} \text{ [N]} \tag{4.48}$$

$$Z^A = -\delta_T \text{ [N]} \tag{4.49}$$

$$L^A = d_m \delta_A + L_H + L_{gyro} \text{ [N m]} \tag{4.50}$$

$$M^A = d_m \delta_E + M_H + M_{gyro} \text{ [N m]} \tag{4.51}$$

$$N^A = R_N \delta_R + N_H \text{ [N m]} \tag{4.52}$$

where, d_m is the boom length distance to the vehicle CoM perpendicular to the individual rotor thrust vectors, as illustrated in Figure 4.6, and R_N is the virtual yaw moment arm which relates the rotor thrust output to the resulting rotor drag torque, as described in Chapter 3.3.4.

4.4.2 Tether Forces

The tether forces acting on the vehicle are due to the tether mass, dynamics and aerodynamic drag. The tether is also capable of exerting a 'tether moment' on the aircraft due to the tether attachment point being offset a distance d_t from the vehicle CoM in the positive z_B direction, as illustrated in Figure 4.7.

The tether model outputs the horizontal (F_H) and vertical (F_V) components of the total tether force at the vehicle attachment point in the tether coordinate system.

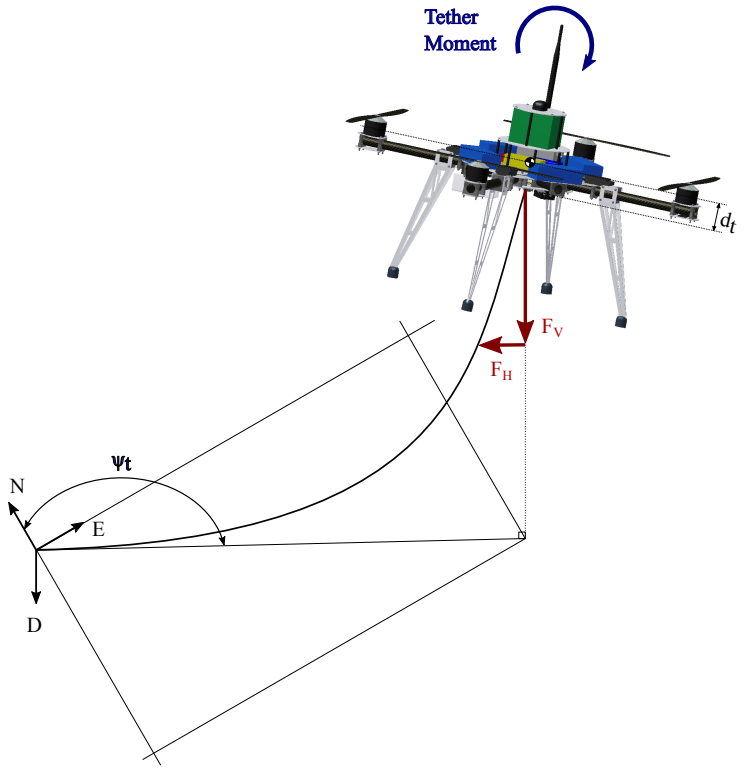

Figure 4.7: Illustration of Tether Notation and Coordinate System

The horizontal tether force is then transformed into the inertial axis system using the tether direction azimuth (ψ_t), as in Equations 4.53 – 4.54.

$$F_N^t = -F_H \cos\psi_t \text{ [N]} \tag{4.53}$$

$$F_E^t = -F_H \sin\psi_t \text{ [N]} \tag{4.54}$$

These forces are then resolved into the aircraft body axis coordinate system using the DCM $\mathbf{R}_V$, that was previously defined in Equation 4.23.

$$\begin{bmatrix} F_x^t \\ F_y^t \\ F_z^t \end{bmatrix} = \mathbf{R}_V \begin{bmatrix} F_N^t \\ F_E^t \\ F_V \end{bmatrix} \tag{4.55}$$

The tether forces in the the x_B and y_B axes generate additional pitching and rolling moments about the vehicle CoM. Mechanical swivel joints are installed at either end of the tether to prevent the build-up of any torsional forces in the tether due to the cable twisting. The frictional forces in the swivel joints are small enough to be assumed irrelevant, and the tether-vehicle attachment point is located directly below the aircraft CoM, near enough to the z_B axis to ensure that the tether effects on the yaw dynamics are negligible ($N^T \approx 0$). The final tether forces and moments

acting on the aircraft are summarised in Equations 4.56 – 4.60.

$$X^T = F_x^t \text{ [N]} \tag{4.56}$$

$$Y^T = F_y^t \text{ [N]} \tag{4.57}$$

$$Z^T = F_z^t \text{ [N]} \tag{4.58}$$

$$L^T = -d_t F_y^t \text{ [N m]} \tag{4.59}$$

$$M^T = d_t F_x^t \text{ [N m]} \tag{4.60}$$

4.4.3 Body aerodynamics

When a solid object immersed in a fluid experiences relative motion between itself and the fluid, it is subjected to pressure forces normal to the body surfaces and shear forces parallel to the body surfaces. These pressure and shear forces on each of the body surfaces are aggregated to form resultant pressure and shear forces acting on the object. The drag force is the component of these resultant pressure and shear forces parallel to the flow direction.

This section models the dominant aerodynamic drag forces acting on the aircraft due to relative motion between the vehicle body (excluding the rotor blades) and the surrounding fluid stream. External flow problems are notoriously complex with exact analytical solutions typically unobtainable. CFD analyses can provide useful results but experimental wind-tunnel testing remains the most accurate method of analysis. An alternative pragmatic approach, whereby the aerodynamic forces are inferred from practical flight data under 'known' wind conditions, is limited by the accuracy of the GPS sensor. In the absence of both CFD techniques and empirical approaches, this analysis makes a number of simplifying assumptions in the derivation of the aerodynamic model.

4.4.3.1 Aerodynamic Forces

The drag force calculations are based on laminar incompressible flow, with the fluid properties assumed constant throughout the flow field. The fluid properties selected throughout this thesis are those of air at 15°C and 1 atm, as defined by Çengel and Cimbala [48, Table A-9]. The aerodynamic drag forces acting on the vehicle are calculated using Equations 4.61 – 4.62 as,

$$F_{D_i} = q_i C_{D_i} \text{ [N]} \tag{4.61}$$

$$q_i = \frac{1}{2}\rho V_i |V_i| \text{ [Pa]} \tag{4.62}$$

with the equation variables defined as:

C_{D_i}	lumped vehicle drag coefficient
q_i	dynamic fluid pressure
ρ	fluid density
V_i	relative fluid velocity

where the subscript i denotes either of the x_B, y_B or z_B body-axis directions.

The drag force can, depending on the aircraft velocity vector, orientation and prevailing wind conditions, act in either the positive or negative z_B directions, where it will either reduce or augment the total thrust output; manifesting as either an upwards or downwards force on the vehicle. The lumped vehicle drag coefficients are determined for each of the body-axis directions in Chapter 3.3.3.

The dynamic fluid pressure from Equation 4.62 is a function of the fluid density and relative fluid velocity. The relative fluid velocity, in turn, is determined as the sum of the aircraft velocity and any external wind. Wind is added to the simulation model to improve the model fidelity, with details of the wind model provided in Chapter 8.3.1.

The wind model outputs a reference wind vector, $\mathbf{V}_I^{w*}$, with wind magnitudes in the inertial axis frame at an altitude of 10 m. The final wind magnitudes acting on the vehicle are determined as a function of the vehicle altitude as,

$$\begin{bmatrix} V_N^w \\ V_E^w \\ V_D^w \end{bmatrix} = \left(\frac{|D|}{10}\right)^{\eta_w} \begin{bmatrix} V_N^{w*} \\ V_E^{w*} \\ V_D^{w*} \end{bmatrix} \text{ [m/s]} \tag{4.63}$$

where, D is the vehicle altitude and η_w is the Hellmann exponent as specified in Chapter 5.1.

The final wind magnitudes are then resolved in the aircraft body axis coordinate system using the DCM $\mathbf{R}_V$ from Equation 4.23,

$$\begin{bmatrix} V_x^w \\ V_y^w \\ V_z^w \end{bmatrix} = \mathbf{R}_V \begin{bmatrix} V_N^w \\ V_E^w \\ V_D^w \end{bmatrix} \text{ [m/s]} \tag{4.64}$$

The final relative fluid velocity is then simply the sum of the wind and the airflow components resulting from the aircraft velocity as in Equation 4.65.

$$\begin{bmatrix} V_x \\ V_y \\ V_z \end{bmatrix} = - \begin{bmatrix} U \\ V \\ W \end{bmatrix} + \begin{bmatrix} V_x^w \\ V_y^w \\ V_z^w \end{bmatrix} \text{ [m/s]} \tag{4.65}$$

The final aerodynamic forces in the body-axis coordinate system are summarised in

Equations 4.66 – 4.68.

$$X^D = q_x C_{D_x} \text{ [N]} \tag{4.66}$$
$$Y^D = q_y C_{D_y} \text{ [N]} \tag{4.67}$$
$$Z^L = q_z C_{L_z} \text{ [N]} \tag{4.68}$$

These forces are applied directly to the vehicle CoM, which implies that the effects of wind shear are neglected. In practice, any drag surfaces away from the vehicle CoM provide potential sources of wind shear, which can generate additional rolling, pitching and yawing moments on the aircraft. Wind shear effects about the z_B body axis are expected to be small due to the highly symmetric nature of the vehicle layout about the XZ and YZ planes. Contrarily, the aircraft is noticeably asymmetric about the XY plane, which results in the effects of wind shear about the x_B and y_B body axes having a more pronounced impact on the vehicle dynamics. Drag surfaces above and below the vehicle CoM will have opposing effects on one another, in proportion to their respective shapes, sizes, orientations and distances from the vehicle CoM. These effects are difficult to accurately quantify and any attempt at doing so is ultimately prevented by the lack of available empirical data on how the body drag coefficients vary for various orientations relative to the fluid stream.

Ultimately the wind shear assumption is, in any case, overshadowed by the inherent limitations of a simplified analytical approach such as the method of superposition. The model neglects the potentially significant effects of the rotor downwash on the fluid stream, nor does it account for the effects of the already simplified 3-Dimensional bodies on one another. Deficiencies in the aerodynamic model are, however, tempered by their overall (in)significance. In the analyses of multirotor systems, with the exception of the vehicle actuators, the remaining aerodynamic forces are significantly less dominant relative to their fixed-wing counterparts. This is due to differences in both the aircraft designs and flight velocities. Therefore the simplified modelling approach is deemed sufficient for the purposes of this research project, especially considering the limited flight envelope.

4.4.4 Gravitational Force

The effects of gravitational acceleration on the vehicle are modelled as a force corresponding to Newton's 2nd law, which acts exclusively in the positive Z_I direction of the inertial axis system. Using the flat, non-rotating earth assumption the gravitational field is assumed uniform which causes the vehicle CoM and centre of gravity (CoG) to coincide. Therefore the gravitational force does not generate any moments on the vehicle ($L^G = M^G = N^G = 0$). The inertial force vector can therefore be

defined as,

$$\mathbf{F_I^G} = \begin{bmatrix} 0 \\ 0 \\ mg \end{bmatrix} \text{ [N]} \tag{4.69}$$

The force vector in the body axis system is determined using the transformation matrix defined in Equation 4.23.

$$\mathbf{F_B^G} = \mathbf{R_v F_I^G} \tag{4.70}$$

The final gravitational forces acting on the vehicle CoM in the body axis system are summarised as,

$$\mathbf{F_B^G} = \begin{bmatrix} X^G \\ Y^G \\ Z^G \end{bmatrix} = \begin{bmatrix} -\sin\theta \\ \cos\theta\sin\phi \\ \cos\theta\cos\phi \end{bmatrix} mg \text{ [N]} \tag{4.71}$$

4.4.5 Summary of Aircraft Forces and Moments

The final forces and moments acting in and about the aircraft's body axes can be summarised as,

$$\sum X_i = X^A + X^T + X^D + X^G \quad \text{[N]} \tag{4.72}$$

$$\sum Y_i = Y^A + Y^T + Y^D + Y^G \quad \text{[N]} \tag{4.73}$$

$$\sum Z_i = Z^A + Z^T + Z^L + Z^G \quad \text{[N]} \tag{4.74}$$

$$\sum L_i = L^A + L^T \quad \text{[N m]} \tag{4.75}$$

$$\sum M_i = M^A + M^T \quad \text{[N m]} \tag{4.76}$$

$$\sum N_i = N^A \quad \text{[N m]} \tag{4.77}$$

These forces are used in Equations 4.11–4.16 to determine the dynamic response of the vehicle in the non-linear simulation environment.

Chapter 5

Tether Modelling

The tether influence is expected to be substantial in the context of the UAV system and, therefore, the tether model forms a critical element of the analysis. A representative mathematical model of the tether is required for both the development and evaluation of the autonomous flight control strategy before practical testing can be attempted. Of particular interest is the 'loose to taut' tether transitions where the aircraft is potentially vulnerable to large impact forces. Thus, the tether model aims to best represent this scenario.

The chapter begins with the identification and characterisation of the primary tether forces in order to better coordinate the tether modelling strategy. Thereafter the tether modelling strategy is presented, before the chapter culminates with an analysis of the potential tether dynamics.

5.1 Tether Forces

The primary forces acting on the tether consist of the aerodynamic drag force, the tether weight and additional tether tension forces generated by the constraining nature of the tether on the vehicle. Due to the low tension forces, the tether lengths employed and the pedestrian vehicle flight envelope, centripetal forces can be shown to be sufficiently small to be neglected from the analysis.

5.1.1 Aerodynamic Drag

The aerodynamic drag force can be separated into friction and pressure drag components. The pressure drag component acts perpendicular to the tether and forms the major contributor. Conversely, the friction component acts tangential to the tether and is typically an order of magnitude (or greater) smaller than the pressure

drag component [24], and is therefore neglected. The frictional drag component is typically considered in high-altitude applications (such as tethered aerostats or inflatable kite systems) which incorporate tether lengths upwards of 1 km in length; but its omission is deemed a reasonable assumption in the context of this project.

The aerodynamic drag force is calculated in a similar manner to the vehicle drag force from Equation 4.61 as,

$$F_{D_t} = q_t C_{D_t} d_t L_t \text{ [N]} \tag{5.1}$$

$$q_t = \frac{1}{2}\rho \bar{V}_t^2 \text{ [Pa]} \tag{5.2}$$

where,

C_{D_t}	tether pressure drag coefficient
d_t	tether cross-sectional diameter
L_t	total length of the elevated portion of the tether
q_t	dynamic fluid pressure acting on the tether
ρ	fluid density
$\bar{V}_t$	average relative fluid velocity perpendicular to the tether

The tether pressure drag coefficient of $C_{D_t} = 1.2$ is determined empirically by Hoerner [24, 3-9], and is valid for $10^3 \geq Re < 2 \times 10^5$,

$$Re = \frac{\rho V_t d_t}{\mu} \tag{5.3}$$

where, μ is the dynamic viscosity of the fluid.

Justus and Mikhail [58] provide a means of estimating the windspeed variation with altitude via a reference windspeed V_R at a corresponding reference altitude h_r,

$$\frac{V}{V_R} = \left(\frac{h}{h_R}\right)^{\eta_w} \tag{5.4}$$

where, $\eta_w = 0.2$ is the Hellmann exponent based on neutrally stable air above relatively flat terrain[1].

The average windspeed, $\bar{V}$, over the vehicle altitude interval $[0, |D|]$ is used to determine the aerodynamic drag force on the tether, based on a reference altitude of

[1] Technically defined as terrain with ground objects and/or shrubbery $\leq$5 m in height.

$h_R = 10$ m.

$$\bar{V} = \frac{V_R}{|D|} \int_0^{|D|} \left(\frac{h}{10}\right)^{0.2} dh \text{ [m/s]} \tag{5.5}$$

$$\bar{V} = V_R K (|D|)^{0.2} \text{ [m/s]} \tag{5.6}$$

$$K = \frac{0.1^{0.2}}{1.2} \tag{5.7}$$

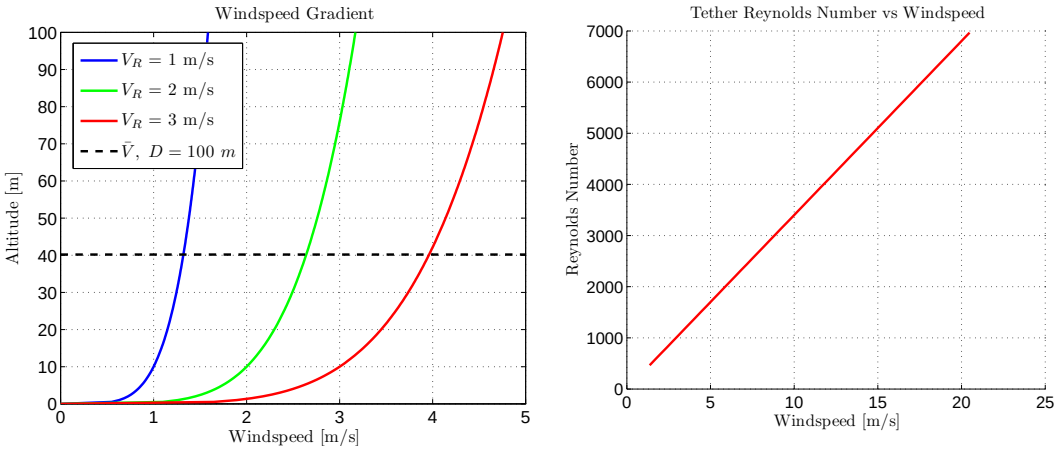

(a) Windspeed gradient and average. (b) Tether Reynolds number vs windspeed.

Figure 5.1: Illustration of the windspeed gradient, average windspeed and Tether Reynolds Number

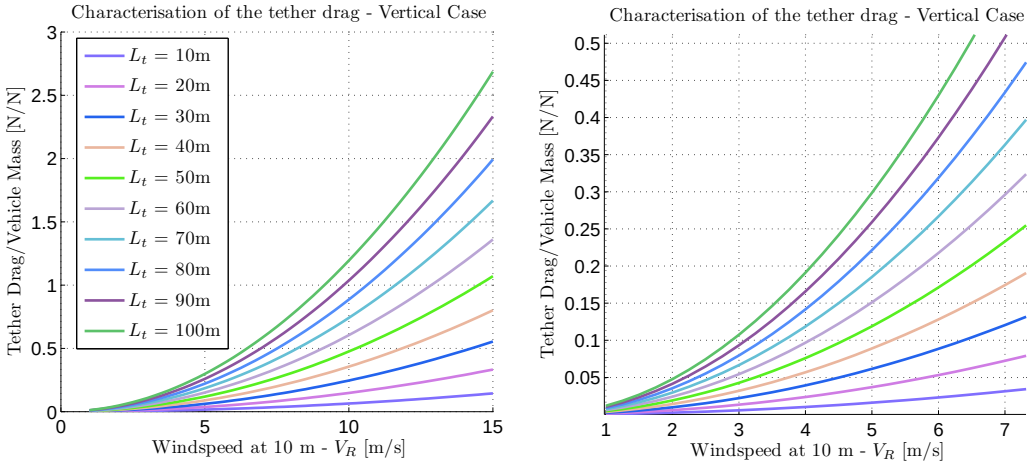

(a) $\frac{\text{Tether Drag Force}}{\text{Vehicle Weight}}$ (b) Figure 5.2a expanded.

Figure 5.2: Characterisation of the tether drag vs windspeed

Figure 5.2 illustrates the variation of the tether-drag-force to untethered-vehicle-weight ratio, relative to both the windspeed and tether length. The ratio provides a simple means of gauging the impact of the drag force on the tethered system in a static sense. The analysis considers the vertical tether case, with a steady wind parallel to the ground.

Unsurprisingly, the tether drag force is increasingly sensitive to fluctuations in windspeed for longer tether lengths. This is primarily due to the quadratic drag term in Equation 5.2, in addition to the increases in the mean windspeed and the drag surface area for longer tether lengths. Nevertheless, at low to moderate windspeeds the static drag force magnitudes remain small relative to the vehicle inertia for the majority of tether lengths.

5.1.2 Tether Weight

The weight is the gravitational force acting on the tether due to it's own mass. The tether mass increases linearly with the tether length, L_t, while the tether weight, w_t, is the product of the tether mass and gravity, $g = 9.81\,\mathrm{ms}^{-2}$. The tether weight always acts vertically in the inertial coordinate system and is determined as,

$$w_t = \mu_t L_t \text{ [N]} \tag{5.8}$$

For 'shorter' ($L_t \ll 1\,\mathrm{km}$) low-altitude applications, tethers are commonly modelled as massless, with the effects of the tether weight neglected. However, this assumption is limited to non-conducting tethers, which can be manufactured from high-strength and low-weight synthetic materials; or applications where the tether weight is small relative to the vehicle reaction forces and/or inertia. In contrast, the tether weight is expected to be significant for the quadrotor UAV case, considering the 'conducting' tether, the limited reaction forces and small aircraft inertia.

Figure 5.3 provides a comparison of the tether weight and aerodynamic forces with respect to the vehicle weight, w_v. For general operating conditions, with moderate to low windspeeds, the tether weight constitutes the primary static disturbance force on the aircraft, with the tether weight comparable in magnitude to a $9\,\mathrm{ms}^{-1}$ cross-wind at the 10 m reference altitude.

5.1.3 Tether Tension

The final tether force considered is the additional static tension forces that may arise due to the restraining action of the tether on the aircraft. The static tension force is inherently limited by the thrust capabilities of the aircraft, and is inversely proportional to the tether weight and aerodynamic drag forces, as per Figure 5.4.

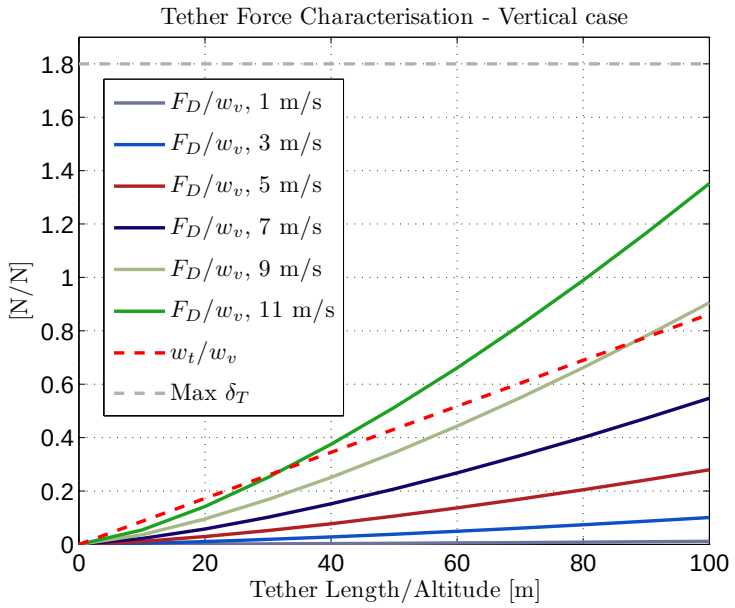

Figure 5.3: Comparison of the tether weight and drag forces.

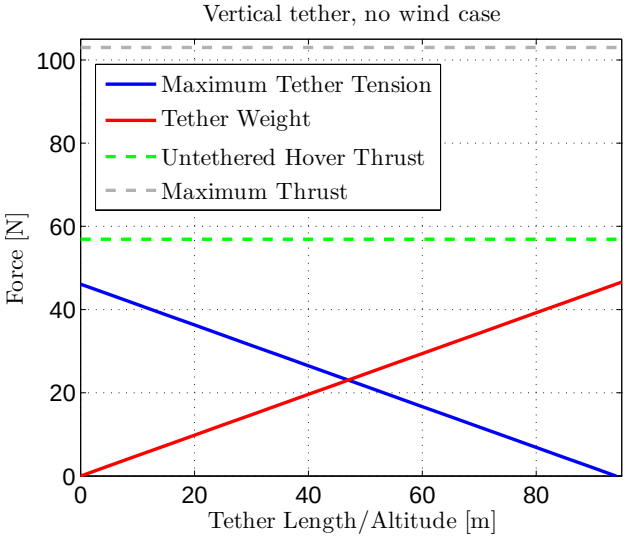

Figure 5.4: Tension force capability of the tethered system.

An additional tension capability is desirable from a design perspective in order to counter tether disturbances and maintain a desired altitude set-point. Consequently, the aircraft's altitude tracking ability is diminished as the tension headroom decreases with a corresponding increase in altitude. As a result, Figure 5.4 provides an indication of the maximum altitude capabilities of the tethered system.

5.2 Modelling Strategy

As perhaps is indicated by the tether force analysis, the major underlying assumption employed in the derivation of the tether model is that the tether remains in a constant state of equilibrium, enabling it to be treated quasi-statically. In reality the tether forces fluctuate continuously, but the tether is assumed to reach equilibrium quickly enough to validate this assumption. This approach is one commonly employed in the analysis of tethered kite systems [21, 22, 23, 25].

The modelling strategy is indicated below for three alternative tether configurations; namely, a partially-elevated tether state, a general case for the fully-elevated tether state and the vertical case for the fully-elevated tether state.

5.2.1 Partially-Elevated Tether

The first, and simplest, tether configuration is that of the partially-elevated tether, which occurs in three possible scenarios:

i. During and after take-off as the vehicle climbs to it's operational altitude.

ii. In the event of large 'shock' impacts where the aircraft loses sufficient altitude for the tether to become slack.

iii. In the event that the aircraft is incapable of lifting the tether in it's entirety.

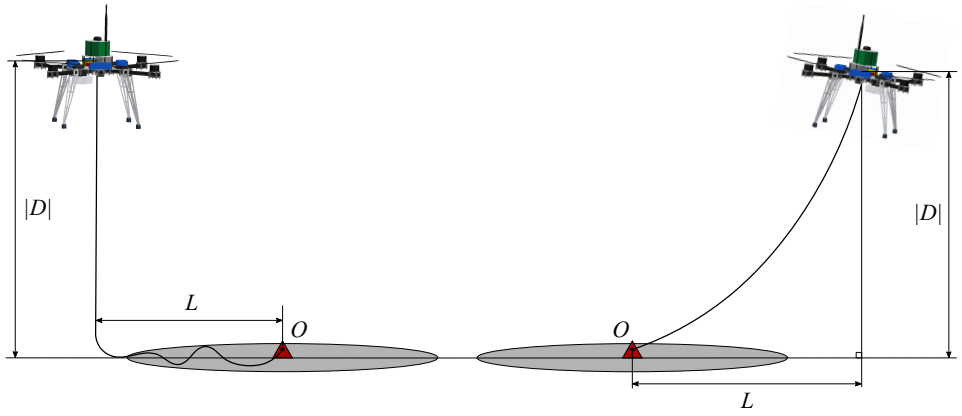

Figure 5.5: Illustration of the partially- and fully-elevated (general case) tether configurations.

The partially-elevated state is entered when the aircraft satisfies the following positional condition,

$$\sqrt{L^2 + D^2} \leq L_t \tag{5.9}$$

where, L is the horizontal span distance between the aircraft and the tether mounting point, O.

This condition is conservative and it leads to a slight overestimation of the tether force vector as the system transitions between the partially and fully elevated states, but it is a reasonable assumption as the forces in this state are typically small.

The tether is incapable of supporting additional tension forces in this state, and consequently, the dominant forces consist of the tether weight and aerodynamic forces. Aerodynamic forces are expected to have an increased influence on the orientation of the tether force vector in this state, due to the smaller force magnitudes involved. The vertical tether force component is determined from the vehicle altitude as,

$$F_D^t = \mu_t |D| \text{ [N]} \tag{5.10}$$

While the horizontal tether force components are determined using the aerodynamic drag reaction forces at the vehicle, neglecting any frictional forces between the tether and the ground.

$$F_N^t = \frac{1}{2} q_{tN} C_{D_t} d_t |D| \text{ [N]} \tag{5.11}$$

$$F_E^t = \frac{1}{2} q_{tE} C_{D_t} d_t |D| \text{ [N]} \tag{5.12}$$

Resulting in the tether force vector, $\mathbf{F}^T$, in the inertial axis system,

$$\mathbf{F}^T = \begin{bmatrix} F_N^t \\ F_E^t \\ F_D^t \end{bmatrix} \text{ [N]} \tag{5.13}$$

5.2.2 Fully-Elevated Tether

The equilibrium equations for the general case of the fully-elevated tether are developed in Chapter 5.3 following a similar approach to the analyses of guy cables by Irvine [59] and Dean [60]. The governing equations are derived based on the simplifying assumption that the tether aerodynamic drag force component is small relative to the total tether tension. The equations are developed by applying a static force balance to an elemental length of the tether, with the aircraft and tether mounting point providing positional boundary conditions at each end of the tether.

The resulting system of equations reduces to that of a catenary, which provides an effective means of modelling the tension force gradients during the critical ‘loose to

taut' transitions. The catenary equations consist of both algebraic and transcendental functions, and therefore, require iterative numerical solution methods. Approximate 'explicit' solutions are determined by replacing the transcendental terms with their respective power series expansions. These solutions are used as initial conditions to an iterative scheme based on Newton's Method.

The solutions diverge from the actual solutions for the vertical tether case, where the tether angle of inclination to the ground approaches 90° and the catenary representation is no longer valid. For this scenario the tether force is estimated via the Lagrangian methods described in Appendix A.2. The 'pre-impact' kinetic energy of the vehicle is used to estimate the resulting elastic deformation of the tether as a function of the vehicle's initial impact velocity. Thereafter, Hooke's Law is used to determine the impact force as a linear function of strain.

5.3 Quasi-static Tether Governing Equations

The tether is modelled as per Figure 5.6, with the tether mounting position at point O and the airborne aircraft at point P. Notation choices are based on those typically found in literature, with the lower-case letters s, l and h representing the tether length, span and vehicle altitude respectively.

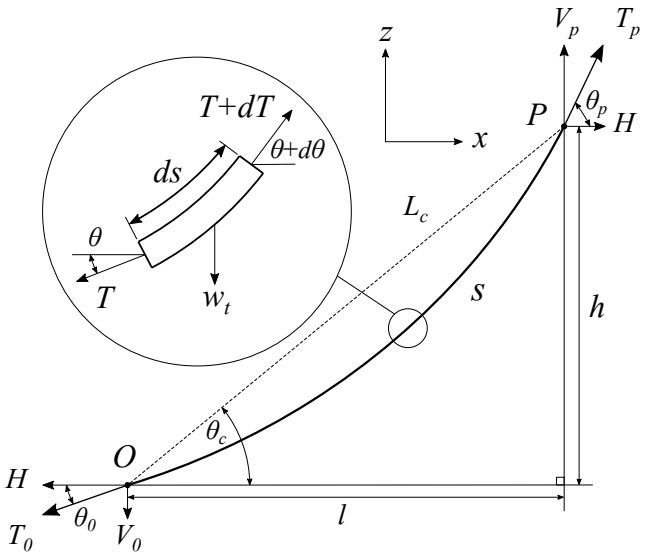

Figure 5.6: Free-body diagram for the general fully-elevated tether case.

Applying a static force balance to the elemental tether length, ds, in the vertical

axis, z, the equilibrium equations can be derived as,

$$\sum F_z = 0 \quad \rightarrow \quad dT \sin\theta = \mu_t ds \tag{5.14}$$

$$T = \frac{H}{cos\theta} \tag{5.15}$$

$$\tan\theta = \frac{dz}{dx} \tag{5.16}$$

Substituting Equations 5.15 and 5.16 into Equation 5.14 yields,

$$\frac{d^2z}{dx^2} = \frac{\mu_t}{H} ds \tag{5.17}$$

The element length is given by,

$$ds = \sqrt{dx^2 + dz^2} \tag{5.18}$$

Substituting Equation 5.18 into 5.17 yields,

$$\frac{d^2z}{dx^2} = \frac{\mu_t}{H} \sqrt{1 + \left(\frac{dz}{dx}\right)^2} \tag{5.19}$$

Integrating Equation 5.19 yields,

$$\frac{dz}{dx} = \sinh\left(\frac{\mu_t}{H}x + C_1\right) \tag{5.20}$$

$$z(x) = \frac{H}{\mu_t} \cosh\left(\frac{\mu_t}{H}x + C_1\right) + C_2 \tag{5.21}$$

The integration constants C_1 and C_2 are evaluated using the known positional boundary conditions for the vehicle and tether mounting point, $z = 0$ at $x = 0$ and $z = h$ at $x = l$.

$$C_2 = -\frac{H}{\mu_t} \cosh\left(C_1\right) \tag{5.22}$$

$$C_1 = \sinh^{-1}\left(\frac{\mu_t h}{2H \sinh\left(\frac{\mu_t l}{2H}\right)}\right) - \frac{\mu_t l}{2H} \tag{5.23}$$

Now substituting Equation 5.20 into 5.18 yields,

$$\frac{ds}{dx} = \sqrt{1 + \left(\sinh\left(\frac{\mu_t}{H}x + C_1\right)\right)^2} \tag{5.24}$$

$$\frac{ds}{dx} = \cosh\left(\frac{\mu_t}{H}x + C_1\right) \tag{5.25}$$

Integrating Equation 5.25 yields an equation for the tether length s,

$$s(x) = \frac{H}{\mu_t} \sinh\left(\frac{\mu_t}{H}x + C_1\right) + C_3 \tag{5.26}$$

The integration constant C_3 is evaluated at the boundary condition for the tether mounting point $s = 0$ at $x = 0$.

$$C_3 = -\frac{H}{\mu_t}\sinh\left(C_1\right) \tag{5.27}$$

Using the known tether length, $s(l) = L_t$, and hyperbolic trigonometry identities, Equation 5.26 can be manipulated to yield the simplified expression,

$$L_t = \sqrt{h^2 + \frac{4H^2}{\mu_t^2}\sinh^2\left(r\right)} \tag{5.28}$$

or,

$$\sqrt{L_t^2 - h^2} = \frac{2H}{\mu_t}\sinh\left(r\right) \tag{5.29}$$

where,

$$r = \frac{\mu_t l}{2H} \tag{5.30}$$

The tether slope angles θ_0 and θ_P are determined by substituting Equation 5.16 into Equation 5.20 and evaluating at $x = 0$ and $x = l$.

$$\theta_O = \tan^{-1}\left(\sinh\left(C_1\right)\right) \tag{5.31}$$

$$\theta_P = \tan^{-1}\left(\sinh\left(\frac{\mu_t}{H}l + C_1\right)\right) \tag{5.32}$$

The vertical reaction forces are then determined using the tether slope and horizontal reaction force, H.

$$V_O = H\tan\theta_0 \tag{5.33}$$

$$V_P = H\tan\theta_P \tag{5.34}$$

Solution Method

The solution method focusses on determining the horizontal tether force component, H, for a given vehicle position $P = \{N, E, D\}$ and a known tether length L_t. Thereafter, the tether inclination angle at the vehicle, θ_P, and the vertical tether force component, V_P, are easily obtainable from Equations 5.32 and 5.34 respectively.

The catenary equations with their transcendental terms are smooth functions which are well-suited to numerical iteration techniques to approximate the function roots.

An iterative scheme based on Newton's Method is developed in order to determine solutions for the horizontal force component for a given vehicle position and a known tether length. The formula for the iterative scheme is derived in terms of the horizontal force component and the zero function f_0 as,

$$H_{n+1} = H_n - \frac{f_0}{\partial f_0 / \partial H_n} \tag{5.35}$$

From Equation 5.29 the zero function is defined as,

$$f_0 = \frac{2H_n}{\mu_t} \sinh\left(\frac{\mu_t l}{2H_n}\right) - \sqrt{L_t^2 - h^2} \tag{5.36}$$

The zero function derivative, in terms of the horizontal force component, is subsequently derived as,

$$\frac{\partial f_0}{\partial H_n} = \frac{2}{\mu_t} \sinh\left(\frac{\mu_t l}{2H_n}\right) - \frac{l}{H_n} \cosh\left(\frac{\mu_t l}{2H_n}\right) \tag{5.37}$$

The performance of the iterative scheme is largely dependent on the selection of an appropriate initial estimate H_0 sufficiently close to the real function root. To that end, the transcendental function in Equation 5.29 is approximated by its corresponding Maclaurin series expansion which enables an explicit solution for H_0. The Maclaurin series expansion of the hyperbolic sine function is given by Stewart [61] as,

$$\sinh(x) = x + \frac{x^3}{3!} + \frac{x^5}{5!} + \dots \tag{5.38}$$

Substituting Equation 5.38 into 5.29 and retaining powers up to and including r^5, yields an approximate solution for the tether length, L_t, in terms of the chord length L_c (from Figure 5.6) as,

$$L_t \approx L_c + \frac{l^2 r^2}{6L_c} + \frac{l^2 r^4}{45L_c} - \frac{l^4 r^4}{72L_c^3} \tag{5.39}$$

Equation 5.39 can be subsequently expressed in terms of r as,

$$ar^4 + br^2 + c = o \tag{5.40}$$

where,

$$a = \frac{1}{5} - \frac{l^2}{8L_c^2} \tag{5.41}$$

$$b = \frac{3}{2} \tag{5.42}$$

$$c = -\frac{9L_c\left(L_t - L_c\right)}{l^2} \tag{5.43}$$

Equation 5.40 is a biquadratic equation and can be easily solved for r^2 using the quadratic formula,

$$r^2 = \frac{-b + \sqrt{b^2 - 4ac}}{2a} \tag{5.44}$$

Thereafter, H_0 is determined via Equation 5.30 as,

$$H_0 = \frac{\mu_t l}{2\sqrt{r^2}} \tag{5.45}$$

Equation 5.45 provides a well-defined initial estimate of the horizontal tether force component, which aids numerical stability and improves the rate of convergence. A solution accurate to within 0.01 N is typically found within 3 iterations.

5.4 Tether Dynamics

The quasi-static assumption employed in the derivation of the tether model assumes that the tether maintains a state of equilibrium and uniform tension. While this assumption is reasonable for the general flight case, there are specific instances where the tether dynamics may result in significant tension fluctuations that could have a destabilising effect on the aircraft.

5.4.1 Fundamental Tether Frequency

Changes in tension are communicated through the tether by transverse and longitudinal waves. Longitudinal waves act tangentially through the tether and are attenuated primarily through internal friction forces, which renders them well damped. Transverse waves, contrarily, act perpendicular to the tether and are poorly damped due to aerodynamic drag being the primary dissipation mechanism.

Treating the tether as a vibrating string, the fundamental frequency, f_t, of the tether can be determined in terms of the transverse and longitudinal wave velocities, $c_{t/l}$, as,

$$f_{i0} = \frac{c_i}{2L_t} \text{ [Hz]} \tag{5.46}$$

where,

$$c_t = \sqrt{\frac{T}{\lambda_t}} \quad \text{[m/s]} \tag{5.47}$$

$$c_l = \sqrt{\frac{k+T}{\lambda_t}} \text{ [m/s]} \tag{5.48}$$

where, T is the tension in the tether, λ_t is the tether mass per unit length and k is the tether stiffness constant defined in Equation A.5.

5.4.2 Mechanisms of Excitation

The aircraft dynamics and external wind form the two possible mechanisms of excitation for the tether. Disturbances with frequencies matching that of the tether fundamental frequency (or even perhaps harmonics of the fundamental) can potentially cause the tether to resonate, generating high-amplitude longitudinal and transverse waves.

Longitudinal Excitation

Prolonged excitation of the tether longitudinal dynamics is unlikely due to the low-energy nature of the tethered system. The tether stiffness constant in Equation 5.48 is several orders of magnitude larger than the tension forces ($k \ggg T$) which results in a fundamental frequency well above that of the aircraft dynamics, $f_{l0} \ggg f_a$. Similarly, the high-frequency aerodynamic forces acting on the tether are small relative to the forces required to elastically deform the cable. Snap loading scenarios present the only means of longitudinal wave excitation, the effects of which are mitigated by the extremely short loading durations and the effective attenuation mechanism.

Transverse Excitation

The formation of transverse waves in the tether can alter both the magnitude and direction of the tether force vector. The equation for transverse waves on a string is derived by Hartog [62] from Hooke's Law as,

$$\frac{\partial^2 u(r,t)}{\partial r^2} = \frac{1}{c_t^2}\frac{\partial^2 u(r,t)}{\partial t^2} \tag{5.49}$$

With a solution of the form,

$$u(r,t) = \sum_{n=0}^{\infty} B_n \sin\left(2\pi n f_{t0} t + \phi\right) \sin\left(\frac{n\pi}{L}x\right) \tag{5.50}$$

where, u is the direction normal to the straight tether and r is the radial direction along the tether.

Thus, resonant transverse excitation of the tether would manifest as a fluctuating tether force vector, that is magnified by the inertia of the dynamic tether and periodic in both magnitude and direction.

The transverse excitation of wind-loaded flexible cable structures is a well-documented phenomenon caused by aeroelastic flutter. Cable systems are vulnerable to two alternative flutter regimes; namely, conductor gallop and vortex shedding.

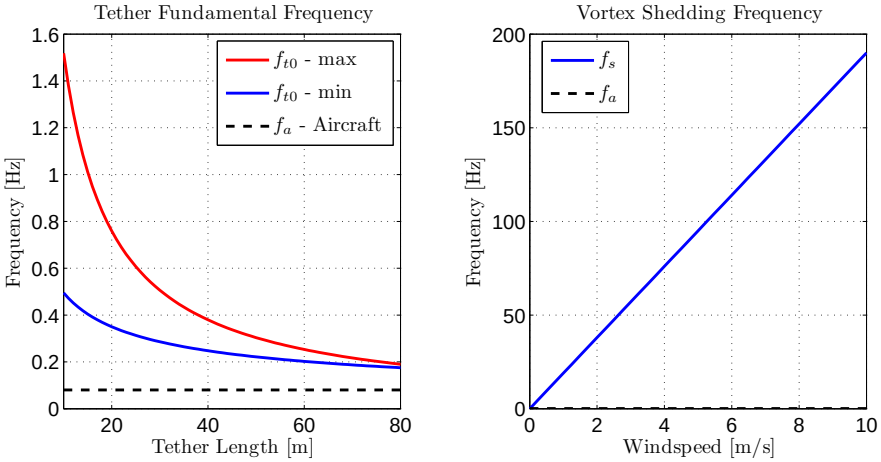

Figure 5.7: Separation of the aircraft and tether dynamics.

Vortex shedding is a high-frequency, low-amplitude oscillatory flow state caused by alternating low-pressure vortices in the tether wake. The alternating nature of these pressure vortices causes the cable to oscillate normal to the flow direction at a frequency, f_s. The vortex shedding frequency for a circular cylinder is given by Equation 5.51 as,

$$f_s = \frac{St \cdot V}{d_t} \text{ [Hz]} \tag{5.51}$$

where, V is the flow velocity, d_t is the cylinder diameter and St is the Strouhal number equal to $St \approx 0.2$ for $250 \geq Re < 10^5$.

Vibration in the tether can be resonant, for a suitably periodic wind load, if the fundamental frequency, f_{t0}, of the tether coincides with the vortex shedding frequency. It is clear from Figure 5.7 that is an unlikely scenario as the vortex shedding frequency is well separated from the fundamental tether frequency and any significant harmonics.

Conductor gallop is a low-frequency ($0.1 - 1$ Hz), high-amplitude oscillatory phenomenon encountered by cable structures with asymmetrical cross-sections. The nonsymmetric profile causes the cable to become aerodynamically unstable, which results in the high-amplitude oscillatory response. While the frequency range coincides with f_{t0}, conductor gallop is expected to be suppressed by utilising a tether with a circular cross-section.

In addition to the possible wind excitation mechanisms, transverse waves can result from changes in the aircraft position. High-energy radial positional changes, that typically result in snap loading scenarios, can cause transverse oscillations due to the kinetic energy of the tether as it transitions from a loose to taut configuration. While these oscillations are poorly damped, they are expected to be small relative to the initial impact force, and will decay over time.

Perhaps of greater concern is the possibility of the aircraft dynamics exciting the tether's resonant modes through tangential positional changes. Figure 5.7 illustrates the degree of separation between the aircraft positional dynamics and the fundamental tether frequency. While the aircraft's positional dynamics are lower than the tether fundamental frequency, they are within an order of magnitude of one another and could feasibly result in some degree of transverse excitation. The effects of such an excitation are inherently confined by the physical limitations of the aircraft as a forcing function, but the forces could be significant enough to destabilise the autonomous flight controllers. In such a scenario the tether excitation should be obvious to an observer, at which point the safety pilot can take evasive action by reducing altitude and/or releasing tether if required.

Chapter 6

General Features of Tethered Flight

The introduction of a tether introduces unique control challenges for the quadrotor UAV. This section aims to identify the idiosyncrasies of tethered flight in the pursuit of a viable autonomous control strategy for the aircraft.

6.1 Simplified Governing Equations

The tethered flight strategy is based on the assumption that tether may be treated as a disturbance, which implies that the tether dynamics may be neglected from the linear aircraft model. This assumption is not valid for short tether lengths, where the tether force vector is significantly greater than the tether weight ($F_t \gg w_t$).

Due to the symmetric nature of the aircraft, the dominant aircraft dynamics can be sufficiently encapsulated by the simplified 2-Dimensional case ($\{\phi, \dot{\phi}, \ddot{\phi}, \dot{\psi}, \ddot{\psi}\} = 0$) illustrated in Figure 6.1. The yaw angle, ψ, is set such that the aircraft's x_B axis is aligned with the horizontal component tether force vector. The yaw dynamics remain unchanged for the tethered case and are neglected as they are sufficiently decoupled. Neglecting aerodynamic effects and the actuator gyro moments, the governing equations for the aircraft can be further simplified to,

$$\ddot{z} = \frac{-\delta_T}{m} + gcos(\theta_v) + \frac{F_t}{m}sin(\theta_v + \theta_p) \tag{6.1}$$

$$\ddot{x} = -gsin(\theta_v) + \frac{F_t}{m}cos(\theta_v + \theta_p) \tag{6.2}$$

$$\ddot{\theta}_v = \frac{\delta_E d_m}{I_{yy}} + \frac{d_t F_t}{I_{yy}}cos(\theta_v + \theta_p) \tag{6.3}$$

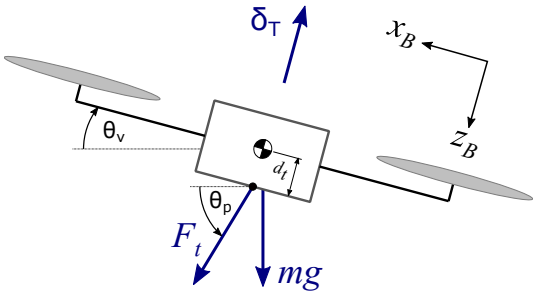

Figure 6.1: 2-Dimensional Case: Forces and Notation.

6.2 Tether as a Constraint

The most obvious feature of tethered flight is the constraining nature of the tether on the aircraft position. This feature becomes particularly problematic, from a conventional position feedback control perspective, when coupled with any uncertainty in the aircraft's position state vector. Estimates of the aircraft's inertial position state vector are provided by the kinematic state estimator by propagating measurements from the onboard inertial measurement unit. However, these estimates tend to drift from the actual state over time due to sensor biases and numerical integration errors. To counter this, the propagated estimates are corrected at intervals of 5 Hz using position measurements from a GPS receiver. The 5 Hz corrections are fast relative to the aircraft's positional dynamics, which results in the propagated estimates quickly settling at the GPS measurement values.

The positional accuracy attainable through GPS is highly variable for differing hardware and measurement techniques, and can range from several metres to centimetre precision. As stated in Chapter 3.2.2.1, the GPS receiver used on the aircraft is a NEO-7P module by ublox, which is a standalone single-point GPS receiver. Static position tests (illustrated in Figure 6.2) were conducted to provide an indication of the GPS measurement drift at the practical testing facility over the duration of a typical flight. The test results are presented in Table 6.1 and compared against performance specifications provided by ublox.

Table 6.1: GPS Position Accuracy

	50% CEP	σ	2σ	3σ	Unit
Horizontal - Specification	<1	<1.2	<2.4	<3.6	[m]
Horizontal - Measured	0.87	1.04	2.086	3.129	[m]
Vertical - Specification	-	2.4–3.6	4.8–7.2	7.2–10.8	[m]
Vertical - Measured	-	2.60	5.2	7.80	[m]

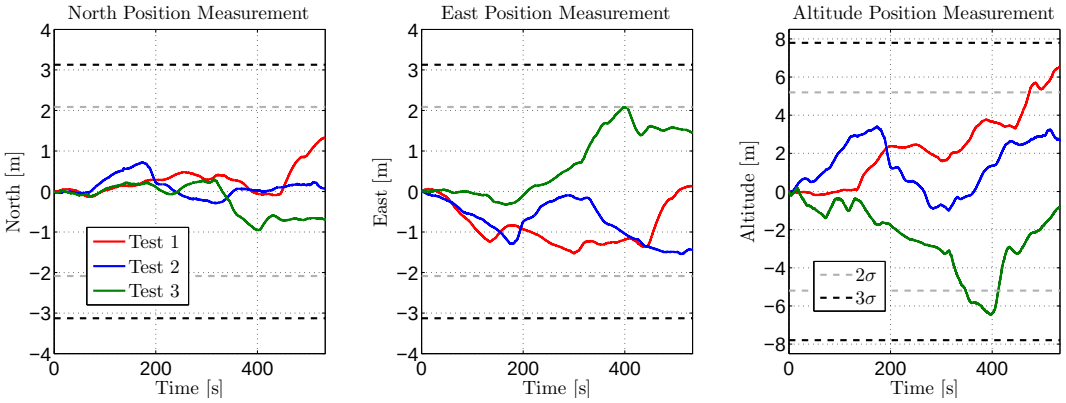

Figure 6.2: Illustration of the GPS Measurement Drift

The measured data correlates well with the performance specifications provided by the manufacturer for both the horizontal and vertical position measurements. It is clear that the tethered system requires a dedicated vertical control strategy that is robust to the significant uncertainty in the altitude measurements. The uncertainty in the horizontal position measurements is less problematic. Conventional longitudinal and lateral control strategies are expected to be feasible within a suitably defined flight envelope.

6.2.1 Flight Envelope

Equations 6.1–6.2 can be used to determine the theoretical positional limits where the aircraft is capable of maintaining a static equilibrium ($\{\ddot{z}, \ddot{x}, \ddot{\theta}_v\} = 0$), based on the maximum thrust vector, $\delta_{T_{max}}$, and a maximum desired aircraft orientation angle of $\theta_{v_{max}} = \pm 25°$.

By equating $\ddot{z} = 0$, Equation 6.1 can be manipulated into the form,

$$F_t = \frac{\delta_T - mg\cos(\theta_v)}{\sin(\theta_v + \theta_p)} \tag{6.4}$$

Substituting Equation 6.4 into 6.2 the tether inclination angle is calculated as,

$$\theta_p = \cot^{-1}\left(\frac{mg\sin(\theta_v)}{\delta_T - mg\cos(\theta_v)}\right) - \theta_v \quad |\delta_T > mg\cos(\theta_v)| \tag{6.5}$$

The minimum tether inclination angle, and by implication the maximum horizontal span limit, can be determined from Equation 6.6, based on the desired tether length and horizontal position certainty limit.

$$\theta_{p_{min}} = cos^{-1}\left(\frac{L_t cos(\hat{\theta}_p) - n\sigma}{L_t}\right) \tag{6.6}$$

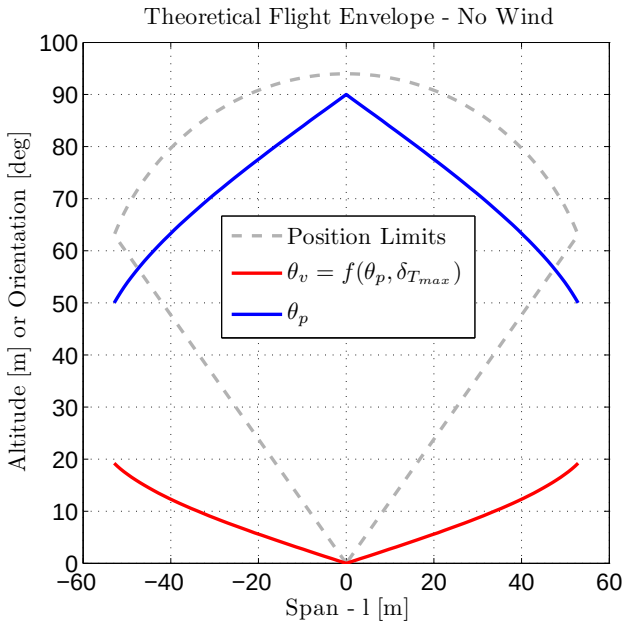

Figure 6.3: Positional flight envelope and equilibrium conditions.

where, $\hat{\theta}_p = f(\delta_{T_{max}}, \theta_{v_{max}})$ from Equation 6.5.

The ideal vertical position limits are calculated using Equation 6.7, based on the maximum tether force, $F_{t_{max}}$, for a given tether inclination angle.

$$h_{max} = \frac{F_{t_{max}} sin^2(\theta_p)}{\mu_t} \tag{6.7}$$

An iterative scheme (again based on Newton's Method) is developed in order to determine solutions for the aircraft orientation angle, θ_v, accurate to within 0.01°. The aircraft orientation angle, in turn, is required for the computation of $F_{t_{max}}$ in Equation 6.4. The iterative method is defined as,

$$\theta_v^{n+1} = \theta_v^n - \frac{f_0}{\partial f_0 / \partial \theta_v^n} \tag{6.8}$$

Where the zero function, f_0, is defined by once again substituting Equation 6.4 into 6.1.

$$f_0 = mg \left\{ cos(\theta_v) + sin(\theta_v) tan(\theta_v + \theta_p) \right\} - \delta_{T_{max}} \tag{6.9}$$

The zero function partial derivative is subsequently derived as,

$$\frac{\partial f_0}{\partial \theta_v^n} = mg \left\{ cos(\theta_v) tan(\theta_v + \theta_p) + sin(\theta_v) sec^2(\theta_v + \theta_p) - sin(\theta_v) \right\} \tag{6.10}$$

The aircraft positional limits, based on the $\approx 99.7\%$ horizontal position certainty limit of $3\sigma = 3.6\,\text{m}$, and a minimum operational altitude of 10 m, are illustrated in Figure 6.3.

6.3 Tether Disturbance Forces

This section aims to quantify the effects of the tether disturbance forces on the aircraft, by considering the aircraft sensitivity to variations in the tether force vector. Thereafter, the natural damping properties of the tether are investigated.

6.3.1 Sensitivity

Variations in the tether force vector are expected to arise due to the aircraft dynamics, the unmodelled tether dynamics and environmental disturbances such as wind. For the 'static' hover case, these variations are expected to manifest as small fluctuations in the static tether force vector; while, away from the hover flight condition, larger fluctuations can arise as the tether transitions suddenly between the loose and taut tether configurations.

Equations 6.1–6.3 can be derived in terms of F_t to determine the sensitivity of the aircraft parameters $\ddot{z}$, $\ddot{x}$ and $\ddot{\theta}_v$ to fluctuations in the tether force vector.

$$\frac{\partial \ddot{z}}{\partial F_t} = \frac{1}{m} sin(\theta_v + \theta_p) \tag{6.11}$$

$$\frac{\partial \ddot{x}}{\partial F_t} = \frac{1}{m} cos(\theta_v + \theta_p) \tag{6.12}$$

$$\frac{\partial \ddot{\theta}_v}{\partial F_t} = \frac{d_t}{I_{yy}} cos(\theta_v + \theta_p) \tag{6.13}$$

Equations 6.11–6.13 illustrate the effect of the aircraft's mass and rotational inertia on the overall sensitivity of the aircraft to tether force fluctuations. The sensitivity of $\ddot{\theta}_v$ is also highly dependent on the tether attachment offset distance, d_t, from the vehicle's CoM. Figure 6.4 illustrates the sensitivity functions for various tether inclination angles, with the vehicle orientation used to represent the two alternative loading conditions. The sensitivity of $\ddot{z}$ remains relatively constant regardless of the vehicle orientation and the tether inclination angle, while $\ddot{x}$ and $\ddot{\theta}_v$ are significantly more sensitive for an increasingly orthogonal tether force vector. This feature is further aggravated during impulse loading conditions where the aircraft is initially in a near-level orientation state ($\theta_v \approx 0$).

The results serve to validate one's intuitive expectations but can be misleading when considered in isolation. For instance, the results indicate that the aircraft is more

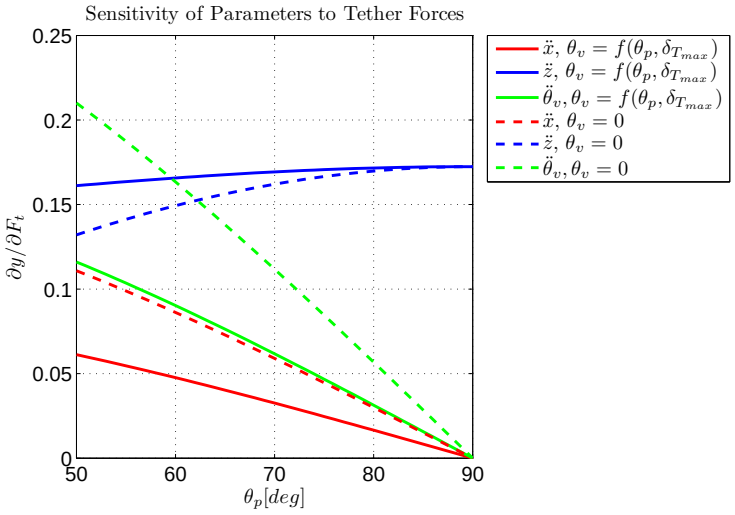

Figure 6.4: Sensitivity of aircraft parameters to tether forces for a range of tether inclination angles.

robust to tether force fluctuations at larger tether inclination angles, but this must be considered in the context of the expected tether force magnitudes. Similarly, the physical properties of the aircraft must be increased relative to the expected tether force magnitudes in order to be effective. Additional compromises to a larger aircraft include a potential reduction in bandwidth, as well as larger aerodynamic drag forces and increased power requirements.

6.3.2 Tether Catenary Effect

Large fluctuations in the tether force vector are possible as the system transitions between the loose and taut tether configurations. Such transitions can result from vertical and horizontal aircraft position steps, changes in the tether length, and from external disturbances, such as wind gusts and atmospheric turbulence. In certain scenarios these transitions can manifest as 'snap loading' conditions, where the tether deforms elastically and generates high-amplitude impulse forces at the tether attachment point. These impulse forces are proportional to the pre-impact kinetic energy of the tethered system, and can be significant even for low transition velocities (see Figure 3.8).

Both the magnitudes and frequencies of occurrence, of these transition impulse forces, can be diminished by exploiting the natural damping properties of the tether's own weight. As the horizontal span distance increases, so too does the component of the tether weight that counteracts any efforts by the aircraft to tighten the tether. The increased tether weight component serves to reduce the tether force and angle gradients, which provide a more gradual dissipation of the system's kinetic energy. This, in turn, results in reduced transition forces. The catenary effect can be sig-

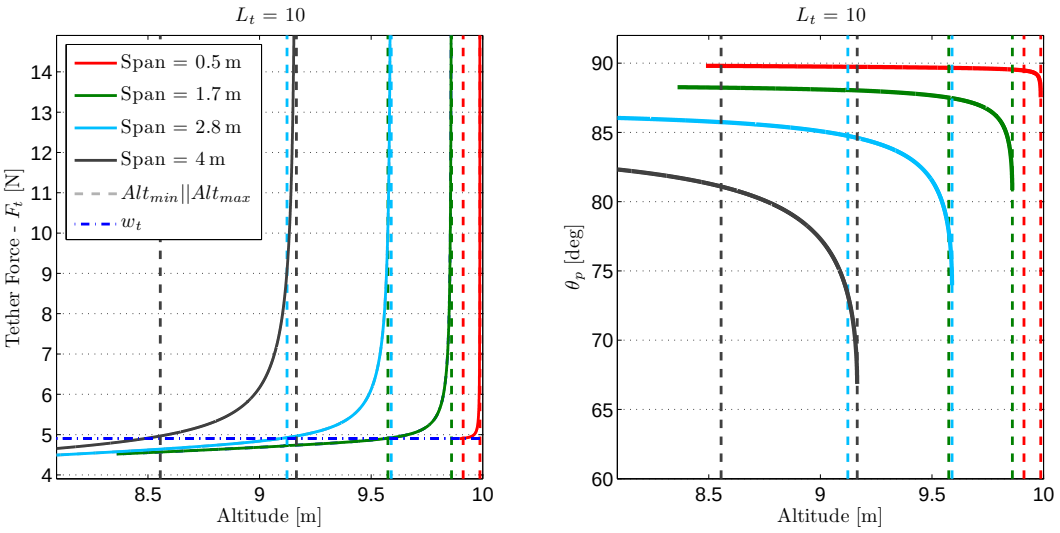

Figure 6.5: Variation of the tether force and angle gradients with span.

nificant even for short tether lengths. Figure 6.5 illustrates how the tether force and angle gradients vary for differing horizontal span distances for a tether length of $L_t = 10\,\text{m}$; while Figure B.2, in Appendix B.2, illustrates the concept for longer tether lengths.

The vertical dashed lines from Figure 6.5 represent the minimum and maximum altitude limits for a given horizontal span distance and total tether length. The maximum altitude is simply the maximum attainable altitude as determined by Pythagoras' Theorem. While the minimum altitude is defined as the minimum required altitude, to elevate the tether in it's entirety, resulting in the tether angle at the origin satisfying the condition, $\theta_0 \geq 0$. From Figure 6.5 it is clear that the minimum altitude approaches the maximum altitude for increasingly vertical tether configurations, resulting in the narrowing of the potential altitude band as the horizontal span distance approaches zero. In addition to the more abrupt tether force gradients at reduced span distances, narrow altitude bands are similarly undesirable as they increase the susceptibility of the tethered system to disturbances, resulting in more frequent loose to taut tether transitions.

From a control strategy perspective, the kinetic energy of the system may be limited by imposing a suitable velocity limit near the expected transition altitude. However, this method is limited by the uncertainty in the GPS position measurements, but can be augmented using the catenary effect, in order to maintain an adequate dynamic response. Exploitation of the catenary effect has the added benefit of increasing the potential altitude band, thereby reducing the frequency of transition events. The caveat, of course, is the reduced operational efficiencies caused by the increased static tether force vector, which further constrains the maximum altitude limit (as illustrated in Figure 6.3) and/or results in additional power consumption. This could be mitigated, to a degree, by positioning the aircraft downwind from

the tether mounting point, O. The horizontal tether weight and aerodynamic drag force components would counter one another, resulting in a larger horizontal relative airflow component to the vehicle actuators (from Equation 4.34) and improved thrust generation efficiencies. For longer tether lengths, span offsets may not even be necessary as the larger tether weight will inherently limit the kinetic energy of the system, while additional 'natural' damping will be provided by the increased aerodynamic drag forces.

6.4 Stability of the Tethered Aircraft

This section aims to quantify the effects of the tether disturbance forces on the aircraft stability by analysing the influence of several tether parameters on the aircraft's open-loop dynamics.

6.4.1 Linear Aircraft Model

The 2-Dimensional model is linearised about the static hover trim condition based on a desired trim thrust command, $\bar{\delta}_T$, and vehicle orientation, $\bar{\theta}_v$. The remaining trim variables, $\bar{\theta}_p$ and $\bar{F}_t$, are determined via Equations 6.5 and 6.4 respectively.

For convenience, additional variables $\{w, u\}$ are defined as,

$$w = \dot{z} \tag{6.14}$$

$$u = \dot{x} \tag{6.15}$$

Recall the virtual actuator lag dynamics that were provided in Chapter 3.3.2 as,

$$\dot{\delta}_i = -\frac{1}{\tau}\delta_i + \frac{1}{\tau}\delta_{i_R} \tag{6.16}$$

where, δ_i represents the output in newtons for the ith actuator and δ_{i_R} represents the commanded/reference value.

With $\phi = 0$, the orientation dynamics from Equation 4.19 resolve to,

$$\dot{\theta}_v = Q = q_v \tag{6.17}$$

Equations 6.1, 6.2, 6.3, 6.16 and 6.17 constitute the primary dynamics of the 2-Dimensional system. By treating the tether as a disturbance, the inertial position states are assumed not to form part of the primary dynamics and are omitted from the linear model. The yaw dynamics are similarly omitted as they are not specifically influenced with the introduction of the tether. The dynamic equations may be

represented in state space form as,

$$\dot{\mathbf{x}} = \mathbf{f}(\mathbf{x}, \mathbf{u}) \tag{6.18}$$

where,

$$\mathbf{x} = \begin{bmatrix} \delta_T & \delta_E & q_v & \theta_v & u & w \end{bmatrix}^T \tag{6.19}$$

$$\mathbf{u} = \begin{bmatrix} \delta_{T_R} & \delta_{E_R} \end{bmatrix}^T \tag{6.20}$$

The state and control input vectors can be represented at the sum of the trim state and a small perturbation as,

$$\mathbf{x} = \mathbf{x}_T + \mathbf{\Delta x} \tag{6.21}$$

$$\mathbf{u} = \mathbf{u}_T + \mathbf{\Delta u} \tag{6.22}$$

Equation 6.18 can be linearised via a Taylor series expansion about the hover trim condition as,

$$\dot{\mathbf{x}}_T + \mathbf{\Delta}\dot{\mathbf{x}} = \mathbf{f}(\mathbf{x}_T, \mathbf{u}_T) + \frac{\partial \mathbf{f}}{\partial \mathbf{x}}\Big|_T \Delta\mathbf{x} + \frac{\partial \mathbf{f}}{\partial \mathbf{u}}\Big|_T \Delta\mathbf{u} + h.o.t. \tag{6.23}$$

Linearising about an equilibrium trim condition implies the state dynamics at these trim conditions are zero, $\dot{\mathbf{x}}_T = \mathbf{f}(\mathbf{x}_T, \mathbf{u}_T) = 0$. Furthermore, assuming the state perturbations are small enables the omission of the higher order terms (h.o.t.) of the Taylor series expansion.

$$\mathbf{\Delta}\dot{\mathbf{x}} \approx \frac{\partial \mathbf{f}}{\partial \mathbf{x}}\Big|_T \Delta\mathbf{x} + \frac{\partial \mathbf{f}}{\partial \mathbf{u}}\Big|_T \Delta\mathbf{u} \tag{6.24}$$

Expanding Equation 6.24 yields,

$$\begin{bmatrix} \dot{\delta}_T \\ \dot{\delta}_E \\ \dot{q}_v \\ \dot{\theta}_v \\ \dot{u} \\ \dot{w} \end{bmatrix} = \begin{bmatrix} \frac{\partial \dot{\delta}_T}{\partial \delta_T} & \frac{\partial \dot{\delta}_T}{\partial \delta_E} & \frac{\partial \dot{\delta}_T}{\partial q_v} & \frac{\partial \dot{\delta}_T}{\partial \theta_v} & \frac{\partial \dot{\delta}_T}{\partial u} & \frac{\partial \dot{\delta}_T}{\partial w} \\ \frac{\partial \dot{\delta}_E}{\partial \delta_T} & \frac{\partial \dot{\delta}_E}{\partial \delta_E} & \frac{\partial \dot{\delta}_E}{\partial q_v} & \frac{\partial \dot{\delta}_E}{\partial \theta_v} & \frac{\partial \dot{\delta}_E}{\partial u} & \frac{\partial \dot{\delta}_E}{\partial w} \\ \frac{\partial \dot{q}_v}{\partial \delta_T} & \frac{\partial \dot{q}_v}{\partial \delta_E} & \frac{\partial \dot{q}_v}{\partial q_v} & \frac{\partial \dot{q}_v}{\partial \theta_v} & \frac{\partial \dot{q}_v}{\partial u} & \frac{\partial \dot{q}_v}{\partial w} \\ \frac{\partial \dot{\theta}_v}{\partial \delta_T} & \frac{\partial \dot{\theta}_v}{\partial \delta_E} & \frac{\partial \dot{\theta}_v}{\partial q_v} & \frac{\partial \dot{\theta}_v}{\partial \theta_v} & \frac{\partial \dot{\theta}_v}{\partial u} & \frac{\partial \dot{\theta}_v}{\partial w} \\ \frac{\partial \dot{u}}{\partial \delta_T} & \frac{\partial \dot{u}}{\partial \delta_E} & \frac{\partial \dot{u}}{\partial q_v} & \frac{\partial \dot{u}}{\partial \theta_v} & \frac{\partial \dot{u}}{\partial u} & \frac{\partial \dot{u}}{\partial w} \\ \frac{\partial \dot{w}}{\partial \delta_T} & \frac{\partial \dot{w}}{\partial \delta_E} & \frac{\partial \dot{w}}{\partial q_v} & \frac{\partial \dot{w}}{\partial \theta_v} & \frac{\partial \dot{w}}{\partial u} & \frac{\partial \dot{w}}{\partial w} \end{bmatrix} \begin{bmatrix} \delta_T \\ \delta_E \\ q_v \\ \theta_v \\ u \\ w \end{bmatrix} + \begin{bmatrix} \frac{\partial \dot{\delta}_T}{\partial \delta_{T_R}} & \frac{\partial \dot{\delta}_T}{\partial \delta_{E_R}} \\ \frac{\partial \dot{\delta}_E}{\partial \delta_{T_R}} & \frac{\partial \dot{\delta}_E}{\partial \delta_{E_R}} \\ \frac{\partial \dot{q}_v}{\partial \delta_{T_R}} & \frac{\partial \dot{q}_v}{\partial \delta_{E_R}} \\ \frac{\partial \dot{\theta}_v}{\partial \delta_{T_R}} & \frac{\partial \dot{\theta}_v}{\partial \delta_{E_R}} \\ \frac{\partial \dot{u}}{\partial \delta_{T_R}} & \frac{\partial \dot{u}}{\partial \delta_{E_R}} \\ \frac{\partial \dot{w}}{\partial \delta_{T_R}} & \frac{\partial \dot{w}}{\partial \delta_{E_R}} \end{bmatrix} \begin{bmatrix} \delta_{T_R} \\ \delta_{E_R} \end{bmatrix} \tag{6.25}$$

$$\begin{bmatrix} \dot{\delta}_T \\ \dot{\delta}_E \\ \dot{q}_v \\ \dot{\theta}_v \\ \dot{u} \\ \dot{w} \end{bmatrix} = \begin{bmatrix} -\frac{1}{\tau} & 0 & 0 & 0 & 0 & 0 \\ 0 & -\frac{1}{\tau} & 0 & 0 & 0 & 0 \\ 0 & \frac{d_m}{I_{yy}} & 0 & \frac{\partial \dot{q}_v}{\partial \theta_v} & 0 & 0 \\ 0 & 0 & 1 & 0 & 0 & 0 \\ 0 & 0 & 0 & \frac{\partial \dot{u}}{\partial \theta_v} & 0 & 0 \\ -\frac{1}{m} & 0 & 0 & \frac{\partial \dot{w}}{\partial \theta_v} & 0 & 0 \end{bmatrix} \begin{bmatrix} \delta_T \\ \delta_E \\ q_v \\ \theta_v \\ u \\ w \end{bmatrix} + \begin{bmatrix} \frac{1}{\tau} & 0 \\ 0 & \frac{1}{\tau} \\ 0 & 0 \\ 0 & 0 \\ 0 & 0 \\ 0 & 0 \end{bmatrix} \begin{bmatrix} \delta_{T_R} \\ \delta_{E_R} \end{bmatrix} \tag{6.26}$$

$$\frac{\partial \dot{q}_v}{\partial \theta_v} = -\frac{d_t \bar{F}_t}{I_{yy}} sin\left(\bar{\theta}_v + \bar{\theta}_p\right) \tag{6.27}$$

$$\frac{\partial \dot{u}}{\partial \theta_v} = -gcos\left(\bar{\theta}_v\right) - \frac{\bar{F}_t}{m} sin\left(\bar{\theta}_v + \bar{\theta}_p\right) \tag{6.28}$$

$$\frac{\partial \dot{w}}{\partial \theta_v} = -gsin\left(\bar{\theta}_v\right) + \frac{\bar{F}_t}{m} cos\left(\bar{\theta}_v + \bar{\theta}_p\right) \tag{6.29}$$

For short tether lengths, such as during take-off and landing, the aircraft state vector can be augmented by the tether dynamics. This yields similar open-loop dynamics to that of an inverted pendulum (with an unstable real pole) and requires a dedicated control solution. For longer tether lengths the effects of the tether dynamics are expected to be diminished to the extent that they may be neglected from the analysis.

6.4.2 Open-loop Dynamics

Figure 6.6 provides a comparison of the open-loop poles for the untethered and tethered aircraft configurations. The open-loop poles give insight into the unforced response of the aircraft, known as the natural modes of motion.

The open-loop dynamics of the linear untethered aircraft consist of fast, critically-damped poles and poles at the origin. The fast, real poles correspond with the first-order lag dynamics of the actuators. While the poles at the origin correspond with the aircraft's linear and angular dynamics; which, excluding aerodynamic drag forces, illustrate the aircraft's inability to naturally counter any external disturbances.

The introduction of the tether force yields a pair of complex oscillatory poles on the imaginary axis, which result from the interaction between the tether moment and the aircraft's angular dynamics. Any disturbance in the aircraft's orientation

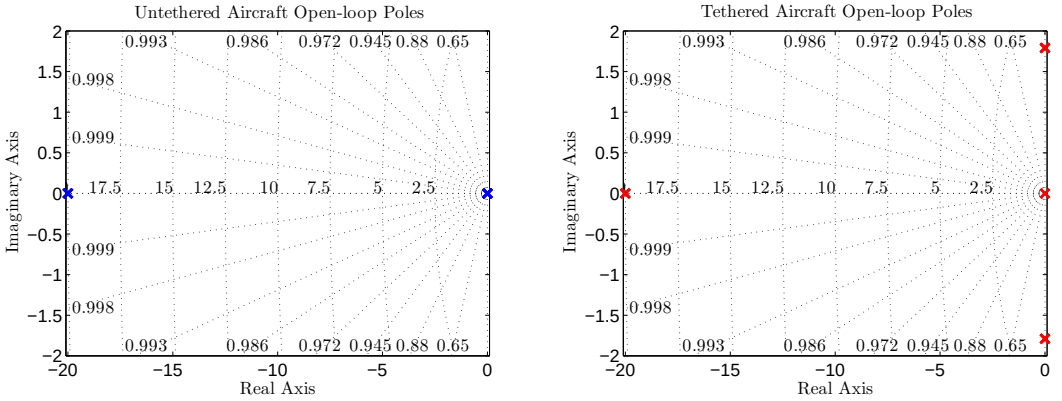

Figure 6.6: Comparison of the open-loop poles of the untethered and tethered† aircraft.

changes the magnitude of the tether moment which drives the oscillatory response. Aerodynamic drag serves as the primary damping mechanism. The omission of these drag terms from the linear model results in the poles being situated on the imaginary axis. In reality one can expect the poles to have a small real component resulting in a slow, underdamped natural response. The poles at the origin correspond to the translational dynamics of the tethered configuration. This is similar to the untethered configuration and is a result of the assumption that the tether may be treated as a disturbance, which neglects the position feedback property of the tether. When considering the tether dynamics (for scenarios where the tether tension is significantly larger than the tether weight $F_t \gg w_t$) the pole relating to the translational dynamics moves into the RHP, with the root-locus resembling that of an inverted pendulum.

†$\bar{\theta}_v = 0°$, $\bar{\delta}_T = mg + 20\mu_t$ N

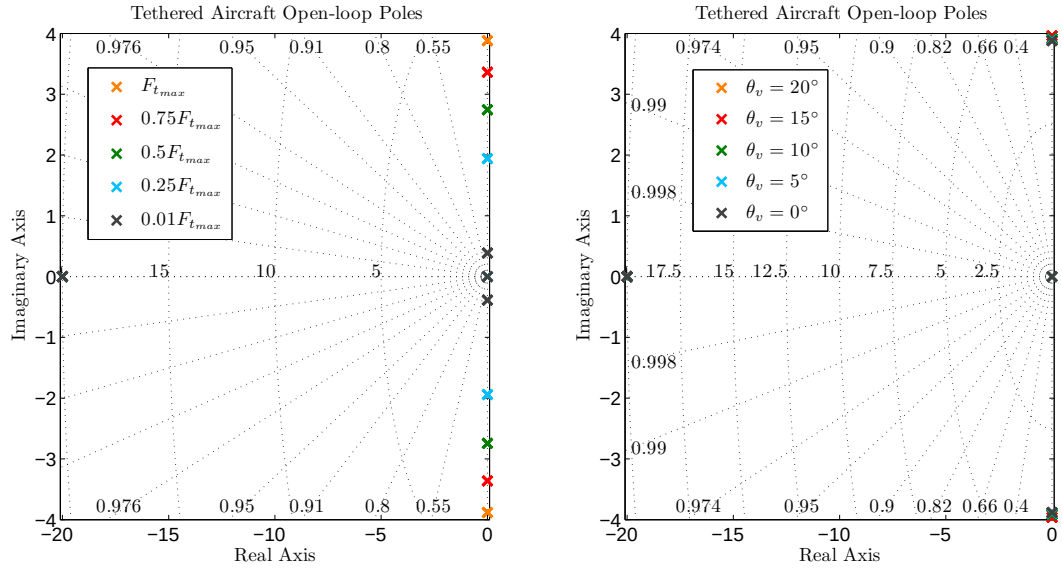

Figure 6.7: Illustration of the effect of $\bar{F}_t$ and $\bar{\theta}_v$ on the open-loop dynamics of the tethered aircraft.

Figure 6.7 illustrates the open-loop pole locations for various $\bar{F}_t$ and $\bar{\theta}_v$ trim conditions. The tether force trim condition is varied for the vertical tether case ($\bar{\theta}_p = 90°, \bar{\theta}_v = 0°$), while the trim vehicle orientation is varied for the case, $\bar{\delta}_T = \delta_{T_{max}}$ and $\bar{\theta}_p = f(\delta_{T_{max}}, \bar{\theta}_v)$.

From Figure 6.7 it is clear that the magnitude of the tether force has a significant effect on the complex conjugate pole locations. The pole locations indicate an increased oscillatory response for a corresponding increase in the tether force, with the pole locations approaching those of the untethered aircraft as $F_t \to 0$. This is in contrast to the trim orientation angle $\bar{\theta}_v$, which is significantly less influential on the open-loop dynamics; presumably due to the fact that $\bar{\theta}_v$ and $\bar{\theta}_p = f(\bar{\theta}_v)$ counteract one another, minimising any changes to the tether moment.

Chapter 7

Control System Design

The autonomous control system developed for this project is intended for the near-hover, tethered flight condition. The design philosophy is one that favours functionality and stability over precision and speed of response, resulting in an autonomous performance that is conservative in a traditional sense.

A conventional control system is initially developed for the untethered system, and thereafter adapted to cater for the unique aspects of tethered flight. This is primarily due to the uncertainty and variability of the pole locations of the tethered system. Furthermore, the untethered aircraft can be linearised to yield decoupled systems for the aircraft dynamics which enables independent, SISO controllers for pitch, roll, yaw and heave.

7.1 Linearised Quadrotor Model

The untethered aircraft is linearised about the static hover trim condition in a similar manner to the linearisation process from Chapter 6.4.1. By applying small perturbation theory and ignoring the actuator gyro moments and aerodynamic effects, the rigid body dynamics[1] (from Equations 4.11–4.16) at the hover trim condition resolve to,

$$\dot{u} = -g\theta \qquad \dot{\phi} = \frac{d_m \delta_A}{I_{xx}}$$

$$\dot{v} = g\phi \qquad \dot{\theta} = \frac{d_m \delta_E}{I_{yy}}$$

$$\dot{w} = g - \frac{\delta_T}{m} \qquad \dot{\psi} = \frac{R_N \delta_R}{I_{zz}}$$

[1] Note that lower case symbols are used to represent the perturbation dynamics.

With $\phi_0 = \theta_0 = 0$, the kinematic dynamics from Equation 4.19 resolve to,

$$\begin{aligned}\dot{\phi} &= p \\ \dot{\theta} &= q \\ \dot{\psi} &= r\end{aligned}$$

While the inertial position dynamics are related to the body-axis position dynamics by,

$$\begin{aligned}\dot{N} &= u\cos(\psi) - v\sin(\psi) \\ \dot{E} &= u\sin(\psi) + v\cos(\psi) \\ \dot{D} &= w\end{aligned}$$

The first-order lag dynamics of the virtual actuators form the remaining state variables and are restated here for convenience,

$$\dot{\delta}_i = -\frac{1}{\tau}\delta_i + \frac{1}{\tau}\delta_{i_R}$$

The state and control input vectors for the aircraft are defined as,

$$\mathbf{x} = \begin{bmatrix} \delta_E & \delta_A & \delta_R & \delta_T & p & q & r & \phi & \theta & \psi & u & v & w & \dot{N} & \dot{E} & \dot{D} \end{bmatrix}^T \tag{7.1}$$

$$\mathbf{u} = \begin{bmatrix}\delta_{E_R} & \delta_{A_R} & \delta_{R_R} & \delta_{T_R}\end{bmatrix}^T \tag{7.2}$$

The linearisation process yields four decoupled linear systems representing the longitudinal, lateral, directional and heave dynamics of the untethered aircraft. They may be represented in state space form as,

Longitudinal Dynamics:

$$\dot{\mathbf{x}}_{lon} = \mathbf{A}_{lon}\mathbf{x}_{lon} + \mathbf{B}_{lon}\mathbf{u}_{lon} \tag{7.3}$$

$$\begin{bmatrix}\dot{\delta}_E \\ \dot{q} \\ \dot{\theta} \\ \dot{u}\end{bmatrix} = \begin{bmatrix}-\frac{1}{\tau} & 0 & 0 & 0 \\ \frac{d_m}{I_{yy}} & 0 & 0 & 0 \\ 0 & 1 & 0 & 0 \\ 0 & 0 & -g & 0\end{bmatrix}\begin{bmatrix}\delta_E \\ q \\ \theta \\ u\end{bmatrix} + \begin{bmatrix}\frac{1}{\tau} \\ 0 \\ 0 \\ 0\end{bmatrix}\delta_{E_R} \tag{7.4}$$

Lateral Dynamics:

$$\dot{\mathbf{x}}_{lat} = \mathbf{A}_{lat}\mathbf{x}_{lat} + \mathbf{B}_{lat}\mathbf{u}_{lat} \tag{7.5}$$

$$\begin{bmatrix} \dot{\delta}_A \\ \dot{p} \\ \dot{\phi} \\ \dot{v} \end{bmatrix} = \begin{bmatrix} -\frac{1}{\tau} & 0 & 0 & 0 \\ \frac{d_m}{I_{xx}} & 0 & 0 & 0 \\ 0 & 1 & 0 & 0 \\ 0 & 0 & g & 0 \end{bmatrix} \begin{bmatrix} \delta_A \\ p \\ \phi \\ v \end{bmatrix} + \begin{bmatrix} \frac{1}{\tau} \\ 0 \\ 0 \\ 0 \end{bmatrix} \delta_{A_R} \tag{7.6}$$

Directional Dynamics:

$$\dot{\mathbf{x}}_{dir} = \mathbf{A}_{dir}\mathbf{x}_{dir} + \mathbf{B}_{dir}\mathbf{u}_{dir} \tag{7.7}$$

$$\begin{bmatrix} \dot{\delta}_R \\ \dot{r} \\ \dot{\psi} \end{bmatrix} = \begin{bmatrix} -\frac{1}{\tau} & 0 & 0 \\ \frac{R_N}{I_{zz}} & 0 & 0 \\ 0 & 1 & 0 \end{bmatrix} \begin{bmatrix} \delta_R \\ r \\ \psi \end{bmatrix} + \begin{bmatrix} \frac{1}{\tau} \\ 0 \\ 0 \end{bmatrix} \delta_{R_R} \tag{7.8}$$

Heave Dynamics:

$$\dot{\mathbf{x}}_{hea} = \mathbf{A}_{hea}\mathbf{x}_{hea} + \mathbf{B}_{hea}\mathbf{u}_{hea} \tag{7.9}$$

$$\begin{bmatrix} \dot{\delta}_T \\ \dot{w} \\ \dot{D} \end{bmatrix} = \begin{bmatrix} -\frac{1}{\tau} & 0 & 0 \\ -\frac{1}{m} & 0 & 0 \\ 0 & 1 & 0 \end{bmatrix} \begin{bmatrix} \delta_T \\ w \\ D \end{bmatrix} + \begin{bmatrix} \frac{1}{\tau} \\ 0 \\ 0 \end{bmatrix} \delta_{T_R} + \begin{bmatrix} 0 \\ g \\ 0 \end{bmatrix} \tag{7.10}$$

With the nonlinear navigation dynamics given as,

$$\begin{bmatrix} \dot{N} \\ \dot{E} \end{bmatrix} = \begin{bmatrix} \cos\psi & -\sin\psi \\ \sin\psi & \cos\psi \end{bmatrix} \begin{bmatrix} u \\ v \end{bmatrix} \tag{7.11}$$

7.2 Control Structure

The aircraft control structure is illustrated in Figure 7.1 and is based on a design by Peddle [7]. The control architecture implements variations of linear PID control in a successive loop closure approach. This approach is an intuitive control strategy for the quadrotor case, that has proved both effective and notably robust in literature, where it has been well researched and is widely implemented. The nested architecture has the additional benefit of allowing individual control loops to be armed independently which enables easy transitioning between the autonomous and stability-augmented manual flight modes.

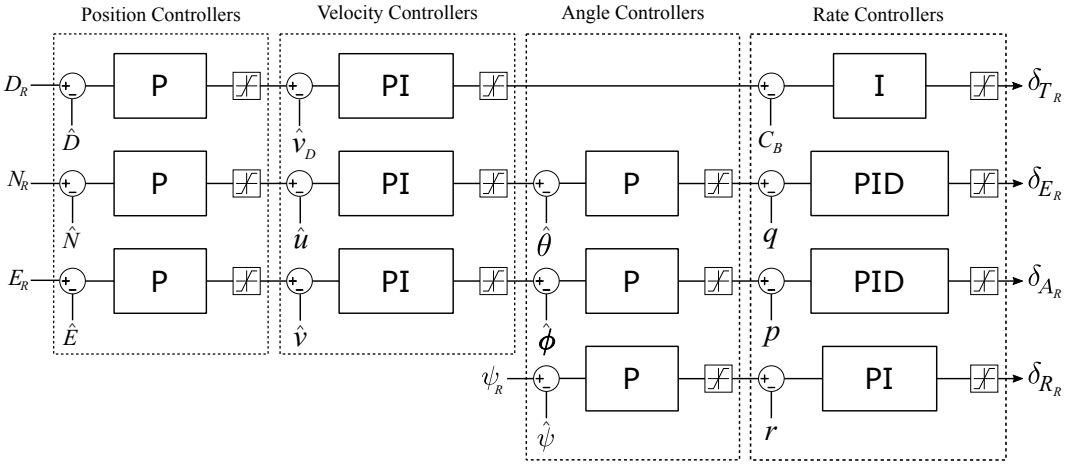

Figure 7.1: Overview of the control architecture for the untethered aircraft[2].

The virtual actuator references form the final outputs of the control system. These references are converted to individual motor commands by a mixing matrix. The mixing matrix is derived by taking the inverse of Equation 7.12, which in turn, is derived from the virtual actuator definitions in Equations 4.26–4.29 as,

$$\begin{bmatrix} \delta_{T_R} \\ \delta_{E_R} \\ \delta_{A_R} \\ \delta_{R_R} \end{bmatrix} = \begin{bmatrix} 1 & 1 & 1 & 1 \\ 1 & 0 & -1 & 0 \\ 0 & -1 & 0 & 1 \\ -1 & 1 & -1 & 1 \end{bmatrix} \begin{bmatrix} T_{1_R} \\ T_{2_R} \\ T_{3_R} \\ T_{4_R} \end{bmatrix} \tag{7.12}$$

With the mixing matrix subsequently derived as,

$$\begin{bmatrix} T_{1_R} \\ T_{2_R} \\ T_{3_R} \\ T_{4_R} \end{bmatrix} = \begin{bmatrix} 0.25 & 0.5 & 0 & -0.25 \\ 0.25 & 0 & -0.5 & 0.25 \\ 0.25 & -0.5 & 0 & -0.25 \\ 0.25 & 0 & 0.5 & 0.25 \end{bmatrix} \begin{bmatrix} \delta_{T_R} \\ \delta_{E_R} \\ \delta_{A_R} \\ \delta_{R_R} \end{bmatrix} \tag{7.13}$$

Estimates of the aircraft's inertial position $\{\hat{N}, \hat{E}, \hat{D}\}$, velocity $\{\hat{v}_N, \hat{v}_E, \hat{v}_D\}$ and attitude $\{\hat{\phi}, \hat{\theta}, \hat{\psi}\}$ states are provided by the kinematic state estimator; while measurements of the aircraft's angular rate and specific force states $\{p, q, r, \dot{u}, \dot{v}, \dot{w}\}$ are provided directly by the onboard IMU. The kinematic state estimator is an extended Kalman filter (EKF) that was previously developed in the ESL. The estimator is vehicle independent by design in order to accommodate various UAV platforms. State estimates are initially determined by propagating measurements from the onboard inertial measurement unit. Thereafter, these propagated estimates are corrected by

[2]Note that conversions between the inertial and body-axis states are included, but not shown, in Figure 7.1.

measurements from the magnetometer and GPS receiver, in order to counter the effects of sensor drift. The EKF combines these propagated estimates and correction measurements in an optimal way[3], and updates at a frequency of 50 Hz.

The control laws are executed on the OBC at a frequency of 50 Hz. The innermost angular rate controllers are the only exception. These controllers execute at an increased rate of 100 Hz, and receive gyro feedback measurements at the same frequency. This improves the disturbance rejection capabilities of the aircraft. With a maximum closed-loop bandwidth of ≈ 14 rad/s the control execution rates are well separated from the system bandwidths. This enables the implementation of the control laws via direct digital conversion, with no significant loss in accuracy.

7.3 Longitudinal and Lateral Control Systems

Due to the aircraft symmetry the longitudinal and lateral control systems are identical in architecture. The only difference between the two control systems is a subtle variation in gain in the innermost control loops, which serves only to offset the small discrepancy in the mass moments of inertia about the x_B and y_B axes.

Each control system comprises of four nested control loops. The nested loop structure enables the sequential arming of controllers which is a useful feature during the initial commissioning of the vehicle. The innermost controllers consist of the pitch and roll rate controllers. Along with the innermost directional controller, described in Chapter 7.4, these controllers form the minimum requirement for manually piloted flight and receive attitude rate feedback directly from the onboard IMU. In the *manual rate* flight mode, the rate controllers receive pilot input commands directly as controller references; while in the *manual angle* and *autonomous* flight modes, references are received from the encompassing pitch and roll angle controllers. The angle controllers offer an additional augmented manual flight mode, receiving controller references from either the pilot or the horizontal velocity controllers. The horizontal velocity controllers form the penultimate control loop and receive reference commands from either the ground station or the outermost horizontal position controllers. When initially armed the horizontal position controllers store the aircraft's current position state information as the controller reference commands, and otherwise only receive updated position references from the ground station.

The overall structure of the longitudinal and lateral control systems remains unchanged for the tethered case. Local controller stability is verified for various trim conditions of the tethered case. Controller saturation issues, due to uncertainty in the aircraft's position state information and the constraining nature of the tether, are otherwise avoided through the definition of a suitable flight envelope in Chapter 6.2.1.

[3]Detailed operational specifics of the kinematic state estimator are provided in [54].

7.3.1 Pitch and Roll Rate Controllers

In order to avoid repetition only the design of the pitch rate controller is presented here. Neglecting the pitch angle and linear velocity states, the longitudinal state space matrices from Equation 7.4 may be abridged to yield,

$$\dot{\mathbf{x}}^*_{lon} = \mathbf{A}^*_{lon}\mathbf{x}^*_{lon} + \mathbf{B}^*_{lon}\mathbf{u}^*_{lon} \tag{7.14}$$

$$\begin{bmatrix} \dot{\delta}_E \\ \dot{q} \end{bmatrix} = \begin{bmatrix} -\frac{1}{\tau} & 0 \\ \frac{d_m}{I_{yy}} & 0 \end{bmatrix} \begin{bmatrix} \delta_E \\ q \end{bmatrix} + \begin{bmatrix} \frac{1}{\tau} \\ 0 \end{bmatrix} \delta_{E_R} \tag{7.15}$$

The transfer function from virtual elevator command input to pitch rate output may subsequently be determined from Equation 7.16 as,

$$G_q(s) = \frac{q(s)}{\delta_E(s)} = \mathbf{C}_q \left(s\mathbf{I} - \mathbf{A}^*_{long}\right)^{-1} \mathbf{B}^*_{lon} \tag{7.16}$$

$$G_q(s) = \frac{\frac{1}{\tau I_{yy}}}{s(s + \frac{1}{\tau})} \tag{7.17}$$

where,

$$\mathbf{C}_q = \begin{bmatrix} 0 & 1 \end{bmatrix} \tag{7.18}$$

The system plant contains a fast real pole corresponding to the actuator time constant, and a pole at the origin as a result of the aircraft's neutrally stable attitude rate dynamics. From the root loci shown in Figure 7.2, it is clear that the actuator time constant has a significant effect on the system bandwidth. This confirms what one would expect intuitively as the dynamics are inherently limited by the fundamental mechanical limits of the system. However, this dependency does raise concerns about the performance of the controllers considering the potential variability of the motor time constant that was highlighted in Chapter 3.3.2. As a precaution, these effects were investigated through simulation; with increases in the time constant having shown to marginally reduce the controller damping and response times. Overall these effects were found to be small and are therefore neglected for the remainder of the control system design.

As the innermost control loops, the pitch and roll rate controllers directly command the control and restoring moments. As such, they form the foundation of the horizontal control system. The aircraft is especially sensitive to disturbances in pitch and roll, which yields the pitch and roll rate controllers extremely influential on the overall performance and stability of the vehicle. High-bandwidth, well damped control is therefore required to negate the effects of any disturbance torques quickly and effectively. Furthermore, integral action is necessary to counter the many potential sources of steady state disturbance torques. These include the induced tether moment, the effects of wind shear, uncertainty in the aircraft's physical properties and/or discrepancies in the actuator performance and mounting positions.

The controller design specifications are determined in terms of bandwidth, damping, and steady state tracking requirements. A minimum $-3\,\text{dB}$ closed-loop bandwidth of $\omega_{bw} \geq 12\,\text{rad s}$ is desired for good disturbance rejection and adequate time-scale separation between the outer control loops. The damping requirement is specified in terms of a desired phase margin of $PM \geq 80°$, and an overshoot specification of $M_p \leq 5\%$. Integral control action will ensure that the system is capable of tracking steady state disturbance torques with zero steady state error.

A Proportional-Integrator (PI) controller is initially implemented to meet the bandwidth and tracking requirements. The proportional gain is designed for dynamic response while a slow integrator is implemented to counter steady-state disturbances. The integrator action features a zero at $s = -0.15\,\text{rad/s}$; the effects of which are limited by pole-zero cancellation with the closed-loop pole originating from the open-loop pole at the origin. The resulting root locus features a departure point at $\sigma = -10\,\text{rad/s}$, after which the response becomes increasingly underdamped with a further increase in gain. The proportional gain required to meet the minimum closed-loop bandwidth requirement results in a phase margin of $PM = 52°$ and 11% overshoot. Consequently, derivative control action is implemented to improve the system damping.

The pitch rate control structure is illustrated in Figure 7.3, with the final control law given by Equation 7.19. The controller features added trim contributions, and saturation limits for both the integrator and the final controller output. Anti-windup logic is also implemented for the integrator as an additional precaution.

$$D_q(s) = \frac{17(s+10)(s+0.15)}{(s+40)} \tag{7.19}$$

Lead compensation is preferred over pure derivative control (as illustrated in Figure 7.1) to mitigate against the amplification of the measurement noise introduced by the IMU. The lead compensator features a zero at $z_D = -10\,\text{rad/s}$, and a pole well

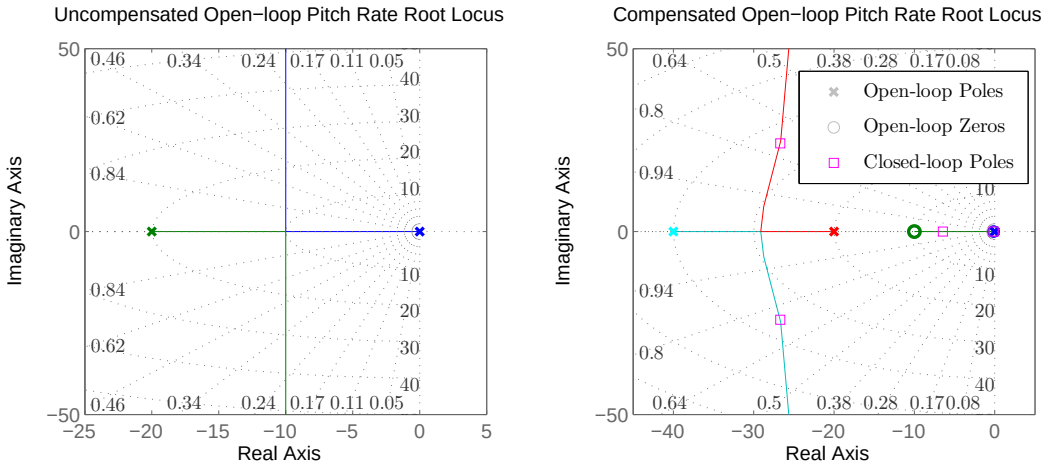

Figure 7.2: Open-loop pitch rate system root loci.

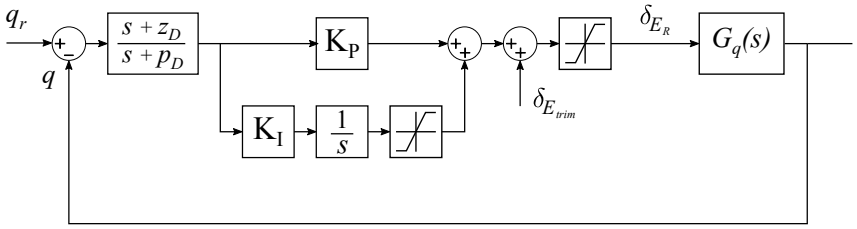

Figure 7.3: Illustration of the pitch rate control structure.

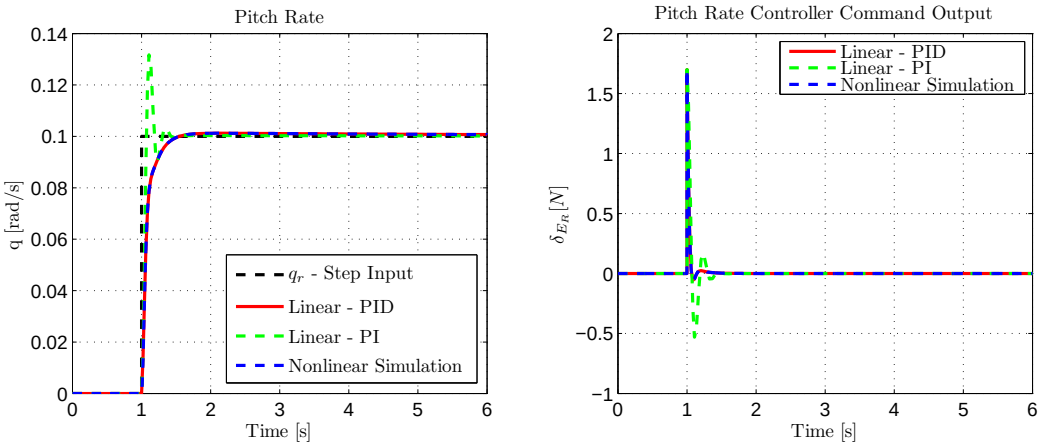

Figure 7.4: Pitch rate controller responses.

above the desired closed-loop bandwidth at $p_D = -40\,\text{rad/s}$. This leads to a phase contribution of $\phi_D = 35.4°$ at the final closed-loop bandwidth of $\omega_{bw} = 14.3\,\text{rad/s}$. The damping specifications are similarly satisfied with a final phase margin of $PM = 88.7°$ and 1% overshoot. The proportional gains for the pitch and roll rate controllers are selected as $K_{p_q} = 17$ and $K_{p_p} = 16.5$, respectively. Pitch rate step responses for both the linear and nonlinear systems are given by Figure 7.4, and illustrate the added damping provided by the lead compensator. The controller performance correlates extremely well for the linear and nonlinear aircraft models, indicating that the effects of the cross-coupling terms present in the nonlinear dynamic equations are in fact small.

7.3.2 Pitch and Roll Angle Controllers

The pitch angle controller forms the first of the outer control loops in the longitudinal control system, and commands the pitch rate reference, q_r. Considering both the high-bandwidth and steady state disturbance rejection capabilities of the inner rate controller, the pitch angle control requirements are less rigorous.

The controller design specifications are determined only in terms of bandwidth and damping requirements. A $-3\,\text{dB}$ closed-loop bandwidth between $3.5 \geq \omega_{bw} \leq 4\,\text{rad/s}$, is specified for a suitably fast and smooth dynamic response, and for good

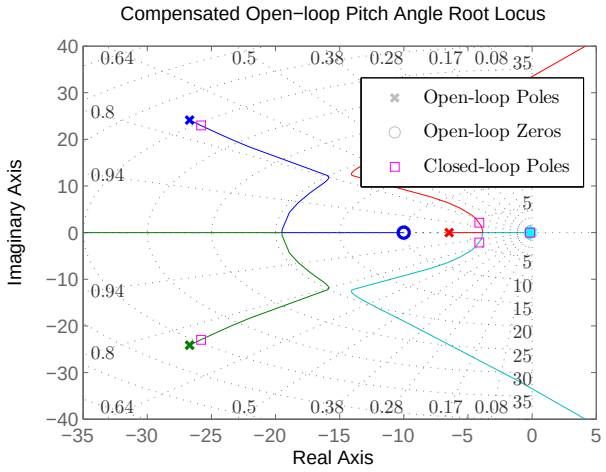

Figure 7.5: Open-loop pitch angle system root locus.

time-scale separation between the dynamics of the inner pitch rate controller. The damping requirement is specified in terms of a desired phase margin of $PM \geq 70°$, and an overshoot specification of $M_p \leq 2\%$.

The root locus of the open-loop pitch angle system is shown in Figure 7.5. The open-loop pole and zero locations correspond to those of the closed-loop pitch rate system with an additional integrator at the origin due to the neutrally stable dynamics of the aircraft's pitch angle. The root locus indicates a relatively fast, well damped response for a wide range of linear gain values. A Proportional (P) feedback controller is employed to that end, with the control structure illustrated in Figure 7.6.

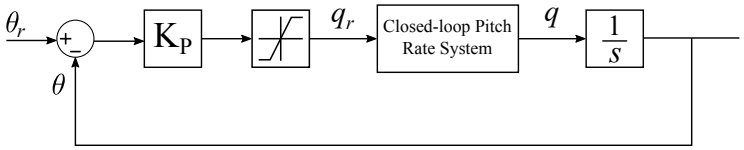

Figure 7.6: Illustration of the pitch angle control structure.

In the absence of integral control action, the controller is vulnerable to a non-zero steady error between the actual and commanded pitch angles should the gyroscope exhibit a measurement bias. This effect is illustrated by Figures 7.7 and 7.8, where a 1 deg /s measurement bias was introduced at $t = 4$ sec, on the pitch rate feedback. The linear system response illustrates the resulting increase in the 'perceived' pitch angle measurement due to the integration of the angular rate feedback measurement; while the nonlinear response illustrates the effect on the actual pitch angle of the aircraft and the resulting steady state error in the pitch rate reference. This will manifest as a slow positional drift which will ultimately be countered by the outer loop controllers. A positional drift is, in any event, inevitable considering the inherent sensing limitations of the GPS receiver. Through simulation the effects of a

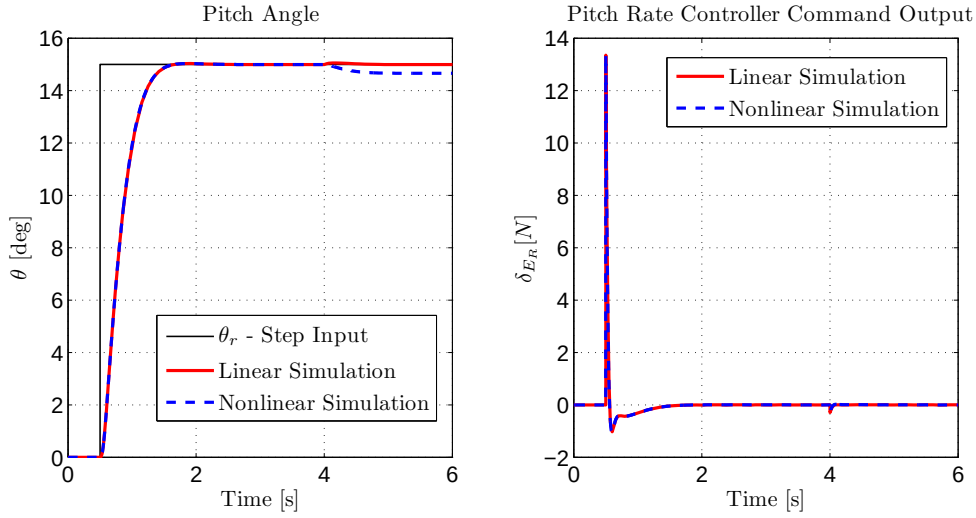

Figure 7.7: Pitch Angle controller responses.

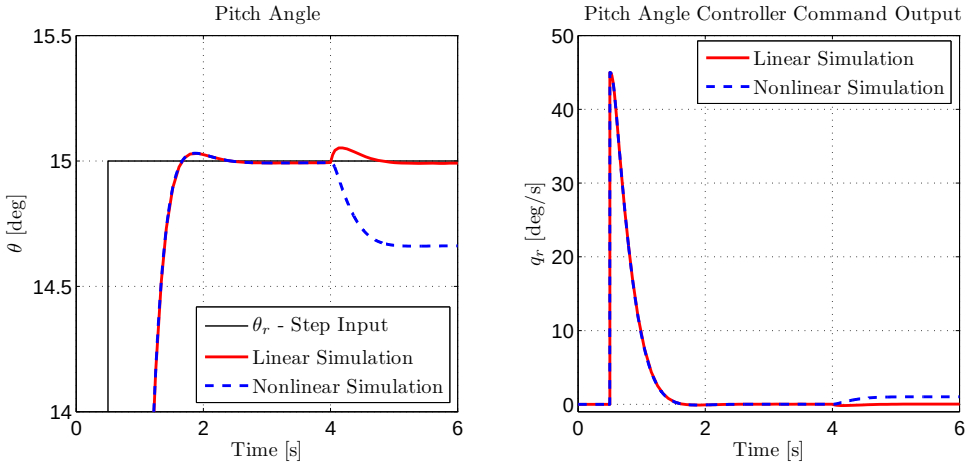

Figure 7.8: Pitch angle response enlarged and the pitch angle controller output.

gyro measurement bias are shown to have an indifferent effect on the station keeping capabilities of the aircraft, rendering integral control action superfluous.

A proportional gain of $K_{p_\theta} = 3$, yields a final $-3\,\text{dB}$ closed-loop bandwidth of $\omega_{bw} = 3.8\,\text{rad/s}$. The damping specifications are similarly met with a final phase margin of $PM = 75.2°$ and $< 1\%$ overshoot. Figures 7.7 and 7.8 illustrate the controller performance for a 15° pitch angle step input, with the controller performance again correlating extremely well for the linear and nonlinear aircraft models.

7.3.3 Horizontal Velocity Controllers

The bandwidth of the horizontal velocity and position controllers is inherently limited by the underactuated nature of the vehicle. This is evident from Figure 7.9, in

the open loop root locus of the longitudinal velocity system, which is dominated by slow poles near the origin, and is conditionally stable for only a small range of linear gain values. However, in the context of a tethered application, the intrinsically low bandwidth of the positional dynamics is in fact a desirable feature as it reduces the risk of exciting the tether's fundamental frequency, and alleviates both the frequency and severity of the tether impact events by reducing the aircraft's kinetic energy.

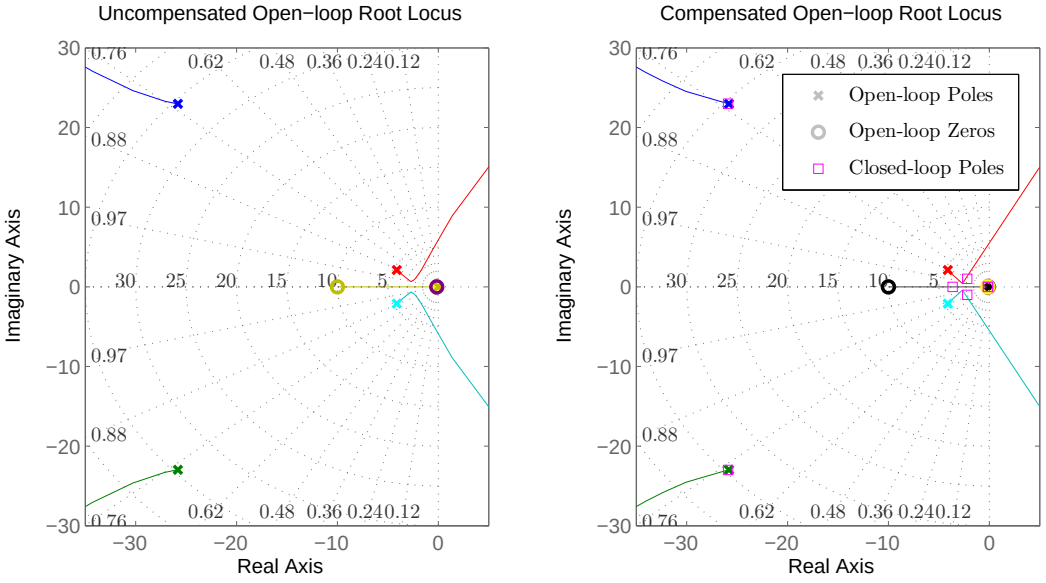

Figure 7.9: Open-loop longitudinal velocity system root loci.

The design of the horizontal velocity controller, therefore, places more of an emphasis on the steady state disturbance rejection capabilities of the controller as opposed to dynamic response. Integral control action is required to counter the effects of steady-state disturbances resulting from the tether forces, aerodynamic drag and any potential measurement biases present in the gyroscope or accelerometer. A $-3\,\text{dB}$ closed-loop bandwidth between $1.5 \geq \omega_{bw} \leq 2\,\text{rad/s}$, is specified solely for good time-scale separation between the dynamics of the inner pitch angle controller, and the outermost longitudinal position loop. Efforts are made to maximise the controller phase margin within those design parameters, with a minimum acceptable phase margin set at $PM \geq 60°$.

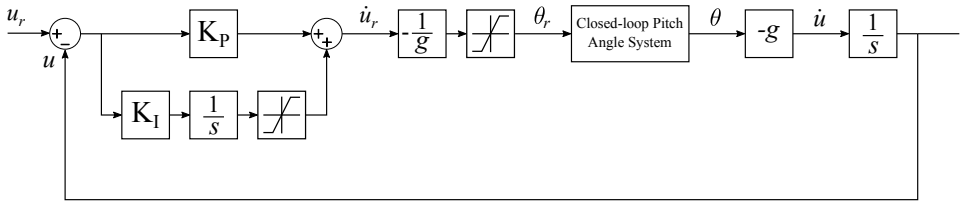

Figure 7.10: Illustration of the longitudinal velocity control structure.

The structure of the longitudinal velocity controller is illustrated in Figure 7.10, with the final control law given by Equation 7.20. The controller features saturation limits for both the integrator and the final controller output, with the final output limited to the maximum vehicle pitch/roll angle of $\pm 25°$.

$$D_u(s) = \frac{1.1(s + 0.1)}{s} \tag{7.20}$$

PI control is employed to meet the controller design specifications. The controller yields a final $-3\,\text{dB}$ closed-loop bandwidth of $\omega_{bw} = 1.75\,\text{rad/s}$ with a phase margin of $PM = 65°$. The phase margin is reflected in the controller step response from Figure 7.11 which is characterised by overshoot of 8% that is slow to settle. Considering the compensated root locus from Figure 7.9, the slow transient is expected with the large number of poles near the origin. The overshoot is attributable to the proximity of the controller zero at $s = -0.1\,\text{rad/s}$ to the dominant system poles. The slower poles from the closed-loop pitch angle system result in the effects of this zero being more pronounced. Nevertheless, the controller satisfies the required design criteria and is adequate for the tethered application.

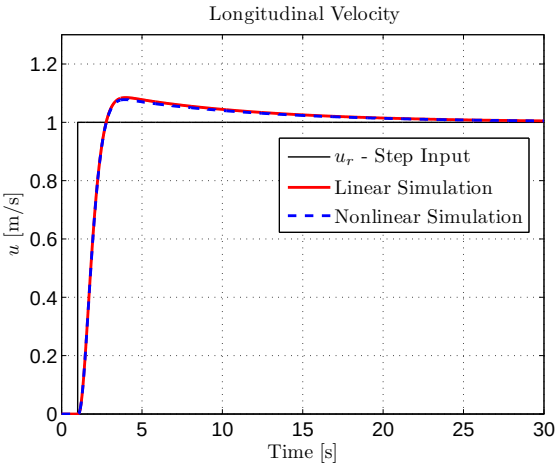

Figure 7.11: Longitudinal velocity controller step response.

7.3.4 Horizontal Position Controllers

The horizontal position controllers are the outermost control loops in the longitudinal and lateral control systems. The position controllers are unique in that they act in the inertial coordinate system as opposed to the aircraft's body axes. The inertial position dynamics are given by Equation 7.11, and restated here for convenience as,

$$\begin{bmatrix} \dot{N} \\ \dot{E} \end{bmatrix} = \begin{bmatrix} \cos\psi & -\sin\psi \\ \sin\psi & \cos\psi \end{bmatrix} \begin{bmatrix} u \\ v \end{bmatrix}$$

From the above equation it is clear that the horizontal inertial position dynamics are over controlled with three independent control inputs $\{N_R, E_R, \psi\}$. The omni-directional flight capability of the quadrotor enables translational movement in the inertial axis system independent from the aircraft's heading angle, ψ. Therefore, we proceed by setting the heading angle arbitrarily.

For a given inertial position reference $\{N_R, E_R\}$, the position error is defined as,

$$\begin{bmatrix} N_E \\ E_E \end{bmatrix} = \begin{bmatrix} N_R \\ E_R \end{bmatrix} - \begin{bmatrix} \hat{N} \\ \hat{E} \end{bmatrix} \tag{7.21}$$

Assuming that ϕ and θ are small, the inertial position error can be converted to body axis coordinates via Equation 4.23 as,

$$\begin{bmatrix} x_E \\ y_E \end{bmatrix} = - \begin{bmatrix} \cos\psi & \sin\psi \\ -\sin\psi & \cos\psi \end{bmatrix} \begin{bmatrix} N_E \\ E_E \end{bmatrix} \tag{7.22}$$

The time derivative of Equation 7.22 can be computed via the chain rule to yield the dynamics of the body axis error coordinates as,

$$\begin{bmatrix} \dot{x}_E \\ \dot{y}_E \end{bmatrix} = \begin{bmatrix} \cos\psi & \sin\psi \\ -\sin\psi & \cos\psi \end{bmatrix} \begin{bmatrix} \dot{N}_E \\ \dot{E}_E \end{bmatrix} - \dot{\psi} \begin{bmatrix} \sin\psi & -\cos\psi \\ \cos\psi & \sin\psi \end{bmatrix} \begin{bmatrix} N_E \\ E_E \end{bmatrix} \tag{7.23}$$

Assuming a constant inertial position reference, the inertial position error dynamics may be calculated as,

$$\begin{bmatrix} \dot{N}_E \\ \dot{E}_E \end{bmatrix} = - \begin{bmatrix} \cos\psi & -\sin\psi \\ \sin\psi & \cos\psi \end{bmatrix} \begin{bmatrix} u \\ v \end{bmatrix} \tag{7.24}$$

Equation 7.24 can be substituted into Equation 7.23 to yield,

$$\begin{bmatrix} \dot{x}_E \\ \dot{y}_E \end{bmatrix} = - \begin{bmatrix} u \\ v \end{bmatrix} - \dot{\psi} \begin{bmatrix} \sin\psi & -\cos\psi \\ \cos\psi & \sin\psi \end{bmatrix} \begin{bmatrix} N_E \\ E_E \end{bmatrix} \tag{7.25}$$

By setting the saturation limit appropriately on the yaw rate controller, we can ensure that the yaw rate remains low during horizontal translational motion. This reduces the dynamics of the body axis error coordinates to the uncoupled linear dynamics,

$$\begin{bmatrix} \dot{x}_E \\ \dot{y}_E \end{bmatrix} = - \begin{bmatrix} u \\ v \end{bmatrix} \tag{7.26}$$

Due to the constraining nature of the tether, the design of the horizontal position controller places an emphasis on a slow, well damped positional response. As the effects of steady state disturbances on the horizontal translational dynamics of the aircraft are already compensated for by the horizontal velocity controller, integral control action is not required. A $-3\,\text{dB}$ closed-loop bandwidth between $0.4 \geq \omega_{bw} \leq 0.6\,\text{rad/s}$, is specified for good time-scale separation between the dynamics of the inner horizontal velocity controller, and the tether's fundamental frequency from Figure 5.7. Due to the damping requirements a phase margin of $PM \geq 70^\circ$ is required with little to no overshoot.

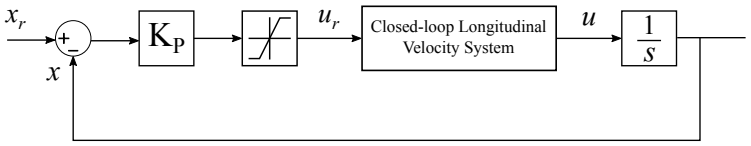

Figure 7.12: Illustration of the longitudinal position control structure.

A proportional control law is designed to meet the controller design criteria, with the control law given by Equation 7.27. For control design purposes the controller is analysed in terms of the body axis coordinates as illustrated in Figure 7.12, which is equivalent to setting $\psi = 0$ from Equation 7.27.

$$\begin{bmatrix} u \\ v \end{bmatrix} = \begin{bmatrix} K_{p_N} & 0 \\ 0 & K_{p_E} \end{bmatrix} \begin{bmatrix} \cos\psi & \sin\psi \\ -\sin\psi & \cos\psi \end{bmatrix} \begin{bmatrix} N_R - \hat{N} \\ E_R - \hat{E} \end{bmatrix} \tag{7.27}$$

where,

$$K_{p_N} = K_{p_E} = 0.35$$

The controller yields a final $-3\,\text{dB}$ closed-loop bandwidth of $\omega_{bw} = 0.6\,\text{rad/s}$ with a phase margin of $PM = 70.6^\circ$, and an over damped response to a longitudinal position step input illustrated in Figure 7.11.

The low overshoot is surprising considering the overshoot that characterised the response of the longitudinal velocity controller. The root locus of the open-loop longitudinal position system provides more insight, and is shown in Figure 7.14. The response is once again dominated by slow poles near the origin, similar to the longitudinal velocity system from Figure 7.9. However, the effects of the lead compensator zero on the complex pole pair at $s_{1,2} \approx -2.19 \pm 1.01j\,\text{rad/s}$ are alleviated to an extent, due to the real pole introduced by the closed-loop longitudinal velocity system at $s \approx -3.7\,\text{rad/s}$. This enables the design specifications to be met through pure proportional control and concludes the analysis of the longitudinal and lateral control systems.

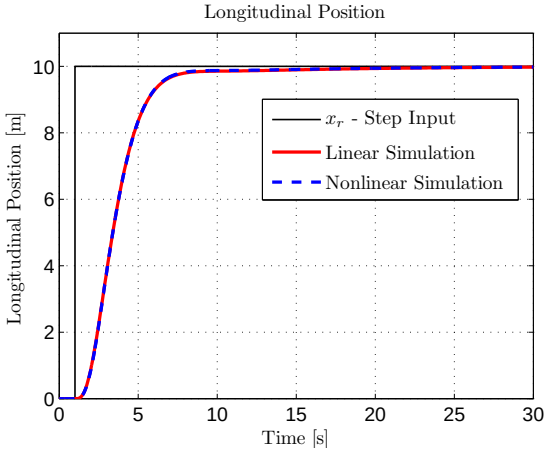

Figure 7.13: Longitudinal position controller step response.

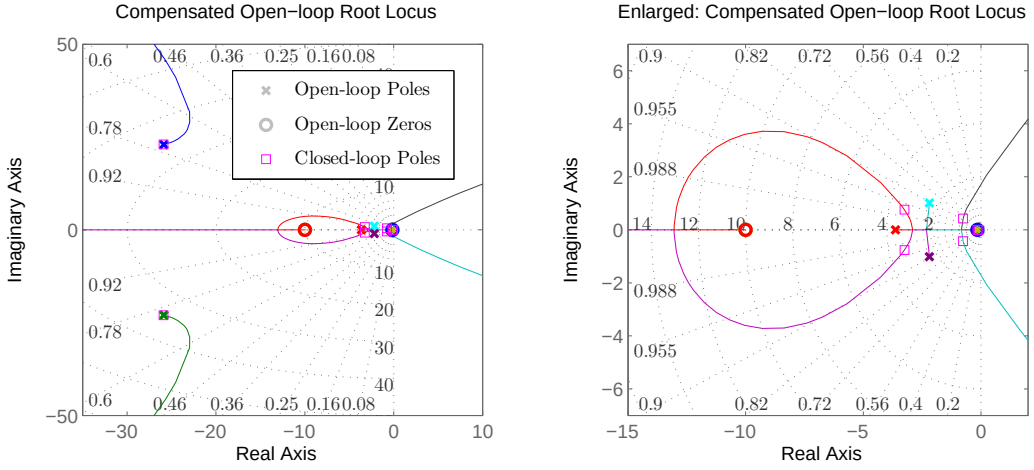

Figure 7.14: Open-loop longitudinal position system root locus.

7.4 Heading Control System

The aircraft's yaw dynamics are unquestionably the most poorly actuated dynamic mode of the aircraft. This is due to the indirect mechanism of actuation which exploits the aerodynamic drag forces acting on the aircraft's rotor blades. This yields the actuators especially susceptible to saturation for large step inputs or high-bandwidth control. Fortunately, unlike pitch and roll, it is not a prominent failure mode for the vehicle; with the only real consequence to poor performance in yaw being the degradation of the horizontal positional performance of the aircraft. This is due to dynamic cross-coupling terms not accounted for in the linear model. Furthermore, the yaw dynamic mode is inherently less susceptible to disturbances due to mechanical lineaments such as it's larger relative inertia, I_{zz}. The effects of wind shear are also minimised by the aircraft symmetry, while disturbances from the tether are expected to be small due to the swivel mounting joints employed at

either end of the tether. These allow the tether and aircraft to rotate independently from one another, and prevent the build-up of torsional forces in the tether.

The heading control system consists of an inner yaw rate controller, encompassed by an outer heading angle controller. The heading control system enables the control of the heading angle independent from the aircraft's direction of travel. Although, in the context of this project, there is no specific requirement to do so and so the heading angle is generally set arbitrarily.

7.4.1 Yaw Rate Controller

By neglecting the yaw angle state from Equation 7.8, the directional state space matrices may be abridged to yield,

$$\dot{\mathbf{x}}^*_{dir} = \mathbf{A}^*_{dir}\mathbf{x}^*_{dir} + \mathbf{B}^*_{dir}\mathbf{u}^*_{dir} \tag{7.28}$$

$$\begin{bmatrix} \dot{\delta}_R \\ \dot{r} \end{bmatrix} = \begin{bmatrix} -\frac{1}{\tau} & 0 \\ \frac{R_N}{I_{zz}} & 0 \end{bmatrix} \begin{bmatrix} \delta_R \\ r \end{bmatrix} + \begin{bmatrix} \frac{1}{\tau} \\ 0 \end{bmatrix} \delta_{R_R} \tag{7.29}$$

The transfer function from virtual rudder command input to yaw rate output, may subsequently be determined from Equation 7.30 as,

$$G_r(s) = \frac{r(s)}{\delta_R(s)} = \mathbf{C}_r \left(s\mathbf{I} - \mathbf{A}^*_{dir}\right)^{-1} \mathbf{B}^*_{dir} \tag{7.30}$$

$$G_r(s) = \frac{\frac{R_N}{\tau I_{zz}}}{s(s + \frac{1}{\tau})} \tag{7.31}$$

where,

$$\mathbf{C}_r = \begin{bmatrix} 0 & 1 \end{bmatrix} \tag{7.32}$$

The root locus for the yaw rate system is identical to that of the pitch rate system from Figure 7.2. Like the longitudinal pitch rate system, the yaw rate plant contains a fast real pole corresponding to the actuator time constant, and a pole at the origin as a result of the aircraft's neutrally stable attitude rate dynamics. The only difference between the longitudinal and directional systems is a reduction (albeit a significant one) in the open-loop gain due to the virtual moment arm, R_N, and the larger mass moment of inertia, I_{zz}.

Similar to the pitch and roll rate controllers, as the innermost controller, integral action is necessary to counter disturbance torques in the steady state; while high-bandwidth control is required to negate any disturbances quickly before their effects can become more pervasive. However, in the case of the yaw rate controller, the bandwidth is fundamentally limited by the available control authority. This can lead to the potentially dangerous situation of the directional control system hogging

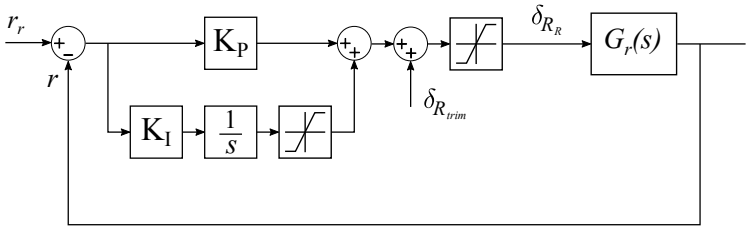

Figure 7.15: Illustration of the yaw rate control structure.

the actuator bandwidth, which inhibits the ability of the aircraft to respond to disturbances in pitch, roll and heave. Thus, the commandable control authority of the heading control systems are limited by design as a safety precaution.

A PI controller is designed with the final control law given by Equation 7.33. The control structure is similar to the horizontal velocity controllers and is illustrated in Figure 7.15. The controller features added trim contributions, and saturation limits for both the integrator and the final controller output.

$$D_r(s) = \frac{28(s + 0.1)}{s} \tag{7.33}$$

The proportional gain is designed for dynamic response while the slow integrator is designed to counter disturbances in the steady-state. The controller design requirements are not specified in a conventional sense. Instead the proportional gain is determined iteratively through simulation to find a suitable compromise between speed of response and the resulting control authority required. The compensated root locus is shown in Figure 7.16. The low overall loop gain results in a dominant closed-loop pole at $s = -1.96\,\text{rad/s}$, while the zero placement results in an additional pole at $s \approx -0.1\,\text{rad/s}$ and a transient that is slow to settle.

The controller exhibits a final closed-loop bandwidth of $\omega_{bw} = 2.15\,\text{rad/s}$, a phase margin of $PM = 81.6°$ and 4% overshoot. Yaw rate step responses for both the linear and nonlinear systems are given by Figure 7.17.

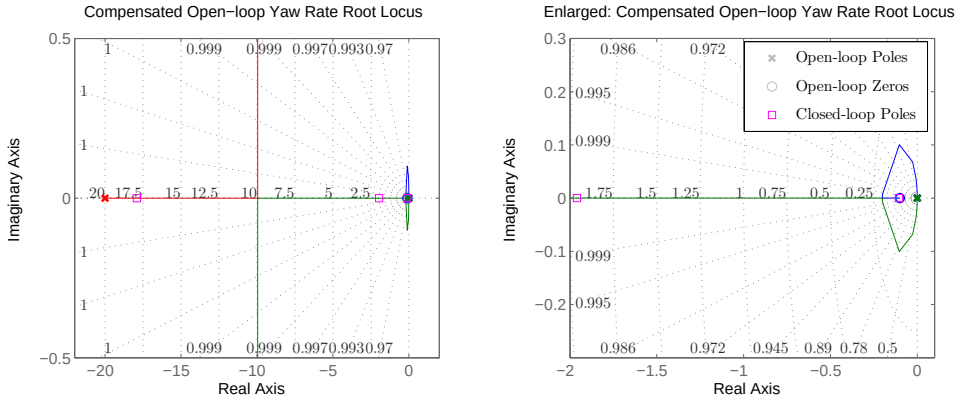

Figure 7.16: Open-loop yaw rate system root loci.

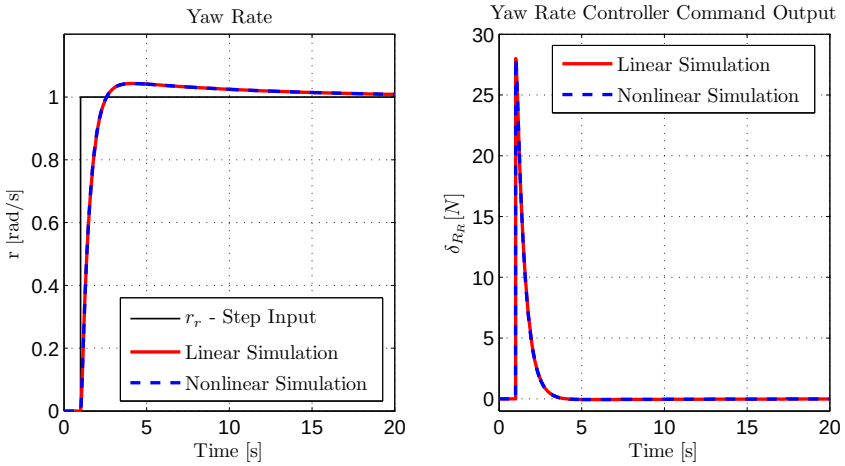

Figure 7.17: Yaw rate controller responses.

7.4.2 Heading Angle Controller

The heading angle controller forms the outermost control loop in the directional control system. It enables the independent control of the aircraft's absolute heading angle[4] and receives reference commands from the ground station. Proportional control is employed to drive the heading angle error to zero over time. Integral control action is not deemed necessary for similar reasons to those stated in the design of the pitch and roll angle controllers. Once again, should the gyroscope contain a measurement bias, the controller will exhibit a non-zero steady error between the actual and commanded heading angles. However, such an error will be small with the effects well contained considering the that the heading angle controller is the outermost control loop. The project also lacks the requirement for precise heading angle control, which leaves the added complications of integral control difficult to justify.

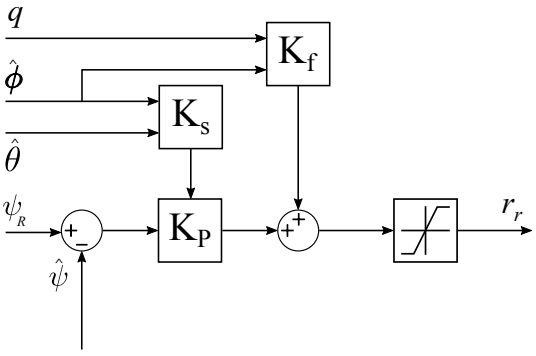

Figure 7.18: Illustration of the heading angle control implementation.

[4]Note that in this section the terms heading and yaw angle are used to differentiate between the aircraft's orientation angle about the inertial z_I, and body axis z_B, axes respectively.

The implemented heading angle controller is illustrated in Figure 7.18 and features both gain scheduling and a feedback linearisation term to remove the coupling term and additional non-linearities between the orientation dynamics in the inertial and body axis coordinate systems. The heading angle dynamics in the inertial coordinate system are derived in Equation 4.19 and restated here for convenience as,

$$\dot{\psi} = q \sin\phi \sec\theta + r \cos\phi \sec\theta \tag{7.34}$$

The control law aims to negate the effects of the pitch rate coupling, while the proportional gain is scheduled by K_s in order to remove the non-linearity in the body axis angular rate, r. The control law is defined as,

$$r_r = K_f q + K_P^*(\psi_R - \hat{\psi}) \tag{7.35}$$

where,

$$K_f = -\tan\hat{\phi} \tag{7.36}$$

$$K_P^* = K_P K_s = K_P \cos\hat{\theta} \sec\hat{\phi} \tag{7.37}$$

Ignoring the effects of the actuator lag dynamics (which assumes that the commanded yaw rate is instantaneous) and assuming that the estimated orientation states represent the aircraft's actual orientation states $\{\hat{\phi} \approx \phi, \hat{\theta} \approx \theta, \hat{\psi} \approx \psi\}$, one can substitute Equation 7.35 into Equation 7.34 to yield,

$$\dot{\psi} = q \sin\phi \sec\theta + r_r \cos\phi \sec\theta \tag{7.38}$$

$$\dot{\psi} = q \sin\phi \sec\theta + [K_f q + K_P^*(\psi_R - \psi)] \cos\phi \sec\theta \tag{7.39}$$

$$\dot{\psi} = K_P(\psi_R - \psi) \tag{7.40}$$

In practice the scheduling gain, K_s, and the feedback linearisation gain, K_f, contributions are limited to the to maximum permissible pitch and roll orientations.

$$0 \geq K_s \leq 1.1 \tag{7.41}$$

$$-0.46 \geq K_f \leq 0.46 \tag{7.42}$$

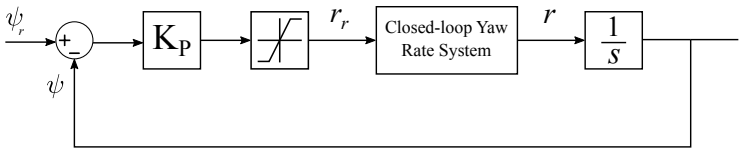

Figure 7.19: Illustration of the heading angle control structure used for design purposes.

For design purposes we consider the case of $\phi = \theta = 0$ and $K_s = 1$, which yields the simplified control structure shown in Figure 7.19. The controller design specifications

are determined in terms of bandwidth and damping requirements. A $-3\,\text{dB}$ closed-loop bandwidth between $0.7 \geq \omega_{bw} \leq 1\,\text{rad/s}$, is specified for adequate time-scale separation between the dynamics of the inner yaw rate controller. The damping requirement is specified in terms of a desired phase margin of $PM \geq 70°$, and an overshoot specification of $M_p \leq 2\%$, to prevent against aggressive control actuation.

The root locus of the open-loop system is shown in Figure 7.20. The additional integrator at the origin, due to the relationship between yaw rate and yaw angle, results in a break point in the root locus at $s \approx -1\,\text{rad/s}$ which quickly becomes unstable and restricts the bandwidth of the controller. A proportional gain of $K_p = 0.65$ results in a dominant closed-loop pole pair at $s_{1/2} = -0.944 \pm 0.685j\,\text{rad/s}$, a phase margin of $PM = 70.1°$, and a gain margin of $GM = 30\,\text{dB}$. This suggests a well damped response, within the the required bandwidth limitations, that is suitably robust to changes in the loop gain.

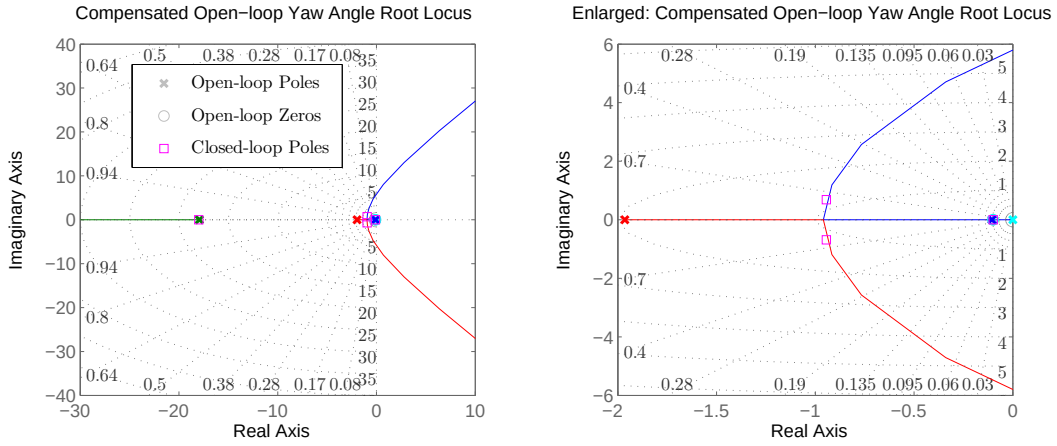

Figure 7.20: Open-loop yaw angle system root locus.

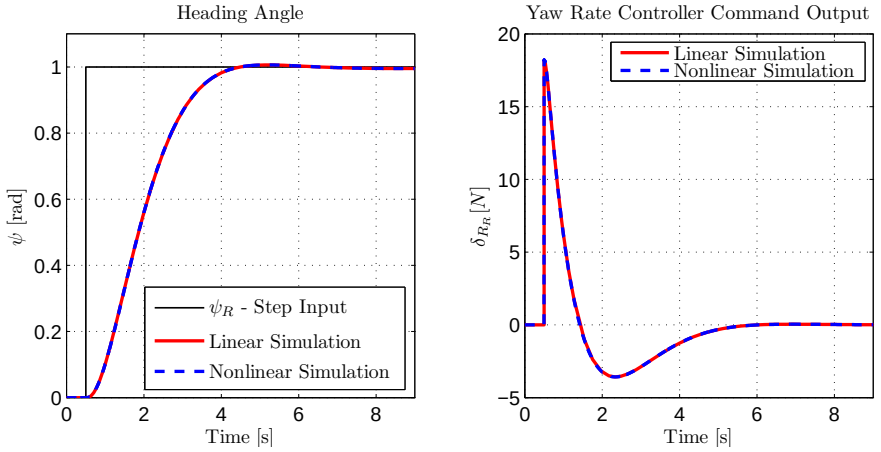

Figure 7.21: Yaw angle controller responses.

Figure 7.21 illustrates the controller performance for a 1 rad ($\approx 57°$) heading angle step input. The controller yields a final -3 dB closed-loop bandwidth of $\omega_{bw} = 0.967$ rad/s and less than 1% overshoot; meeting the design requirements and thereby concluding the analysis of the directional control system.

7.5 Heave Control System

The heave control system is responsible for controlling the vertical position, velocity and acceleration states of the aircraft. It is also the control system most affected by the introduction of the tether, requiring a dedicated control strategy for tethered flight.

The heave control system consists of three nested controllers. The innermost loop consisting of the normal specific acceleration (NSA) controller, followed by the vertical velocity or climb rate controller, and finally the vertical position or altitude controller. The control strategy, and the subsequent controllers, are designed on the premise that the total tether length is known. The control system uses this information to ensure that the tether is elevated in it's entirely ($\theta_0 \geq 0°$).

Designs of the controllers developed for the untethered aircraft are first presented. Following this, details of the control modifications for tethered flight are described.

7.5.1 NSA Controller

The heave dynamic mode of the aircraft is particularly well actuated due to the actuators acting in the aircraft's negative z_B body axis direction. This is reflected in the heave dynamics which correspond directly with the actuator lag dynamics. The normal specific acceleration of the aircraft is related to perturbations in the total thrust force (from trim) via Newton's 2nd law, with dynamics derived as,

$$\dot{C}_B = -\frac{1}{\tau} C_B - \frac{1}{\tau m} \delta_{T_R} \tag{7.43}$$

where, C_B is the normal specific acceleration in body axes.

The transfer function from thrust command input to NSA output, may subsequently be determined by taking the Laplace transform of Equation 7.43 as,

$$G_c(s) = \frac{C_B(s)}{\delta_T(s)} \tag{7.44}$$

$$G_c(s) = \frac{-\frac{1}{\tau m}}{s + \frac{1}{\tau}} \tag{7.45}$$

The root locus for the NSA system contains a single, fast real pole that corresponds with the actuator lag dynamics. The NSA controller is unique in the sense that it acts on an acceleration state of the aircraft. Until now, the control strategy has implemented integral action to remove any steady state disturbances in the aircraft's angular and linear velocity states. The heave control system is no exception. Pure integral control action is employed to provide damping against disturbances, and to filter the high frequency measurement noise introduced by the accelerometer feedback. The latter is in fact a critical feature of the NSA controller, considering that the aircraft is susceptible to vibrations caused by the spinning rotor blades. Proportional control is omitted to prevent the measurement noise from driving the control command. This would dilute the control precision and generate an agitated response. Pure integral control results in a type 1 system that is incapable of tracking type 2 acceleration inputs. Steady state disturbances are instead countered through integral control action in the climb rate controller.

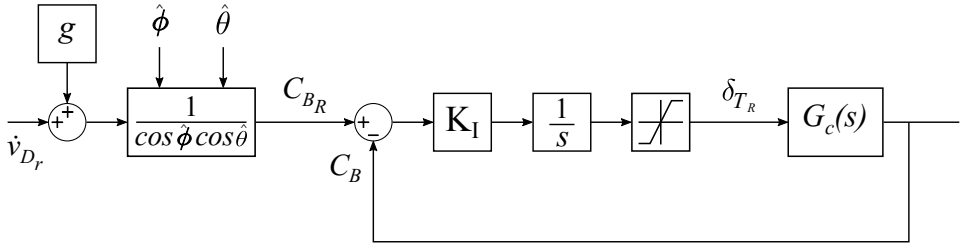

Figure 7.22: Illustration of the NSA control structure.

The NSA control structure is illustrated in Figure 7.22. The controller receives input commands from the climb rate controller. The altitude and climb rate controllers control the aircraft's heave states in the inertial coordinate system, while the NSA operates strictly in the aircraft's body axis coordinate system. Therefore, the vertical acceleration command inputs from the climb rate controller, are compensated to account for the tilting of the thrust vector due to the aircraft's pitch and roll orientation. Gravity compensation is also included to account for the gravity bias in the accelerometer measurement. The controller saturation limit is set at 75% of the aircraft's maximum thrust to retain adequate margin for pitch and roll stability control.

The root loci of the NSA system are shown in Figure 7.23. The additional pole at the origin, due to the integral control action, results in a compensated root locus similar to the uncompensated root loci of the attitude rate systems. These all feature a break point at $s = -10\,\text{rad/s}$ and have an infinite gain margin. This indicates a good closed-loop bandwidth will be achievable with pure integral control.

A 'fast' integrator is designed, with a controller gain of $K_I = -35$, in an effort to maximise the controller bandwidth whilst maintaining a well damped response. The controller exhibits a final closed-loop bandwidth of $\omega_{bw} = 8\,\text{rad/s}$, a phase margin of $PM = 73.8°$ and $< 1\%$ overshoot. NSA step responses for both the linear and

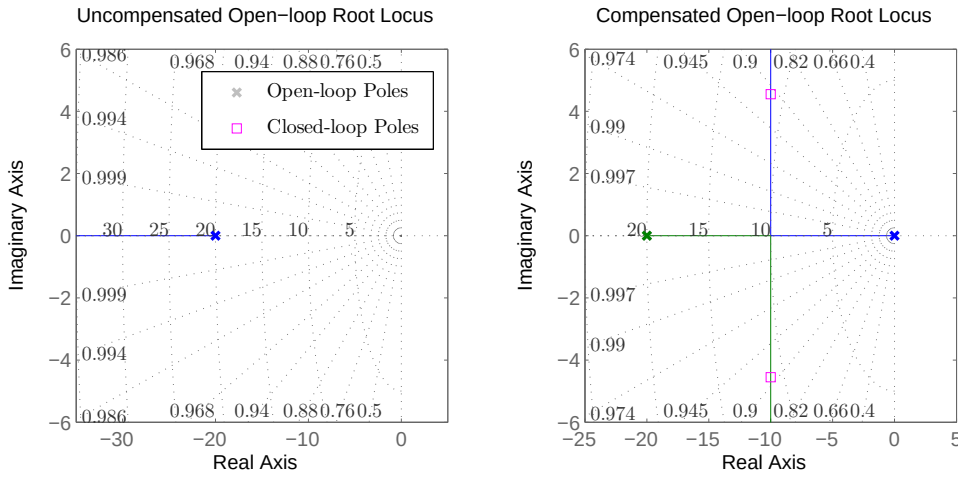

Figure 7.23: Open-loop yaw rate system root loci.

nonlinear systems are given by Figure 7.24. The inclusion of aerodynamic drag in the nonlinear model illustrates the inability of the controller to track an acceleration input. Aerodynamic forces are subsequently removed from the model to illustrate the comparative performance with the linear model. The controller command outputs, δ_{T_R}, from the nonlinear model are also centred about zero for similar comparative purposes.

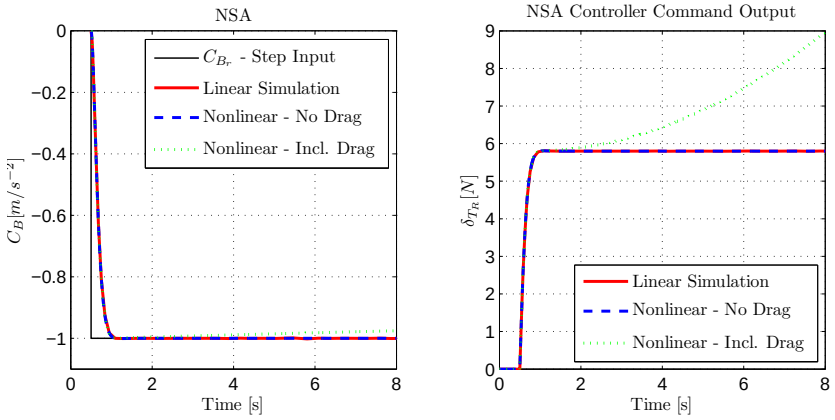

Figure 7.24: NSA controller responses.

7.5.2 Climb Rate Controller

The performance of the outer loop controllers in the heave control system is ultimately limited by the fidelity of the GPS measurements in climb rate and altitude. In addition to the delay associated with the GPS measurement update frequency of 5 Hz, further timing delays were observed between the accelerometer propagated states and those measured by the GPS. These delays proved to be variable in practise, within the range of 200–500 ms. To account for this, the open-loop climb rate

and altitude plants were augmented with 200 ms time delays by means of a first order Padé approximant of the form,

$$e^{-T_d s} \approxeq \frac{1 - \frac{T_d s}{2}}{1 + \frac{T_d s}{2}} \tag{7.46}$$

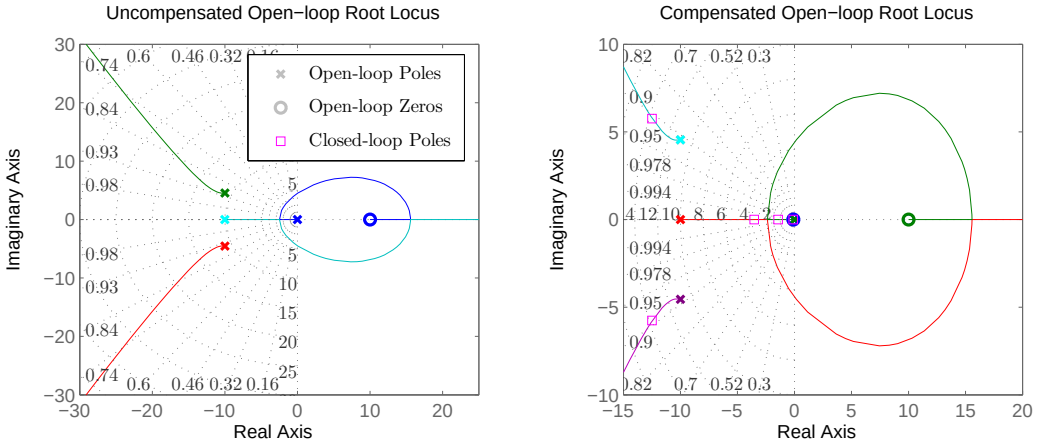

Figure 7.25: Open-loop climb rate system root loci.

The root locus of the open-loop climb rate system is illustrated in Figure 7.25. The time delay results in a nonminimum phase system with the zero in the right half plane. This nonminimum phase zero is responsible for decreasing the system phase as opposed to the phase increase associated with zeros in the left half plane. This loss of phase is more clearly illustrated through the open-loop bode plot in Figure 7.26. The time delay results in an additional 180° of phase loss over the frequency range shown. The phase loss is also more significant at higher frequencies, and ultimately limits the attainable closed-loop bandwidth of the controller.

PI control is employed for the climb rate controller to compensate for any unmodelled disturbances. The proportional gain is designed conservatively in light of the aforementioned timing issues; with the aim of limiting the total phase loss to less than $\leq 20°$[5] at the crossover frequency. A minimum phase margin of $PM \geq 60°$ is also specified for robustness against further variabilities in the observed time delays. The structure of the climb rate controller is illustrated in Figure 7.27, with the final control law given by Equation 7.47. The controller features saturation limits for both the integrator and the final controller output, in addition to the anti-windup logic applied universally to all the integrators in the autonomous control system.

$$D_w(s) = \frac{0.9(s + 0.1)}{s} \tag{7.47}$$

[5]For a 200 ms delay.

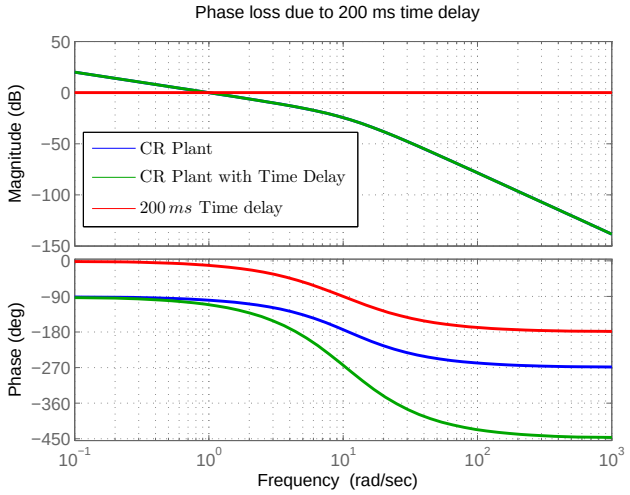

Figure 7.26: Open-loop bode plots of the climb rate system.

The controller yields a final $-3\,\text{dB}$ closed-loop bandwidth of $\omega_{bw} = 1.55\,\text{rad/s}$ with a phase margin of $PM = 64.8°$. This is in contrast to the unhindered, open-loop compensated system with a phase margin of $PM = 75.1°$ at the same frequency. This correlates to a phase loss of $10.3°$ attributable to the $200\,\text{ms}$ time delay.

The proportional gain results in a closed-loop pole at $s = -1.43\,\text{rad/s}$ that dominates the dynamic response, while the slow integrator pole at $s = -0.114\,\text{rad/s}$ results in a transient that is slow to settle.

Figure 7.28 illustrates the controller step response for various time delay scenarios. The time delay in the nonlinear simulation environment is modelled as a generic transport delay of the appropriate magnitude. From the figure it is clear that the first-order Padé approximant used in the controller design compares favourably with the generic transport delay. Furthermore, the results indicate an increasingly under damped response for an increase in the time delay, although crucially, the controller remains stable even in the presence of a $400\,\text{ms}$ delay. While this does not guarantee controller stability in an absolute sense, it does suggest the controller is suitably robust to timing issues in the climb rate measurement, and thereby concludes the analysis of the climb rate controller.

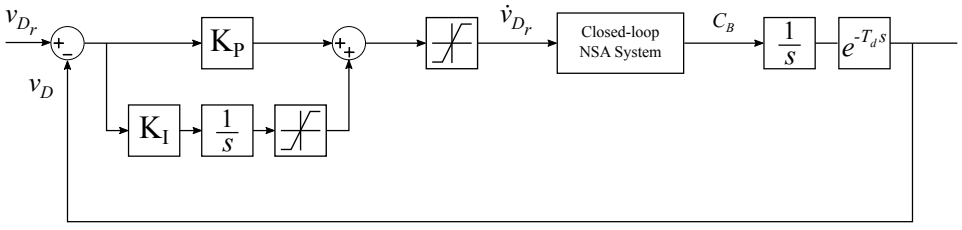

Figure 7.27: Illustration of the climb rate control structure.

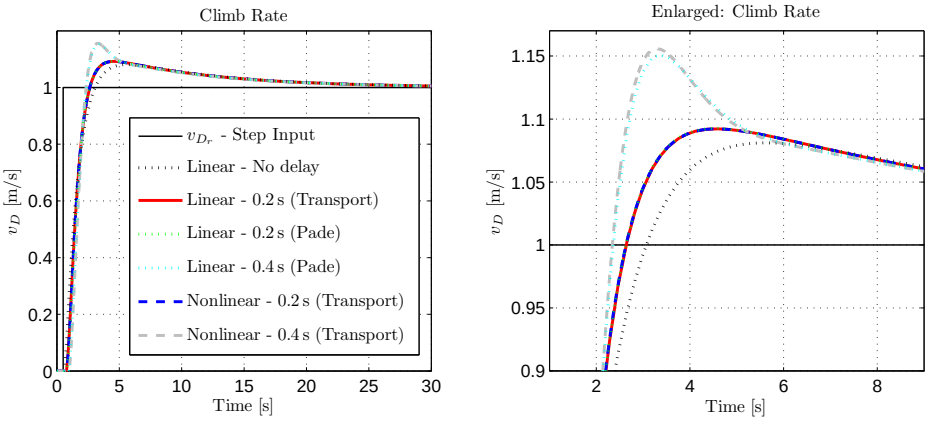

Figure 7.28: Climb rate controller step response.

7.5.3 Altitude Controller

The altitude controller is the outermost control loop in the heave control system and receives altitude reference commands directly from the ground station. The GPS altitude position measurements proved to be more reliable than the GPS climb rate measurements with delays typically limited to between 100–200 ms. Like the climb rate controller plant, the altitude system is augmented with a 200 ms delay via the Padé approximant described in the previous section.

The design of the altitude controller focusses first and foremost on stability, and thereafter prioritises a smooth, well damped positional response to mitigate against the constraining effects of the tether. Pure proportional control is employed as any steady state disturbances acting on the vertical translational dynamics of the aircraft are already compensated for by the integral control action in the climb rate controller. A maximum closed-loop bandwidth of $\omega_{bw} \leq 0.6\,\text{rad/s}$, is specified to ensure good time-scale separation between the dynamics of the inner climb rate controller, and the tether's fundamental frequency. Similar to the climb rate controller, a minimum phase margin of $PM \geq 60^\circ$ is specified for robustness in light of the GPS delays.

The root locus of the altitude system is illustrated in Figure 7.29. The Padé approximant, once again, results in a nonminimum phase system with zeros in the right half plane. The pole locations otherwise correlate with those of the closed-loop climb rate system, with two additional poles. The first is due to the Padé approximant, and the second due to the integration between the velocity and position states. The result is a cluster of slow poles near the imaginary axis which dominate the controller dynamics.

The controller structure is illustrated in Figure 7.30. The proportional gain is selected as $K_D = 0.29$, which yields a final $-3\,\text{dB}$ closed-loop bandwidth of $\omega_{bw} = 0.56\,\text{rad/s}$ and a phase margin of $PM = 66.8^\circ$. The closed-loop poles located at $s = -0.479 \pm 0.433j\,\text{rad/s}$ dominate the dynamic response while the pole at $s = -0.0954\,\text{rad/s}$ results in a slow transient. This is evident from the controller

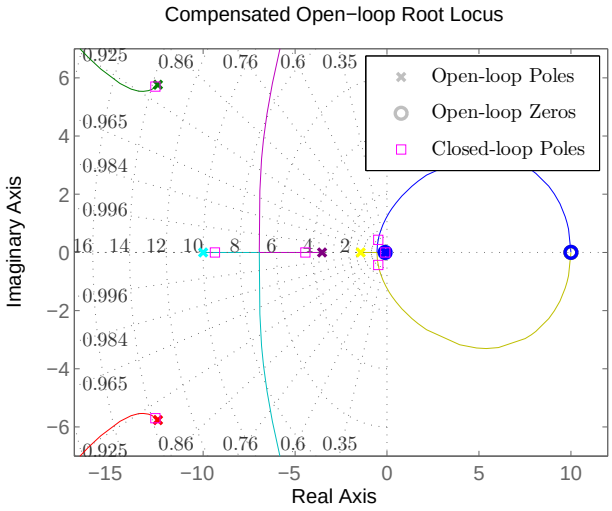

Figure 7.29: Open-loop altitude system root locus.

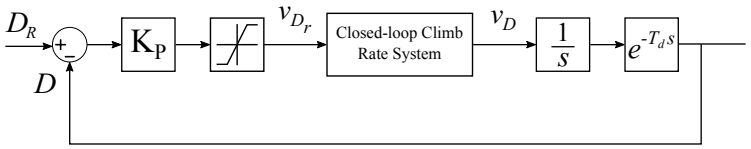

Figure 7.30: Illustration of the altitude control structure.

step response illustrated in Figure 7.31.

The controller response ostensibly resembles that of an over damped system, but this is simply a result of the low proportional gain value employed. In reality the system is decisively under damped, and yields unacceptable levels of overshoot for higher gain values. This is more apparent from the enlarged step response in Figure 7.30. This is also the first control loop with an appreciable difference in performance between the linear and nonlinear models. This is likely due to the added damping that results from the aerodynamic drag forces modelled in the nonlinear simulation. Once again the response illustrates increased overshoot in the presence of a time delay, although, the effects are far less pronounced in comparison to the climb rate system. While the current controller is slow to settle at a commanded reference point, the performance is satisfactory considering the tethered application. This concludes the analysis of the autonomous flight controller designs for the untethered quadrotor vehicle.

7.5.4 Modifications for Tethered Flight

The constraining nature of the tether, coupled with the positional uncertainty emanating from the GPS, renders the current heave control system unsuitable for taut tethered flight. Modifications are subsequently made with the aim of addressing the control challenges associated with tethered flight, both simply and at a low cost.

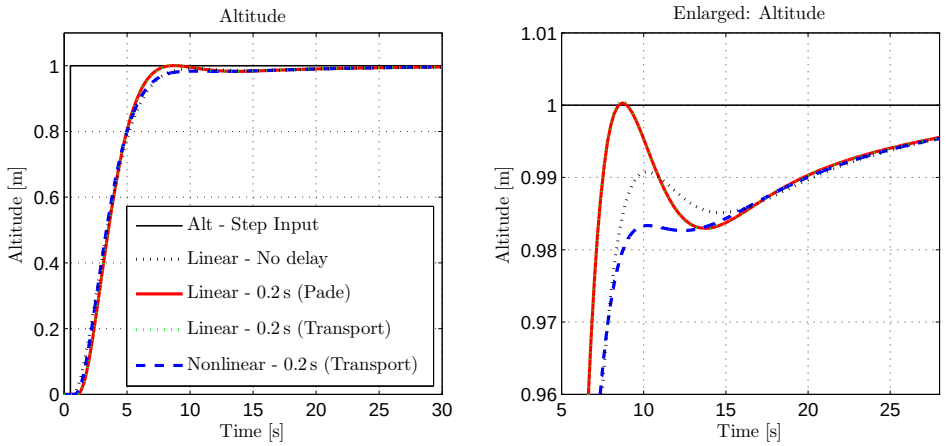

Figure 7.31: Altitude controller step response.

The modified controller is essentially based on the premise of open loop control, with the constraining action of the tether utilised for positional feedback of the aircraft in altitude. The approach is a pragmatic one that requires only the aircraft's onboard inertial sensors, which serve as a basic sensor configuration for full autonomous flight.

The modified controller aims to ensure that the tether remains in a fully elevated state at all times, barring take-off and landing. The fully elevated tether state is defined by the tether angle at the origin being greater than or equal to zero degrees ($\theta_0 \geq 0$). The tether angle is controlled indirectly by ensuring that the vehicle maintains a {N,E,D} position in space that satisfies the tether angle criterion. The user inputs for tethered flight consist of the total tether length, L_T, the desired horizontal span, L, and the additional thrust force buffer, $\Delta\delta_{T_{buf}}$, over and above the total vehicle and tether weight. Neglecting any sag in the tether due to wind, a minimum required altitude, h_{min}, can be defined for a given tether length and span offset, from the catenary equations derived in Chapter 5.3.

Considering the definition of the minimum altitude, it follows that h_{min} represents the boundary between the loose and taut tether configurations. At and above the minimum altitude the tether force can increase significantly for small increases in altitude, leading to tether impact events. The modified controller aims to optimise the open-loop control strategy to minimise the kinetic energy of the system near the loose to taut tether boundary, without resulting in a dynamic response that is impractically slow.

The structure of the modified heave control system is illustrated in Figure 7.32. Changes to the controller include new saturation limits on the altitude and NSA controller outputs, as well as switches on the altitude reference input and the integral control loop in the altitude and climb rate controllers respectively.

Considering the GPS measurement uncertainty, the altitude reference parameter, h_T, represents the minimum altitude (with 3σ certainty) where a tether impact event may occur. This concept is perhaps more clearly illustrated in Figure 7.33.

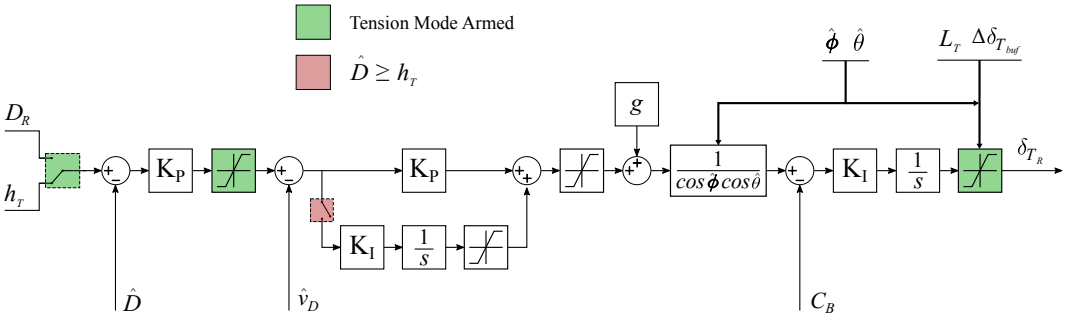

Figure 7.32: Layout of the heave control system for tethered flight.

The 3σ vertical and horizontal certainty levels used are the worst-case certainty levels as provided by the manufacturer in Table 6.1. The horizontal certainty level, σ_H, is specified as a circular error probability and, is therefore, sufficiently encapsulated through the consideration of the 2-Dimensional case. Values for h_T are predetermined for various tether lengths and spans, and are uploaded to the ground station for in-flight use.

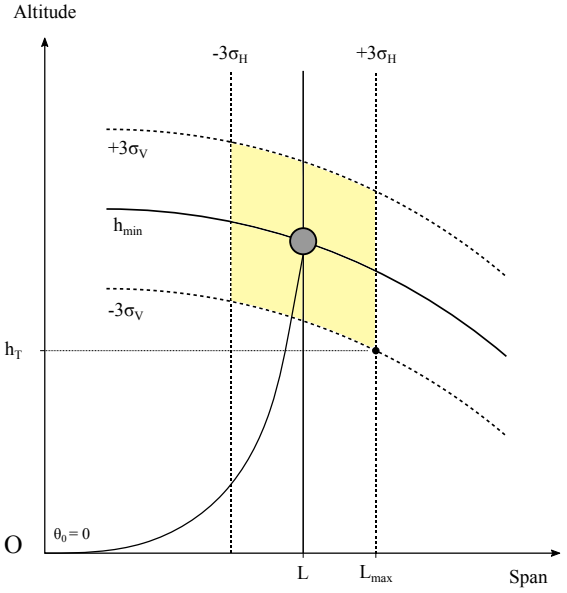

Figure 7.33: Illustration of the controller altitude parameters.

A thorough description of the practical flight strategy is provided in Chapter 9.3, but a basic summary is required to better understand the implemented control choices. The description begins after take-off with the system stationary in a loose tether configuration and in the conventional full autonomous, flight control mode.

As the tethered heave controller is armed, dubbed Tension Mode, the altitude reference command changes to h_T from some initial altitude command, $D_R = \hat{D}$; with the altitude and NSA controller saturation limits simultaneously set to their respective Tension Mode values. The altitude controller saturation limit determines the

maximum and minimum commandable climb rates for the aircraft, defined for the untethered and tethered configurations are per Equations 7.48–7.51.

Untethered:

$$v_{D_{max}} = \quad 2 \text{ [m/s]} \tag{7.48}$$
$$v_{D_{min}} = -1 \text{ [m/s]} \tag{7.49}$$

Tethered:

$$v_{D_{max}} = \quad 2 \text{ [m/s]} \tag{7.50}$$
$$v_{D_{min}} = 0.3 \text{ [m/s]} \tag{7.51}$$

Setting the altitude controller reference and saturation limit in this way serves two purposes. Firstly, it maintains the dynamic response of the untethered controllers when the initial arming altitude is far from the tethered reference altitude ($D_R \ll h_T$). Secondly, it ensures the saturation of the NSA controller even for an initialisation scenario where $D_R \geq h_T$. It also serves as a natural means of tapering the kinetic energy of the system, as the commanded climb rate will drop below the minimum value as the altitude error approaches zero ($\hat{D} \rightarrow h_T$). This enables the vehicle to command a reduced climb rate through the loose to taut tether transition phase, which would otherwise severely limit the dynamic response of the aircraft for longer tether lengths. The lower limit value is determined through simulation and serves as a conservative compromise between the tether impact forces and the aircraft's dynamic response.

An additional switch is employed by the climb rate controller to disable the integral control action as the system approaches the transition point. The switch triggers in Tension Mode when the condition $\hat{D} \geq h_T$ is satisfied. This is to prevent the integrator from saturating under the taut tether configuration. The climb rate integrator is a slow one designed to counter disturbances in the steady state. The low bandwidth will perpetuate the effects of integrator wind-up after the tether is released. The omission of the integrator does not negatively affect the stability of the climb rate controller and, in fact, increases the phase margin to $PM = 71.3°$. The only consequence is the loss of the ability to counter steady state disturbances. Any measurement bias in the accelerometer is expected to be small, while the effects of aerodynamic drag are similarly negligible at these reduced velocities. However, a small offset will arise between the commanded and realised vehicle climb rate as a result of the linear increase in the tether weight with altitude. These effects are investigated with the results (illustrated in Figure 7.34) indicating an acceptably small offset of 0.05 m/s.

The remaining saturation limit on the NSA controller output effectively commands the desired open-loop thrust. The limit is variable in nature with the aim of improving the system efficiency by tailoring the thrust limit to the length of the tether employed. The limit is determined as a function of the vehicle altitude, h, as per

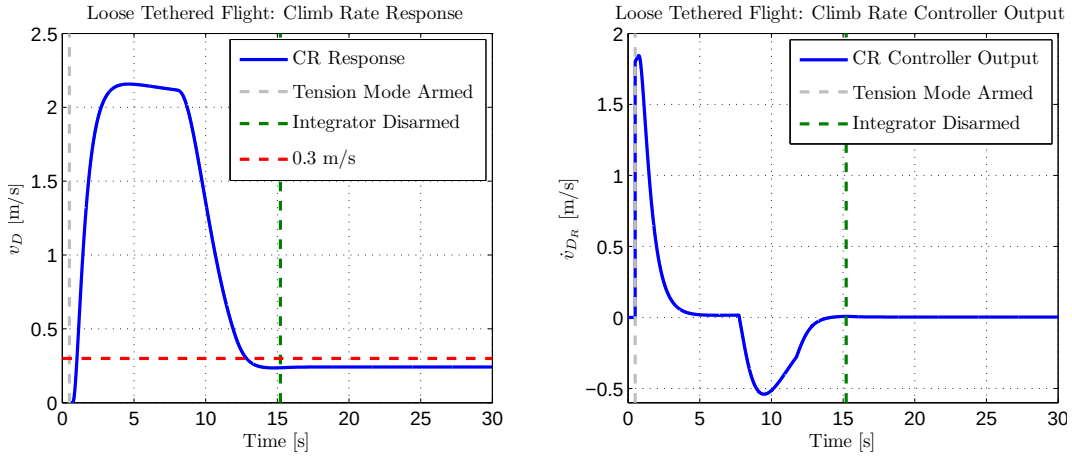

Figure 7.34: Climb rate controller output and response in Tension Mode.

Equation 7.52. The limit includes an additional thrust force buffer, $\Delta\delta_{T_{buf}}$, to counter any aerodynamic forces acting on the tether. The remaining equation parameters are defined according to Figure 7.35.

$$\delta^*_{T_R} = f(h) = \begin{cases} 0.75\delta_{T_{max}}, & \text{if } h < h_L \\ ah + b, & \text{if } h_t \geq h \geq h_L \\ mg + \mu_T L_T + \Delta\delta_{T_{buf}}, & \text{if } h > h_T \end{cases} \tag{7.52}$$

where,

$$h_L = h_{min} - 1.5(h_{min} - h_T) \tag{7.53}$$

$$a = \frac{0.75\delta_{T_{max}} - mg - \mu_T L_T - \Delta\delta_{T_{buf}}}{h_L - h_T} \tag{7.54}$$

$$b = 0.75\delta_{T_{max}} - ah_L \tag{7.55}$$

Thereafter, the limit is scaled to compensate for the aircraft's pitch and roll angles

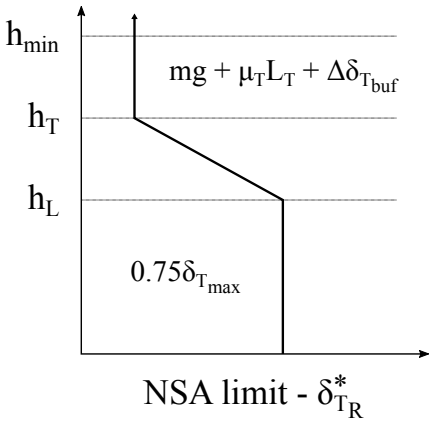

Figure 7.35: Variation of the NSA saturation limit.

as,

$$\delta_{T_R}^{max} = \frac{\delta_{T_R}^{*}}{\cos\hat{\phi}\cos\hat{\theta}} \tag{7.56}$$

Finally, the scaled limit from Equation 7.56 is passed through a first-order low-pass filter with a cut-off frequency of 1 rad/s. The filter cut-off frequency is selected well below the bandwidth of the NSA controller (≈ 8 rad/s) in order to prevent the limit from driving the command output.

The modified heave control system aims to offer a simple means of addressing the control challenges emanating from the constraining nature of the tether coupled with the position state uncertainty. A potential drawback of the control strategy is the impairment of the controllers disturbance rejection capabilities in heave. The aircraft is expected to have a slow response to intermittent disturbances such as wind gusts or impact events. This, in turn, leaves the aircraft more vulnerable to further impact events. This may be mitigated by operating at increased span distances and exploiting the catenary effect, or by simply increasing the tether tension through the thrust force buffer, $\Delta\delta_{T_{buf}}$. The thrust force buffer is designed to be manually editable from the ground station for such a purpose. Nevertheless, the proposed open-loop strategy is expected to be suitable for the control of the aircraft's heave dynamics as it is not a prominent failure mode for the vehicle, and therefore not critical in terms of the overall system stability.

Chapter 8

Non-linear Simulation

This chapter provides details of the non-linear simulation environments used in this project. Numerical simulations are critical to the project as they serve as the primary means of validating the autonomous flight controllers, prior to practical flight testing.

The chapter begins with an overview of the two primary simulation environments and their respective relevancies to the project. Thereafter, details are provided of the ground station and additional mathematical models employed but not previously discussed in this thesis. Finally the chapter concludes with the presentation and discussion of the simulation results for various untethered and tethered flight scenarios.

8.1 Overview

The two primary simulation environments employed in this project consist of the Software-In-the-Loop (SIL) and Hardware-In-the-Loop (HIL) simulation environments. The SIL environment provides an intermediary verification step of the discretised control algorithms, which are programmed in C and executed at the appropriate frequency. It also incorporates additional wind and sensor models, with the latter modelling the noise and variance of the various sensor measurements. The SIL environment is a self-contained system run exclusively in MATLAB, which enables quick debugging. It is used primarily to validate the controller designs for the untethered aircraft prior to testing in the more complex, and bug prone, HIL environment.

The HIL environment, as the name suggests, incorporates the on-board avionics hardware within the simulation loop, as illustrated in Figure 8.1. This provides a comprehensive validation of the system functionality prior to practical flight test-

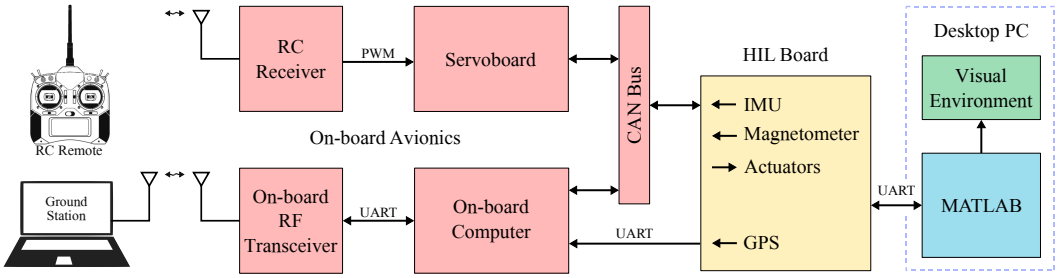

Figure 8.1: Hardware-In-the-Loop Setup

ing. Control, estimation, communication and data logging algorithms are executed by the OBC while the aircraft dynamic equations are executed in MATLAB on an accompanying computer. A separate HIL interface PCB board, featuring it's own microcontroller, facilitates communication between MATLAB and the OBC. The OBC control commands are received as inputs to the non-linear aircraft model in MATLAB, while the resulting simulated state measurements are packaged to emulate the onboard sensor measurements before being communicated back to the OBC. The OBC is also capable of receiving commands from both the RC remote and the ground station. The ground station communicates wirelessly with the OBC, commanding higher-level autonomous functions and receiving pertinent telemetry data. MATLAB's Real-Time Toolbox is used to synchronise the simulated model with the real-time execution of the OBC.

8.2 Ground Station

The ground station application, like the on-board avionics hardware and firmware, is a legacy component in the ESL that is adapted to suit the requirements of this project. The application provides a graphical user interface from which the autonomous functionality of the aircraft can be monitored and controlled.

The ground station serves as a bilateral communication link between the user and the aircraft, enabling commands from the user and status feedback from the aircraft. User commands relate to the initialisation and operation of the kinematic state estimator, the data logging routines, the autonomous flight controllers and the tether release servo. Due to the bandwidth limitations of the RF link, the status information from the aircraft is prioritised into different classes that are updated at intervals of 0.5Hz, 1Hz and 2Hz. The status feedback information can be classified as either controller, estimator, sensor, or general status information with more details provided in Table 8.1.

An image of the GUI (during a HIL simulation) is provided in Figure 8.2, illustrating the modifications made for the tethered application.

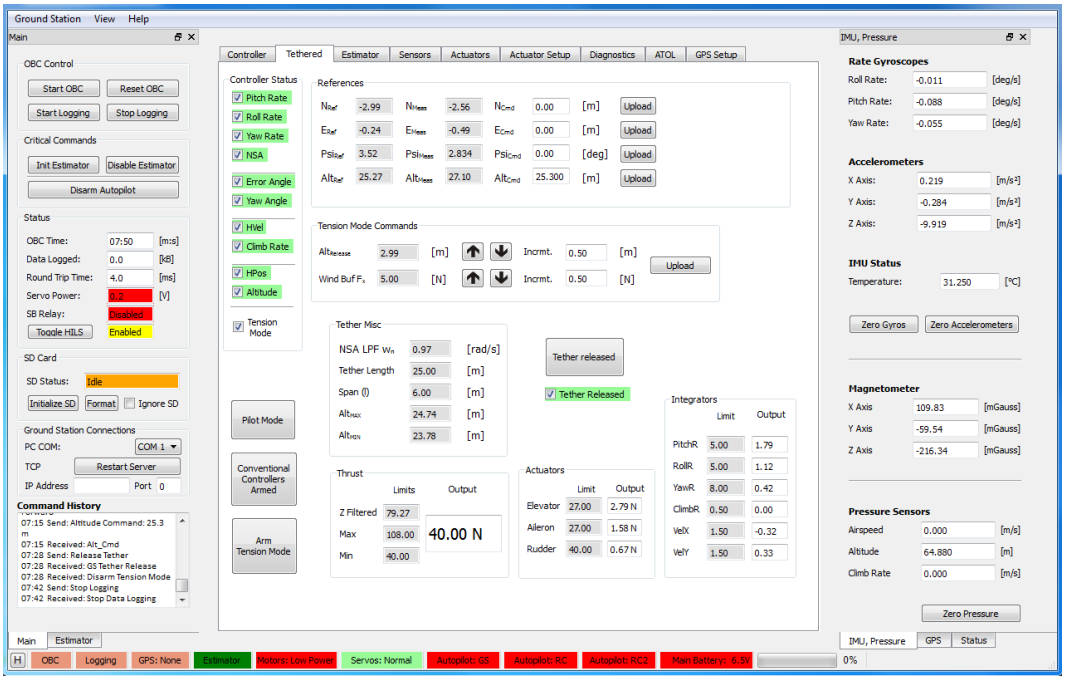

Figure 8.2: Illustration of the Ground Station GUI.

Table 8.1: Ground Station Status Information

Controller	Consists of individual controller status flags, references commands, limits and output values.
Estimator	Consists of the estimator status and state values.
Sensor	IMU, magnetometer, GPS, voltage and current sensor measurements. Additional GPS information including fix status, estimated accuracy, satellites visible and satellites used.
General	Includes a user command history, OBC running time and data logging status.

8.3 Additional Simulation Models

In addition to the non-linear vehicle and tether models discussed in previous chapters, the simulation environments include supplementary wind and sensor models to improve the simulation fidelity.

8.3.1 Wind Model

The non-linear simulation environment includes environmental considerations such as the atmospheric and magnetic field properties at the location of the practical testing facility. This is extended to include a rudimentary wind model. The wind model consists of a constant wind vector, applied in the inertial axis frame, which is perturbed via low-pass-filtered band-limited white noise, as per Figure 8.3. The final wind output vector constitutes the reference wind magnitudes at an altitude of 10 m.

The tether model neglects the aerodynamic drag forces acting on the tether, based on the assumption that these forces are small relative to the tether tension. Nevertheless, the wind model is included to simulate the effects of aerodynamic drag on the vehicle as well as the influence on the actuator thrust coefficients.

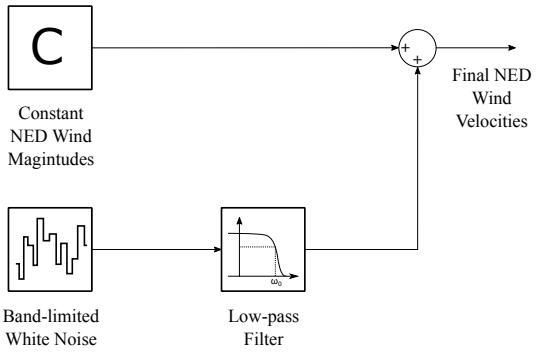

Figure 8.3: Wind Model Block Diagram

8.3.2 Sensor Models

The sensor models employed in the simulation environments aim to represent the noise and drift characteristics of the real-world sensor measurements. Measurement noise is applied to the IMU and magnetometer measurements via Simulink's Band-Limited White Noise (BLWN) blocks, with the noise power spectral densities (PSD) used as provided by the manufacturer data-sheets. The GPS noise model is illustrated in Figure 8.4, and features low-pass filters to replicate the low-frequency measurement drift. The filter cut-off frequencies are determined by taking the fast Fourier transform (FFT) of the position data taken from static position tests. This identified a dominant harmonic at $\approx 0.01\,\text{Hz}$. The PSD values are determined to correlate with the measured drift magnitudes.

The on-board IMU (including both the 3-axis accelerometer and gyroscope) and magnetometer were calibrated prior to practical flight testing to mitigate against the effects of any sensor biases. The accelerometer was calibrated in each axis using the gravity vector. The gyroscope was similarly calibrated in each axis, for various

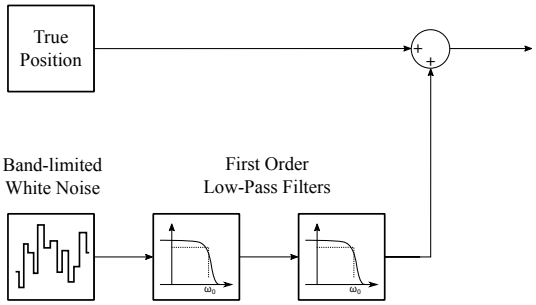

Figure 8.4: GPS Measurement Drift Model

angular rates, using a rate table. While the magnetic field around the aircraft was manipulated using a Helmholtz cage, enabling the calibration of the magnetometer.

8.4 Simulation Results

Simulation results are presented for both the untethered and tethered systems. The results provide an indication of the real-world performance and serve as the primary, and final, verification step prior to practical flight testing.

8.4.1 Untethered Aircraft

A simplified set of results is presented for the untethered aircraft in terms of the outer loop controller step responses, which sufficiently illustrates the autonomous performance. Comparisons are provided between the various simulation platforms to illustrate the effect of individual components on the final performance.

The SIL simulation implementation features the discretised control laws, implemented as s-functions in MATLAB, and the non-linear aircraft model. Apart from the Hardware-In-the-Loop implementation, comparisons between the SIL and HIL environments further serve to illustrate the influence of the kinetic state estimator. Figures 8.5 and 8.6 indicate that the outer-loop autonomous performance generally correlates well between the two environments; with sensor inaccuracies ultimately providing the dominant constraint. This is most apparent from the slight oscillations in heave, which is a result of the time delays in the GPS climb rate measurement.

Furthermore, Figure 8.7 illustrates the effect of sensor noise on the angle tracking abilities of the aircraft. Noise in the gyroscope measurements is integrated to yield an error in the orientation state estimates which manifests as angular random walk.

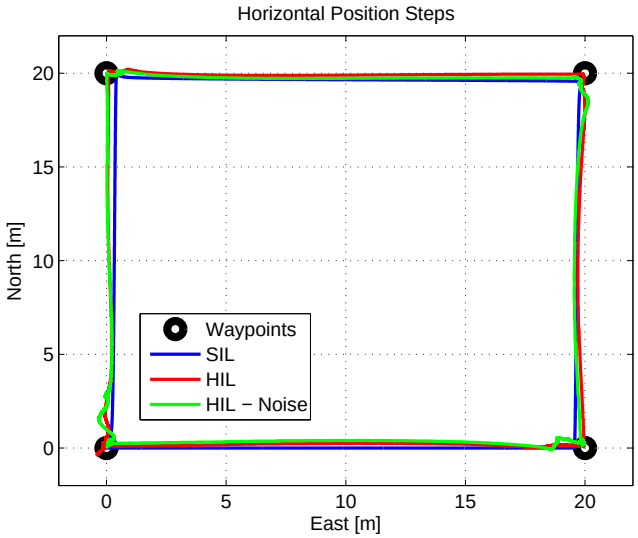

Figure 8.5: Horizontal Position Step Responses

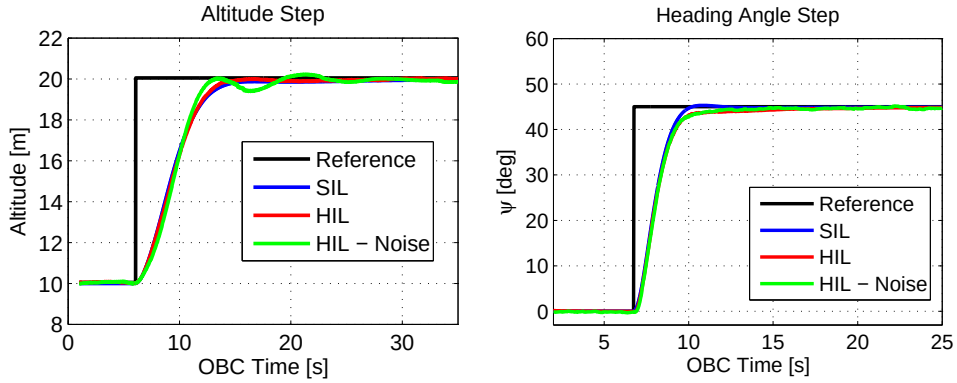

(a) Altitude Step Response

(b) Heading Angle Step Response

Figure 8.6: Altitude and Heading Angle Step Responses

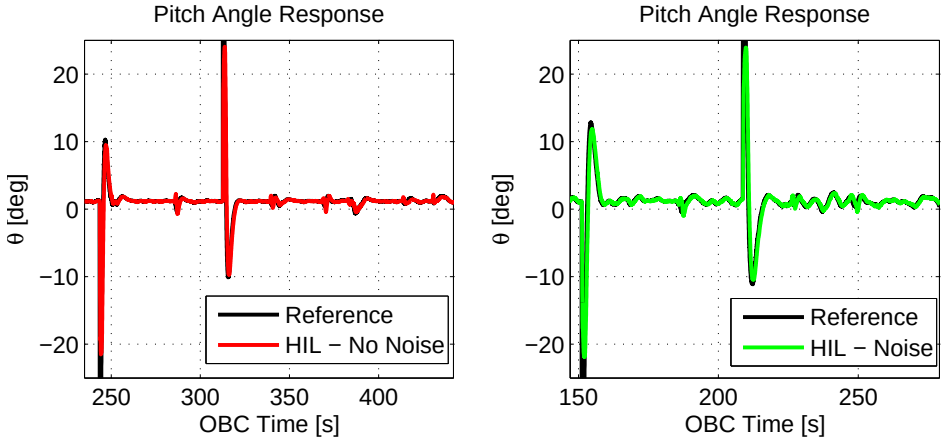

Figure 8.7: Illustration of the angular random walk phenomenon.

8.4.2 Tethered Aircraft

Simulations of the tethered system are conducted in the HIL environment and illustrate the feasibility of the control strategy, in terms of functionality and controller stability, as well as notable variations between the vertical and offset flight cases.

Vertical Tether Case

Simulation results are presented for a 25 m tether length with the autonomous controllers armed at some altitude < 25 m, after which tension mode was enabled. Figure 8.8a illustrates a well damped altitude response through the loose to taut transition, indicating that the NSA controller's limited output does not significantly hamper the aircraft's ability to maintain a desired altitude set-point in the presence of disturbances forces resulting from the tether impact events. This is supported by the throttle command outputs in Figure 8.8b, which only saturate roughly 25 s after the initial impact event at $t \approx 110$ s. The steps in the throttle command output are congruous with the observed tether tension forces at the vehicle, as illustrated in Figure 8.10a. The tether tension force response is characterised by a series of abrupt spikes in tension at the tether impact events; this correlates with the sharp tension force gradients associated with the vertical tether case. However, apart from the initial impact spike at $t \approx 110$ s, subsequent spikes are agreeably small, primarily due to the low bandwidth of the climb rate and altitude controllers. The measured altitude, in excess of the 25 m tether length, is a consequence of the elevated tether mounting point, which is further discussed in Chapter 9.3.

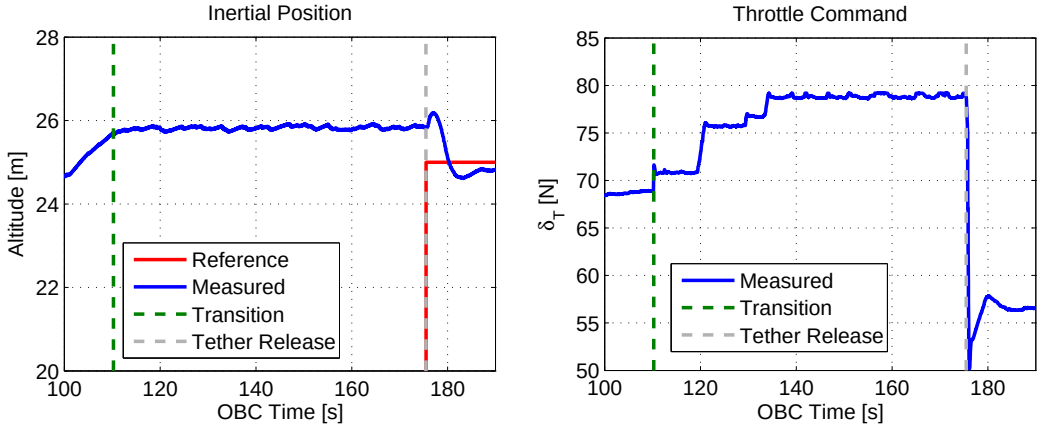

(a) Altitude Response (b) Throttle Commands

Figure 8.8: Altitude Response and Throttle Commands

The aircraft is initialised at a small horizontal offset distance to illustrate the effects of the tether restoring forces on the aircraft as the tension increases through the transition point. This is clearly illustrated in Figure 8.9 where the aircraft is

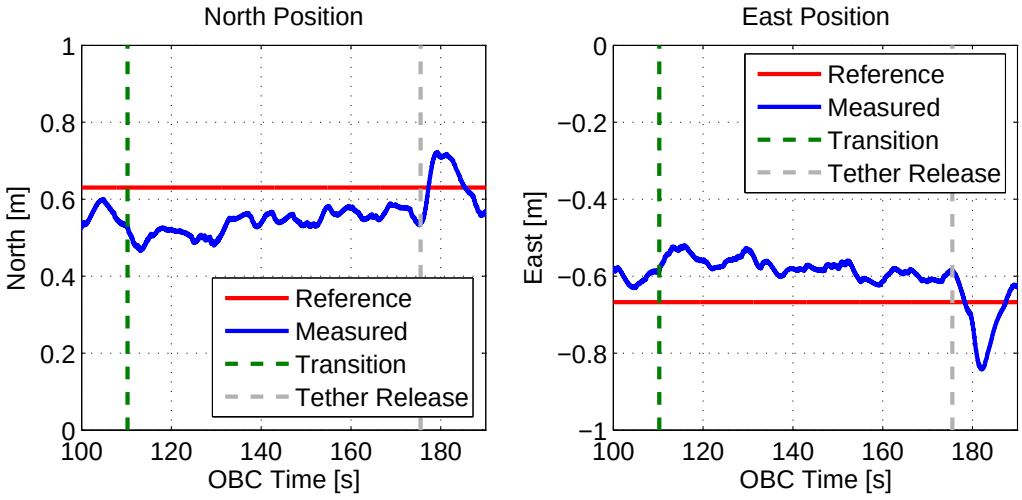

Figure 8.9: Horizontal Position Step Responses

displaced towards the origin immediately after the initial transition impact. The horizontal position response further serves to illustrate the detrimental effect of the unmodelled tether tension and inertia on the aircraft's ability to track commanded position references. Although it is also worth reiterating that the simulation contains GPS measurement drift, which further exasperates the tracking abilities. Nevertheless, the response is noticeably faster immediately after the tether is released. The initial overshoot observed after the tether release is a result of integrator wind-up in the horizontal velocity controllers. The integrator limits are kept small to minimise these effects, to the detriment of the steady state tracking abilities.

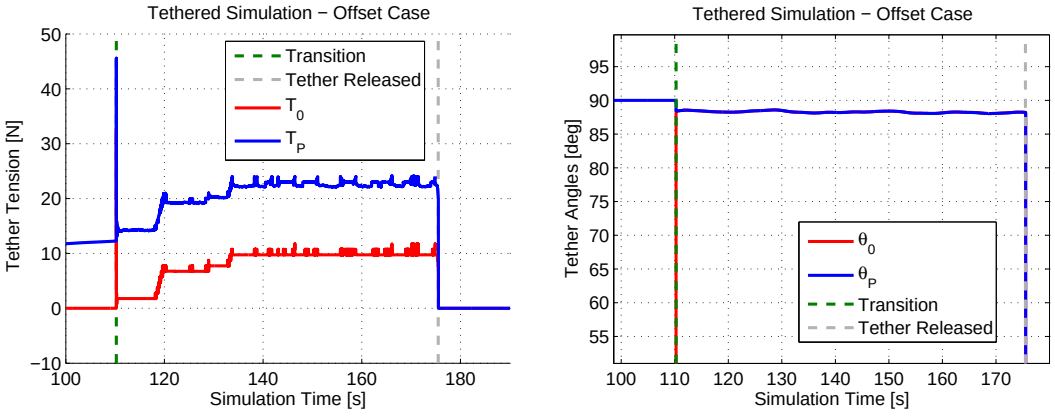

(a) Tether Tension

(b) Tether Angles

Figure 8.10: Tether Tension and Angles

The tether angles in Figure 8.10b illustrate near-vertical tether configuration, with the angle at the origin increasing exponentially at the tether impact point. This is consistent with the elevator commands and the pitch angle response in Figures 8.11a and 8.11b which indicate a small horizontal tether force component.

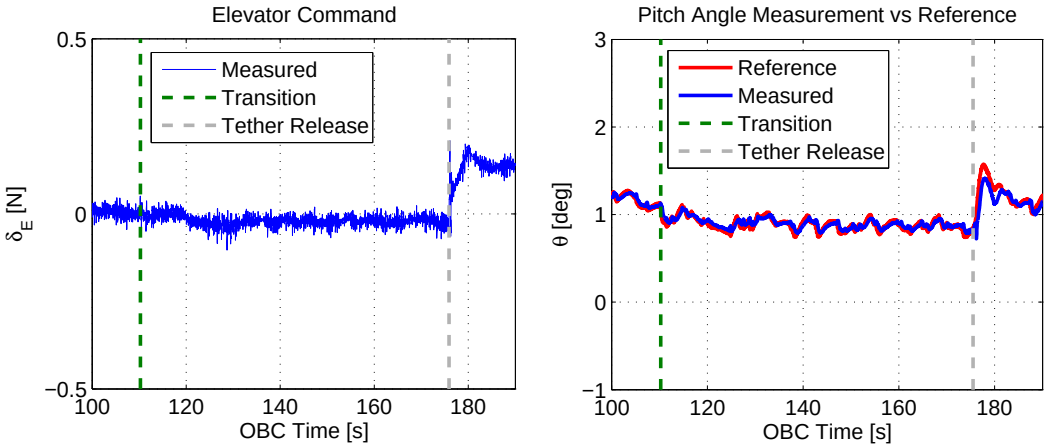

(a) Elevator Commands (b) Aircraft Pitch Angle

Figure 8.11: Aircraft Longitudinal States

Offset Case

Results for the offset case are presented for a horizontal span distance of $L \approx 6\,\text{m}$. Figure 8.12a indicates a similarly well damped response in altitude relative to the vertical tether case. Notable differences from the vertical tether case are, however, observed in the throttle commands, from Figure 8.12b, which saturate at the initial transition point. This is a result of the reduced tension force gradients associated with the increase in span. This feature is well illustrated by the tether tension forces in Figure 8.13a, which increase more gradually through the transition point relative to the vertical case[1]. Furthermore, the tension forces are far more consis-

[1] A small discontinuity can be observed at $t \approx 200\,\text{s}$ in the tension force at the origin due to the condition in Equation 5.9 being satisfied; although this can be seen to have a negligible effect on the tension force observed at the aircraft.

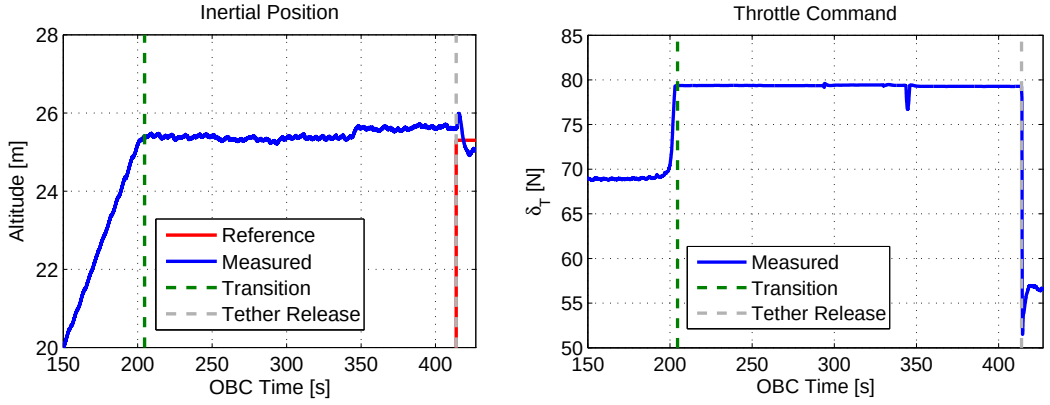

(a) Altitude Response (b) Throttle Commands

Figure 8.12: Altitude Response and Throttle Commands

tent throughout the course of the flight; although this does not have a significant impact on the resulting altitude response, relative to the vertical case, for the 25 m tether length. These effects can, however, be shown through simulation to be more significant for shorter tether lengths.

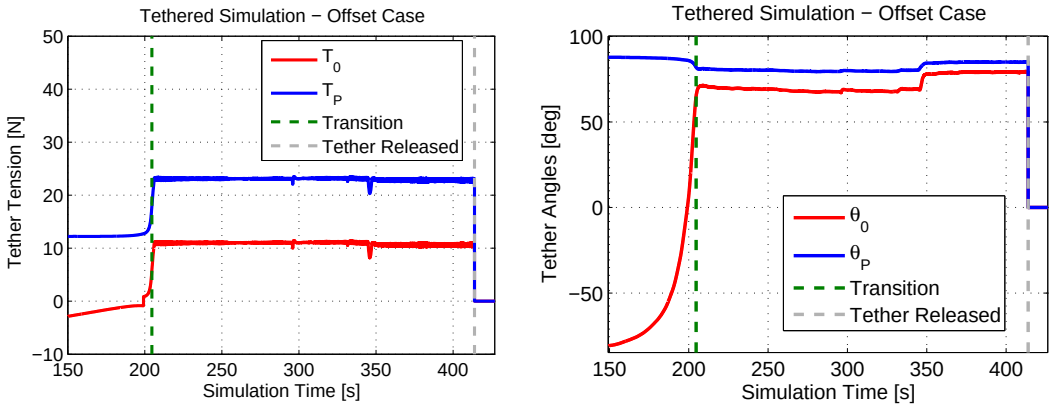

(a) Tether Tension

(b) Tether Angles

Figure 8.13: Tether Tension and Angles

The consequence of the offset case is the increased horizontal force component and increased tether tension values for a given operational altitude, relative to the vertical case. These effects are clearly illustrated through the tether angles in Figure 8.10b and aircraft's longitudinal states in Figures 8.11a and 8.11b. The aircraft is required to settle into a new trim state, away from the horizontal, in order to counteract the horizontal force component. This results in a marginally more oscillatory pitch angle response at increased span distances, as the aircraft becomes more sensitive in pitch to fluctuations in the tether force vector.

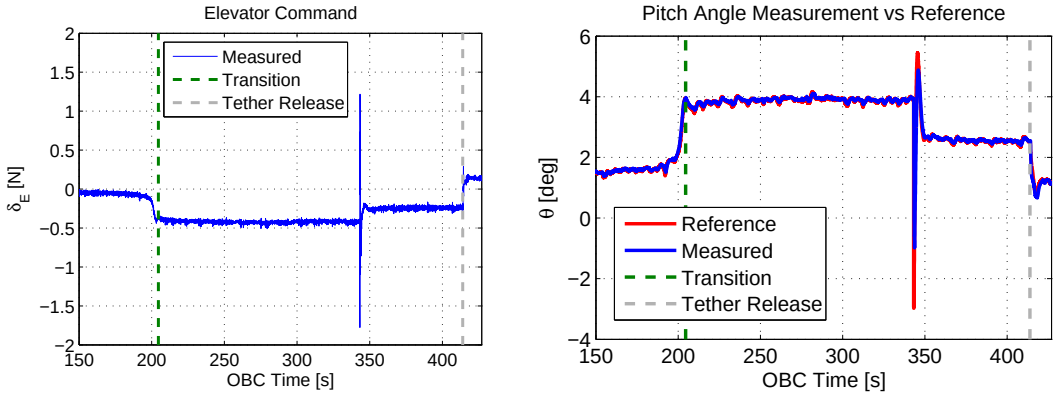

(a) Elevator Commands

(b) Aircraft Pitch Angle

Figure 8.14: Aircraft Longitudinal States

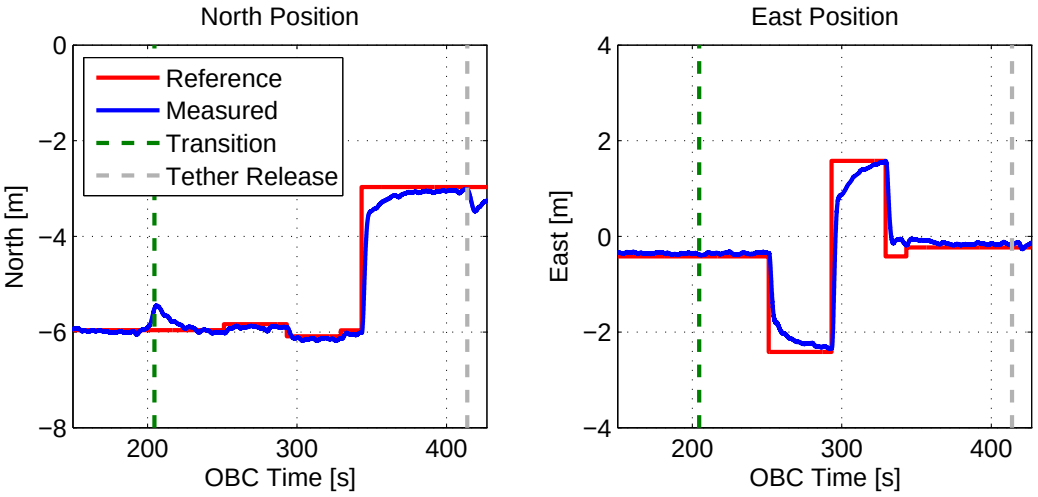

Figure 8.15: Horizontal Position Step Responses

Figure 8.15 further illustrates the coupling between the horizontal and vertical translational dynamics which is a consequence of the constraining action of the tether. This is apparent from the Northerly position response, where the aircraft is displaced towards the origin through the transition point; as well as from the altitude response where the aircraft experiences an altitude gain at $t \approx 350\,\mathrm{s}$ with a reduction in span. This is less evident for position steps perpendicular to the span distance, as in the Easterly position response from Figure 8.15. However, the Easterly position steps in particular, again highlight the detrimental effect of the tether on the aircraft's ability to track commanded position references. For this simulation the GPS drift models were deactivated, which results in an improved steady state tracking response relative to the vertical tether case.

Chapter 9

Practical Testing

This chapter details the evaluation of both the untethered and tethered flight control strategies through a series of practical tests. While the simulation models aim to be representative of the real-world system and generally provide a good indication of the autonomous performance, practical flight testing provides a more comprehensive evaluation of the system in the presence of any unmodelled phenomena.

The chapter begins with an outline of the practical tests conducted with their associated outcomes and limitations. Thereafter, the performance of the untethered control system is presented and discussed. The chapter culminates with the evaluation of the autonomous performance for various tethered flight scenarios and highlights the influence of the tether on the aircraft dynamics.

9.1 Testing Outline

Practical testing of the aircraft is split into three phases; namely, the initial commissioning of the aircraft, the verification of the autonomous controllers on the untethered aircraft, and finally, practical flight testing of the tethered system.

The first phase focussed on validating the functionality of the aircraft and the associated testing hardware. This included ensuring that the aircraft was controllable from a manual flight perspective. A test jig was manufactured to enable the testing of the stability augmented manual flight mode without the risk associated with practical flight testing. The test jig, pictured in Figure 9.1, constrained the aircraft's translational degrees of freedom but allowed angular rotation in pitch and yaw. This enabled the testing of the innermost pitch and yaw rate controllers, as well as the outer pitch and yaw angle controllers. Thereafter, the aircraft was rotated and fixed in the y_B body axis to enable the testing of the roll rate and angle controllers. Following the successful jig tests a maiden RC flight was conducted at the practical

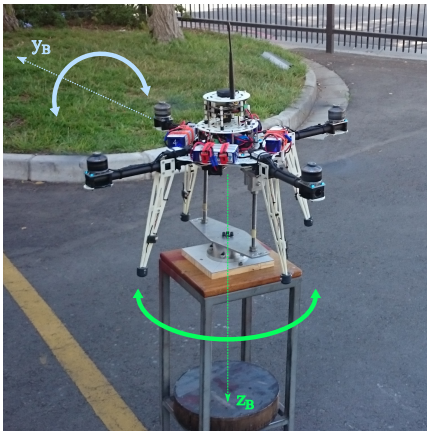

Figure 9.1: Illustration of the test jig setup.

testing facility. This was done specifically at the test facility to validate the performance of the magnetometer and GPS in the test environment. Furthermore, it enabled the tuning of the flight trim values and pilot sensitivity gains, in addition to serving as an opportunity for the pilot to familiarise himself with the aircraft prior to autonomous flight testing.

With the aircraft successfully commissioned, autonomous flight testing of the untethered aircraft was subsequently begun. This included four separate flights, with the controllers armed successively; beginning with the innermost control loops and progressing outwards until full autonomous flight was realised. It was at this point that the delays in the GPS climb rate measurements were first observed which resulted in the instability of the climb rate and altitude controllers. Consequently, the controllers were redesigned[1] to improve their robustness to said delays.

Once satisfactory performance of the untethered aircraft's autonomous behaviour had been achieved, testing of the tethered system was initiated. This final testing phase consisted of five separate flights, the first of which being exclusively under the loose tether configuration. As a safety precaution the tethered tests were limited to an upper altitude limit of 25 m. This decision was made in consultation with the safety pilot who felt that, in the event of an emergency, his abilities to successfully recover the aircraft were significantly impaired at altitudes greater than 25 m. This was an acceptable limitation considering the desired testing outcomes, which aimed to determine the feasibility of the control strategy, in addition to providing insight into the dynamics associated with tethered flight. Thus, the four remaining flight tests consisted of taut tethered flights; two with a tether length of 25 m and two with a tether length of 15 m. The tether span was varied for each tether length to investigate it's influence on the system response and dynamics. Limited control optimisation was performed during these final flight tests with the author instead providing recommendations on any observed phenomena.

[1]Note: The controller designs presented in Chapter 7.5 constitute the redesigned controllers.

9.2 Untethered Flight Results

The untethered flights served to validate the performance of the autonomous controllers on the untethered aircraft before the tethered flight tests could be attempted. As previously mentioned, testing comprised of four separate flights with the control loops armed successively in order to individually verify their stability. The results presented here are for a single flight with the aircraft subjected to a series of position and velocity steps. This sufficiently illustrates the autonomous performance of the aircraft.

The flight test was conducted at Helderberg Radio Flyers airfield, colloquially known as HRF. Weather conditions were favourable with an average wind-speed of 1 m/s with intermittent gusts up to 4 m/s. The test focussed on the testing of the redesigned climb rate and altitude controllers after the longitudinal, lateral and directional control systems had previously been proven to be stable. The aircraft was manually piloted to an altitude of approximately 15 m, at which point the autonomous control system was fully enabled. To ease transitioning between the manual and autonomous flight modes, the position controller references are assigned the current position state measurements as the controllers are subsequently armed.

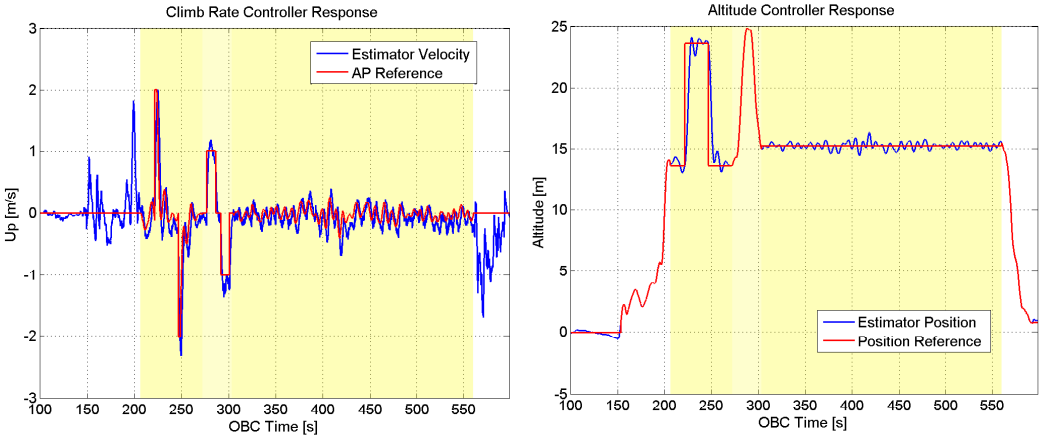

(a) Climb Rate Controller

(b) Altitude Controller

Figure 9.2: Heave Response

Once the vehicle was seen to accurately regulate it's position, a positive 10 m altitude step was commanded from the ground station. This was followed by a negative 10 m altitude step as the aircraft was returned to it's original altitude set-point. Following this, the altitude controller was disarmed with the aircraft subjected to climb rate steps of ±1 m/s. The climb rate and altitude controller tracking responses are illustrated in Figures 9.2a and 9.2b respectively. The shaded areas of the graphs indicate the periods when the heave control system is active, with the shading intensity corresponding to the number of individual controllers active[2].

[2]Shading is lighter during the climb rate steps when the altitude controller was disarmed.

The heave controllers were found to generally function as designed in the presence of the GPS measurement delays. The only notable exception being during commanded periods of descent where there was a noticeable degradation in performance. This is due to unmodelled variations in the rotor thrust outputs as the rotors enter the vortex ring flow state, previously discussed in Chapter 4.1.3. This is particularly apparent during the negative altitude step which resulted in a significant disturbance of the aircraft's angular dynamics. This was primarily due to the aggressive sink rate, which was initially limited to $v_{D_{min}} = -2\,\text{m/s}$. This aggravated the unsteady flow effects that characterise the vortex ring state. Nevertheless, this was easily negated by altering the saturation limit to a maximum permissible sink rate of $v_{D_{min}} = -1\,\text{m/s}$, with a significant resultant improvement in performance. This was tested specifically in a subsequent flight but is further evidenced by the negative climb rate step at approximately 300 s. The altitude controller exhibits good altitude tracking in hover, accurate to within 30 cm for the static case. The performance is diminished slightly for the dynamic case where it is accurate to within 0.5 m for large longitudinal and lateral translational steps. The position controllers, in general, are characterised by a small-magnitude oscillatory response, which is a feature of quadrotors using inertial sensor feedback. This is primarily due to the high noise levels present in the IMU measurements, resulting from the high levels of vibration prevalent in rotary wing aerial vehicles. Errors in the accelerometer are integrated to yield a quadratic error in position, while errors in the gyroscope measurements are integrated to yield a quadratic error in velocity and a cubic error in position. For the quadrotor case, this has a larger affect on the heave dynamics due to the coupling between the longitudinal, lateral and heave dynamics; which is a result of the actuators being fixed in the aircraft's z_B body axis.

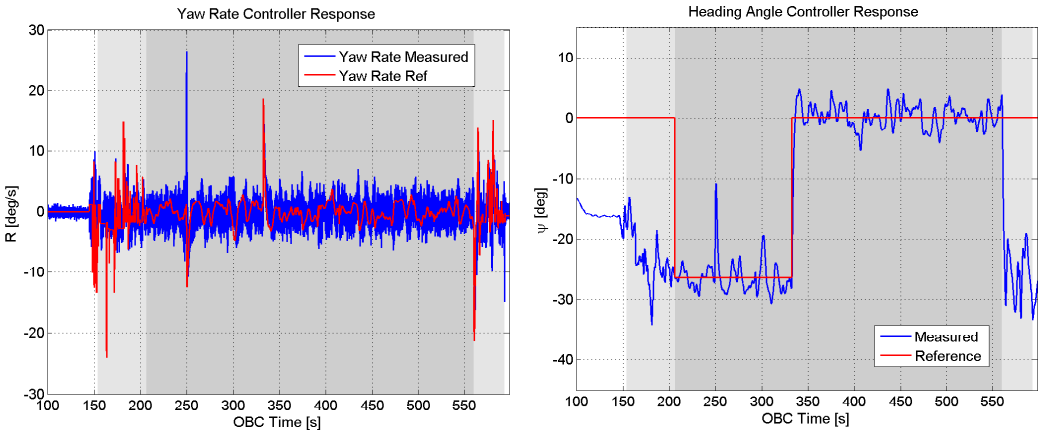

(a) Yaw Rate Controller

(b) Heading Angle Controller

Figure 9.3: Directional Response

Following the climb rate step, the altitude controller was rearmed and the aircraft subjected to a 26° heading angle step. The step command was specifically made to align the heading angle with the inertial coordinate system prior to the testing of the

longitudinal and lateral control systems. Figure 9.3a illustrates the extensive noise levels associated with the gyroscope feedback measurements. This, coupled with the low-bandwidth directional control capability of the aircraft, yields the heading angle controller accurate to within $\pm 4°$, as is clear from Figure 9.3b. Furthermore, the responses highlight the effects of the negative altitude ($t \approx 250\,\text{s}$) and climb rate ($t \approx 300\,\text{s}$) steps on the directional dynamics of the aircraft. While the controller counters both of these disturbances well, the reduced sink rate of the climb rate step results in the effects of the unsteady flow regime being far less pronounced, and almost indistinguishable from the gyro noise levels. Similar to the heave control system, the shaded areas of the graphs indicate the periods when the directional control system is active. In this instance the lightly shaded areas correspond to the activation of the yaw rate controller only, in the manual flight mode.

With the body and inertial axis systems suitably aligned, the aircraft was subjected to 10 m position steps and $\pm 1.5\,\text{m/s}$ velocity steps applied in the aircraft's longitudinal and lateral body axis directions. The aircraft's heading angle is aligned with the inertial axis system purely for illustrative purposes. The horizontal position controller responses are illustrated in Figures 9.4a and 9.4b, with both controllers performing well in practice. Similar to the altitude controller, the oscillatory nature of the steady state tracking response is once again evident but not problematic. Figures 9.5a and 9.5b illustrate the good performance of the horizontal velocity controllers which track both the dynamic and static velocity reference commands accurately. The inner pitch and roll angle controllers, pictured in Figures 9.6a and 9.6b, exhibit improved tracking relative to the heading angle controller due to the higher control bandwidth and improved disturbance rejection capabilities. The improved response to disturbances is especially evident when considering the disturbance induced by the negative altitude step. Comparing the aircraft's pitch and yaw rate responses it is clear that the initial disturbance is greater in pitch than it is yaw; but the reduced control bandwidth of the directional control system results in a greater

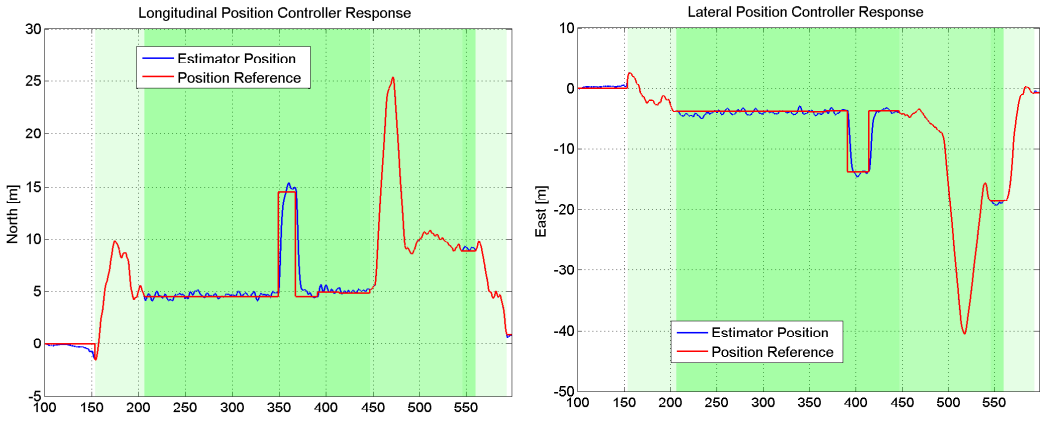

(a) Longitudinal Position Controller

(b) Lateral Position Controller

Figure 9.4: Horizontal Position Response

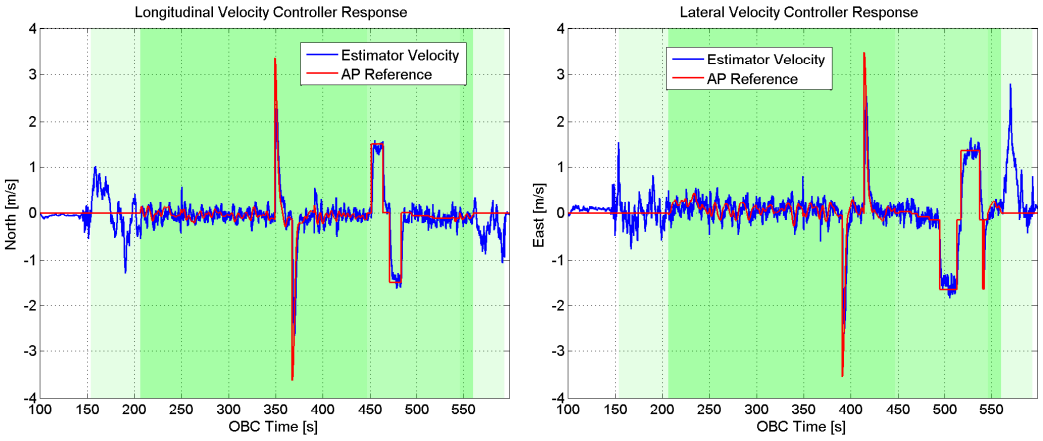

(a) Longitudinal Velocity Controller (b) Lateral Velocity Controller

Figure 9.5: Horizontal Velocity Response

displacement in yaw angle than it does in pitch angle. This would also seem to indicate that actuator 1 experienced a sudden loss of thrust causing the aircraft to pitch nose down. This correlates with the positive yaw disturbance which is attributable the rotor torques no longer being in equilibrium.

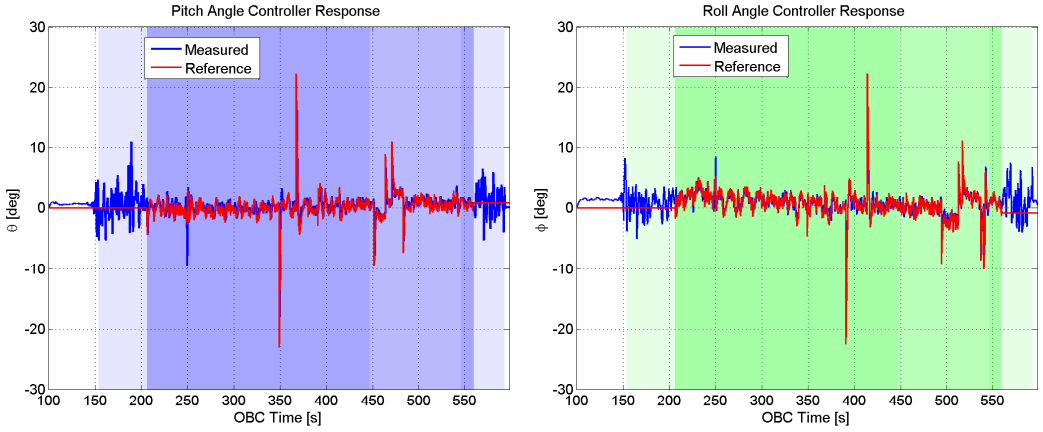

(a) Pitch Angle Controller (b) Roll Angle Controller

Figure 9.6: Pitch and Roll Angles

This concludes the presentation and analysis of the autonomous performance of the untethered aircraft. The final controllers were determined to perform satisfactorily, enabling the commencement of practical flight testing of the tethered system.

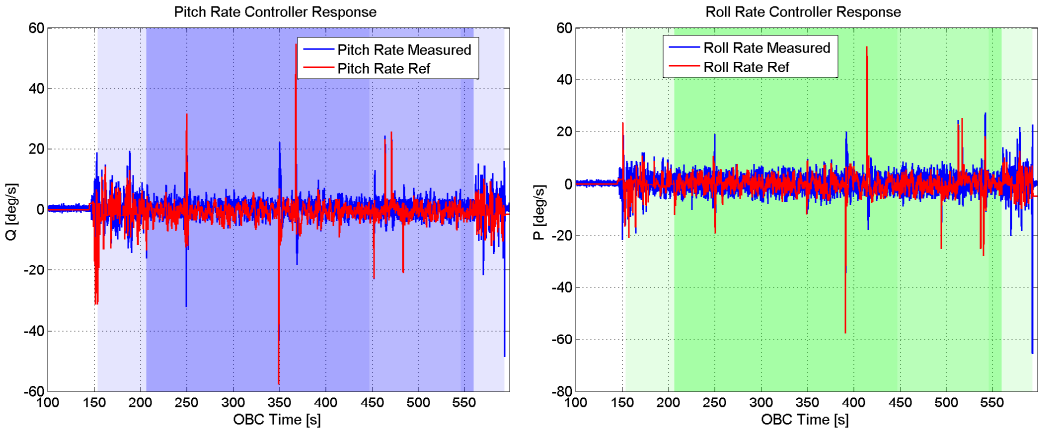

(a) Pitch Rate Controller (b) Roll Rate Controller

Figure 9.7: Pitch and Roll Rates

9.3 Tethered Flight Results

The tethered flight tests consisted of five individual flights. The first was conducted under a 'loose' tether configuration using the unmodified control system. This served primarily as a precautionary safety flight. Thereafter, four further flight tests were conducted under the 'taut' tether configuration using the modified control system; each with subtle differences in the tether configurations. More specifically, the four alternative tether configurations tested were:

(a) 25 m tether length, vertical case ($L \approx 0$).

(b) 25 m tether length, offset case ($L \approx 6\,\text{m}$).

(c) 15 m tether length, vertical case ($L \approx 0$).

(d) 15 m tether length, offset case ($L \approx 6\,\text{m}$).

The tests served to simultaneously validate the tethered control strategy and to illustrate the characteristics unique to each of the tether configurations. The results, however, are largely similar, with each successfully validating the tethered flight control strategy. In order to avoid repetition, the full results from Test 1 ($L_T = 25\,\text{m}, L \approx 0$) are presented. Results from the remaining tests are presented more specifically, highlighting notable differences in the system response for variations in the tether configuration.

(a) Test 1: $L_T = 25\,\text{m}, L \approx 0$

(b) Test 2: $L_T = 25\,\text{m}, L \approx 6\,\text{m}$

(c) Test 3: $L_T = 15\,\text{m}, L \approx 0$

(d) Test 4: $L_T = 15\,\text{m}, L \approx 6\,\text{m}$

9.3.1 General Performance

Test 1 was conducted at HRF, in good weather conditions with little to no wind. The test commenced with the aircraft manually piloted from take-off to an altitude of approximately 8 m, at which point the autonomous control system was fully enabled. With the controllers armed, the aircraft was given an altitude step prior to manoeuvring it into position above the ground-based tether mounting point. The tether mounting point consisted of a weighted stand, which resulted in the final mounting position being elevated off the ground by approximately 0.5 m. As a result, the aircraft take-off point was offset from the mounting point by a pre-determined horizontal distance. This required repositioning the aircraft prior to tension mode being armed. The initial altitude step was given as a precautionary measure to reduce the risk of the tether entangling in the mounting stand.

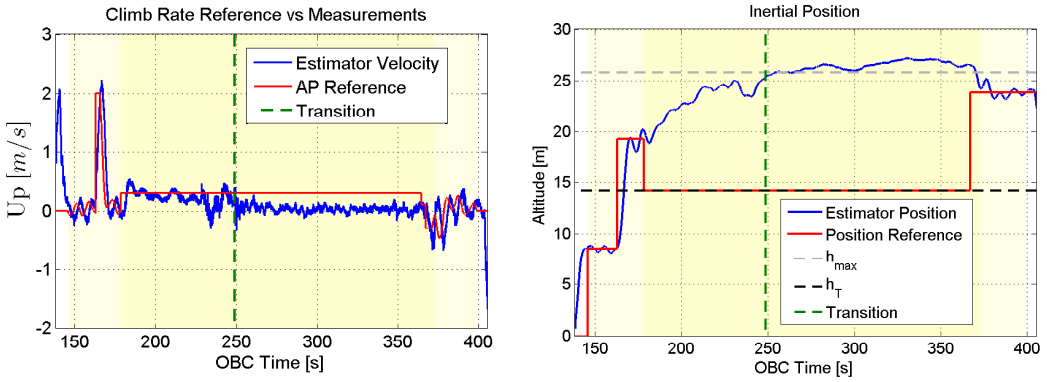

(a) Test 1: Climb Rate Response

(b) Test 1: Altitude Response

Figure 9.9: Heave Response

After the aircraft had been successfully positioned above the mounting point, tension mode was armed and the aircraft proceeded to climb into the taut tether configuration. Figure 9.9a illustrates the aircraft's climb rate response for the duration of the autonomous flight. The lightly shaded areas in the figures illustrate when the autonomous control system was active, while the darker shaded area indicates when tension mode was armed. The aircraft tracked the climb rate reference reasonably well, that is, until roughly 20 seconds prior ($t \approx 230$ s) to the transition point, where the aircraft's progress was momentarily halted. This point coincided with the tether being completely elevated for the first time and proved to be a general feature for each of the flight tests. The sudden elevation of the tether results in a fluctuation in the tension force due to the swinging action of the tether as it settles in a new suspended equilibrium. This is also thought to contribute to the mildly oscillatory climb rate response. Prior to take-off the tether is dispersed over a wide area to prevent entanglement. Thus, as the aircraft ascends the tether is continually settling in a new positional equilibrium. Prior to full elevation, these movements are mitigated by the shorter tether lengths and the frictional resistance with the ground; but they reach somewhat of a crescendo upon complete elevation due to the increased inertia

and lack of damping. This did not have a significant effect on the stability of the aircraft and is almost unidentifiable in the aircraft's angular dynamics. Nevertheless, the climb rate response recovered quickly with the aircraft entering the transition point soon afterwards, near the commanded climb rate of 0.3 m/s.

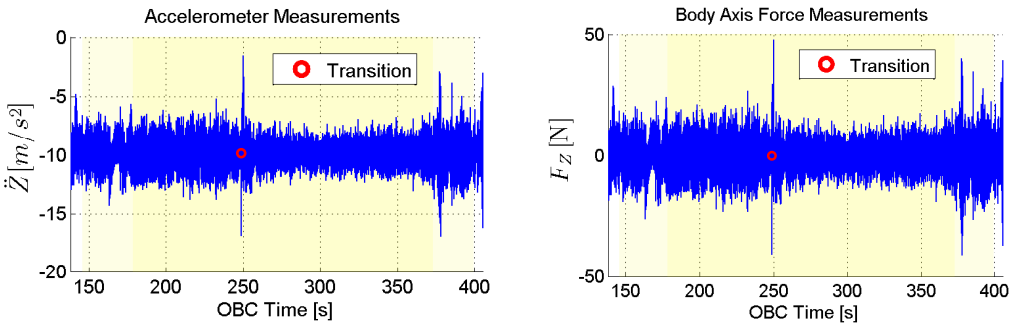

(a) Test 1: Accelerometer Measurements (b) Test 1: Estimated Impact Force

Figure 9.10: Impact Forces

The moment of transition is clearly illustrated through the z_B axis accelerometer measurements in Figure 9.10a, which contain a definite spike near $t \approx 250$ s. These measurements can be converted into a force estimate using Newton's law. These force estimates are illustrated in Figure 9.10b, after compensating for gravity and the aircraft orientation. The result is an estimated impact force of $F_Z \approx 48$ N, which is slightly lower than the 62 N force predicted by the snap loading approximation in Appendix A.2, but this is based on the assumption that the tether is perfectly vertical and that the initial impact velocity is precisely 0.3 m/s.

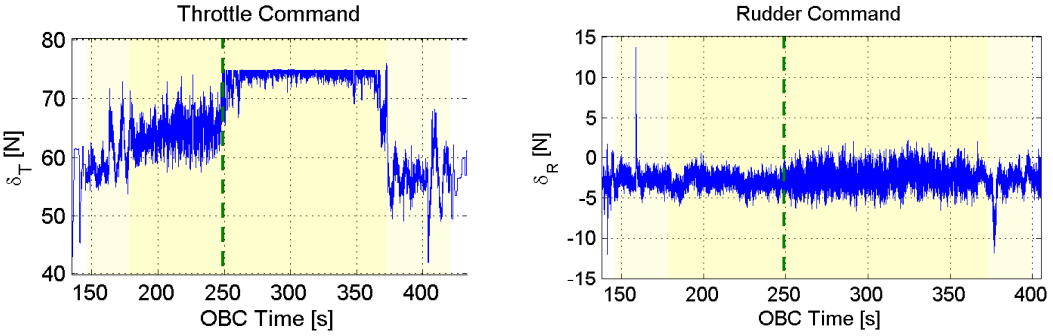

(a) Test 1: Throttle Commands (b) Test 1: Rudder Commands

Figure 9.11: Actuator Commands

Similarly definitive is the change in thrust command output through the transition point, as illustrated per Figure 9.11a. The thrust output settles at the saturation limit ≈ 15 s after the initial transition impact. The discrepancy relative to the HIL simulation is due to the reduced thrust buffer force employed during the practical test and unmodelled additional tether damping that results from the tether's flex

characteristics. This contributes to a marginally improved performance through the transition point with only a minor transient in the climb rate response, and none whatsoever in the altitude response. It is worth reiterating at this point that the steady state altitude measurements are largely meaningless. Figure 9.9b illustrates this fact as the measurements quickly drift past the maximum theoretical altitude limit. However, because the estimator measurements feature accelerometer propagation they are useful when analysing sudden events such as the loose to taut transition impact.

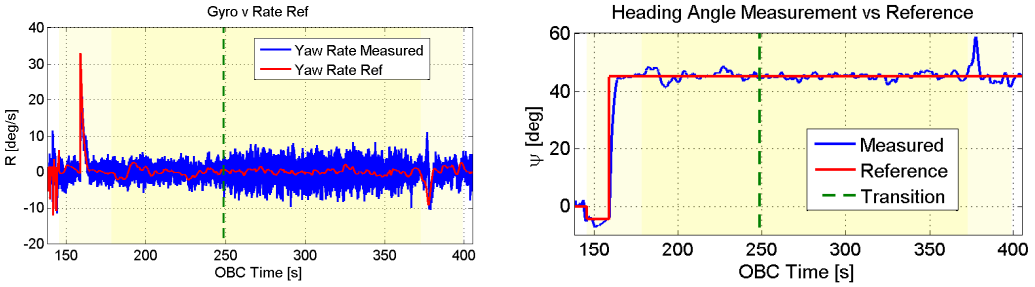

(a) Test 1: Yaw Rate Response

(b) Test 1: Heading Angle Response

Figure 9.12: Directional Response

Soon after the transition point the climb rate measurement settles around zero for the remainder of the taut tethered flight, without any deviations of significance. During this period the aircraft experiences subtle improvements in it's autonomous performance, relative to the loose tether configuration. The first of which is a definite reduction in the noise levels present in the accelerometer measurements from Figure 9.10a. This is due to the nature of the saturated thrust output which is no longer responsive to noise in the accelerometer measurements, culminating in a smoother response. Contrastingly, there is a pronounced increase in the rudder command outputs from Figure 9.11b. While the tether does not explicitly influence the yaw dynamic mode, the total thrust increase (and subsequently the increase in the rotational speed of the rotors) contributes to an increase in the aerodynamic drag forces acting on the rotors which serve as the control mechanism for the aircraft in yaw. This effectively results in an increase in the virtual yaw moment arm[3] which improves the control bandwidth. This, in turn, contributes to the amplification of noise in the gyroscope measurements as is evident from Figure 9.12a; but also results in a marginal improvement in the performance of the heading angle controller, as is visible from Figure 9.12b.

From Figures 9.13a and 9.13b, it is clear that the elevator control commands experience a similar increase in agitation immediately after the transition point, while the aileron commands remain largely unchanged. This is due to the positional feedback property of the tether, and indicates that the aircraft was not directly above the mounting point prior to the loose to taut transition. The GPS coordinates of

[3]This was originally determined in Chapter 3.3.4 around the hover thrust set-point

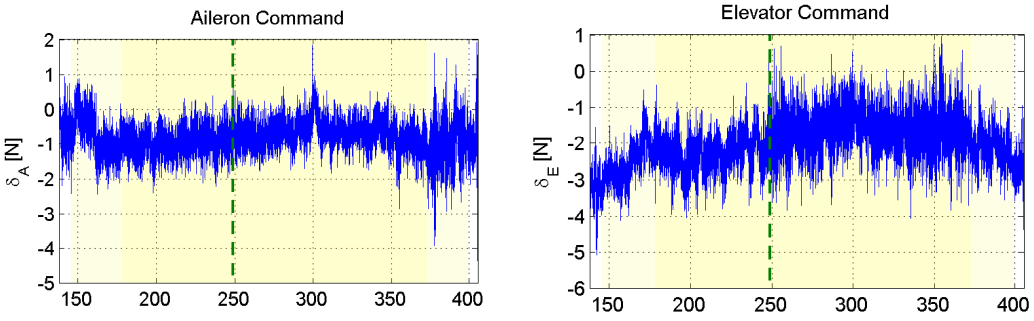

(a) Test 1: Aileron Commands

(b) Test 1: Elevator Commands

Figure 9.13: Actuator Commands

the mounting point are stored prior to take-off which leaves the relative distance between the aircraft and the mounting point susceptible to measurement drift for the duration of the flight. This is evident from the horizontal inertial position measurements in Figures 9.14a and 9.14b. The North position measurement specifically, experiences a sudden 1 m offset from the commanded value at the point of transition as the tension in the tether increases. This is consistent with the pitch and roll angle measurements from Figures 9.15a and 9.15b, which illustrates the aircraft settling into a new trim state in order to track the commanded horizontal position references. These trim states constantly adapt during flight as the aircraft is subjected to horizontal position steps. The pitch angle trim state experiences a greater net change during the course of the taut tethered flight, which is congruous with the noisier elevator commands.

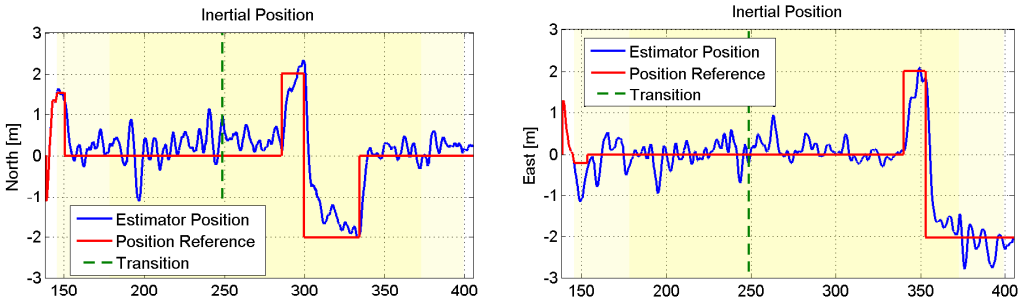

(a) Test 1: Position Step Response (N)

(b) Test 1: Position Step Response (E)

Figure 9.14: Horizontal Position Response

Overall, the introduction of the tether has a negative impact on the aircraft's ability to track changes in the inertial position references; with the effects becoming more pervasive with an increase in the tether length. This is understandable considering the additional tether mass, inertia and tension forces acting on the aircraft, that were neglected during the controller design. Under the loose tether configuration the tether has a similarly adverse influence on the aircraft's longitudinal and lateral

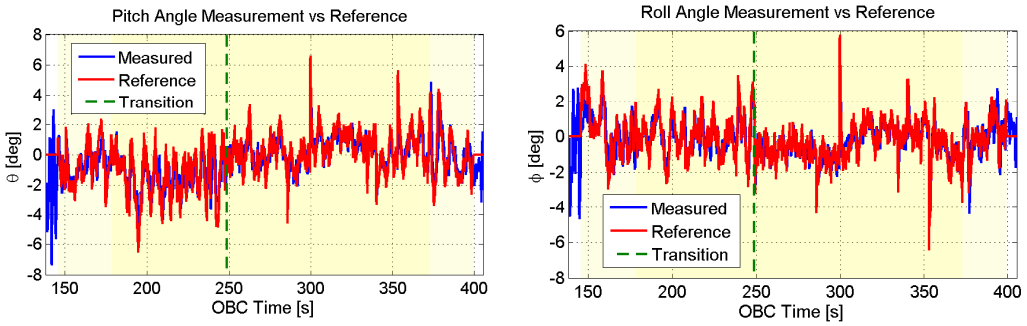

(a) Test 1: Pitch Angle Response

(b) Test 1: Roll Angle Response

Figure 9.15: Pitch and Roll Angles

angular dynamics, resulting in a more oscillatory response relative to the untethered aircraft. Under the taut tether configuration, however, the performance varies between the various testing scenarios. For the scenario presented in Test 1, the taut tether configuration contributes to an improved performance in pitch and roll, as is evidenced by Figures 9.15a and 9.15b. These effects are discussed in more detail in Chapter 9.3.2 below. The position tracking response results correlate well with those observed HIL. A slight increase in the oscillatory nature of the steady state tracking response is observed as a result of the increased vibration levels which were not adequately modelled in HIL. This exacerbates the effects of angular random walk. Notice that these effects are reduced somewhat under the taut tether configuration as a result of the subsequent angular stability benefits.

A final safety feature, not previously discussed during the design of the control system, is a change in the altitude reference command prior to the tether being released. This is done to reduce the tension force in the tether and minimise the resulting disturbance on the aircraft that accompanies the tether release. The new altitude reference is commandable from the ground station and set to a small distance below (2 m in this case) the current altitude measurement. The climb rate saturation limits are configured to simultaneously reset to their original pre-tension values to enable the negative altitude step. Following the altitude step, the tether is promptly released to prevent any tether entanglement. The resulting transient (at $t \approx 370\,\mathrm{s}$) is clear in each of the above figures, but particularly in the climb rate and altitude responses. The high bandwidth of the NSA controller results in a rapid throttle response and ensures that the sudden acceleration is effectively countered. Once the release transient had diminished and the aircraft had shown to be stable, manual flight mode was enabled with the pilot then bringing the aircraft in to land.

9.3.2 Influence of the Tether Length and Span

The general performance of the control strategy is well represented by the results presented above. The remaining flight tests serve to illustrate how variations in the tether length and span influenced the system response. For the four alternative

tether configurations practically tested, notable variations were observed in the trim states, impact events, the aircraft stability and the aircraft mobility.

Trim States

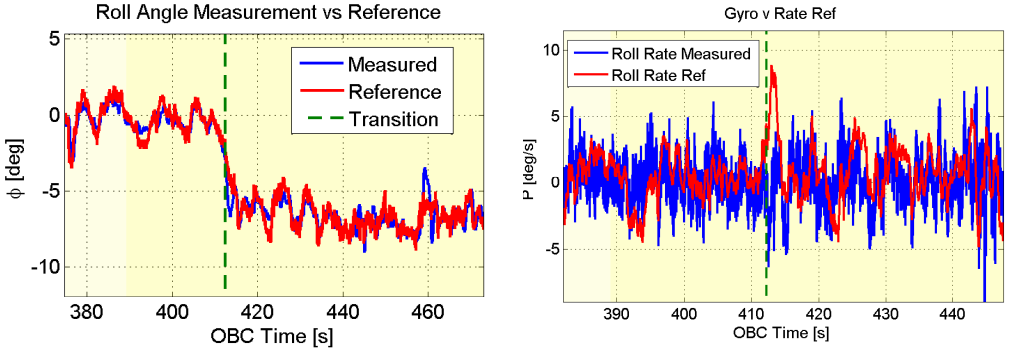

(a) Test 4: Roll Angle Response

(b) Test 4: Roll Rate Response

Figure 9.16: Variation in the angular trim state for the offset case.

A significant change in the angular trim state of the vehicle is required when operating at increased span distances, in order to counter the horizontal force component of the tether weight. This is clearly illustrated through the roll angle and rate responses from Test 4, as shown in Figures 9.16a and 9.16b. The aircraft experiences a significant change in the steady state roll angle, with an accompanying disturbance in the roll rate response, as the tension force increases through the transition point. The angular rate disturbance is a result of the tether mounting point being offset from the vehicle CoM, subsequently resulting in an induced tether moment. The integral control action in the innermost angular rate controllers counteracts the tether moment in the steady state, and assists the vehicle in maintaining the non-zero angular trim state with good accuracy. Figures 9.17a and 9.17b illustrate the changes in the virtual aileron and elevator control commands required to maintain the offset equilibrium position. The non-zero commanded values prior to the transition point are the result of discrepancies in the actuator performance and/or mounting

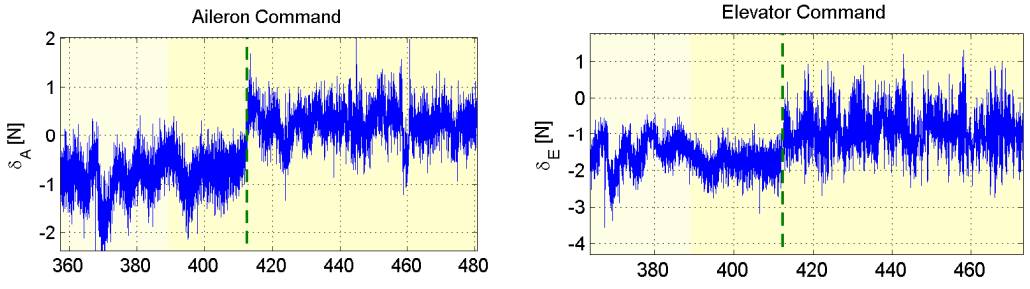

(a) Test 4: Aileron Commands

(b) Test 4: Elevator Commands

Figure 9.17: Actuator Commands

positions and illustrate the need for integral control action in the innermost control loops.

Impact Events

The dominant feature of the offset flight case is the moderation of both the frequency and severity of the tether impact events by means of exploiting the catenary effect. This serves as the primary justification for operating at non-zero span distances, which is otherwise less efficient. The catenary effect minimises the severity of transition impact events by reducing the tension force gradients between the loose and taut tether configurations. This ensures that the aircraft's kinetic energy is reduced prior to the full extension of the tether. This feature is evident when comparing the climb rate responses near the transition point for Tests 3 and 4, in Figures 9.18a and 9.18b respectively. For the vertical tether case the aircraft experiences a sudden change in climb rate through the transition point which causes large impact force at the tether attachment point. For the offset case the change is significantly more gradual. Figure 9.19b indicates the estimated impact forces for Test 4. The acceleration spike at the initial transition point is indistinguishable from general flight, while the spike at $\hat{v}_D \approx 0$ is only marginally larger and correlates with an estimated impact force of 17 N.

For the offset case the transition point is defined as the point at which the tether is first fully elevated off the ground. This is in contrast to the vertical tether case where the transition point is defined as the point where the climb rate is limited to zero. This is done in agreement with the saturation of the throttle command and the transition to the new angular trim state, as illustrated in Figures 9.20b and 9.16a respectively.

Under the taut tether configuration the aircraft experiences differentiating dynamic behaviour in heave for the vertical and offset cases. This is best illustrated by the enlarged climb rate responses in Figures 9.18a and 9.18b. The offset case features

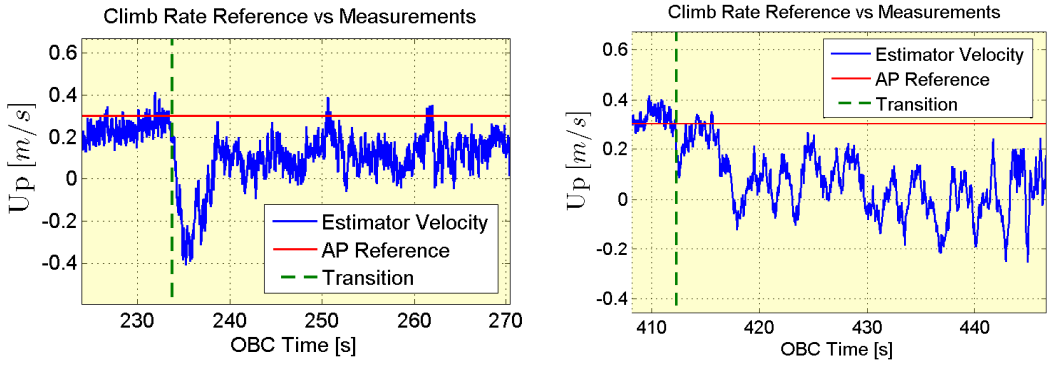

(a) Test 3: Climb Rate Response

(b) Test 4: Climb Rate Response

Figure 9.18: Effect of Tether Span on Transition Velocity

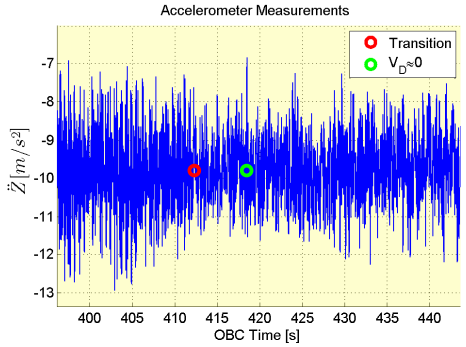

(a) Test 4: Accelerometer Measurements

(b) Test 4: Estimated Impact Force

Figure 9.19: Influence of the tether span on the transition forces.

a lower frequency and more oscillatory climb rate response relative to the vertical tether case. This indicates an almost 'elastic' behaviour which is less sensitive to fluctuations in the tether tension. The increased sensitivity of the vertical case contributes to the erratic throttle actuation requirements illustrated in Figure 9.20a. An additional contributing factor is the reduced operational altitude band[4] that accompanies a reduction in the span distance. This yields the vehicle more susceptible to transition events for small losses in altitude. These effects compound one another, and result in the volatile performance in heave for Test 3, as is further evidenced by the extended climb rate response in Figure 9.21a. This response differs substantially from the climb rate response observed during Test 1 in Figure 9.9a. The discrepancy in performance is due to a combination of two factors; namely, the longer tether length employed and the choice of thrust force buffer, $\Delta\delta_{T_{buf}}$. The thrust force buffer is the additional thrust allocation over and above the vehicle and tether weight. It is implemented to counteract unmodelled disturbances such as aerodynamic drag and any flexural rigidity in the tether. The buffer was set at constant value of $\Delta\delta_{T_{buf}} = 5\,\text{N}$ for the duration of the practical flight tests. This resulted in a larger tension force, relative to the tether weight and disturbance forces,

[4]The operational altitude band was previously discussed in Chapter 6.3.2.

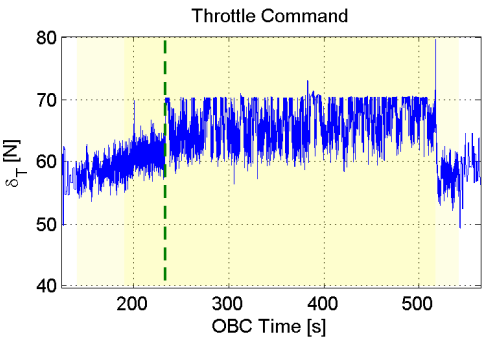

(a) Test 3: Throttle Commands

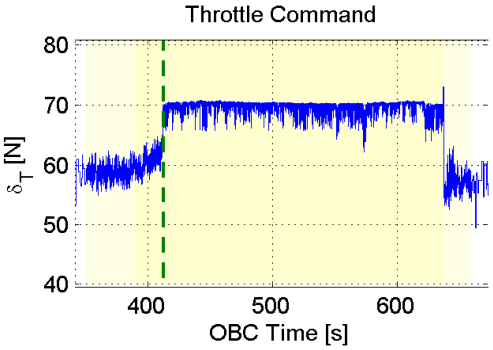

(b) Test 4: Throttle Commands

Figure 9.20: Actuator Commands

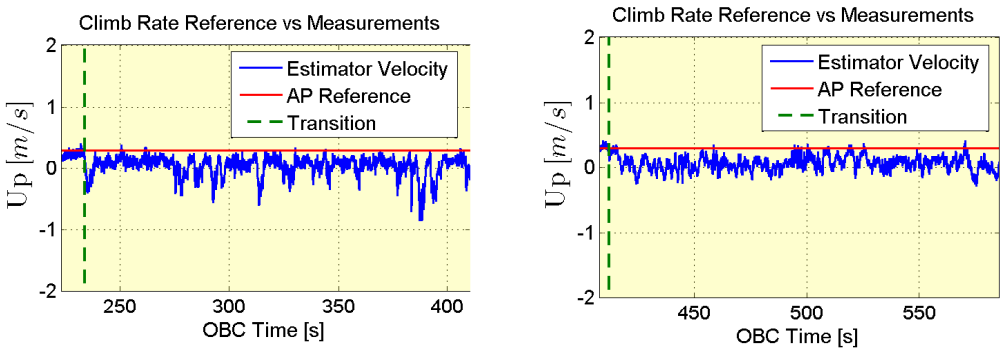

(a) Test 3: Climb Rate Response

(b) Test 4: Climb Rate Response

Figure 9.21: Frequency of Impact Events

for the shorter tether length. The tether tension[5] forces originate at the tether mounting point due to the constraining action of the tether, and are transmitted to the aircraft along the cable length. Thus, the tether acts as a filter with fluctuations in the tension force better attenuated by the longer tether length. This is due to the tether's mechanisms of energy dissipation; which consist of, internal friction and strain energy in the tether, kinetic energy of the tether and aerodynamic drag in the surrounding fluid. At lower tension values a larger proportion of the total energy is dissipated as kinetic energy and aerodynamic drag. While at higher tension values lateral movement of the tether is constrained by the larger restoring forces. This results in a greater proportion of the total energy dissipated as elastic strain energy through the elastic deformation of the tether. This leaves the aircraft more sensitive to fluctuations in the tether force vector and ultimately degrades the autonomous performance.

Stability

The aircraft's longitudinal and lateral angular dynamic modes serve as the most prominent failure mode for the quadrotor UAV; with attitude stabilisation forming the bedrock of the autonomous control system. This is a characteristic of the quadrotor design with the longitudinal, lateral and heave translational dynamic modes inextricably intertwined with the aircraft's angular dynamics. Thus, we evaluate the stability of the aircraft in terms of it's attitude stabilisation performance, specifically in pitch and roll.

Table 9.1 provides an indication of the attitude tracking performance observed during the practical flight tests. Measurements were taken over a 30 s window whilst the aircraft was in a static hover state, and are rounded to the nearest 0.5°. Overall the measurements correlated extremely well for the untethered flight condition, with Test 4 being the only notable exception. Test 4 was conducted in blustery conditions

[5]For the purposes of this discussion the **tension force** represents the additional force in the tether over and above the tether weight and any additional disturbance forces.

Table 9.1: Pitch and Roll Angle Tracking Performance.

Config.		Loose	Taut	Free
Test 1	$\leq$	5°	2.5°	3°
Test 2	$\leq$	11°	8°	5°
Test 3	$\leq$	3.5°	5°	3°
Test 4	$\leq$	3°	4°	3°
Loose (10m)	$\leq$	3.5°	-	-
Loose (20m)	$\leq$	5°	-	-
Untethered	$\leq$	-	-	3°

with an mean wind speed of 3 m/s and intermittent gusts up to 5 m/s. Oscillations in the angle measurements are generally the result of variations in the magnitude and direction of the tether force vector, aerodynamic disturbances and measurement errors in the gyroscope which manifest as angular random walk.

Under the loose tether configuration a general degradation in the attitude stabilisation performance of the aircraft was observed, with these effects becoming more prominent with an increase in the tether length. This is congruous with the stability analysis conducted in Chapter 6.4.2, which indicated an increasingly oscillatory response for an increase in the tether force. Intuitively one would expect this to be the case as larger disturbance forces and moments accompany an increase in the tether force, which results in a more pronounced effect on the aircraft dynamics.

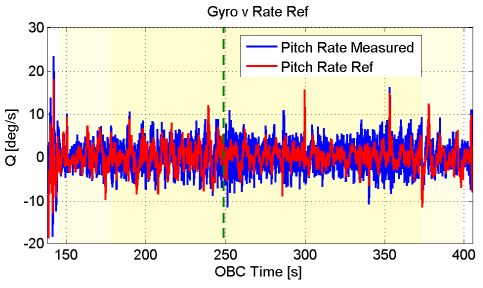

(a) Test 1: Pitch Rate Response

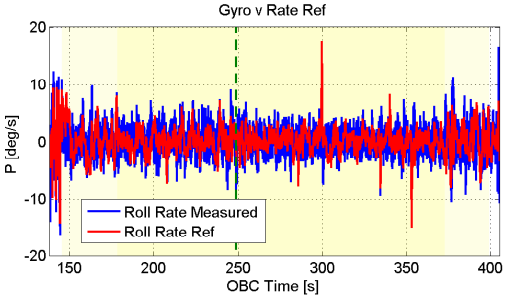

(b) Test 1: Roll Rate Response

Figure 9.22: Test 1: Pitch and Roll Rates

Under the taut tether configuration the performance varied between the two tether lengths tested, as well as between the offset and vertical test cases, although to a lesser degree. For the longer tether lengths employed during Tests 1 and 2, the taut tether configuration contributed to an improved performance in pitch and roll,

relative to the loose tether configuration. This is clear from the pitch and roll angle controller responses from Test 1, previously shown in Figures 9.15a and 9.15b, which are palpably smoother under the taut tether condition. The pitch and roll rate responses in Figures 9.22a and 9.22b display a similar improvement, particularly in the controller reference commands, although this is less clear from the angular rate feedback measurements due the high noise levels present. The improvement in attitude stabilisation under the taut tether condition is attributable to the positional feedback property of the tether which provides a restoring force that counters perturbations in the aircraft's translational dynamics, and further serves to reduce the variability in the orientation of the tether force vector.

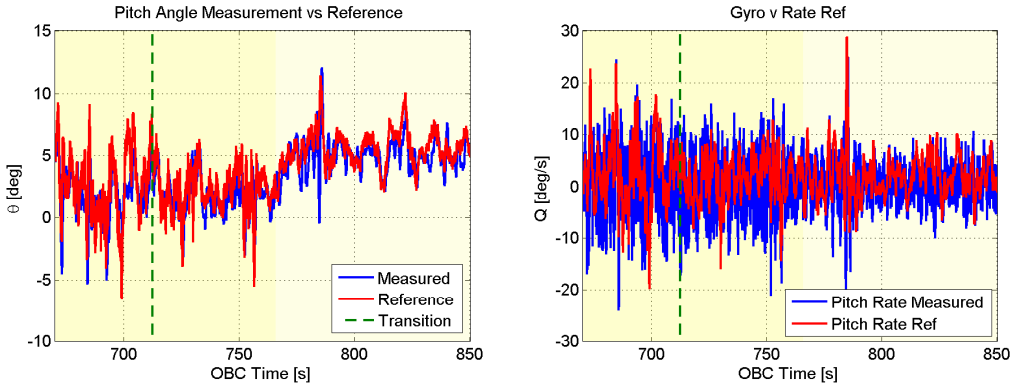

(a) Test 2: Pitch Angle Response

(b) Test 2: Pitch Rate Response

Figure 9.23: Test 2: Longitudinal Angular Dynamic Response

In Test 2 the aircraft exhibits a similarly improved performance under the taut tether configuration relative to the loose tether configuration. Although in this instance both tether configurations result in a degraded performance relative to the untethered aircraft. The longitudinal angular dynamic response data from Test 2 are significantly noisier due to the windy conditions. The additional aerodynamic drag acting on the aircraft is evident from the pitch angle response in Figure 9.23a which required a positive pitch angle of roughly 5° in order for the aircraft to maintain it's horizontal position after the tether was released. By aligning the aircraft downwind from the mounting point the aerodynamic drag force could be countered using the horizontal component of the tether weight. Whether this resulted in any efficiency benefits is inconclusive. The degraded performance under the taut tether configuration, relative to the untethered aircraft, is likely due to the increased sensitivity of the angular dynamics to fluctuations in the tether force at increased span distances where the horizontal tether force component is larger.

In contrast to the results from Tests 1 and 2, the shorter tether lengths employed in Tests 3 and 4 contributed to a degraded performance in attitude under the taut tether configuration, relative to both the loose and untethered configurations. The atmospheric conditions during Tests 1, 3 and 4 were highly favourable with very

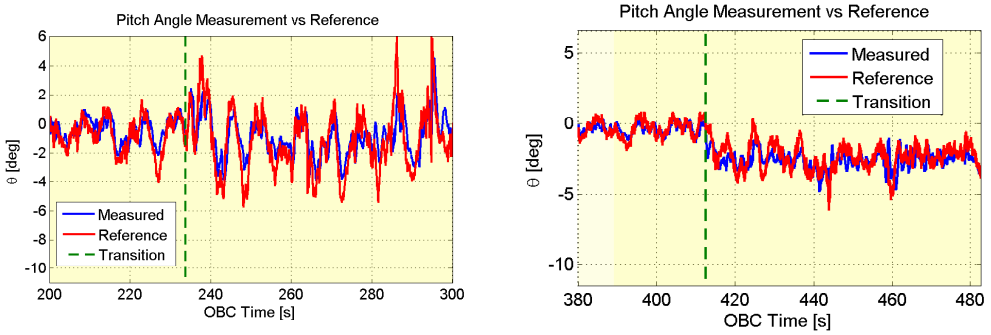

(a) Test 3: Pitch Angle Response

(b) Test 4: Pitch Angle Response

Figure 9.24: Tests 3 and 4: Pitch Angle Responses

little wind, which aids comparisons between the flight data. From the pitch angle and angular rate response comparisons in Figures 9.24 and 9.25 it is clear that the vertical case performance from Test 3 is noticeably degraded relative to the offset case from Test 4; while both test cases exhibit a reduction in performance relative to their respective loose tether configurations. The general reduction in performance for the shorter tether length is due to the higher tension values relative to the tether weight and disturbance forces. At higher tension values the tether dynamics become increasingly dominant with the system dynamics eventually resembling that of an inverted pendulum when the tether force is much greater than the tether weight $F_T \gg w_T$. This increases the degree of coupling between the translational and rotational dynamic modes. This feature is emphasised by the discrepancy in performance between the vertical and offset cases, as the additional tension forces are reduced with an increase in the horizontal span distance.

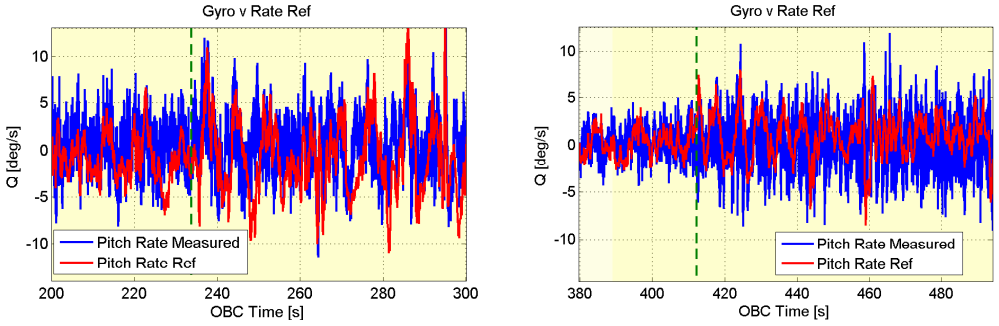

(a) Test 3: Pitch Rate Response

(b) Test 4: Pitch Rate Response

Figure 9.25: Tests 3 and 4: Pitch Rate Responses

Finally, the performance under the loose tether configuration was also observed to differ between the two cases. A marginal improvement in performance was observed for the offset case (at the final span distance) due to the frictional forces between the tether and the ground, which provide similar positional feedback benefits to the taut tether configuration at lower tension values. This was not observed for the

offset case of the longer tether length in Test 2, where the frictional forces near the transition point were smaller relative to the total tether mass and disturbance forces.

Mobility

As one would expect, the addition of the tether has a negative impact on the mobility of the aircraft relative to the untethered case. From a static perspective, the steady state tracking benefits realised due to the position feedback property of the tether are less evident, relative to Test 1. This is due to the reduced angular stability benefit for the shorter tether lengths, which no longer counteracts the effects of angular random walk. Similar to Test 1, the extra mass associated with the tether effectively lowers the bandwidth of position controllers. This translates into a slower response. Although these effects are reduced for the shorter tether lengths, as is evident by comparing the horizontal step response plots from Test 1 (in Figures 9.14a and 9.14b) with those of Tests 3 and 4 in Figures 9.26a and 9.26b.

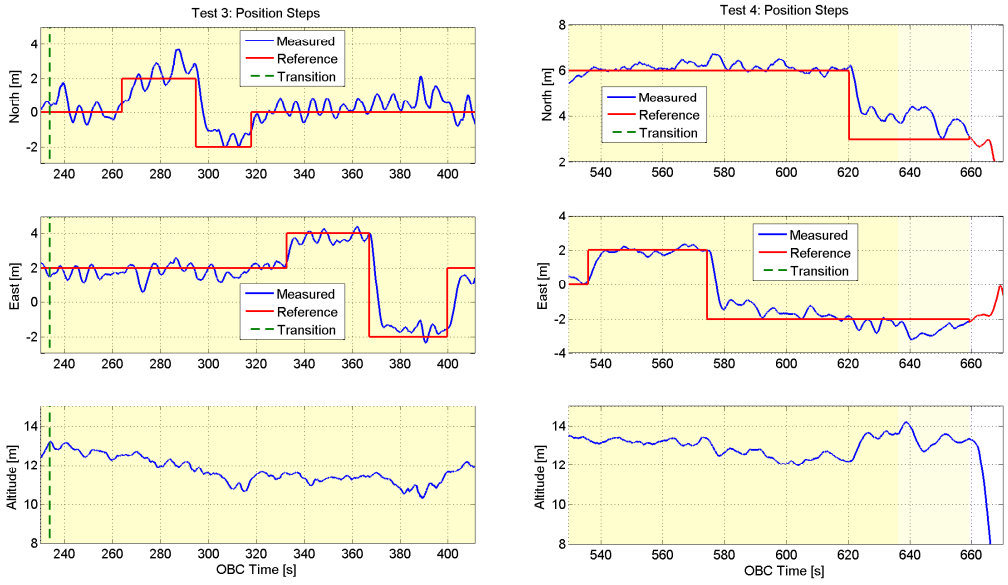

(a) Test 3: Position Step Response

(b) Test 4: Position Step Response

Figure 9.26: Horizontal Position Step Response

Apart from the reduced position tracking performance, the horizontal position steps further serve to illustrate the coupling between the vertical and horizontal inertial position states, brought about by the constraining action of the tether. This is also evident from the inertial position plots from Test 1, although to a lesser extent due to the commanded position step distances, which are smaller relative to the total tether length. The smoother altitude responses also illustrate the improved damping

of the tether forces from Tests 1 and 4 relative to the more disjointed response from Test 3.

9.3.3 Conclusion

Overall the practical flight tests successfully validated the autonomous flight control strategy; ratifying the open-loop control strategy in heave and illustrating that the constraining action of the tether can be exploited to provide an effective means of altitude feedback. The PID control architecture was shown to be capable of successfully stabilising the aircraft, thereby validating the assumption that the tether may be treated as a disturbance for general flight at longer tether lengths.

The control strategy proved to be highly effective for the longer tether length tested and required very little optimisation. For shorter tether lengths there remains room for potential control optimisation to improve the performance in heave for the vertical tether case. Alternatively, the offset case was shown to offer a simple means of improving the autonomous performance without the need for more complicated control optimisation. It should be noted that the test results and the inferences drawn are based on general flight in mild atmospheric conditions, where lower tension values were shown to be adequate. Higher tension values may be desirable during take-off and landing or in the presence of strong winds. Such pursuits would stand the risk of altering the fundamental behaviour and would likely require dedicated control solutions.

Chapter 10

Conclusion and Recommendations

10.1 Conclusion

Persistent aerial platforms, and the benefits that come with an increase in horizon, have historically been the boon of the military and similarly resource-rich institutions. This is predominantly a reflection of the current technology, as the industry is serviced almost exclusively by tethered aerostat systems. These systems are capital intensive, in addition to being prohibitorily cumbersome and impractical. The recent emergence of the quadrotor, as a simple and cost-effective UAV platform, has led to it's implementation in an ever-increasing range of civilian applications. However, current battery technology currently limits the utility of such systems to short flight times and small payload capabilities. A tethered multirotor solution offers the possibility of continuous power transmission, enabling indefinite flight times and improved payload capabilities for low to medium altitude applications. It does this with significant mobility and deployability benefits relative to current aerostat systems.

This project presented the design, modelling, control and successful demonstration of a tethered multirotor UAV system; as a first iteration towards an alternative, and more accessible, persistent aerial platform. The project focussed specifically on the development of appropriate modelling and flight control strategies, in addition to the development of a suitable practical testing platform. The tether model was developed based on the quasi-static catenary assumption, which proved to sufficiently encapsulate the dominant tether forces in order to validate the autonomous flight control strategy. The control system was developed and successfully demonstrated on the untethered aircraft before being adapted for the tethered case. Modifications to the controller were catered towards tethered flight with a minimalist sensor configuration; and aimed to be adaptable for future implementation with a suitable

winch system. The system offers a novel and pragmatic approach to the tethered flight problem that was demonstrated to be effective in practice.

A key outcome of the project includes the ratification of the multirotor platform for the tethered application. The multirotor layout proved to be notably robust to disturbances from the tether in the aircraft's dominant failure modes of pitch and roll. This was primarily due to the well actuated nature of the aircraft in the pitch and roll dynamic modes, which simplified the control challenge. The PID control architecture proved similarly suitable and robust to model uncertainty.

Practical flight tests demonstrated the control strategy to be both feasible and effective for tether lengths up to 25 m; simultaneously validating the assumption that the tether may be treated as a disturbance for general flight at low tension values relative to the tether weight. The loose tether configuration was found to have a detrimental effect on both the aircraft stability and positional dynamics, with these effects exacerbated with an increase in the tether length. The taut tether configuration was found to have a similar detrimental effect on the aircraft's positional dynamics, while it's influence on the aircraft stability varied between the test cases. A noticeable improvement in stability was observed for the vertical tether case at low tension values, while at higher tension values a degradation in the aircraft stability was observed. This is attributable to the change in the fundamental system dynamics at higher tension values.

10.2 Recommendations

1. The practical flight tests were generally limited to mild atmospheric conditions, which limits the comprehensiveness of the results. Similarly, the tether simulation model currently neglects the effects of aerodynamic drag. These effects are expected to become more significant for higher altitude applications. Additional testing is required to validate these results at higher altitudes and in the presence of stronger winds.

2. The quadrotor design proved to be a robust platform for the tethered application, and suitable as a research prototype. However, a final working product would likely benefit from the component redundancy afforded by the hex- and octocopter configurations. This would mitigate against the risk of failures in persistent flight applications.

3. There remains room for potential control optimisation for the vertical tether case at shorter tether lengths. The current strategy was found to be vulnerable to disturbances, particularly during horizontal position steps. The control strategy can be optimised to reduce the resulting altitude loss during horizontal movements. This can be easily improved somewhat by increasing the filter frequency of the NSA saturation limit to correlate with the pitch and roll angle controller bandwidths. Thereafter, additional feed-forward control action can be investigated as required.

4. The high noise levels present in the IMU measurements, as induced by the vibration associated with the spinning rotor blades, are not currently adequately modelled in HIL. This exacerbates the effects of angular random walk which has a pervasive effect on the aircraft dynamics. Improved efforts are required to better isolate sensitive sensor equipment from these effects; as well as to ensure these effects are accurately modelled as they proved to be more significant than initially thought.

5. The GPS measurement in climb rate proved to be particularly prone to time delays, which limited the aircraft's dynamic performance in heave. This was not especially problematic considering the limited flight envelope but there maintains scope for improvement; either through an alternative sensor choice or by optimising the kinetic state estimator.

6. While the current project aimed to minimise the requirement for additional sensor equipment, greater automation can be achieved with feedback of the tension forces at the origin. These forces may be inferred, relatively cost-effectively, by measuring the current draw to the motor of an appropriate winch system.

7. Considering that an additional student is currently developing a winch system and extending the control system to include tethered landings; a logical next step would be the development of an optimal tether design and power transmission strategy, in order to realise the final goal of persistent autonomous flight.

Appendix A

Mechanical Analyses

A.1 Servo Torque Capability

A safety factor for the release servo torque capability is determined based on the maximum steady-state tether force vector that the vehicle is capable of supporting in hover. The torque required by the servo to release the tether is equivalent to the product of the servo moment arm and the frictional force between the release pin and the attachment bracket. This frictional force is, in turn, proportional to the tether force vector at the vehicle attachment point and the material friction coefficients.

The maximum static loading condition on the tether release pin is inherently limited by the total available vertical thrust output. Furthermore, the maximum vehicle thrust command $\delta_{T_{max}}$ is limited to 75% of the total available thrust in order to preserve control bandwidth for attitude stabilisation. Thus, the maximum frictional force between the release pin and attachment bracket under a worst-case static loading condition is determined by Equation A.1.

$$F_f = \mu_s \frac{\delta_{T_{max}}}{g} \text{ [kg]} \tag{A.1}$$

where, μ_s is the static friction coefficient between aluminium and mild steel provided in Table A.1.

The servo employed is a JR NES 591 servo with a torque rating of 5.11 kg cm. The safety factor for the release servo can subsequently be determined by Equation A.2 as,

$$SF_s = \frac{5.11/r_s}{F_f} \approx 1.25 \tag{A.2}$$

where, r_s is the servo moment arm in centimetres.

A.2 Snap Loading Forces

Snap loading arises as the aircraft causes the tether to suddenly transition from a loose to taut tether state. These transitions can generate significant short-duration impact forces at the tether attachment point. This analysis aims to quantify these force magnitudes for various vehicle velocities and tether lengths.

Accurate impact loading analyses are extremely complex and generally require comprehensive experimental testing in order to cater for typically unknown material nonlinearities [63]. This analysis makes a number of simplifying assumptions and is based on the conservation of energy principle. For this analysis we consider the simplified case illustrated by Figure A.1, of vertical aircraft motion with the tether perpendicular to the ground attachment point.

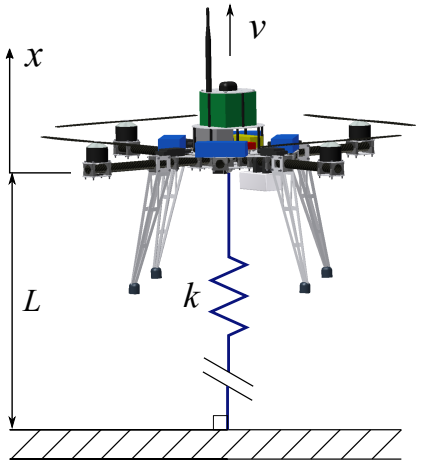

Figure A.1: Tether snap loading analysis.

The analysis assumes that the tether is perfectly elastic with the kinetic energy of the vehicle converted to strain energy within the tether, and potential energy proportional to the vehicle mass and tether deformation distance x. The tether is modelled as a single spring element with the damping and frictional tightening effects of the cable neglected, although the elastic modulus of the tether (determined in Chapter 3.3.6) does incorporate these effects to a degree. The impact force is then determined using Hooke's Law, neglecting the transient response and assuming that the cross-sectional area of the cable remains constant.

From the conservation of energy principle we can equate the total energy of the loose tether state with the aircraft moving freely at some velocity, v, to the taut tether

state of maximum tether deflection, x, and the system at rest $v = 0$.

$$\sum E_1 = \sum E_2 \tag{A.3}$$

$$\frac{1}{2}mv^2 = \frac{1}{2}kx^2 + mgx \tag{A.4}$$

where, m is the total aircraft mass.

The tether stiffness constant k is determined as,

$$k = \frac{AE}{L} \text{ [N/m]} \tag{A.5}$$

where, A and E are the cross-sectional area and elastic modulus of the tether respectively.

For a given tether length, L, and initial vehicle velocity, v, Equation A.4 can be solved quadratically for the maximum tether displacement x as,

$$x = \frac{-b + \sqrt{b^2 - 4ac}}{2a} \text{ [m]} \tag{A.6}$$

where,

$$a = \frac{k}{2} \tag{A.7}$$

$$b = mg \tag{A.8}$$

$$c = -\frac{1}{2}mv^2 \tag{A.9}$$

An estimate for the resulting impact force magnitude, F_i, can then be determined from Hooke's Law as,

$$F_i = kx \text{ [N]} \tag{A.10}$$

A.3 Structural Analysis of Critical Parts

The central vehicle hub, tether attachment and release mechanism pin are identified as critical parts as they are exposed to significant impact forces during flight. A basic structural assessment of these parts is conducted in order to identify any potential mechanical vulnerabilities. A safety factor against yielding is determined for each component, based on the simplified loading conditions illustrated in Figure A.2.

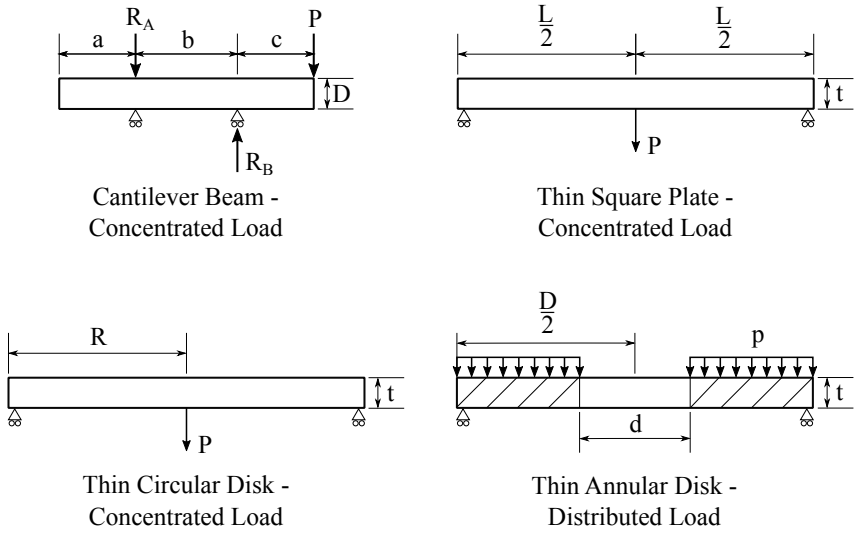

Figure A.2: Component loading and boundary conditions.

The tether release pin is at its most vulnerable immediately after the tether release is activated. The bending stress in the bar will be at a maximum when the furthest end of the pin becomes unsupported whilst still under load. In this scenario the pin experiences tensile and compressive stresses along the top and bottom surfaces respectively. The pin is modelled as a simply supported cantilever beam with a concentrated load P applied to the unsupported free-end. The maximum bending stress in the pin is determined as,

$$\sigma_{max} = \frac{My}{I} \text{ [Pa]} \tag{A.11}$$

where, M is the maximum bending moment in the beam, I is the moment of inertia of the pin and y is the distance to the furthest point on the pin from the horizontal neutral axis $y = \frac{D}{2}$.

The maximum bending moment in the beam occurs about the support B and can be computed as,

$$M = Pc \text{ [N m]} \tag{A.12}$$

Stresses in the tether attachment components and the vehicle hub are determined using the theory of thin plates with small deflections, based on work by Young

and Budynas [64]. The attachment bracket and plate are each modelled as a thin square plate and a thin circular disk respectively, while the vehicle hub interface is modelled as a thin annular disk, all with simply supported boundary conditions. The attachment bracket and plate loading conditions are approximated by concentrated loads applied on a small area with a radius, r_o, at the centre of the components, while the vehicle hub loading condition is approximated by a distributed load over the surface of the annular disk.

The maximum bending stress in the square attachment bracket is determined from Equation A.13 as,

$$\sigma_{max} = \frac{3P}{2\pi t^2}\left[(1+v)\ln\frac{2L}{\pi r_o} + 0.435\right] \text{ [Pa]} \tag{A.13}$$

where,

P	applied load force
v	material Poisson's ratio
r_o	radius of contact, $r_o = 0.5t$

The maximum bending moment in the circular attachment plate is determined from Equation A.14 as,

$$M_{max} = \frac{P}{4\pi}\left[(1+v)\ln\frac{R}{r_o} + 1\right] \text{ [N m]} \tag{A.14}$$

The bending moment in the vehicle hub is determined from Equation A.15 using an empirical coefficient, K_M, for annular disks with uniformly distributed loads.

$$M_{max} = \frac{1}{4}K_M p D^2 \text{ [N m]} \tag{A.15}$$

where,

$K_M = 0.3272$, and p is the applied load per unit area,

$$p = \frac{4P}{\pi\left(D^2 - d^2\right)} \frac{\text{N}}{\text{m}^2} \tag{A.16}$$

The maximum bending stress in the circular attachment plate and the annular vehicle hub can then be determined from,

$$\sigma_{max} = \frac{6M_{max}}{t^2} \text{ [Pa]} \tag{A.17}$$

Safety factors against yielding, for an external impact load P, can then be determined for each of the individual components using Equation A.18.

$$SF = \frac{\sigma_Y}{\sigma_{max}} \tag{A.18}$$

A.4 Finite Element Analysis: Tether Attachment Plate

A Finite Element Analysis (FEA) of the tether attachment plate is conducted in order to provide a precise indication of the bending stresses under load, by more accurately represent the specific boundary and loading conditions.

The analysis is conducted using the SimXpert 2015 Student Edition software package by the MacNeal-Schwendler Corporation (MSC). SimXpert is a visual environment with pre- and post-processing capabilities, and interfaces with MSC's Nastran FEA program which acts as the primary solver.

A 3-Dimensional CAD model of the plate is generated in Autodesk's Inventor 2012 and imported into SimXpert. The plate material is assumed both homogeneous and isotropic with mechanical properties of 6082 T6 aluminium as listed in Table A.1. A mesh is applied to the component using 3-Dimensional shell elements, with a patch test conducted to verify the mesh quality.

Figure A.3 illustrates the boundary and loading conditions applied in the FEA of the attachment plate. The plate boundary conditions are applied at the mounting locations to the vehicle hub as fully-fixed[1] supports, while the plate loading is modelled as four individual concentrated forces of 100 N, applied perpendicular to the plate surface at the mounting locations to the attachment bracket.

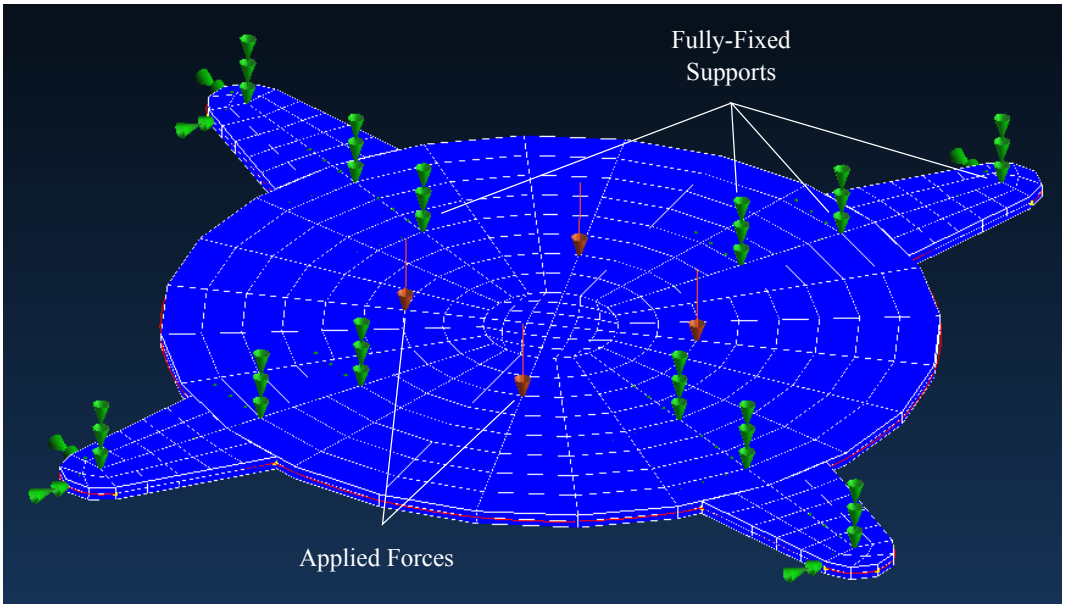

Figure A.3: FEA plate load and boundary conditions.

[1] Constrained against both translations in, and rotations about, all axes.

The results of the FEA are presented in Figure A.4 for the stress distribution in the attachment plate under a total 400 N load. Stress concentrations in the plate are observed at the load application points and around the innermost mounting locations where the maximum stress of $\sigma_{max} = 73$ MPa occurs. This results in a revised safety factor against yield of $SF = 3.9$, for the plate under a 400 N load.

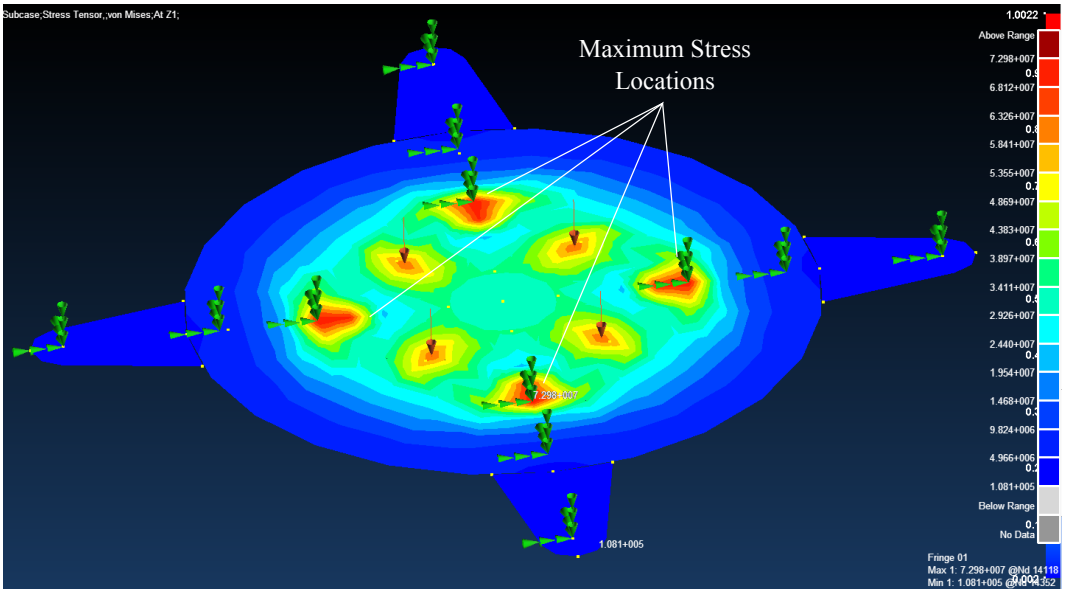

Figure A.4: FEA plate stress contours under load.

A.5 Material Properties

The material properties of 6082 T6 aluminium and tool steel are taken from Gale and Totemeier [46], while those of FR-4 are taken from Shigley [51].

Table A.1: Material properties of 6082 T6 aluminium.

Density	ρ	2.69	kg/m^3
Modulus of Elasticity	E	69	GPa
Yield Stress	σ_Y	285	MPa
Tensile Stress	σ_T	310	MPa
Poisson's Ratio	v	0.33	
Relative Permeability	$\frac{\mu_{Al}}{\mu_0}$	1.000022	
Static Friction Coefficient (Al-steel)	μ_s	0.6	
Kinetic Friction Coefficient (Al-steel)	μ_k	0.47	

Table A.2: Miscellaneous Mechanical Properties

Material	E [GPa]	σ_Y [MPa]	Poisson's Ratio
W1 Tool Steel	211	640	0.28
FR-4	24	448	0.136

A.6 Mass Moment of Inertia Experiment

The moment of inertia experiment is based on work by Treurnicht [50], and is used to determine the mass moment inertia, I_{zz}, about the z_B body axis.

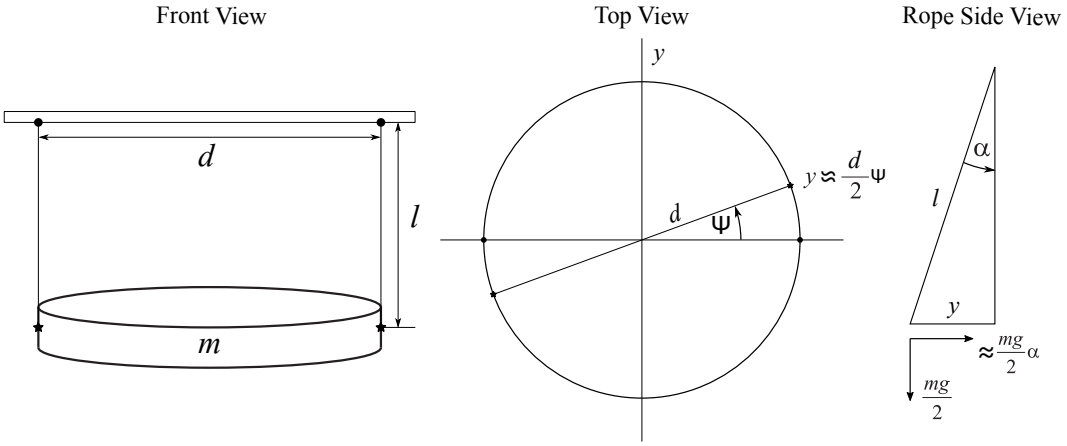

Figure A.5: Moment of Inertia Experiment Model.

The test setup is illustrated in Figure 3.16, and is modelled as per Figure A.5. The aircraft is modelled as a circular mass m of diameter d and inertia I. The aircraft is suspended by two massless and inextensible ropes of length l, such that the load on each rope is equivalent, $F_m = 2F_r = mg$.

By perturbing the system in yaw by a small angle ψ, the suspended object will be subjected to a counter-torque, τ. Assuming the perturbation angle is small the attachment offset y can be approximated as,

$$y = \frac{d}{2}\psi \text{ [m]} \tag{A.19}$$

Continuing with small angle approximation the resulting rope angle, α, can be approximated as,

$$\alpha = \frac{d\psi}{2l} \text{ [rad]} \tag{A.20}$$

The horizontal force exerted by each rope on the suspended system is determined as,

$$F_y = F_r\alpha \text{ [N]} \tag{A.21}$$

The counter-torque, τ, acting on the system can then be calculated as,

$$\tau = F_y d \approx \frac{mgd^2}{4l}\psi \text{ [N m]} \tag{A.22}$$

A torque balance in yaw for the system results in the following second-order equation,

$$I\ddot{\psi} = \tau \tag{A.23}$$

$$I\ddot{\psi} - \frac{mgd^2}{4l}\psi = 0 \tag{A.24}$$

With a natural frequency, ω_n, of,

$$\omega_n = \sqrt{\frac{mgd^2}{4Il}} \text{ [rad/s]} \tag{A.25}$$

The natural frequency is related to the measured period of oscillation, t_p, by,

$$t_p = \frac{2\pi}{\omega_n} \text{ [s]} \tag{A.26}$$

Equation A.25 can be solved for the moment of inertia I via algebraic manipulation as,

$$I = \frac{mgd^2}{16\pi^2 l}t_p^2 \text{ [kgm}^2\text{]} \tag{A.27}$$

Table A.3: PWM vs Thrust polynomial curve coefficients.

Test	Periods	Time [s]	Frequency [Hz]	t_p [s]
1	27	30.7	0.88	1.137
2	30	34.1	0.88	1.137
3	28	31.8	0.88	1.136
4	27	30.6	0.88	1.133
5	27	30.6	0.88	1.133
Average	27.8	31.56	0.88	1.135

From the test results in Table A.3, using a rope length of $l = 0.83$ m, a separation $d = 0.69$ m and a vehicle mass $m = 5.79$ kg, the mass moment of inertia about the z_B body axis is determined as,

$$I_{zz} \approx 0.266 \text{ [kgm}^2\text{]} \tag{A.28}$$

Appendix B

Miscellaneous Data

B.1 Additional PWM vs Thrust Mapping Results

Table B.1: PWM vs Thrust polynomial curve coefficients.

	Motor 1	Motor 2	Motor 3	Motor 4
a_0	1051.87	1051.85	1046.52	1053.90
a_1	20.60	21.89	20.05	20.43
a_2	0.73	0.54	0.66	0.88
a_3	-0.05	-0.04	-0.04	-0.06
b_0	1073.45	849.66	1150.22	1011.67
b_1	30.84	60.29	16.51	39.17
b_2	-1.05	-2.30	-0.40	-1.36
b_3	0.02	0.04	0.01	0.02

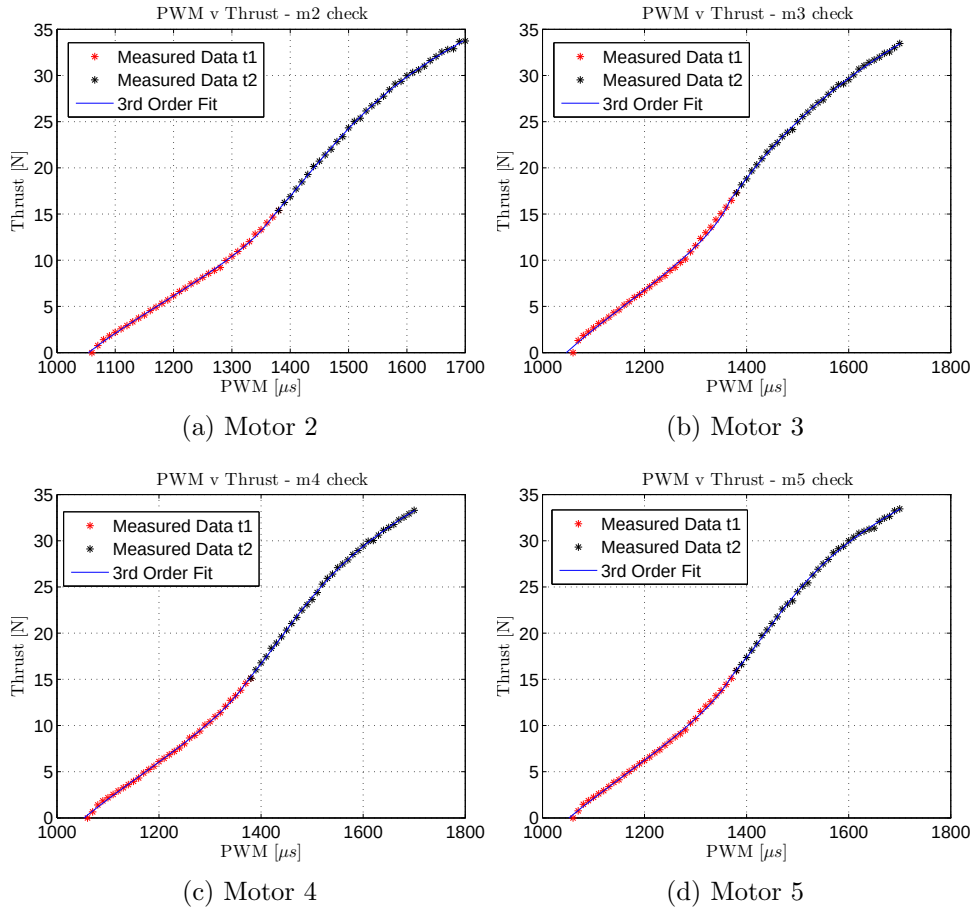

(a) Motor 2 (b) Motor 3

(c) Motor 4 (d) Motor 5

Figure B.1: PWM vs Thrust Curve Verification

B.2 Catenary Effect for various Tether Lengths

The catenary tension force and angle gradients are illustrated for 30, 50 and 70 m tether lengths.

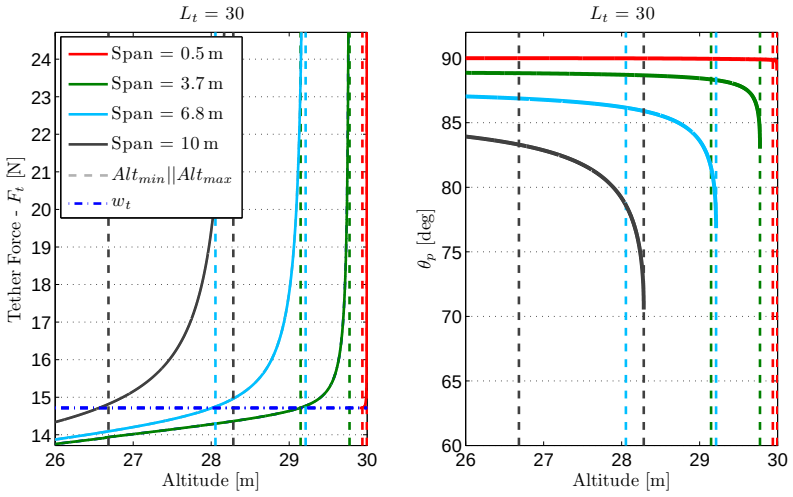

(a) 30 m Tether Length

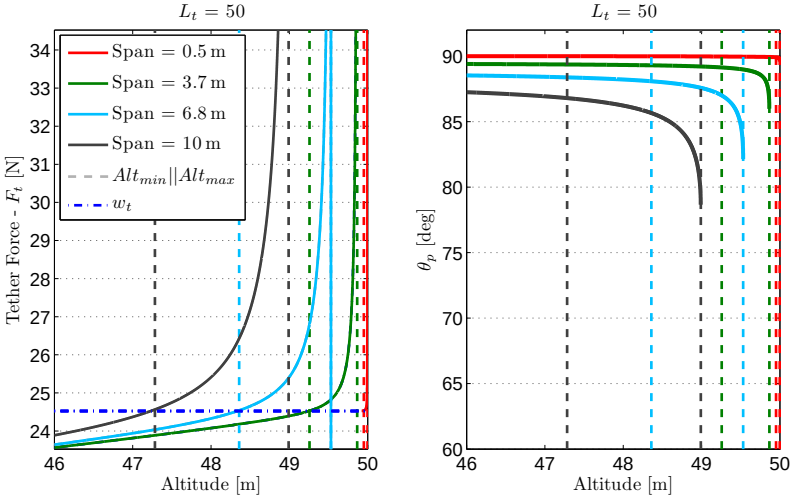

(b) 50 m Tether Length

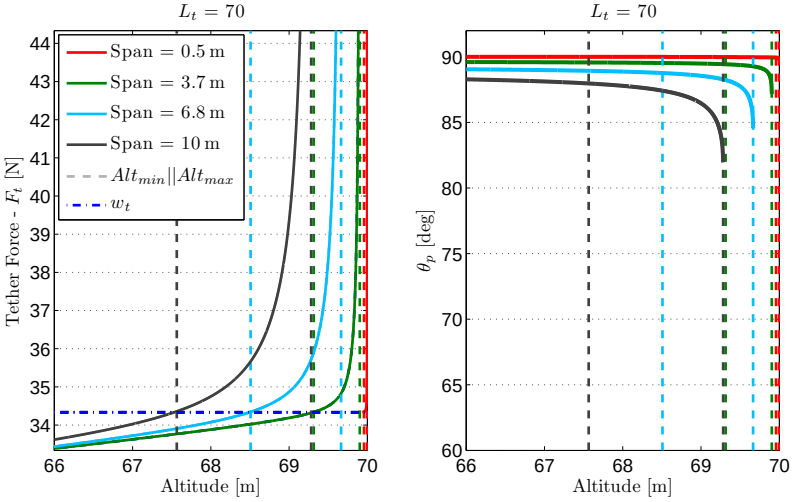

(c) 70 m Tether Length

Figure B.2: Illustration of the catenary effect for various tether lengths.

Bibliography

[1] S. Driessens and P. Pounds, "Towards a more efficient quadrotor configuration," in *Proc. IEEE International Conference on Intelligent Robots and Systems*, pp. 1386–1392, 2013.

[2] P. Pounds, R. Mahony, and P. Corke, "Modelling and control of a large quadrotor robot," *Control Engineering Practice*, vol. 18, no. 7, pp. 691 – 699, 2010.

[3] T. Nugent and J. Kare, "Laser power for UAVs," tech. rep., Laser Motive, 2010.

[4] Skysapience, "The HoverMast Family." `http://www.skysapience.com/products/hovermast-family`, 2012. [Online; accessed 2014-04-20].

[5] Cyphyworks, "The Persistent Aerial Reconnaissance and Communications (PARC) vehicle." `http://cyphyworks.com/parc/`, 2014. [Online; accessed 2014-06-10].

[6] Perspective Robotics AG, "Fotokite." `http://fotokite.com/`, 2014. [Online; accessed 2014-06-10].

[7] I. K. Peddle, "SLADe Project: Control and Simulation Report," tech. rep., Stellenbosch University, 2009.

[8] S. Lupashin and R. D'Andrea, "Stabilization of a Flying Vehicle on a Taut Tether using Inertial Sensing," in *Proc. International Conference on Intelligent Robots and Systems (IROS)*, 2013.

[9] N. Slegers, "Modelling and Control of a Tethered Rotorcraft," tech. rep., University of Alabama, 2010.

[10] L. Sandino, M. Bejar, K. Kondak, and A. Ollero, "On the use of tethered configurations for augmenting hovering stability in small-size autonomous helicopters," *Journal of Intelligent & Robotic Systems*, vol. 70, no. 1-4, pp. 509–525, 2013.

[11] L. Sandino, M. Bejar, K. Kondak, and A. Ollero, "Improving hovering performance of tethered unmanned helicopters with nonlinear control strategies," in *Proc. International Conference on Unmanned Aircraft Systems (ICUAS)*, pp. 443–452, 2013.

[12] G. Schmidt and R. Swik, "Automatic hover control of an unmanned tethered rotorplatform," *Automatica*, vol. 10, no. 4, pp. 393–403, 1974.

[13] Altaeros Energies, "Cost-effective tethered airborne platforms." `https://www.altaerosenergies.com/`, 2014. [Online; accessed 2014-06-05].

[14] Makani, "Energy Kites." `https://www.google.com/makani/`, 2013. [Online; accessed 2014-06-01].

[15] KITEnergy, "Prototype." `https://www.kitenergy.net/technology-2/prototype/`, 2014. [Online; accessed 2014-06-01].

[16] Sky WindPower, "Flying Electric Generators." `http://www.skywindpower.com/science_generators.htm?_p=Y`, 2013. [Online; accessed 2014-06-05].

[17] P. Williams, B. Lansdorp, and W. Ockels, "Modeling and Control of a Kite on a Variable Length Flexible Inelastic Tether," *AIAA Modeling and Simulation Technologies Conference and Exhibit*, 2007.

[18] P. Williams, B. Lansdorp, R. Ruiterkamp, and W. Ockels, "Modeling, Simulation, and Testing of Surf Kites for Power Generation," in *Proc. AIAA Modelling and Simulation Technologies Conference and Exhibit, Guidance, Navigation, and Control*, 2008.

[19] J. Breukels and W. Ockels, "A Multi-Body Dynamics Approach to a Cable Simulation for Kites," tech. rep., Delft University of Technology, 2007.

[20] S. De Groot, J. Breukels, R. Schmehl, and W. Ockels, "Modelling Kite Flight Dynamics Using a Multibody Reduction Approach," *Journal of Guidance, Control, and Dynamics*, vol. 34, no. 6, pp. 1671–1682, 2011.

[21] J. Goela, "Project report II on wind energy conversion through kites," Tech. Rep. No. DST/ME (JSG)/81-84/26/2, Indian Institute of Technology Kanpur, 1983.

[22] S. Hobbs, *A Quantitative Study of Kite Performance in Natural Wind with Application to Kite Anemometry*. Phd, Cranfield Institute of Technology, 1986.

[23] J. Goela, N. Somu, R. Abedinzadeh, and R. Kumar, "Wind loading effects on a catenary," *Journal of wind engineering and industrial aerodynamics*, vol. 21, no. 3, pp. 235–249, 1985.

[24] S. Hoerner, *Fluid-dynamic Drag: Practical Information on Aerodynamic Drag and Hydrodynamic Resistance*. Hoerner, 1965.

[25] I. Argatov, P. Rautakorpi, and R. Silvennoinen, "Apparent wind load effects on the tether of a kite power generator," *Journal of Wind Engineering and Industrial Aerodynamics*, vol. 99, no. 10, pp. 1079–1088, 2011.

[26] B. Roberts and W. Blackler, "Various Systems for Generation of Electricity Using Upper Atmospheric Winds," in *Proc. 2nd Wind Energy Innovation Systems Conf.*, pp. 67–80, Solar Energy Res. Institute, 1980.

[27] B. Roberts and D. Shepard, "Unmanned Rotorcraft to Generate Electricity Using Upper Atmospheric Winds," in *Proc. 10th Australian International Aerospace Congress*, 2003.

[28] B. Roberts, D. Shepard, K. Caldeira, E. Cannon, D. Eccles, A. Grenier, and J. Freidin, "Harnessing High Altitude Wind Power," *IEEE Transactions on Energy Conversion*, vol. 22, no. 1, pp. 136–144, 2007.

[29] B. Roberts, "Cost and Security of Electricity Generated by High Altitude Winds," tech. rep., Future Directions International, 2012.

[30] E. Terink, J. Breukels, R. Schmehl, and W. Ockels, "Flight Dynamics and Stability of a Tethered Inflatable Kiteplane," *Journal of Aircraft*, vol. 48, no. 2, pp. 503–513, 2011.

[31] P. Pounds, R. Mahony, and P. Corke, "Modelling and Control of a Quad-Rotor Robot," in *Proc. Australasian Conference on Robotics and Automation, ACRA*, vol. 4, pp. 1–44, Citeseer, 2006.

[32] P. Pounds, *Design, Construction and Control of a Large Quadrotor Micro Air Vehicle*. PhD thesis, Australian National University, 2007.

[33] E. Nice, "Design of a Four Rotor Hovering Vehicle," Master's thesis, Cornell University, 2004.

[34] S. Bouabdallah, *Design and Control of Quadrotors with Application to Autonomous Flying*. PhD thesis, École polytechnique fédérale de Lausanne, 2007.

[35] R. Mahony, V. Kumar, and P. Corke, "Modelling, Estimation, and Control of Quadrotor," *IEEE Robotics and Automation Magazine*, pp. 20–32, September 2012.

[36] G. Hoffmann, H. Huang, and S. Waslander, "Quadrotor helicopter flight dynamics and control: Theory and experiment," *American Institute of Aeronautics and Astronautics*, pp. 1–20, 2007.

[37] A. Zulu and S. John, "A Review of Control Algorithms for Autonomous Quadrotors," *Open Journal of Applied Sciences*, vol. 4, pp. 547–556, 2014.

[38] N. Özbek, M. Önkol, and M. Efe, "Feedback control strategies for quadrotor-type aerial robots: A survey," *Transactions of the Institute of Measurement and Control*, vol. 38, no. 5, pp. 529–554, 2016.

[39] M. Chen and M. Huzmezan, "A Simulation Model and H-infinity Loop Shaping Control of a Quad Rotor Unmanned Air Vehicle," in *Proc. IASTED International Conference on Modelling, Simulation and Optimatization*, pp. 320–325, 2003.

[40] M. Chen and M. Huzmezan, "A combined MBPC/2 DOF H-infinity Controller for a Quad Rotor UAV," in *Proc. AIAA Atmospheric Flight Mechanics Conference and Exhibit*, 2003.

[41] S. Lupashin, A. Schöllig, M. Hehn, and R. D'Andrea, "The flying machine arena as of 2010," in *Proc. IEEE International Conference on Robotics and Automation (ICRA)*, pp. 2970–2971, 2011.

[42] S. Lupashin, A. Schöllig, M. Sherback, and R. D'Andrea, "A simple learning strategy for high-speed quadrocopter multi-flips," in *Proc. IEEE International Conference on Robotics and Automation*, pp. 1642–1648, 2010.

[43] R. Ritz, M. Hehn, S. Lupashin, and R. D'Andrea, "Quadrocopter performance benchmarking using optimal control," in *Proc. IEEE International Conference on Intelligent Robots and Systems*, pp. 5179–5186, 2011.

[44] S. Lupashin and R. D'Andrea, "Adaptive fast open-loop maneuvers for quadrocopters," *Autonomous Robots*, vol. 33, no. 1-2, pp. 89–102, 2012.

[45] D. Brescianini, M. Hehn, and R. D'Andrea, "Quadrocopter pole acrobatics," in *Proc. IEEE/RSJ International Conference on Intelligent Robots and Systems*, pp. 3472–3479, 2013.

[46] W. F. Gale and T. C. Totemeier, *Smithells metals reference book*. Butterworth-Heinemann, 7 ed., 1992.

[47] T. Bresciani, "Modelling, identification and control of a quadrotor helicopter.," Master's thesis, Lund University, 2008.

[48] Y. Cengel and J. Cimbala, *Fluid Mechanics: Fundamentals and Applications*. McGraw-Hill, 2nd ed., 2010.

[49] W. Johnson, *Helicopter theory*. Dover Publications, 1994.

[50] J. Treurnicht, "Two-Rope Inertia Calculation," tech. rep., Stellenbosch University, 2006.

[51] R. G. Budynas and K. Nisbett, *Shigley's Mechanical engineering design*. McGraw-Hill, 9 ed., 2011.

[52] T. Capaccio, "Helicopter Carrying Seals Downed by Vortex, Not Mechanical Flaw." `http://www.bloomberg.com/news/articles/2011-05-05/commando-black-hawk-downed-by-air-vortex-not-mechanics-in-bin-laden-raid/`, 2011. [Online; accessed 2015-08-10].

[53] K. Gross, "Dispelling the myth of the mv-22," *PROCEEDINGS-UNITED STATES NAVAL INSTITUTE*, vol. 130, pp. 38–41, 2004.

[54] J. Engelbrecht and I. Peddle, "Advanced Automation 883: Introduction course to aircraft dynamics," tech. rep., Stellenbosch University, 2014.

[55] J. H. Blakelock, *Automatic control of aircraft and missiles*. John Wiley & Sons, 1991.

[56] B. Etkin and L. Reid, *Dynamics of Flight, Stability and Control*. John Wiley & Sons, 3rd ed., 1996.

[57] G. Fay, "Derivation of the aerodynamic forces for the mesicopter simulation," *Standord University. Stanford, CA*, 2001.

[58] C. Justus and A. Mikhail, "Height variation of wind speed and wind distributions statistics," *Geophysical Research Letters*, vol. 3, no. 5, pp. 261–264, 1976.

[59] H. M. Irvine, *Cable structures*. Dover Publications, 1992.

[60] D. L. Dean, "Static and dynamic analysis of guy cables," *Journal of the Structural Division*, vol. 87, no. 1, pp. 1–22, 1961.

[61] J. Stewart, *Calculus*. Brooks Cole, 6 ed., 2008.

[62] J. P. Den Hartog, *Mechanical vibrations*. McGraw-Hill New York, 3 ed., 1947.

[63] C. M. Harris and A. G. Piersol, *Harris' shock and vibration handbook*, vol. 5. McGraw-Hill New York, 2002.

[64] W. C. Young and R. G. Budynas, *Roark's formulas for stress and strain*, vol. 7. McGraw-Hill New York, 2002.